DISCLAIMER
The publication of papers in International Journal of Engineering does not imply that the editorial board, reviewers or publisher accept, approve or endorse the data and conclusions of authors.

CONTENTS

Transactions C: Aspects

International Journal of Engineering

Journal Homepage: www.ije.ir

Design and Real Time Digital Simulator Implementation of a Takagi Sugeno Fuzzy Controller for Battery Management in Photovoltaic Energy System Application

A. Basu*, M. Singh

Department of Electrical Engineering, National Institute of Technology, Jamshedpur, India

A B S T R A C T

This paper presents a acomprehensive design and control strategy for a photovoltaic (PV) energy storage system. The system consists of a 2kW photovoltaic system, two converter circuits, a resistive load of 6 Ohm and a lithium-ion battery storage integrated with DC Bus applying constant power to the resistive load. This scheme offered two converter topologies, one is a boost converter and another is a DC/DC bidirectional converter. The boost converter is directly connected in series to the PV array whereas the bidirectional DC/DC converter (BDC) is connected to the battery. The boost converter is used to regulate the maximum power point tracking (MPPT) of the PV array. Closed-loop control of the bidirectional controller is implemented with Takagi-Sugeno Fuzzy (TS-Fuzzy) controller to regulate the battery charging and discharging power flow. The proposed scheme provides a good stabilization in the DC bus volatge. Simulation results of the proposed control schema under MATLAB/Simulink are presented and compared with the Proportional Integral (PI) controller. The simulation results obtained from MATLAB are verified on Real Time Digital Simulator (RTDS).

doi: 10.5829/ije.2022.35.12c.01

NOMENCLATURE

I_{pv}	Current from PV cell in amps	V_{oc}	Open-Circuit voltage of PV array in volts
I_O	Reverse saturation current of diode in amps	I_{sc}	Short circuit current of PV array in amps
η	Diode ideality factor	L	Inductor of boost converter in henry
V	Voltage across diode in volts	Io	Output current of boost converter in amps
V_T	Thermal voltage in volts	C_2	Output capacitor of boost converter in farads
V_{mp}	Voltage of PV array at MPP in volts	ΔI_L	Ripple current of bidirectional converter
I_{mp}	Current of PV at MPP in amps	V_O	Output voltage of boost converter in volts
Fsw	Switching frequency in kHz	$Vbat$	Battery voltage in volts
ΔV	Output voltage ripple of boost converter	ΔV_{dc}	Ripple voltage of bidirectional converter
Δi_1	Output current ripple of boost converter	V_{dc}	Voltage of DC bus in volts
D	Duty cycle	ΔI_L	Ripple current of bidirectional converter
Vin	Input voltage of boost converter in volts	I_{bat}	Battery current in amps

1. INTRODUCTION

Sustainable energy has played a vital role to control the global emission. Over the last few decades on average, 300GW renewable energy sources (RES) were grown in the year between 2018 and to reach the goal of the Paris agreement, according to the IEA'S Sustainable Development Scenario (SDC). A country like India has a significant advantages as there is a huge potential for sustainable energy resources. In 2023, the installed renewable energy capacity will be account for 35% [1]. The installed capacity of renewable energy in India is about 150GW in which wind power is 40.08GW, 49.34GW solar power, 10.61GW bio power, 4.83GW

Corresponding Author Institutional Email: 2020rsee004@nitjsr.ac.in
(A. Basu)

small hydro and 46.51 GW large hydro. The Government of India has targeted to expand the renewable energy installed capacity to 500 GW by 2030[2]. Photovoltaic power plays a significant role in power generation and has become essential due to the storage and the environmental impact. PV system is a non-linear system, hence it is too sensitive to determine the characteristics of the magnitude of the systems, which have the single point where the power is maximum. Faranda et al. [2] discussed that the power produced by the PV is more than 45%. Berrera et al. [3] discussed that the PV generation system has two problems i.e., the energy conversion efficiency is low due to the weather changes and hence the power generation of solar array is changed. Liu et al. [4] proposed that the PV array consists of non-linear characteristics, hence the I-V and P-V characteristics are always changing with weather conditions. Esram et al. [5] proposed the P&O method for the MPPT technique irrespective of different irradiation and temperature. Esram et al. [5] also proposed another method of MPPT i.e., the incremental conductance method (INC). The comparison of different types of technique in MPPT methods such as fuzzy controller, neural network, current sweep etc. is discussed in the literature [6-8]. The integration of the PV with the energy storage system (ESS) is an emerging research area. Usually, ESS is constituted by battery. However, the loads are also necessary when PV and battery storage system (BSS) are connected. Samadi and Saif [9, 10] presented the mathematical model for state-of-charging (SOC) estimation for battery management system. However, the performance of the controller in the presence of a non-linear system is not discussed. Based on the literature review, various control algorithms are proposed for the battery management system [11]. The proposed TS-fuzzy control algorithm is compared to the Proportional Integral (PI) control algorithm. The conventional PI controller gains value are fixed for the certain radiation and load. Any change in these values the controller output signal will not be appropriate [12, 13]. Moreover, PI controller has higher overshoot and undershoot values, which is reduced by the proposed controller. The performance of the controller is analyzed in terms of battery current, load current and settling time. In this paper, a circuitry modelling and control strategy of a 2kW PV energy storage system is presented. The PV array directly converts the sunlight into an electrical signal (DC). The DC output of the PV array is given to the boost converter to implement the MPPT. The maximum power is extracted by using Perturb & Observe (P&O) method. A 48 Volts, 200Ah lithium-ion battery is used for the energy storage system. Moreover, the simulation results show the performance parameter of the TS-Fuzzy controller.

2. PHOTOVOLTAIC ENERGY STORAGE SYSTEM

The proposed photovoltaic (PV) energy system is shown in Figure 1. The system is composed of a photovoltaic cell; a boost converter performs MPPT technique of a PV array through P&O algorithm, a 48V battery storage, connected through a bidirectional DC-DC converter. Some authors have proposed a classical controller scheme for the control mechanism of a bidirectional DC/DC converter. Though classical controllers have the advantage of non-zero steady-state error but also have the limitations associated with overshoot, undershoot, high settling time etc. [14]. Given the ongoing limitations, this paper proposes a sophisticated design of Takagi-Sugeno Fuzzy controller scheme.

2. 1. Modelling of Pv Cell   The equivalent circuit topology of a PV model is shown in Figure 2.
    The PV current (*Ipv*) is given by Equation (1) [15, 16].

$$I_{PV} = I_D + I \tag{1}$$

$$I_{PV} = I_O(e^{\frac{V}{\eta V_T}} - 1) \tag{2}$$

$$\text{Since, } I_D = I_O(e^{\frac{V}{\eta V_T}} - 1) \tag{3}$$

$$I = I_{PV} = I_O\left(e^{\frac{V}{\eta V_T}} - 1\right) \tag{4}$$
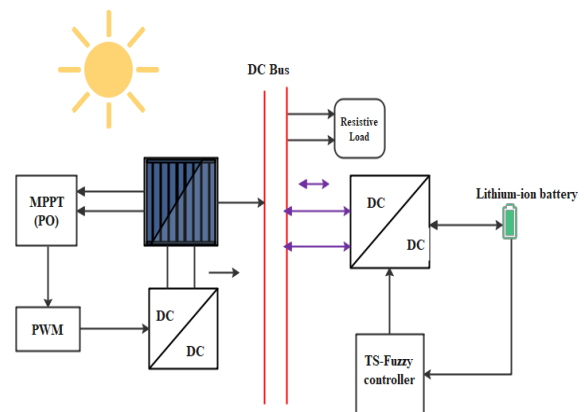
Figure 1. Schematic diagram of photovoltaic Energy System
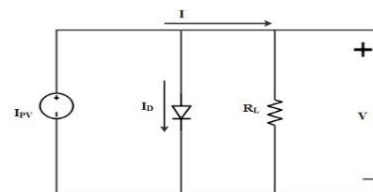
Figure 2. Electrical circuit model of PV panels

where I_D represents the diode current depends upon voltage and temperature. Using the above equations, the PV array is modeled in MATLAB, from the data sheet of 1Soltech 1STH-215-P with a specified temperature of 25° C. The power –voltage curve of PV panel with different irradiation values is presented in Figure 3.

The parameters of the proposed PV system are shown in Table 1.

2. 2. Design of Boost Converter

Figure 4 represents the circuit diagram of a boost converter used in this system. The switching frequency (F_{sw}) is considered as 5 kHz and the output voltage ripple (ΔV) and output current ripple (Δi_l) are considered as 5% and 10 %, respectively.

The design parameters of the boost converter are shown below [17]:

$$Duty\ Cycle(D)=1-(V_{in}/V_o) \tag{5}$$
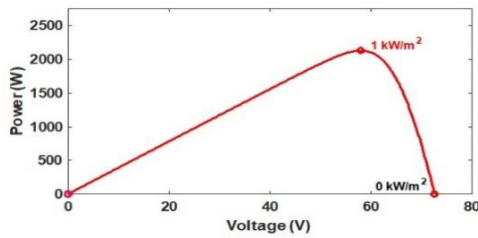
Figure 3. Power-voltage curve at the irradiation of 1000W/m² and 0W/m²

TABLE 1. Parameters of proposed PV array

Parameters	Values
PV array	5 parallel string 2 series connected module per string Total=2kWp
PV array Open circuit voltage (Voc)	36.3 V
PV array Voltage at maximum power point (Vmp)	29V
PV array Short circuit current (Isc)	7.84A
PV array Current at maximum power point (Imp)	7.35A
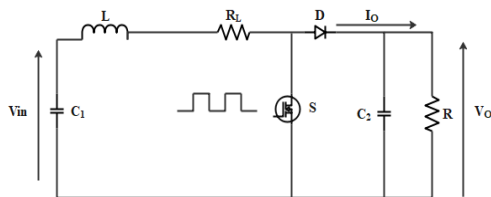
Figure 4. Boost converter Topology

V_{in}= input of boost converter=output of PV array. The inductor value is given as,

$$L=V_{in}\ D/(2\Delta i_l F_{sw}) \tag{6}$$

The output capacitor value is given by,

$$C_2=I_O D/(\Delta V F_{sw}) \tag{7}$$

The parameters of the boost converter are illustrated in Table 2.

3. MAXIMUM POWER POINT TRACKER

The MPPT with PWM control method measure the current and voltage of the PV array and generates the duty cycle for the converter. Due to simplicity, ease of application, periodic tuning is not required and is used in both analogue and digital domains Perturb & Observation (P&O) is preferred for maximum power point tracking (MPPT) [18].

The basic control actions for various operation points in the P&O method are shown in the Table 3.

4. BI-DIRECTIONAL DC/DC CONVERTER

The bidirectional converters allow transferring of power of two DC sources in either direction. The converter consists of two switches S_{buck} and S_{boost} , which manages the charging –discharging process as shown in Figure 5.

In the buck mode switch S_{buck} in on, stored energy in the inductor is supplied to the battery for charging purposes. For operation in buck mode, the inductor filter design is carried out as follows:

$$L_+ = \frac{(V_{dc}-V_{bat})D_+}{\Delta I_L f_{sw}} \tag{8}$$

TABLE 2. Parameters of boost converter

Parameters	Values
Input voltage of boost converter	50-52 Volts
output voltage of boost converter	60 Volts
Duty Cycle	0.15-0.75
inductance	1.7 mH
Output capacitance	1.786 µF

TABLE 3. Various control operation of P&O Algorithm

Case	ΔV	ΔP	Voltage Control Action	Duty Cycle
1	+	+	Increase V by ΔV	Decrease
2	-	-	Increase V by ΔV	Decrease
3	-	+	Decrease V by ΔV	Increase
4	+	-	Decrease V by ΔV	Increase
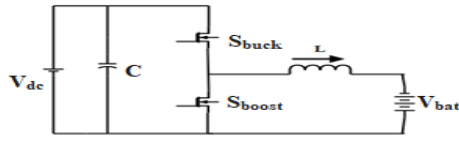
Figure 5. DC/DC non–isolated bi-directional converter
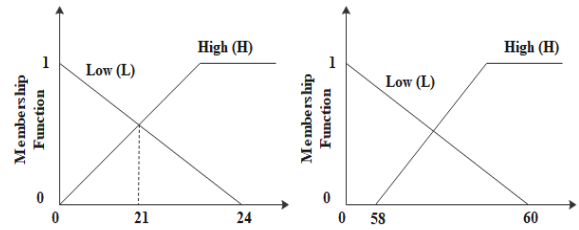
Figure 6. Membership function of TS-Fuzzy control

$$C_+ = \frac{(1-D_+)V_{bat}}{8L+\Delta V_{bat}f^2} \qquad (9)$$

where, ΔI_L and f_{sw} are the ripple current and switching frequency of the buck converter respectively. In the boost mode switch S_{boost} is on, inductor discharges the stored energy. For bidirectional converter operation in the boost mode, the inductor filter design value is carried out as follows:

$$L_- = \frac{V_{bat}\,D_-}{\Delta I_L f_{sw}} \qquad (10)$$

$$C_- = \frac{V_{dc}\,D_-}{R_O \Delta V_{dc}\,f_{sw}} \qquad (11)$$

ΔV_{dc}, is the ripple voltage of the boost converter respectively. The parameters of the bidirectional converter are illustrated in Table 4.

5. BATTERY MANAGEMENT SYSTEM

To charge the battery bank, which is connected to the PV array as the energy storage system (ESS) battery management system (BMS) is used. The charging-discharging of the ESS depends on the power generated by the PV array [19]. If the total power is greater than the desired limit, the battery is charging or vice-versa. The initial state of charge (SOC %) of the battery is considered 80%. Here, TS-fuzzy logic controller is used for BMS.

The Takagi-Sugeno model is considered as an exact representation of the non-linear system. In general, there are two approaches for designing the TS-fuzzy model.
1. Identify the input-output data for the system.
2. Derivation from the given non-linear system.
In this system, load voltage (V_c)/current (i_L) are taken as input variables for designing the TS-fuzzy controller. Input signals are fuzzified by means of two linguistic memberships (MFs) values; L and H for low and high respectively as shown in Figure 6.

TABLE 4. Parameters of bidirectional converter

Parameters	Values
C	$500\ \mu F$
L	$1\ mH$
f_{sw}	5kHz

Here we choose a nonlinear term: i_L
Because the average current is about 21 A
Therefore, we define the range: 0-24

$$\begin{cases} M_{11}(i_L(t)) = \frac{1}{24}i_L(t) \\ M_{12}(i_L(t)) = 1 - \frac{1}{24}i_L(t) \end{cases} \qquad (12)$$

The model rule i (Buck Mode):
If $q_1(t)$ is Mi_1
Then,

$$\dot{x}(t) = A_i x(t) + B_i u(t) + E_i v(t),\ i = 1,2 \qquad (13)$$

where, $q_1(t)$: The non linear term
Mi_1: The ith Membership function
Control Rule i (Buck Mode):
If $q_1(t)$ is Mi_1
Then $u(t) = F_I x(t), i = 1,2$
where, $F_I = Control\ gain$
The closed loop TS-Fuzzy control signal (Buck Mode):

$$\dot{x}(t) = \sum_{i=1}^{2}\sum_{j=1}^{2} h_i(\dot{q}(t))h_j(q(t))(A_i - B_i F_j)\,x(t) + E_i v(t) \qquad (14)$$

Another nonlinear term: V_c
Because the average DC bus voltage is about 58 V
So we define the range: 0-60

$$\begin{cases} M_{21}(V_c(t)) = \frac{1}{60}V_c(t) \\ M_{22}(V_c(t)) = 1 - \frac{1}{60}V_c(t) \end{cases} \qquad (15)$$

Model Rule i (Boost Mode);
If, $q_1(t)$ is M_{P1}, $q_2(t)$ is M_{P2}
Then,

$$\dot{x(t)} = A_i x(t) + B_i u(t) + E_i v(t), i = 1,2,4 \qquad (16)$$

where, $q_1(t), q_2(t)$: The non linear term
M_{P1}, M_{P2}: The ith Membership function
Control Rule i (Boost Mode):
If, $q_1(t)$ is M_{P1}, $q_2(t)$ is M_{p2}
Then, $u(t) = -F_I x(t), i = 1,2..4$
where, $F_I = Control\ gain$
The closed loop TS-Fuzzy control signal (Boost Mode):

$$\dot{x}(t) = \sum_{i=1}^{4}\sum_{j=1}^{4} h_i(\dot{q}(t))h_j(q(t))(A_i - B_i F_j)\,x(t) + E_i v(t) \qquad (17)$$

6. RTDS IMPLEMENTATION AND RESULT DISCUSSION

The real time simulator is powerful modulator, distributed real time simulator, implemented on MATLAB/Simulink model-based design using in hardware-in-loop and off-line simulation. The architecture of RT-LAB is shown in the Figure 7.

It consists of host and target. The host is a Personal Computer in which MATLAB and RT-LAB are loaded. The target machine includes Intel Xeon E3 V5 CPU, Kintex-7 FPGA, 325T, 326,000 logic cells, and 840 DSP slice. The TCP/IP connects target machine and the host computer. The host PC interfaces and communicates with the target through Ethernet. Digital Storage Oscilloscope is used for data observation and verification of real simulation. According to the RT-LAB naming convention, the subsystems are named with a prefix which identifying their function. The prefixes are described as SM_main subsystem (always one). It contains the computational elements of the model. In this scheme, blocks namely PV model, boost converter, bidirectional converter, battery and load are assembled to construct SM_main subsystem (Figure 8). SC_main subsystem (at most one): In general, it includes all user interface blocks. In this scheme, blocks namely scope and manual switches are used as shown in Figure 9.
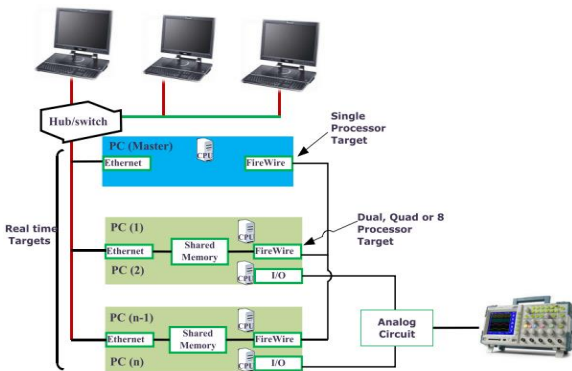
Figure 7. RT-LAB Simulator architecture
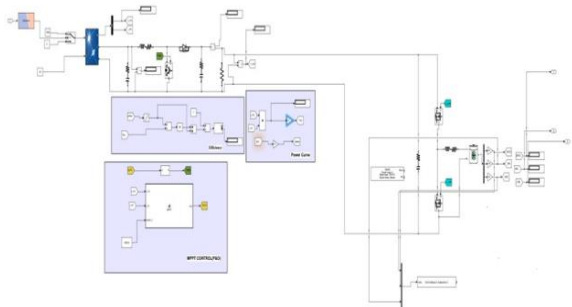
Figure 8. Configuration of the SM_main subsystem
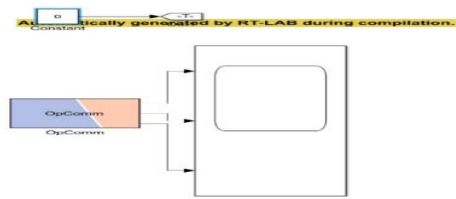
Figure 9. Configuration of the SC_main subsystem

The step size of the simulation is 0.02 ms. Firstly, the closed loop control of the bidirectional converter is implemented in the RT-LAB by using PI Controller. Then the proposed TS-Fuzzy controller is implemented to modify the performance of the parameter.

The real time results of PI controller are shown in Figure 10. It is demonstrated in Figure10 (a) that when the solar isolation is 1000W/m^2, the battery is charging. With a decrease in solar isolation there is a decreased in the produced power and the battery goes discharging. In the discharging mode, the battery current (*Ibat*) flows in reverse direction shown in Figure 10(c). An overshoot is observed during charging mode in case of PI controller.

The overshoot is eliminated in TS-Fuzzy controller. Remarkable ripple in battery current is found with PI but with TS-Fuzzy controller, it is eliminated shown in Figure 11(d).
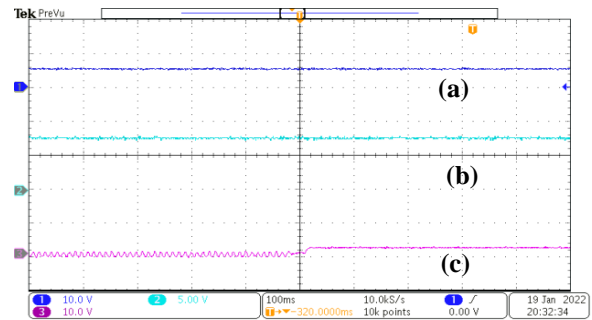
Figure 10. RTDS Hardware results for PI Controller (top to bottom) (a) SOC (20V/div), (b) V$_{bat}$ (10V/div), (c) I$_{bat}$ (5V/div)
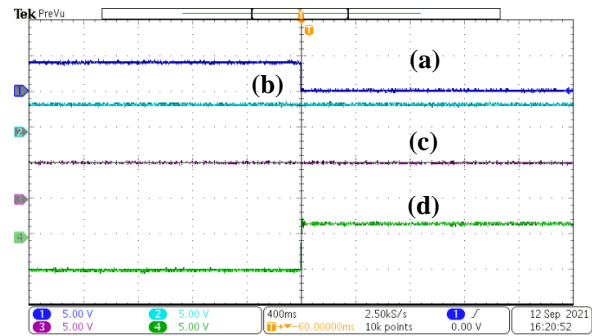
Figure 11. RTDS Hardware results for TS-fuzzy controller (top to bottom) (a)irr (250V/div), (b)SOC (20V/div), (c) V$_{bat}$ (10V/div), (d) I$_{bat}$ (5V/div)

7. SIMULATION RESULTS

Simulated results of the PV system are shown in Figure 12. Figure 12(a) shows that at t=0 to 1.5s, the irradiation is 1000W/m², output voltage of PV array is 60V and the current is 40A. At t=1.5 s to 3s the irradiation decreases at 0 W/m², the voltage and current of the PV array decreases 0V and 0A respectively are shown in Figures 12(b) and 12(c). The DC bus voltage maintain the constant voltage around 60 Volts as shown in Figure 12(d). Meanwhile, from Figure 10(e) it observes that the system can track the maximum power of 2kW with the irradiation of 1000W/m².

The second set of simulations show the closed-loop TS-Fuzzy controller. Figure 13(a) shows the battery state of charging (SOC %) increases from t=0s to 1.5s. The SOC of the battery is reduced from 1.5s, the battery current i.e. *Ibat* is reversed in direction and the battery voltage V*bat* is given a step change from 52 volts to 51 volts as shown in Figures 13(b) and 13(c). Therefore, the BMS starts.

Here, performance parameters of different Controllers are illustrated in Table 5.
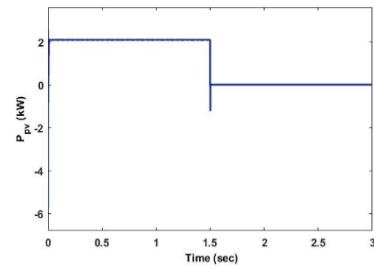
(d)
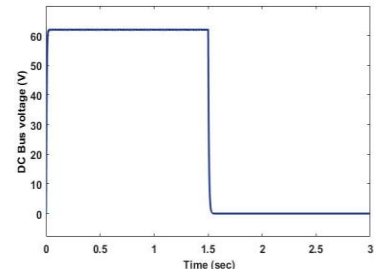
(e)

Figure 12. MATLAB simulation results of (a) irradiance, (b) output voltage, (c) current, (d) DC Bus voltage and (e) output power of PV system

(a)

(b)
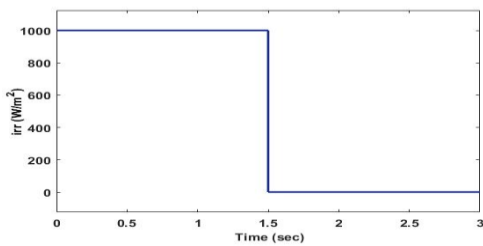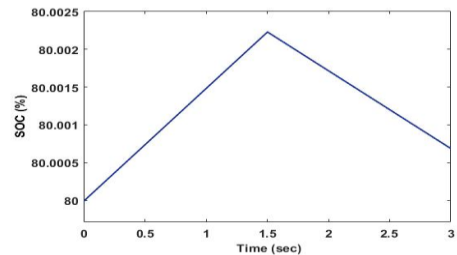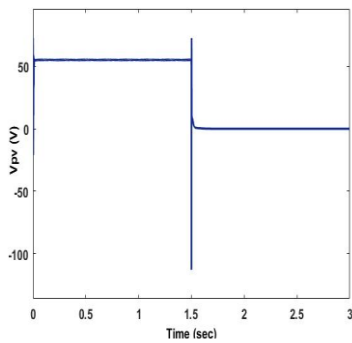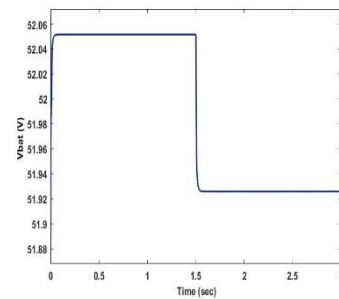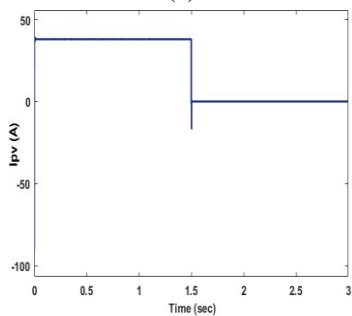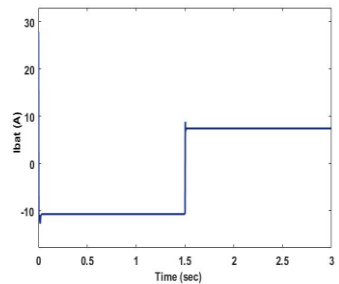
(c)

Figure 13. MATLAB simulation results of TS-Fuzzy controller (a) SOC (%) (b) V_{bat} (V) (c) I_{bat} (A)

(a)

(b)

(c)

TABLE 5. Performance parameters of different controllers

Controller		Ref [13]	Proposed TS-Fuzzy
I_{bat}	Overshoot(s)	0.05	0.002
	Undershoot(s)	0.55	0.035
Load Current	Overshoot(s)	0.4	0.002
	Undershoot(s)	0.43	0.003
Settling Time		61s	13.682ms

8. CONCLUSION

The proposed energy management system proves better performance with TS-Fuzzy controller than PI controller. Due to the advantage of less overshoot, rise time and fast dynamic response the TS-Fuzzy controller is preferred. The battery management system is used to charge and discharge the battery according to the generated power of the system. This is verified using performance parameter of the controllers. Two controller schemes PI and TS-Fuzzy have been simulated in MATLAB/SIMULINK environment and at RT-LAB. The results obtained are analyzed and performance have been compared to identify the best performer in similar conditions.

9. REFERENCES

1. Majid, M., "Renewable energy for sustainable development in india: Current status, future prospects, challenges, employment, and investment opportunities", *Energy, Sustainability and Society*, Vol. 10, No. 1, (2020), 1-36. doi: 10.1186/s13705-019-0232-1.

2. Faranda, R., Leva, S. and Maugeri, V., "Mppt techniques for pv systems: Energetic and cost comparison", in 2008 IEEE Power and Energy Society General Meeting-Conversion and Delivery of Electrical Energy in the 21st Century, IEEE., (2008), 1-6.

3. Berrera, M., Dolara, A., Faranda, R. and Leva, S., "Experimental test of seven widely-adopted mppt algorithms", in 2009 IEEE Bucharest PowerTech, IEEE., (2009), 1-8.

4. Liu, F., Duan, S., Liu, F., Liu, B. and Kang, Y., "A variable step size inc mppt method for pv systems", *IEEE Transactions on Industrial Electronics*, Vol. 55, No. 7, (2008), 2622-2628.

5. Esram, T. and Chapman, P.L., "Comparison of photovoltaic array maximum power point tracking techniques", *IEEE Transactions on Energy Conversion*, Vol. 22, No. 2, (2007), 439-449. http://dx.doi.org/10.1109/TEC.2006.874230

6. Eltamaly, A.M., Performance of mppt techniques of photovoltaic systems under normal and partial shading conditions, in Advances in renewable energies and power technologies. 2018, Elsevier.115-161.

7. Kamal, N.A. and Ibrahim, A.M., "Conventional, intelligent, and fractional-order control method for maximum power point tracking of a photovoltaic system: A review", *Fractional Order Systems*, (2018), 603-671. http://dx.doi.org/10.1016/B978-0-12-816152-4.00020-0

8. Zhang, K., "Control simulation and experimental verification of maximum power point tracking based on rt-lab", *International Journal of Engineering, Transactions A: Basic* Vol. 29, No. 10, (2016), 1372-1379. http://dx.doi.org/10.5829/idosi.ije.2016.29.10a.07

9. Samadi, M.F. and Saif, M., "State-space modeling and observer design of li-ion batteries using takagi–sugeno fuzzy system", *IEEE Transactions on Control Systems Technology*, Vol. 25, No. 1, (2016), 301-308. http://dx.doi.org/10.1109/TCST.2016.2549270

10. Samadi, M.F. and Saif, M., "Takagi-sugeno fuzzy model identification of li-ion battery systems", in 2014 World Automation Congress (WAC), IEEE., (2014), 421-426.

11. Al Alahmadi, A.A., Belkhier, Y., Ullah, N., Abeida, H., Soliman, M.S., Khraisat, Y.S.H. and Alharbi, Y.M., "Hybrid wind/pv/battery energy management-based intelligent non-integer control for smart dc-microgrid of smart university", *IEEE Access*, Vol. 9, (2021), 98948-98961. http://dx.doi.org/10.1109/ACCESS.2021.3095973

12. Subha, S. and Nagalakshmi, S., "Design of anfis controller for intelligent energy management in smart grid applications", *Journal of Ambient Intelligence and Humanized Computing*, Vol. 12, No. 6, (2021), 6117-6127. https://doi.org/10.1007/s12652-022-04177-1

13. Cabrane, Z., Kim, J., Yoo, K. and Ouassaid, M., "Hess-based photovoltaic/batteries/supercapacitors: Energy management strategy and dc bus voltage stabilization", *Solar Energy*, Vol. 216, (2021), 551-563. https://doi.org/10.1016/j.solener.2021.01.048

14. Parise, G., Martirano, L., Kermani, M. and Kermani, M., "Designing a power control strategy in a microgrid using pid/fuzzy controller based on battery energy storage", in 2017 IEEE International Conference on Environment and Electrical Engineering and 2017 IEEE Industrial and Commercial Power Systems Europe (EEEIC/I&CPS Europe), IEEE., (2017), 1-5.

15. Pattanaik, P., "Boost converter based on photovoltaic energy system", *International Journal of Innovative Technology and Exploring Engineering*, Vol. 8, No. 11S, (2019).

16. Awda, L., KHALAF, Y. and Salih, S., "Analysis of temperature effect on a crystalline silicon photovoltaic module performance", *International Journal of Engineering, Transactions B: Applications*, Vol. 29, No. 5, (2016), 722-727. http://dx.doi.org/10.5829/idosi.ije.2016.29.05b.17

17. Verma, A.K., Singh, B. and Kaushik, S., "An isolated solar power generation using boost converter and boost inverter", *International Journal of Engineering and Information Technology*, Vol. 2, No. 2, (2010), 101-108.

18. Femia, N., Petrone, G., Spagnuolo, G. and Vitelli, M., "Optimization of perturb and observe maximum power point tracking method", *IEEE Transactions on Power Electronics*, Vol. 20, No. 4, (2005), 963-973. http://dx.doi.org/10.1109/TPEL.2005.850975

19. Bhattacharyya, S., Puchalapalli, S. and Singh, B., "Battery management and operation of a wind-pv based microgrid", in 2020 IEEE International Conference on Computing, Power and Communication Technologies (GUCON), IEEE., (2020), 423-429.

Persian Abstract

چکیده

این مقاله یک طراحی جامع و استراتژی کنترل برای یک سیستم ذخیره انرژی فتوولتائیک (PV) ارائه می‌کند. این سیستم شامل یک سیستم فتوولتائیک ۲ کیلوواتی، دو مدار مبدل، یک بار مقاومتی ٦ اهم و یک ذخیره‌سازی باتری لیتیوم یونی است که با باس DC یکپارچه شده است که برق ثابتی را به بار مقاومتی اعمال می‌کند. این طرح دو توپولوژی مبدل را ارائه می‌دهد، یکی مبدل تقویت کننده و دیگری مبدل دوطرفه DC/DC. مبدل تقویت کننده مستقیماً به صورت سری به آرایه PV متصل می‌شود در حالی که مبدل دو طرفه DC/DC (BDC) به باتری متصل است. مبدل تقویت کننده برای تنظیم حداکثر ردیابی نقطه توان (MPPT) آرایه PV استفاده می‌شود. کنترل حلقه بسته کنترل کننده دو طرفه با کنترلر Takagi-Sugeno Fuzzy (TS-Fuzzy) برای تنظیم جریان شارژ و تخلیه باتری اجرا می‌شود. طرح پیشنهادی تثبیت خوبی در ولتاژ باس DC فراهم می کند. نتایج شبیه‌سازی طرحواره کنترل پیشنهادی تحت MATLAB/Simulink ارائه شده و با کنترل‌کننده انتگرال متناسب (PI) مقایسه می‌شود. نتایج شبیه‌سازی به‌دست‌آمده از MATLAB در شبیه‌ساز دیجیتالی واقعی (RTDS) تأیید می‌شوند.

International Journal of Engineering

J o u r n a l   H o m e p a g e :   w w w . i j e . i r

Installation Depth and Incident Wave Height Effect on Hydrodynamic Performance of a Flap Type Wave Energy Converter: Experimental Analysis

G. Sadripour, R. Shafaghat*, B. Alizadeh Kharkeshi, R. Tabassom, A. Mahmoudi

Sea-Based Energy Research group, Babol Noshirvani University, Babol, Iran

P A P E R I N F O	*A B S T R A C T*

The effect of installation depth and height of the incident wave on the hydrodynamic and economic performance of an oscillating wave surge converter (OWSC) wave energy converter is crucial. In this study, an OWSC by considering 1:8 scale has been studied under Caspian Sea wave conditions for 8 water depths from the semi-submerged to fully submerged. The study has been conducted to achieve the best draft ratio and evaluate the systems performance imposed to Caspian waves condition by experimantal method. The results are presented in three parts. The first part studied the converter's flow, power, and sensitivity to the installation depth on a laboratory scale. In the second part, the system results were converted to the main scale 1:8 by using Froude scaling method, and finally, the performance from an economic view evaluated. Results showed that the draft depth has a non-linear effect on the power. System's power in the dimensionless draft depth of 0.59 is better, and can produce 61 kW. Also, it can pump up to 50 l/s of water. Likewise, suppose the system is used for electricity generation, In that case, it sells $22500 of electricity to the grid annually, and if it is used as a pump, it can supply water to 4710 households on average.

Symbols

d	Draft (meters)	*P*	Power (W)	
H	Incident wave height (meters)	*Q*	Flow (cubic meters per second)	
h	Water depth (meters)	*AEP*	Annual Energy Production (MWh)	

1. INTRODUCTION

Today, fossil fuel resources have increased due to the high rate of population growth and industry development. Fossil fuels can cause many problems like rising atmospheric carbon dioxide, global warming, and climate change [1]. Therefore, the development of technologies that can produce economical and clean energy from renewable energy sources has become one of the main goals of modern industrial societies. Renewable energy sources include wave energy, solar energy, wind energy, and geothermal energy. Ocean wave energy has a higher energy density than other energy sources. Global wave energy sources are estimated to be more than 1 TW [2].

Wave energy converters come in various designs and sizes that use a wide range of energy conversion techniques. Oscillating Wave Surge Converters (OWSC) is a type of wave energy converters with a higher theoretical efficiency due to oscillations in surge direction [2]. OWSC is designed for areas near the coast, with water depths between 10 and 20 meters [3]. The energy conversion chain in these converters has three stages; In the first stage, the flap is affected by the force of the wave, due to the oscillating motion of the flap, the wave energy is converted into mechanical energy; In the second stage, mechanical energy is converted to potential energy stored in the fluid by the power transmission system, and in the third stage, to convert the energy of the

*Corresponding Author Institutional Email: *rshafaghat@nit.ac.ir*
 (R. Shafaghat)

waves into electrical energy, the high-pressure fluid causes the turbine or hydraulic motor to move [3]. However, these converters are used only to pump seawater in some applications.

Folley et al. [4] experimentally investigated the effect of water depth on the performance of a 1:40 model of an OWSC. Henry [2] experimentally studied the performance of a 1:40 model of an OWSC based on different incident wave characteristics; The results showed that the maximum power occurs in a period of 10s. Gomes et al. [5] investigated an OWSC's hydrodynamics. Their parametric analysis for several configurations showed that the submerged flaps have a smaller excitation torque amplitude than the semi-submerged flaps. Xu et al. [6] conducted an experimental study on OWSC and the effect of wave conditions and water depth in both submerged and semi-submerged flap modes has been studied. Ning et al. [7] experimentally investigated the performance of a 1: 5 model of OWSC. The results showed that the efficiency of the converter is affected by the incident wave amplitude and increasing the amplitude reduces the converter performance. Chow et al. [8] showed that the use of fast cameras can be a good tool for measuring the hydrodynamic responses of a screen converter in experimental studies. Brito et al. [9] experimentally investigated the performance and hydrodynamic response of a 1:10 model of a regular-wave OWSC. Their results showed that the power transmission system, frequency and height of the incident wave have an important effect on the performance and hydrodynamic response of the OWSC.

A review of studies performed on OWSC showed that the studies done on the OWSCs have been based on the conditions of waves in the high seas, and this type of converter has not been studied for supplying water to households from an economic point of view; Therefore In this regard, in this paper, the performance of the converter under the effect of the world's largest lake (Caspian sea) with special and unique wave conditions (high frequency and low wave length) have been studied with two perspectives of electricity production and household water supply. On the other hand, considering the effect of installation depth (water draft depth) on the hydrodynamic performance of the converter, one of the important results presented in the literature is the importance of wave height in determining the appropriate installation depth. Therefore, in this paper, an OWSC wave energy converter with a scale of 1:8 under the effect of wave conditions of the Caspian Sea (with a shorter period and wavelength than the high seas) in the wave flume was experimentally investigated. In order to achieve the appropriate installation depth, the effect of water draft depth on the converter performance for all sea wave conditions was investigated. For better evaluation, water draft depth and wave frequency in each test were considered constant, and the effect of different wave heights (4 dominant heights of the Caspian Sea) on

system performance was evaluated. The tests were repeated for 8 draft depths. Finally, to achieve a realistic assessment, the power and flow of the converter on a laboratory scale were converted to the main scale using Froud scaling method and the performance of the OWSC has been studied for two applications first annual energy production has been calculated and secound the system was considered as water supply pump and the household supply was determined.

2. SYSTEM DESCRIPTION

This study evaluates an OWSC with rectangular cross section and hinges from below. The scale of the model is 1:8 and has been designed and built by the Sea-Based Energy Research Group at Babol Noshirvani University of Technology in Babol. This model includes a floating flap in the form of a rectangular cube with dimensions of 1.1 m in length, 1.2 m in width, and 0.25 m in thickness. The OWSC was placed on the centerline of the wave flume, 13 m from the wave-maker. To measure the wave height, level gauge sensors were installed at 1.2 m and 2.4 m from the converter (Figures 1 and 2). Experimental tests were performed for depths from 0.8 to 1.5 m, wave frequency is 0.4, and wave heights vary from 0.04 to 0.1 m. The OWSC was placed by two bearings on a holder base in the flume bed, and two beams were used as a support to prevent the base from separating from the flume bed. The power transmission system from a hydraulic circuit includes a hydraulic jack, check valves, plastic hoses and a water tank with a diameter of 0.16 m and a height of 0.25 m. The water tank is installed at a vertical distance of 5.5 meters from the pool bed. In order to observe and study the water level inside the water tank, a water index has been installed in the vicinity of the tank (Figure 3). The movement of the flap is converted to hydraulic energy by a pressurized fluid using a hydraulic jack, which pumps water into the tank and stores water in the tank.
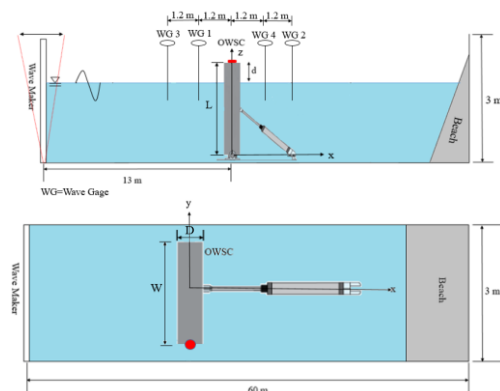
Figure 1. Schematic of a OWSC in a wave pool, Side view and Top view

Figure 2. Views of a 1: 8 scale OWSC wave energy converter made in a laboratory

(a)

(b)
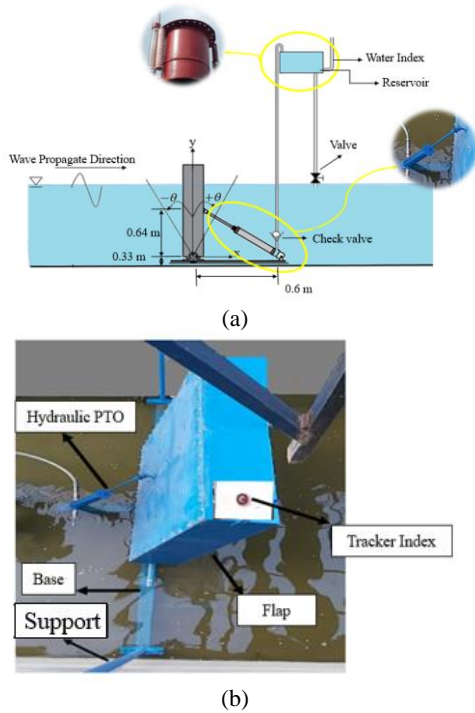
Figure 3. (a) Schematic of power transmission system (b) View of laboratory model including power transmission system

3. EXPERIMENTAL MODELING

The equation for wave maker is in Equation (1) was used to calculate the power of the page converter [10-13].

$$P_{OWSC} = \frac{1}{T} \int_t^{t+T} (P.Q)dt \tag{1}$$

Q is the flow rate in the hydraulic circuit, and P is the pressure in the cylinder chamber. Equations (2) and (3) were used to calculate the flow in the hydraulic circuit.

$$\dot{L} = \frac{L}{\Delta t} \tag{2}$$

$$Q = \dot{L} \times (A_1 + A_2) \tag{3}$$

L is the variation in height of the water level inside the tank and Δt is time for a variation. The variation in height can be measured using a water index installed next to the tank. A_1 is the cross section of the tank and A_2 water index area.

To check the sensitivity of the system to the incident wave, the difference between the maximum power and flow should be calculated. For this purpose, the following equation is used.

$$\Delta P_{max} = P_{max} - P_{min} \tag{4}$$

$$\Delta Q_{max} = Q_{max} - Q_{min} \tag{5}$$

In Equations (4) and (5), P_{max} and P_{min} is maximum power and minimum power in each draft ratio, and Q_{max} and Q_{min} is maximum flow and minimum flow in each draft ratio. In order to study the system's performance in a year, annual energy production in each draft ratio has been calculated as followings:

$$draft\ ratio = \frac{d}{h} \tag{6}$$

$$AEP = \sum_{i=1}^{j} \sum_{i=1}^{j} Pa_{ij} \tag{7}$$

In Equation (6), d is draft and h is the water depth. AEP is annual energy production in MWh and a_{ij} is the wave scatter diagram hours and P is the Power.

The variables used in the equations are shown in Figure 4.

4. LABORATORY EQUIPMENT AND DATA COLLECTION

The wave flume of the Sea-Based Energy Research Group at Babol Noshirvani University of Technology in Babol was used for experimental tests (Figure 5). This
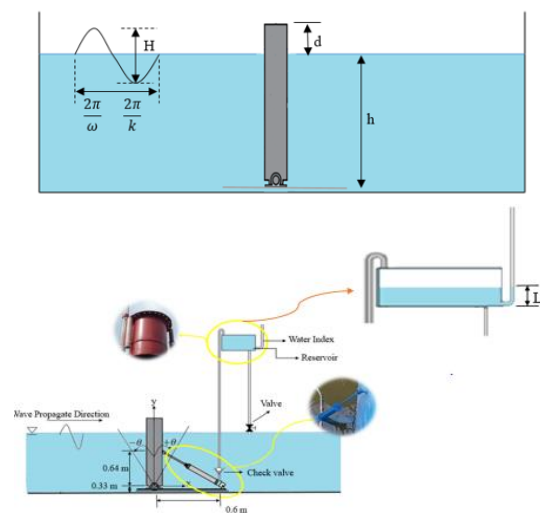
Figure 4. Schematic of the variables used in the equations

Figure 5. Wave, wave flume and damper pool view in the Marine Energy Research Group

flume's length, width, and height are 33 meters, 3 meters, and 3 meters. This pool can generate regular waves in a wide range of height and wave period characteristics. The US-100 ultrasonic sensor was used to measure wave heights (the uncertainty analysis of the system discussed in literature [10-14]) and the Arduino board was used to process it. Also, a webcam was used to measure the height of water in the water tank in order to calculate the water flow rate in the hydraulic circuit (Figure 6 and Table 1).

TABLE 1. Measuring devices information

Equipping measurement	Accuracy	picture
US-100 sensor	Detection range: 2 to 450 cm Measurement error: 1 mm	
Webcam ROTEL-RW120	Video recording speed: 30 frames per second	

5. RESULTS AND DISCUSSIONS

The results of the experimental study in this paper are presented in three parts. In the first part, the experimental results of the incident wave conditions and water draf depth on flow, pressure, and power were presented. In the second part, all the results in the prototype scale were given, and the effect of the incident wave conditions on the performance of the OWSC in the main scale was also shown. Finally, in the last part, the annual energy production of the converter on the prototype scale and water pumping system was studied.

5. 1. Lab Scale Results   The Figure 7 shows the effect of water draft depth on the flow rate of the converter for all wave heights. As shown in the figure, increasing the wave height increase the output flow of the PTO, and increasing the draft depth from the lowest draft depth to the fully submerged state can cause a nonlinear (parabolic) behavior in the converter. Increasing the draft depth to a certain value can increase the output flow of the system. However, the system will decrease the flow rate after passing the dimensionless draft depth value of 0.59.
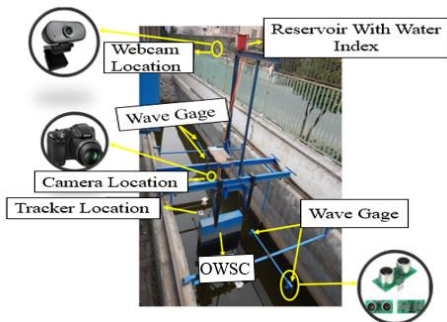
Figure 6. Location of measuring equipment

$y_{0.1} = -0.4613x^2 + 0.4649x + 0.1169$
$y_{0.08} = -0.358x^2 + 0.331x + 0.0879$
$y_{0.06} = -0.2458x^2 + 0.215x + 0.0682$
$y_{0.04} = -0.1613x^2 + 0.1219x + 0.0438$
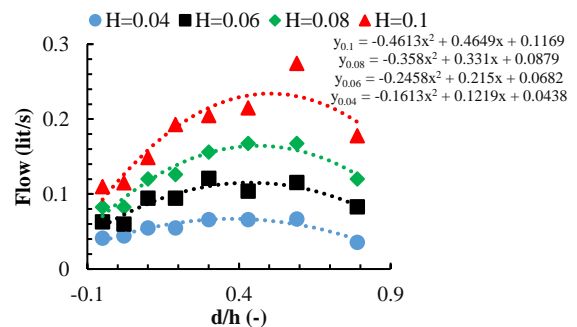
Figure 7. Depth ratio effect on the flow rate

Figure 8 shows the effect of water draft depth on the output power of the converter for all wave heights. As observed in the figure, increasing the draft depth increases the output power of the converter first and then decreases it, so the draft depth has a nonlinear effect on the output power of the converter. The converter has the maximum power at dimensionless water draft depth of0.59, as the water draft depth decreases, the power of the converter decreases due to the decrease in the acceleration of the converter due to the increase in the added mass; Also, with an increase in the water draft depth, the power of the converter decreases due to the decrease in the torque of the wave. Also, the power results showed that increasing the wave height increases the output power of the converter. In fact, when the wave collides with the converter at a higher altitude, the wave is more energetic and causes more power output. Another point that should be considered in the tests is the effect of incident wave conditions on the sensitivity of the OWSC performance for different draft depths.

To show the sensitivity of converter to incident wave conditions, the ΔP_{max} and ΔQ_{max} have been calculated and showed in Figure 9. As it is clear from this diagram, the system is less sensitive to the incident wave at low dimensionless water draft depth. With an increase in dimensionless water draft depth, the system becomes more sensitive to the incident wave, and by reaching the dimensionless water draft depth of 0.59, and after passing this value, the system's sensitivity to the incident wave decreases. In fact, in this diagram, we can see the importance of choosing the right dimensionless water draft depth on the hydrodynamic performance of the OWSC. Adjust the right draft depth in all wave conditions can increase the power and flow.
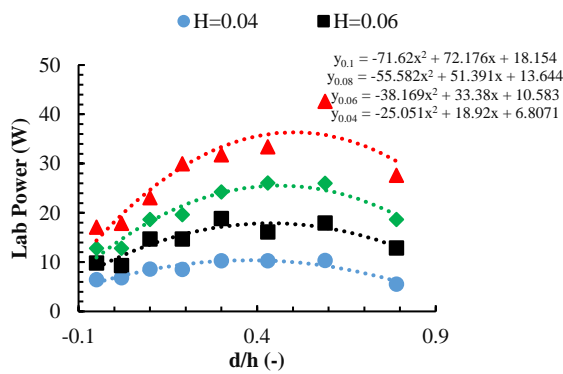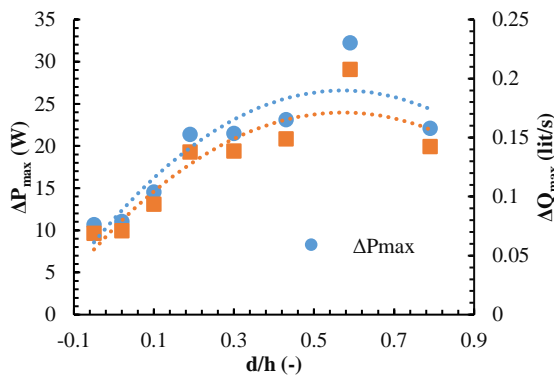
5. 2. Full Scale Results   By Froud scaling method, the power of the laboratory scale OWSC can convert to the power of the prototype scale; Given that the model scale is 1:8, Figure 10 shows the effect of water draft depth on power for all wave heights, as shown in the figure below, the system in optimized draft ratio produces 61.7 kW, and if it is in a fully submerged state, the power drops to 24.8 kW, and if it is in the lowest submerged state, the power decreases to 40.1 kW. In fact, it can be said that if the system is located at a better water draft depth, its performance will increase significantly. Also, the behavior of the diagram shows that with increasing the height of the incident wave, the power will increase so that the OWSC power at the best water draft depth for the maximum wave height is 4.11 times more than the lowest wave height (considering the amplitude of wave height in Caspian Sea). Also, the converter's performance is not affected much at low wave height from the draft depth, but with an increase in wave height, the converter performance is greatly affected by the draft depth.

To investigate the effect of water draft depth on the OWSC behaviour, numerical derivation was performed for OWSC power in each water draft depth at any given wave height; The results can be seen in Figure 11, as shown in the figure below. In 0.59 draft ratio the derivative is zero, which indicates that the converter is at its extreme point. For all wave heights, the power derivative at dimensionless water draft depth reaches 0.59 to zero and tests is in best performance at this point. The second point to be considered in this diagram is that when the system is in a fully submerged state, its performance is very low. Immediately after passing the

$y_{0.1} = -71.62x^2 + 72.176x + 18.154$
$y_{0.08} = -55.582x^2 + 51.391x + 13.644$
$y_{0.06} = -38.169x^2 + 33.38x + 10.583$
$y_{0.04} = -25.051x^2 + 18.92x + 6.8071$

Figure 8. Depth ratio effect on power

Figure 9. Depth ratio effect on ΔP_{max} and ΔQ_{max}

$y_{0.1} = -103.72x^2 + 104.52x + 26.289$
$y_{0.08} = -80.491x^2 + 74.422x + 19.759$
$y_{0.06} = -55.274x^2 + 48.339x + 15.325$
$y_{0.04} = -36.278x^2 + 27.399x + 9.8577$
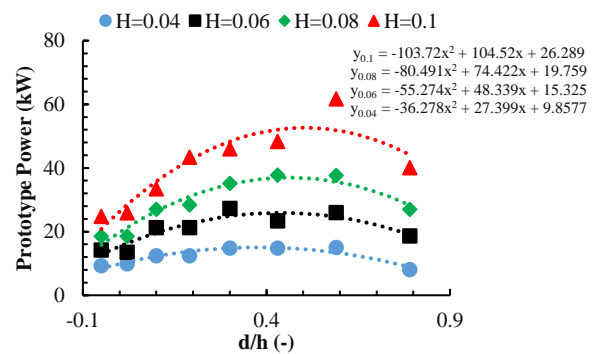
Figure 10. Depth ratio effect on prototype power
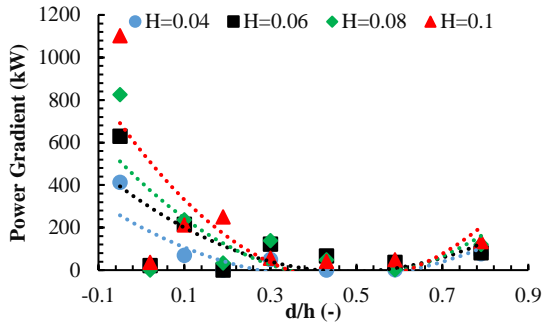
Figure 11. Power gradient with depth ratio in each wave height

Figure 13. Electricity sell to the grid for each draft ratio

fully submerged state, it experiences a sudden increase in power; therefore, the power derivative is very high in that water draft depth.

5. 3. Economic Results   Due to the fact that the conditions of the sea waves change during the day and night, the annual energy production of wave energy converter should be considered; The annual energy production in terms of MWh for all depths of the draft ratio is shown in Figure 12. The state of optimal draft ratio system can produce 878 MWh of power per year. If system is fully submerged, it produces only 406 MWh of power.

Considering that the purchase price of electricity in Iran is \$0.026 per kWh, the optimal system can sell \$22500 of electricity per year. In other words, system optimization can sell \$12095 more electricity per year compared to the maximum performance before optimization.

Another application that can be considered for the OWSC converter is water pumping to water supply systems, so in the following figure, with the help of Froude scaling, it was converted to prototype-scale flow; The electricity sell to the grid for each draft ratio is shown in Figure 13.

As can be seen from the figure below (Figure 14), if the system is installed at an optimal water draft depth, it can provide a maximum water flow rate of 50 liters per second and a minimum water flow rate of 12 liters per second. Also, if the performance of the system in the fully submerged state is compared with the optimal semi-submerged state, it can be concluded that the system in the semi-submerged state pumps 158% more flow.

In designing water supply systems for each household of 3 people, 0.6 liters per second of water can be considered. Therefore, Figure 15 shows the performance of the system to meet the water demand of households. As can be seen from the figure below, if the system is installed at an optimal water draft depth, 8,279 households are supplied for the maximum wave height, also, if the system is installed at an optimal water depth, 1078 households will be supplied at the lowest wave height.

Due to the fact that the height of the waves changes during the day and night and is not constant, the water consumption for the household at each water draft depth was averaged from wave height of 0.4 m to 1 m and the effect of the system at each water draft depth to supply water consumption of household on average is shown in Figure 16, as can be seen from the diagram below, system in best draft ratio can supply water 210% more than fully-submerge state.

Figure 12. Annual energy production with draft ratio
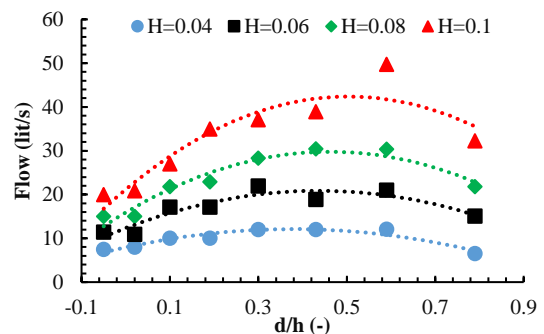
Figure 14. Depth ratio effect on prototype flow
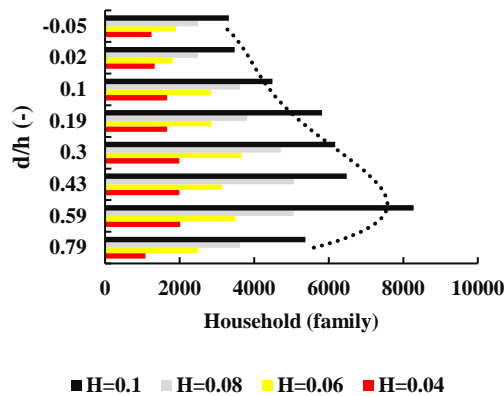
Figure 15. Depth ratio effect on water supply household
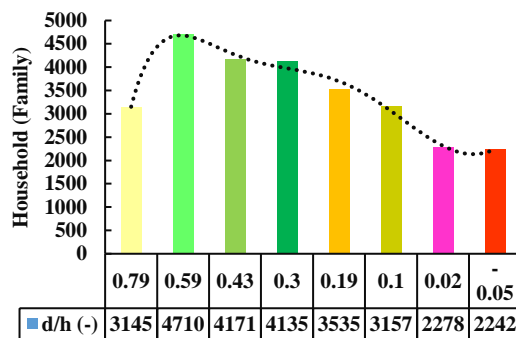
Figure 16. Depth ratio effect on average water supply household

6. CONCLUSIONS

In this paper, the effect of incident wave conditions and installation depth on the power and flow of the OWSC was investigated experimentally. For this purpose, an OWSC converter was constructed and tested in the Sea-Based Energy Research Group of Babol Noshirvani University of Technology in Babol. The installation depth is presented as the dimensionless draft ratio for experimental modeling and determining the optimal depth. The converter operated at a constant frequency of 0.4 Hz for 8 water intakes and 4 wave heights. The results of the experimental study in this paper are presented in three parts. The first part presents the experimental results of the incident wave conditions and water draf depth on flow, pressure, and power. In the second part, all the results in the prototype scale were given, and the effect of the incident wave conditions on the performance of the OWSC in the main scale was also shown. Finally, in the last part, the annual energy production of the converter on the prototype scale and water pumping system was studied, the results obtained show:

- Increasing the height of the incident wave leads to an increase in power and flow of the PTO and also

the effect of installation depth on the performance of the converter is non-linear so that at low draft depth converter performs weak and at high draft depth (fully-submerged) converter performance is also inappropriate

- The results showed that the sensitivity of the system to impact wave conditions is low in two modes and those two modes are low installation depth and high installation depth (submerged). If the installation depth is low or high, the system is less sensitive to the impact wave height, but when the system is at a water intake depth of 0.59, it is more sensitive to the wave height and produces more power by receiving a higher wave.

- The system at a depth of 0.59 can generate 878 MW of power annually, which according to the price of electricity in Iran, with this amount of power, the system sells 607228000 Rials of electricity to the grid annually.

- Suppose the system is also used as a pump for water supply. In that case, it can supply water for 3492 households of 3 people in the main scale for wave height of 0.4 (worst case) and for wave height of 1 meter (best case) for 8279 A three-person household will supply water, since the wave height varies around the clock, so on average the system can respond to 4710 households.

- The maximum values of the performance parameters of the converter are given in Table 2.

TABLE 2. The maximum values of the performance parameters of the converter

	Lab Scale	Full Scale
Power	42.6 W	61.7 kW
Water flow rate	0.3 lit/s	50 lit/s

7. REFERENCES

1. Alizadeh Kharkeshi, B., Shafaghat, R., Mohebi, M., Talesh Amiri, S. and Mehrabiyan, M., "Numerical simulation of a heavy-duty diesel engine to evaluate the effect of fuel injection duration on engine performance and emission", *International Journal of Engineering, Transactions B: Applications*, Vol. 34, No. 11, (2021), 2442-2451. doi: 10.5829/ije.2021.34.11b.08

2. Henry, A.J., "The hydrodynamics of small seabed mounted bottom hinged wave energy conerverters in shallow water", Queen's University Belfast, (2009),

3. Whittaker, T. and Folley, M., "Nearshore oscillating wave surge converters and the development of oyster", *Philosophical Transactions of the Royal Society A: Mathematical, Physical and Engineering Sciences*, Vol. 370, No. 1959, (2012), 345-364. https://doi.org/10.1098/rsta.2011.0152

4. Folley, M., Whittaker, T. and Henry, A., "The effect of water depth on the performance of a small surging wave energy converter", *Ocean Engineering*, Vol. 34, No. 8-9, (2007), 1265-1274. https://doi.org/10.1016/j.oceaneng.2006.05.015

5. Gomes, R., Lopes, M., Henriques, J., Gato, L. and Falcao, A., "The dynamics and power extraction of bottom-hinged plate wave energy converters in regular and irregular waves", *Ocean Engineering*, Vol. 96, (2015), 86-99. https://doi.org/10.1016/j.oceaneng.2014.12.024

6. Xu, C., Wang, X. and Wang, Z., "Experimental study on the dynamics of a bottom-hinged oscillating wave surge converter", In *2016 5th International Conference on Sustainable Energy and Environment Engineering (ICSEEE 2016)*, 210-214. Atlantis Press. https://doi.org/10.2991/icseee-16.2016.38

7. Ning, D., Liu, C., Zhang, C., Göteman, M., Zhao, H. and Teng, B., "Hydrodynamic performance of an oscillating wave surge converter in regular and irregular waves: An experimental study", *Journal of Marine Science and Technology*, Vol. 25, No. 5, (2017), 4. doi: 10.6119/JMST-017-0504-1

8. Chow, Y.-C., Chang, Y.-C., Lin, C.-C., Chen, J.-H. and Tzang, S.-Y., "Experimental investigations on wave energy capture of two bottom-hinged-flap wecs operating in tandem", *Ocean Engineering*, Vol. 164, (2018), 322-331. https://doi.org/10.1016/j.oceaneng.2018.06.010

9. Brito, M., Ferreira, R.M., Teixeira, L., Neves, M.G. and Canelas, R.B., "Experimental investigation on the power capture of an oscillating wave surge converter in unidirectional waves", *Renewable Energy*, Vol. 151, (2020), 975-992. https://doi.org/10.1016/j.renene.2019.11.094

10. Alizadeh Kharkeshi, B., Shafaghat, R., Alamian, R. and Aghajani Afghan, A.H., "Experimental & analytical hydrodynamic behavior investigation of an onshore owc-wec imposed to caspian

11. Shafaghat, R., Fallahi, M., Alizadeh Kharkeshi, B. and Yousefifard, M., "Experimental evaluation of the effect of incident wave frequency on the performance of a dual-chamber oscillating water columns considering resonance phenomenon occurrence", *Iranian (Iranica) Journal of Energy & Environment*, Vol. 13, No. 2, (2022), 98-110. doi: 10.5829/IJEE.2022.13.02.01

12. Alizadeh Kharkeshi, B., Shafaghat, R., Jahanian, O., Rezanejad, k. and Alamian, R., "Experimental evaluation of the effect of dimensionless hydrodynamic coefficients on the performance of a multi-chamber oscillating water column converter in laboratory scale", *Modares Mechanical Engineering*, Vol. 21, No. 12, (2021), 823-834.

13. Yazdi, H., Shafaghat, R. and Alamian, R., "Experimental assessment of a fixed on-shore oscillating water column device: Case study on oman sea", *International Journal of Engineering, Transactions C: Aspects*, Vol. 33, No. 3, (2020), 494-504. doi: 10.5829/IJE.2020.33.03C.14

14. Alizadeh Kharkeshi, B., Shafaghat, R., Jahanian, O., Alamian, R. and Rezanejad, K., "Experimental study on the performance of an oscillating water column by considering the interaction effects of optimal installation depth and dimensionless hydrodynamic coefficients for the caspian sea waves characteristics", *Ocean Engineering*, Vol. 256, (2022), 111513. https://doi.org/10.1016/j.oceaneng.2022.111513

sea wave conditions", *International Journal of Maritime Technology*, Vol. 14, (2020), 1-12.

Persian Abstract

چکیده

تأثیر عمق نصب و ارتفاع موج ورودی بر عملکرد هیدرودینامیکی و اقتصادی مبدل انرژی موج مبدل موج نوسانی (OWSC)بسیار مهم است. در این مطالعه، یک OWSC با در نظر گرفتن مقیاس ۸:۱ در شرایط موج دریای خزر برای ۸ عمق آب از نیمه غوطه‌ور تا کاملاً غوطه‌ور بررسی شده است. این مطالعه به منظور دستیابی به بهترین نسبت پیش نویس و ارزیابی عملکرد سیستم های تحمیل شده به شرایط امواج خزر به روش تجربی انجام شده است. نتایج در سه بخش ارائه شده است. بخش اول جریان، توان و حساسیت مبدل به عمق نصب را در مقیاس آزمایشگاهی مورد مطالعه قرار داد. در بخش دوم، نتایج سیستم با استفاده از روش مقیاس بندی فرود به مقیاس اصلی ۸:۱ تبدیل شد و در نهایت عملکرد از منظر اقتصادی مورد ارزیابی قرار گرفت. نتایج نشان داد که عمق پیشروی اثر غیرخطی بر توان دارد. قدرت سیستم در عمق کشش بدون بعد ۰.۵۹ بهتر است و می تواند ۶۱ کیلو وات تولید کند. همچنین می تواند تا ۵۰ لیتر در ثانیه آب پمپاژ کند. به همین ترتیب، فرض کنید این سیستم برای تولید برق استفاده می شود، در این صورت سالانه ۲۲۵۰۰ دلار برق به شبکه می فروشد و اگر به عنوان پمپ از آن استفاده شود می تواند به طور متوسط ۴۷۱۰ خانوار را آبرسانی کند.

Thermal Analysis of Fluid Flow with Heat Generation for Different Logarithmic Surfaces

B. Jalili[a], A. Mousavi[a], P. Jalili*[a], A. Shateri[a], D. Domiri Ganji[b]

[a] Department of Mechanical Engineering, North Tehran Branch, Islamic Azad University, Tehran, Iran
[b] Department of Mechanical Engineering, Babol Noshirvani University of Technology, Babol, Iran

ABSTRACT

This study investigated the effect of temperature changes on different logarithmic surfaces. One-dimensional heat transfer was considered. The heat generation source term is added to the governing equations. Most scientific problems and phenomena such as heat transfer occur nonlinearly, and it is not easy to find exact analytical solutions. Using the appropriate similarity transformation for temperature and the generation components causes the basic equations governing flow and heat transfer to be reduced to a set of ordinary differential equations. These equations have been solved approximately subject to the relevant boundary conditions with numerical and analytical techniques. According to the given boundary conditions, Collocation, Galerkin, and least squares methods were used to find an answer to the governing differential equations. The validation of the present techniques has been done with the fourth-order Runge-Kutta method as a numerical method. The temperature profiles for different values of β and α have been obtained. The results showed that the proposed methods could consider nonlinear equations in heat transfer. Therefore, the results accepted by current analytical methods are very close to those of numerical methods. Comparing the results provides a more realistic solution and reinforces the conclusions regarding the efficiency of these methods. Furthermore, changes in temperature profiles occur with decreasing and increasing β and α numbers.

doi: 10.5829/ije.2022.35.12c.03

1. INTRODUCTION

Solving differential equations in mathematics helps to understand many physical concepts. Many phenomena can be expressed in engineering with differential equations. In many of these problems, the most widely used heat equations, it is complicated and impossible to obtain accurate solutions to the differential equations governing these problems. In recent studies, the methods developed by Jalili et al. [1, 2], Zangooee et al. [3], Ghadikolae et al. [4], Al-Sankoor et al. [5], Amouzadeh et al. [6] and Etbaeitabari et al. [7] have solved a broad scope of issues. Also, the methods of weighted residuals, including accurate and straightforward trial functions, have been utilized to crack nonlinear differential equations. Least squares methods (LSM), Galerkin, and Collocation are examples of weighted residual methods

presented by Ozisik [8] to solve samples related to heat transfer. The collocation method is utilized to crack a third-order differential equation by Stern and Rasmussen [9]. Conductive and radiative heat transfer in a linear anisotropic cylindrical with the spectral position was investigated by couple of equations and in an unsteady flow by Sun et al. [10]. Basha and Sivaraj [11] investigated how to generate entropy in a porous tube containing nanofluid. Celik and Ozturk [12] investigated the speed and heat transfer in parallel circular surfaces. Nabati et al. [13] proposed the collocation method to solve the equation of thermal performance in a porous medium. Chandrakant et al. [14] proposed a numerical solution for a heat exchanger with helical flow channels. Recently, Biswal et al. [15] used the least-squares method to solve the governing equations of nanofluid flow in a semi-porous channel. Hatami and Ganji [16] discovered

*Corresponding Author Institutional Email: p.jalili@iau-tnb.ac.ir (P. Jalili)

that LSM is more practical than other analytical and semi-analytical methods for cracking nonlinear heat transfer problems in many problems. Recently, several researchers have studied this issue and heat transfer [17-25]. Abbaszadeh et al. [26] have presented the Galerkin method to solve the Navier-Stokes equation in combination with the heat transfer equation. Numerical models for the analysis of unsteady heat transfer in PCM employing the Galerkin method have been carried out by Zhang et al. [27].

This article considers heat transfer on logarithmic levels with heat production. As the novelty of this study, the influence of some physical parameters such as the rate of effectiveness of temperature on non-dimensional temperature profiles is considered. They are mainly used in simple cases and special situations, so numerical methods solve differential equations in many problems. However, these methods can solve stress analysis, fluid flow, heat transfer, and electromagnetic wave equations. These methods approximate the solution of differential equations governing the environment. The present study uses the least-squares, collocation, and Galerkin methods to solve the nonlinear heat transfer issue. The validity of these methods is shown by comparing the outcomes with the numerical method.

2. GEOMETRY AND GOVERNING EQUATIONS

In this research, the level of heat transfer and heat production are indicated by A(x) and G(x), respectively, which change logarithmically. Also, heat transfer is investigated in one dimension. In addition, the coefficient of thermal conductivity k varies as a function of temperature.

In the following, the energy equation and boundary conditions related to the investigated geometry are given.

By considering the governing equation for geometry of the problem (Figure 1):

$$\frac{d}{dx}\left(k_0(1+\beta T) \cdot A(x) \cdot \frac{dT}{dx}\right) + G(x) = 0 \tag{1}$$

$$x = 0 \rightarrow T = T_0, \qquad x = L \rightarrow T = T_L. \tag{2}$$
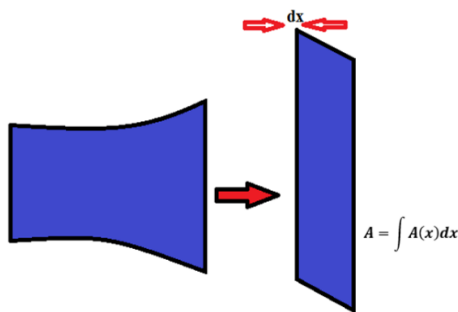
Figure 1. Geometry of the problem

$$A(x) = A_0 e^x \tag{3}$$

$$G(x) = G_0 e^{-x} \tag{4}$$

$$k_T = k_0(1 + \beta T) \tag{5}$$

β indicates the effective rate of temperature change with respect to thermal conductivity, and k_0 defines the fin's thermal conductivity with respect to the environment. T_o simplify this equation [18]:

$$\alpha \left(\frac{d}{dx}\theta(x)\right) + \alpha \cdot \beta \cdot T_0 \cdot \theta(x) \cdot \left(\frac{d}{dx}\theta(x)\right) + \beta \cdot$$
$$T_0 \left(\frac{d}{dx}\theta(x)\right)^2 + \left(\frac{\partial^2}{\partial x^2}\theta(x)\right) + \beta \cdot T_0 \cdot \tag{6}$$
$$\theta(x)\left(\frac{\partial^2}{\partial x^2}\theta(x)\right) + c \cdot e^{-\alpha x} = 0.$$

Here is the dimensionless temperature, θ

$$\theta = \frac{T}{T_0} \tag{7}$$

$$c = \frac{G}{k_0 \cdot A_0 \cdot \beta \cdot T_0} \tag{8}$$

By making the boundary conditions dimensionless in order to apply the desired methods, appropriate boundary conditions should be considered [18]:

$$x = 0 \rightarrow \theta = 1, \quad x = L \rightarrow \theta = \frac{T_L}{T_0} = z \tag{9}$$

3. TECHNIQUES OF SOLUTION

3. 1. Collocation Method   In this technique the answer can be assumed as follows [13]:

$$p(P) = \sum_{l=1}^{N} v_l \gamma_l(P). \tag{10}$$

Coefficients v_l , (l = 1,...,N) are the unknowns and the functions γ_l, are the test functions. A group of N nods Pj of Γ chooses the collocation method. The equations are then noted at these nodes Pj, resulting in the following linear system of equations.

$$\sum_{l=1}^{N} v_l K\gamma_l(P_j) = f(P_j). \quad for \, j = 1, ..., N \tag{11}$$

This set of equations should be solved to compute the coefficient, so the answer p on Γ. The nodes Pj are named collocation nodes [13].

3. 2. GM   The Galerkin technique was employed to Equation (10) consists of selecting an approximate space of p. Besides, p is reported as formerly (10) and, the function γm is the base of this space [16]. The equation defines the coefficient Vm.

$$\langle K_P, \gamma_p \rangle = \langle f, \gamma_p \rangle, \qquad p = 1, ..., M \tag{12}$$

where ⟨ ,⟩ is the numerical product described in the approximate space. This makes the next linear approach:

$$\sum_{m=1}^{N} v_m \langle K\gamma_m, \gamma_p \rangle = \langle f, \gamma_p \rangle, \quad p = 1, \dots, M \quad (13)$$

The numerical procedure is similar to the procedure developed by the collocation method. Evaluate the vector B and the matrix A before solving the linear term.

3. 3. LSM   Fakour et al. [28] represented that the least-squares technique is a kind of the weighted residual technique to make it the least the residuals of the test function presented in the nonlinear differential equation. To understand the basic concept of LSM, evaluate the derivative operator D, which operates on the v to develop the function h.

$$D\left(v\left(x\right)\right) = h(x), \quad (14)$$

v is supposed to be calculated by the function $\tilde{v}$, that is a linear mix of the base functions chosen from the linearly independent system.

$$v \cong \tilde{v} = \sum_{i=1}^{n} c_i \varphi_i, \quad (15)$$

By replacing Equation (15) with D, the differential operator the consequence of the processes typically is not h(x), and a difference will occur. Thus a residual will exist as below:

$$R(x) = D\left(\tilde{v}(x)\right) - h(x) \neq 0, \quad (16)$$

The central idea of LSM is to move the residual to 0 in some moderate insight on the field. Therefore,

$$\int_x R(x)\, W_i(x) = 0, \quad i = 1, 2, \dots, n\,. \quad (17)$$

The number of weight functions and unknown coefficients is indicated by Wi and ci, respectively, and their number equals each other.

3. 4. Problem Solving   By guessing the trial solution with undetermined coefficients and plugging it into the equation, the unknown coefficients are solved to obtain the particular solution. It should be mentioned that the trial answer must please the boundary conditions; therefore, the trial answer can be noted as follows [8]:

$$\theta(x) = \frac{e^{-\alpha L} - z}{-1 + e^{-\alpha L}} + \frac{(z-1)e^{-\alpha x}}{-1 + e^{-\alpha L}} + C_1(x - x^2) + C_2(x - x^3) + C_3(x - x^4) + C_4(x - x^5). \quad (18)$$

The residual part will be seen by instructing Equation (16). By replacing the residual amount with Equation (18), a group of problems with five equations and five unidentified coefficients choice arise; coefficients C1–C4 will be acquired. After applying LSM, CM and GM when β= 0, α = 4, L = 1, T0 = 10, z = 0.1, c = 2 below equations will be obtained from the temperature profile on logarithmic surface.

$$\theta(x)_{LSM} = 0.424701244\, x + 1.384653618\, x^2 + 1.523432162\, x^3 + 0.5634797880\, x^4 \quad (19)$$

$$\theta(x)_{Galerkin} = 0.415091516\, x + 1.329124398\, x^2 + 1.483241831\, x^3 + 0.5692089490\, x^4 \quad (20)$$

$$\theta(x)_{Collocation} = 0.499816241\, x + 1.597444202\, x^2 + 1.999655684\, x^3 + 0.9020277229\, x^4 \quad (21)$$

These equations were obtained by the LSM, Galerkin, and Collocation methods, respectively.

4. RESULTS AND DISCUSSION

This investigation desired to use the weighted residual methods named LSM, CM, and GM to define an analytical explanation for logarithmic area shapes of the heat transfer equation in Figure 1. According to Figure 2, a particular case indicates the efficiency of suggested techniques, and the outcomes are evaluated with the numerical and analytical methods conducted by Vahabzadeh et al. [18]. According to the obtained results, the percentage error of the present study compared to reported data in literature [18] is equal to 1.7%. This paper's approximate solution to the governing equation is

(a)

(b)
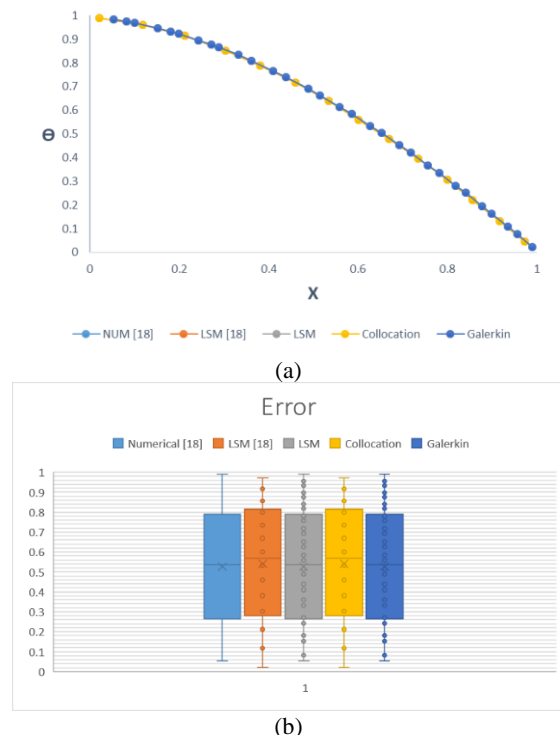
Figure 2. part (a) analogy between LSM solution and the numerical outcomes obtained from [18] and LMS, CM, and GM in the present study for θ(x) when c = 2, β= 0, α = 2, L = 1, T0 = 10, z = 0.1. Part (b) Comparing percentage error between different methods

obtained by applying the WRMs: the CM, LSM, and GM. The approximate solutions accepted that provided the WRMs are reliable and effective methods. A good agreement has been achieved by comparing the numerical solution obtained using the 4th-order Runge-Kutta method explained by Vahabzadeh et al. [18] and the proposed methods. It can be concluded from the figures and table that the maximal error remainder is negligible by these suggested methods. Moreover, the LSM provided the best approximate solution with less error and the Galerkin method reduces the dimensionalilty of the problem hence it is much faster. The collocation method also reaches convergence with more calculations. Finally, this research found that selecting the parameters influenced convergence as well.

For numerical explanation, Vahabzadeh et al. [18] utilized a fourth-order Runge-Kutta approach to solve the nonlinear boundary value problem. The exactness of LSM obtained from literature [18] and the three methods offered in this research are displayed in Table 1.

Figures 3 and 4 show the effect of α on temperature characteristics. As α increases, the temperature profiles in the range $0 < \alpha < 1$ decrease. This trend is established in Figure 3 for α = 4 for the proposed methods. On the other hand, as α increases, the temperature profiles for α =1 decrease. Moreover, the variation of temperature profiles for α = 8 is shown in Figure 4. Furthermore, the dimensionless temperature profile along the fin shell is displayed in Figures 5 and 6. If β> 0, the temperature profile rises with growing x. In the subject of β < 0, the temperature grows as x rises. (Figure 6).

TABLE 1. Comparison between LSM and NUM from literature [18] and LMS, GM and, CM from present study for θ(x) when c = 2,β= 0, α = 2, L = 1, T0 = 10, z = 0.1

X	LSM [18]	NUM [18]	LSM	Galerkin	Collocation
0.0	1.0000000000	1.0000000000	1.0000000000	1.0000000000	1.0000000000
0.1	0.8648242717	0.8648242719	0.8645772366	0.8542549152	0.8562025261
0.2	0.7393106703	0.7393106705	0.7485718835	0.7682940431	0.7710213056
0.3	0.6243979822	0.6243979837	0.6268611235	0.6767081250	0.6802767791
0.4	0.5203671664	0.5203671665	0.5214787627	0.5814893015	0.5859442644
0.5	0.4270489850	0.4270489840	0.4341732679	0.4843450838	0.4895862861
0.6	0.3439779949	0.3439779952	0.3563945577	0.3866851428	0.3923393643
0.7	0.2705054957	0.2705054971	0.2792821640	0.2896094716	0.2949021784
0.8	0.2058812577	0.2058812581	0.1936546291	0.1938977815	0.1975249622
0.9	0.1493116429	0.1493116431	0.1482167345	0.1483782398	0.1481126567
1.0	0.1000000000	0.1000000000	0.1000000000	0.1000000000	0.1000000000
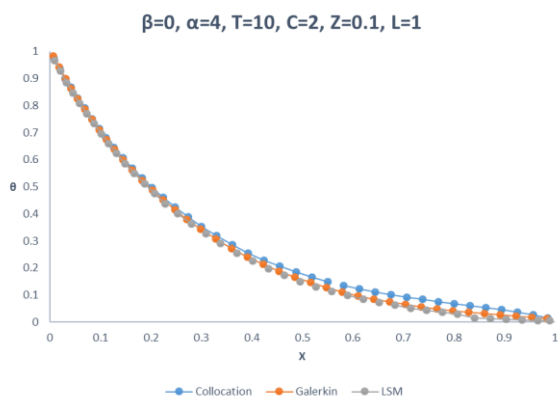
Figure 3. Impact of α on θ where T0 = 10, β = 0, α = 4 , L = 1, c = 2, z = 0.1, for Collocation, Galerkin and LSM methods
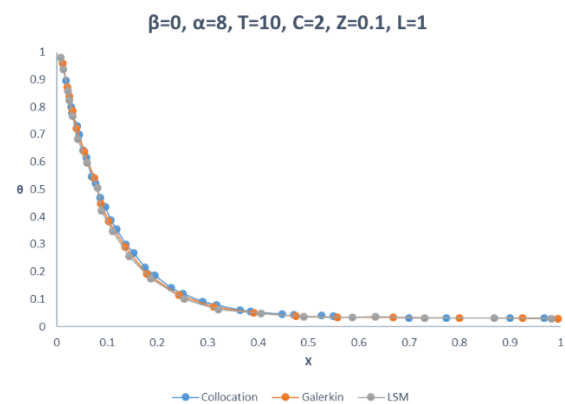
Figure 4. Impact of α on θ where T0 = 10, β = 0, α = 8 , L = 1, c = 2, z = 0.1, for Collocation, Galerkin and LSM methods
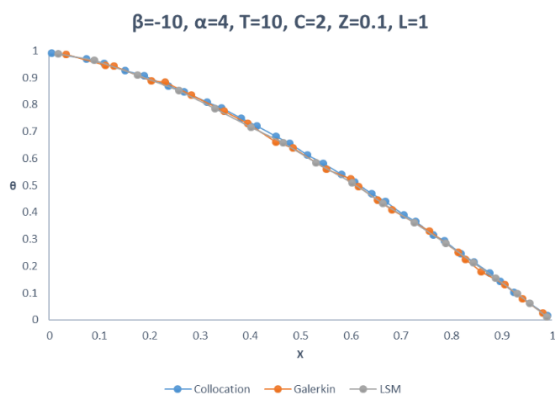
Figure 5. Impact of α on θ where T0 = 10, β = -10, α = 8 , L = 1, c = 2, z = 0.1, for Collocation, Galerkin and LSM methods
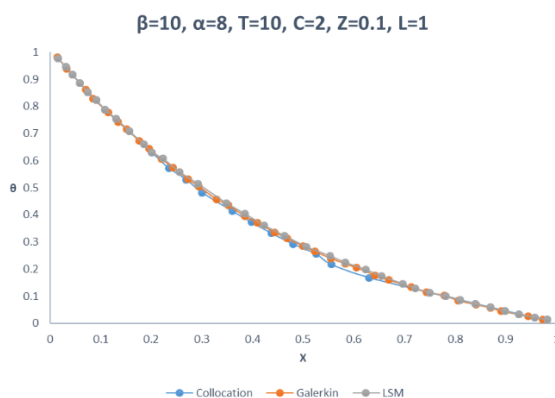
Figure 6. Impact of α on θ where T0 = 10, β = 10, α = 8 , L = 1, c = 2, z = 0.1, for Collocation, Galerkin and LSM methods

5. CONCLUSION

In this study, Galerkin and Collocation methods have been proposed. These techniques have been successfully used for governing differential equations of specified geometries with various logarithmic surfaces. The results were compared to the solution solved using the numerical solution and LSM. The results indicate that these procedures transform complex problems into simple, fast-solvable ones. The fundamental goal of this analysis is to explore the convergence of the Galerkin method and the collocation method. The comparison of the results here provides a more realistic solution and reinforces the conclusions regarding the efficiency of these processes. Thus, the Galerkin and collocation methods are effective mathematical mechanisms and can involve extensive types of linear and nonlinear equations in the field of heat transfer issues. Also, differences in temperature profiles appear with reducing and raising β and α numbers. Future research should consider the potential effects of

geometry more carefully, for example investigation of heat transfer in logarithmic curve. Also, in future work, investigating heat transfer in presence of porous media in logarithmic surface might prove important.

6. REFERENCES

1. Jalili, B., Jalili, P., Sadighi, S. and Ganji, D.D., "Effect of magnetic and boundary parameters on flow characteristics analysis of micropolar ferrofluid through the shrinking sheet with effective thermal conductivity", *Chinese Journal of Physics*, Vol. 71, (2021), 136-150. https://doi.org/10.1016/j.cjph.2020.02.034

2. Jalili, B., Sadighi, S., Jalili, P. and Ganji, D.D., "Characteristics of ferrofluid flow over a stretching sheet with suction and injection", *Case Studies in Thermal Engineering*, Vol. 14, (2019), 100470. https://doi.org/10.1016/j.csite.2019.100470

3. Zangooee, M., Hosseinzadeh, K. and Ganji, D., "Hydrothermal analysis of mhd nanofluid (tio2-go) flow between two radiative stretchable rotating disks using agm", *Case Studies in Thermal Engineering*, Vol. 14, (2019), 100460. https://doi.org/10.1016/j.csite.2019.100460

4. Ghadikolaei, S., Hosseinzadeh, K. and Ganji, D., "Analysis of unsteady mhd eyring-powell squeezing flow in stretching channel with considering thermal radiation and joule heating effect using agm", *Case Studies in Thermal Engineering*, Vol. 10, (2017), 579-594. https://doi.org/10.1016/j.csite.2017.11.004

5. Al-Sankoor, K., Al-Gayyim, H., Al-Musaedi, S., Asadi, Z. and Ganji, D., "Analytically investigating of heat transfer parameters with presence of graphene oxide nanoparticles in williamson-magnetic fluid by agm and hpm methods", *Case Studies in Thermal Engineering*, Vol. 27, (2021), 101236. https://doi.org/10.1016/j.csite.2021.101236

6. Amouzadeh, F., Tondro, M., Asadi, Z. and Ganji, D., "Suction and injection effect on magnetohydrodynamic fluid flow within a vertical annulus for electrical wire cooling", *Case Studies in Thermal Engineering*, Vol. 27, (2021), 101241. https://doi.org/10.1016/j.csite.2021.101241

7. Etbaeitabari, A., Barakat, M., Imani, A., Domairry, G. and Jalili, P., "An analytical heat transfer assessment and modeling in a natural convection between two infinite vertical parallel flat plates", *Journal of Molecular Liquids*, Vol. 188, (2013), 252-257. https://doi.org/10.1016/j.molliq.2013.09.010

8. Ozisik, M.N., "Boundary value problems of heat conduction, courier Corporation, (2002).

9. Stern, R.H. and Rasmussen, H., "Left ventricular ejection: Model solution by collocation, an approximate analytical method", *Computers in biology and medicine*, Vol. 26, No. 3, (1996), 255-261. https://doi.org/10.1016/0010-4825(96)00007-8

10. Sun, Y., Li, X., Zhao, J., Hu, Y., Jing, X., Ma, J. and Zhou, R., "Investigation of transient coupled conduction and radiation heat transfer in the linearly anisotropic scattering cylindrical medium by spectral collocation method", *International Journal of Thermal Sciences*, Vol. 172, (2022), 107308. https://doi.org/10.1016/j.ijthermalsci.2021.107308

11. Basha, H.T. and Sivaraj, R., "Exploring the heat transfer and entropy generation of ag/fe $$ _3 $$3 o $$ _4 $$4-blood nanofluid flow in a porous tube: A collocation solution", *The European Physical Journal E*, Vol. 44, No. 3, (2021), 1-24. https://doi.org/10.1140/epje/s10189-021-00024-x

12. Çelik, İ. and Öztürk, H.K., "Heat transfer and velocity in the squeezing flow between two parallel disks by gegenbauer wavelet collocation method", *Archive of Applied Mechanics*, Vol. 91,

No. 1, (2021), 443-461. https://doi.org/10.1007/s00419-020-01782-4

13. Nabati, M., Salehi, G.H. and Taherifar, S., "Numerical solution for a porous fin thermal performance problem by application of sinc collocation method", *Mathematical Methods in the Applied Sciences*, (2021). https://doi.org/10.1002/mma.7740

14. Chandrakant, S., Panchal, H. and Sadasivuni, K.K., "Numerical simulation of flow-through heat exchanger having helical flow passage using high order accurate solution dependent weighted least square based gradient calculations", *Energy Sources, Part A: Recovery, Utilization, and Environmental Effects*, (2021), 1-26. https://doi.org/10.1080/15567036.2021.1900457

15. Biswal, U., Chakraverty, S., Ojha, B.K. and Hussein, A.K., "Numerical simulation of magnetohydrodynamics nanofluid flow in a semi-porous channel with a new approach in the least square method", *International Communications in Heat and Mass Transfer*, Vol. 121, (2021), 105085. https://doi.org/10.1016/j.icheatmasstransfer.2020.105085

16. Hatami, M. and Ganji, D., "Thermal performance of circular convective–radiative porous fins with different section shapes and materials", *Energy Conversion and Management*, Vol. 76, (2013), 185-193. https://doi.org/10.1016/j.enconman.2013.07.040

17. Talarposhti, R., Jalili, P., Rezazadeh, H., Jalili, B., Ganji, D., Adel, W. and Bekir, A., "Optical soliton solutions to the (2+1)-dimensional kundu–mukherjee–naskar equation", *International Journal of Modern Physics B*, Vol. 34, No. 11, (2020), 2050102. doi. https://doi.org/10.1016/j.enconman.2013.07.040

18. Vahabzadeh, A., Fakour, M., Ganji, D. and Bakhshi, H., "Analytical investigation of the one dimensional heat transfer in logarithmic various surfaces", *Alexandria Engineering Journal*, Vol. 55, No. 1, (2016), 113-117. https://doi.org/10.1016/j.aej.2015.12.027

19. Jalili, P., Ganji, D.D., Jalili, B. and Ganji, D.R.M., "Evaluation of electro-osmotic flow in a nanochannel via semi-analytical method", *Thermal Science*, Vol. 16, No. 5, (2012), 1297-1302. doi: 10.2298/TSCI1205297J.

20. Pasha, P., Nabi, H., Peiravi, M., Pourfallah, M. and Domiri Ganji, D., "The application of analytical methods in the investigation effects of magnetic parameter and brownian motion on the fluid flow between two equal plates", *International Journal of Engineering, Transactions A: Basics*, Vol. 34, No. 10, (2021), 2341-2350. doi: 10.5829/IJE.2021.34.10A.15.

21. Jalili, B., Aghaee, N., Jalili, P. and Ganji, D.D., "Novel usage of the curved rectangular fin on the heat transfer of a double-pipe heat exchanger with a nanofluid", *Case Studies in Thermal Engineering*, (2022), 102086. https://doi.org/10.1016/j.csite.2022.102086

22. Humphries, U., Govindaraju, M., Kaewmesri, P., Hammachukiattikul, P., Unyong, B., Rajchakit, G., Vadivel, R. and Gunasekaran, N., "Analytical approach of fe3o4-ethylene glycol radiative magnetohydrodynamic nanofluid on entropy generation in a shrinking wall with porous medium", *International Journal of Engineering, Transactions B: Applications*, Vol. 34, No. 2, (2021), 517-527. doi: 10.5829/IJE.2021.34.02B.25.

23. Agrawal, Y., Bhadauria, A. and Sikarwar, B., "Towards an analytical model for film cooling prediction using integral turbulent boundary layer", *International Journal of Engineering, Transactions A: Basics*, Vol. 29, No. 4, (2016), 554-562. doi: 10.5829/idosi.ije.2016.29.04a.15.

24. Jalili, P., Kazerani, K., Jalili, B. and Ganji, D., "Investigation of thermal analysis and pressure drop in non-continuous helical baffle with different helix angles and hybrid nano-particles", *Case Studies in Thermal Engineering*, Vol. 36, (2022), 102209. https://doi.org/10.1016/j.csite.2022.102209

25. Jalili, B., Sadighi, S., Jalili, P. and Ganji, D.D., "Numerical analysis of mhd nanofluid flow and heat transfer in a circular porous medium containing a cassini oval under the influence of the lorentz and buoyancy forces", *Heat Transfer*, https://doi.org/10.1002/htj.22582

26. Abbaszadeh, M., Dehghan, M., Khodadadian, A., Noii, N., Heitzinger, C. and Wick, T., "A reduced-order variational multiscale interpolating element free galerkin technique based on proper orthogonal decomposition for solving navier–stokes equations coupled with a heat transfer equation: Nonstationary incompressible boussinesq equations", *Journal of Computational Physics*, Vol. 426, (2021), 109875. https://doi.org/10.1016/j.jcp.2020.109875

27. Zhang, J., Shen, Y., Hu, H., Gong, S., Wu, S., Wang, Z. and Huang, J., "Transient heat transfer analysis of orthotropic materials considering phase change process based on element-free galerkin method", *International Communications in Heat and Mass Transfer*, Vol. 125, (2021), 105295. https://doi.org/10.1016/j.icheatmasstransfer.2021.105295

28. Fakour, M., Ganji, D. and Abbasi, M., "Scrutiny of underdeveloped nanofluid mhd flow and heat conduction in a channel with porous walls", *Case Studies in Thermal Engineering*, Vol. 4, (2014), 202-214. https://doi.org/10.1016/j.csite.2014.10.003

Persian Abstract

چکیده

این مطالعه به بررسی تأثیر تغییرات دما بر سطوح مختلف لگاریتمی پرداخته است. انتقال حرارت یک بعدی در نظر گرفته شد و منبع تولید گرما به معادلات حاکم اضافه می شود. اکثر مسائل و پدیده های علمی مانند انتقال حرارت به صورت غیرخطی رخ می دهند و یافتن راه حل های تحلیلی دقیق آسان نیست. استفاده از تبدیل تشابه مناسب برای دما و مولفه های دیگر باعث می شود که معادلات اساسی حاکم بر جریان و انتقال حرارت به مجموعه ای از معادلات دیفرانسیل معمولی کاهش یابد. این معادلات با توجه به شرایط مرزی مربوطه با تکنیک های عددی و تحلیلی بصورت تقریبی حل شده اند. با توجه به شرایط مرزی حل شده، از روش‌های کالوکیشن، گلرکین و حداقل مربعات برای یافتن پاسخ معادلات دیفرانسیل حاکم استفاده شد. اعتبار سنجی تکنیک های حاضر با روش رانگ–کوتا مرتبه چهارم به عنوان یک روش عددی انجام شده است. پروفیل های دما برای مقادیر مختلف β و α به دست آمده است. نتایج نشان داد که روش های پیشنهادی قابلیت حل معادلات غیرخطی در انتقال حرارت را دارند. بنابراین، نتایج پذیرفته شده توسط روش های تحلیلی فعلی بسیار نزدیک به نتایج روش های عددی است. مقایسه نتایج راه حل های واقعی تری ارائه می دهد و نتیجه گیری در مورد کارایی این روش ها را تقویت می کند. علاوه بر این، تغییرات در پروفایل های دما با کاهش و افزایش اعداد β و α رخ می دهد.

International Journal of Engineering

Mechanical and Microstructural Evaluation of AA6082-T61 Joints Produced by Ultrasonic Vibration Assisted Friction Stir Welding Process

M. S. EL-Wazery*[a, b], O. M. Mabrouk[a], S. M. Khafagy[c], A. R. El-sissy[a]

[a] Production Engineering & Mechanical Design Department, Faculty of Engineering, Menoufia University, Shebin El-Kom, Egypt
[b] Currently, Mechatronics Engineering Department, High Institute of Engineering and Technology – Elmahala Elkobra, Egypt
[c] Mining and Metallurgy Department, Tebbin Institute for Metallurgical Studies

A B S T R A C T

Continuous improvement in the friction stir welding process (FSW) is still growing to improve the process capabilities and overcome certain drawbacks encountered in the process. Low welding speeds, high welding loads, and high torque needed are the main limitations of this process. Applying ultrasonic vibration is one of the versatile approaches that was proposed to tackle these issues. In this paper, a comparative study between the conventional friction stir welding process (CFSW) and the ultrasonic-assisted friction stir welding process (UAFSW) was conducted. The objective is to evaluate quantitively and qualitatively the influence of ultrasonic vibration waves on the weld surface quality, tensile strength, micro-hardness, microstructure, and weld formation of the joints. The results have demonstrated that ultrasonic vibration waves cause grain refinement action by 23.6% at the stirring zone (SZ) as well as its desirable role in enhancing the mechanical properties by a percentage up to 15% for ultimate tensile strength and eliminating weld defects, especially at high welding speed (120 mm/min). However, no profound effect was found for ultrasonic waves on the grain size in the thermomechanical affected zone (TMAZ) or the heat-affected zone (HAZ). A considerable reduction in the elongation % whether in CFSW or UAFSW compared to that of base metal was detected.

1. INTRODUCTION

Materials joining technology has witnessed a lot of developments within the last three decades. One of the most influential innovations in this area is friction stir welding technique (FSW). Furthermore, FSW offers many pros over other fusion welding processes. Few distortions and residual stresses can result in from FSW. In addition, the process is environmentally friendly as it consumes less energy and emits fewer fumes and sputters which makes it overall more favorable than other fusion welding techniques. The process was invented by TWI at in the and the patent was filed in 1991 [1]. Since this date, the process has attracted the attention of many researchers around the world and has received considerable research effort. These efforts included establishing the theoretical approach for the process [2], optimizing the process parameters [3], and developing

mathematical models to predict the characteristics of the joints [4]. However, the process still suffers from certain cons [5]. For instance, Low welding speed and limited productivity, high loading loads on the machine due to the huge friction between the tool and the workpiece and, the high torque needed to accomplish the operation are all drawbacks of the process. FSW process has undergone several modifications and improvements. These variations involved modifications in the tool, the machine, and the process itself [6-8]. As well as, integrating FSW process with a secondary energy source to provide more softening action, especially for welding hard materials [9]. In this regard, several auxiliary energy sources were used. electrical current [10], laser source [11], induction heat [12], electrical arc [13], and ultrasonic vibration [14] were integrated with the process. Among all these secondary energy sources, ultrasonic vibrations have shown specific advantages

*Corresponding Author Email: eng_mahmoudsamir@yahoo.com
(M. S. EL-Wazery)

over the other approaches. For example, it consumes less energy and provides an efficient amount of softening without raising the temperature [9].

The influence of the ultrasonic vibration on the formation and mechanical properties of 2024Al-T4 joints was investigated. The results showed that by applying ultrasonic vibration, the weld formation was improved at high welding speeds and the stir zone was widened. Moreover, the mechanical properties in terms of strength, elongation, and micro-hardness were enhanced [15]. Similar results but for different aluminum alloys were reported, the microstructure of AA6061-T6 weld nuggets produced by UAFSW was compared to those produced by conventional FSW [16]. It was found that higher deformation characteristics are presented in the nugget zone of the joints produced by the UAFSW process and that was attributed to the ultrasonic softening effect. Furthermore, ultrasonic vibrations improved the recrystallization process and leads to better grain refinement. In another, study the welding forces, and weld thermal cycles in the UAFSW process of AA2024-T3 were analyzed to explore the role of ultrasonic vibration in the process [17]. It was concluded that the exerted ultrasonic vibrations lower both the traverse and axial forces and improve the material flow. On the other hand, ultrasonic vibrations do not have a significant effect on preheating the weld zone. The influence of the ultrasonic vibration on material flow and mechanical properties of AA2024-T3 was investigated. It was reported that the joints welded by the assistance of ultrasonic vibration have better material flow and higher mechanical properties than those joined by conventional FSW [18].

As it can be easily realized from the literature review that assessing the potentiality of exerting ultrasonic vibration waves during the FSW process of AA6082-T61 has not been well-established although the wide applications in which this alloy can be selected. This research aims to conduct a comparative study between conventional FSW and UAFSW processes of AA 6082-T61 to reveal the influence of ultrasonic vibration exertion on the tensile strength, microstructure, weld formation, and defects of the welded joints.

2. EXPERIMENTAL WORK

In the current study, aluminum alloy 6082-T61 was selected to be butt-joint welded using CFSW and UAFSW processes for comparing purposes. Due to having the highest strength of all 6xxx series alloys and its excellent corrosion resistance, AA 6082 is one of the most promising alloys. Besides, it has found its way into a wide range of applications such as cranes, bridges, beer barrels, ore skips, and trusses [19]. The composition and

mechanical characteristics of AA6082-T61 in the as-received state are shown in Tables 1 and 2, respectively[1].

An abrasive water jet machine was utilized to cut the aluminum sheet into the required dimensions of the sample (160×100×3 mm). H13 hot work tool steel rod was machined to manufacture the FSW tool with a shoulder diameter and pin diameter of 14mm and 5mm, respectively. An ultrasonic processor (model up 400S) manufactured by Hielscher ultrasonics was used to obtain the required ultrasonic vibration waves. A sonotrode made of titanium with a 22 mm tip diameter and 100 mm in length was used to generate ultrasonic vibration waves at a frequency of 24 kHz, a power of 85 watts, and an adjustable amplitude up to 100 μm.

The ultrasonic processor was fixed to the head of a conventional milling machine via a suitable setup as shown in Figure 1. So that, the sonotrode can move freely along the welding line in front of the FSW tool by nearly 25 mm and with an angle of inclination of 60° between the axis of the sonotrode and the workpiece surface to keep it away from the tool. Thereby, the waves of ultrasonic vibration can be supplied directly into the localized area of the workpiece eliminating any loss in the transmitted energy compared to other methods for transmitting these waves.

2. 1. Process Parameters　　　　In this paper, the experiments were designed and planned to perform a comparative study between conventional FSW and

TABLE 1. Chemical composition of AA 6082-T61, Wt%

Si	Fe	Cu	Mn	Mg	Cr	Ni	Ti	Al
1.1	0.5	0.1	0.7	0.9	0.25	0.2	0.1	REM

TABLE 2. Mechanical properties of AA 6082-T61

UTS (MPa)	YS (MPa)	Elongation (%)	Hardness (HV)
270	185	21	112

UTS: Ultimate tensile strength; YS: Yield strength
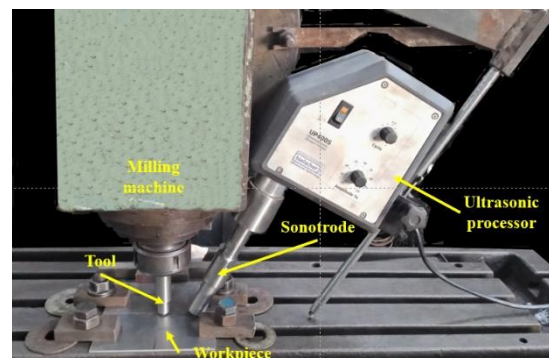
Figure 1. Experimental setup for UAFSW process

---

[1] www.commercialefond.it

UAFSW. For this purpose, the rotational speed was held constant at 800 rpm and at different welding speeds of (40, 80, 120, and 160 mm/min), to figure out how ultrasonic vibration waves can affect the joint performance. A set of experiments were performed according to Table 3. Where samples A, B, C, and D were compared to samples E, F, G, and H, respectively.

2. 2. Tensile Testing   A universal testing machine (Shimadzu-1000KN) with a ram speed of 1 mm/s was utilized to measure the tensile strength of the welded joints. The specimens were prepared based on ASTM E8M-08 standard as shown in Figure 2. The specimens were cut from the transverse cross-section perpendicular to the welding line with an abrasive water jet machine to ensure good dimensional accuracy as well as to avoid any heat effect that may result in from the cutting operation.

2. 3. Micro-hardness Test   Vickers micro-hardness test was performed to obtain the micro-hardness distribution of welded joints using micro-hardness tester (LM-700). A load of 100 grams and a holding time of 10 s were utilized. The measurements were taken along a horizontal line away from the specimen top surface by 1.5 mm, where reading is taken each 1 mm along the horizontal line.

2. 4. Microstructure Evolution   It was essential to evaluate the microstructure of the welded joints to find out the influence of ultrasonic vibration on the grain size and hence the mechanical performance of the joints. The microstructure was revealed mainly using optical light
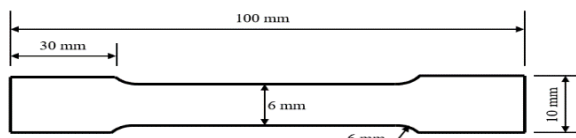
Figure 2. Standard tensile test specimen

TABLE 3. Process parameters for comparison at a constant rotational speed of (800 rpm)

Weld speed (mm/min)	Amplitude (μm)	Sample
40		A
80	Without Ultrasonic vibration	B
120		C
160		D
40		E
80		F
120	20	G
160		H

Microscopy (see Figure 3). The samples of dimensions ($30 \times 5 \times 3\ mm$) were cut from the transverse section of the joint using an abrasive water jet machine. To remove oxide films, scratches, and other impurities, the samples were ground in several stages, ranging from coarse to fine grinding using a different set of silicon carbide papers grades i.e. (220, 500, 800, and 1000) mounted on rotating water-lubricated disc. The samples were finally polished using abrasives suspended in a water solution on an electrically powered wheel covered by a cloth. The etching process was carried out in two immersion stages. In the first stage, the specimen was immersed for 60 s in 0.5M sodium hydroxide solution. In the second stage, the specimen was etched in a composition of 0.25M sodium hydroxide solution with 4% potassium permanganate ($KMnO_4$) for 15 s [20].

3. RESULTS AND DISCUSSION

3. 1. Influence of Ultrasonic Vibration on Weld Appearance   The quality of the weld line is an effective indicator of the success of the welding operation. The absence of visible surface imperfections refers to selecting the process parameters properly leading to generating adequate heat input and proper material flow. On the other hand, external defects such as large grooves, voids, and flashes result from poor material flow. In this respect, the weld surfaces of CFSW and UAFSW joints were compared at different welding speeds as shown in Figure 4. As can be noticed from the figure, the weld line appearance at low welding speeds such as 40 and 80 mm/min is sound and free of external defects for both CFSW and UAFSW. On the other hand, the difference in surface quality started to appear at higher welding speeds. The weld line surface resulting from CFSW had voids defect at a welding speed of 120 mm/min and large grooves at a welding speed of 160 mm, while the weld line appearance in UAFSW was better as it contained less density of defects. This improvement in the weld line appearance can be attributed to the enhanced material flow due to the applied ultrasonic
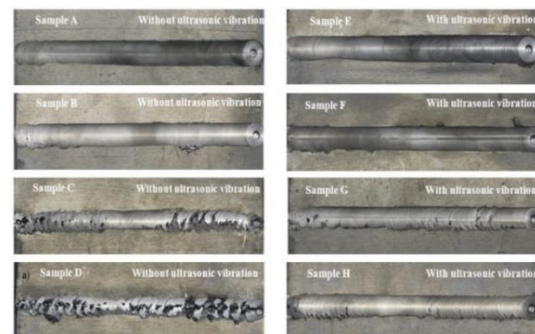
Figure 3. Comparison of weld appearance for all samples
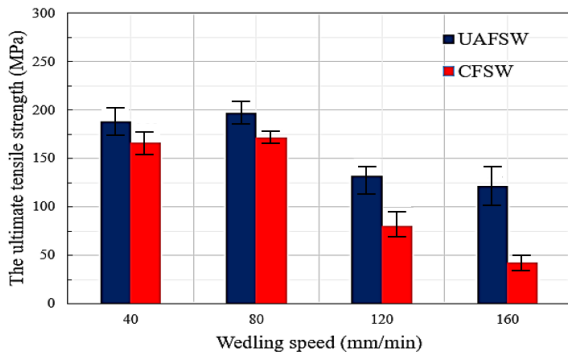
Figure 4. Comparison of UTS for CFSW and UAFSW at different welding speeds

vibrations and this effect is much more profound at high welding speeds [21].

3. 2. Influence of Ultrasonic Vibration on Tensile Properties   The ultimate tensile strength (UTS) for both CFSW and UAFSW samples was evaluated over a range of welding speeds to figure out the effect of ultrasonic vibration on the tensile strength and elongation percentage (elongation %) at different welding speeds. As shown in Figure 5, at a welding speed of 40 mm/min, the CFSW and UAFSW joints have an UTS of 166 and 188 MPa, respectively; showing an enhancement in UTS with a percentage of approximately 13% when ultrasonic vibration is on. Moreover, a similar trend was recorded at a velocity of 80 mm/min, where the UTS of the UAFSW joint is higher than that of CFSW by 15%. This improvement in the UTS can be demonstrated by the grain refinement action which has been detected in the microstructural analysis of the SZ. Conversely, a significant decrease in the UTS was recorded at high welding speeds i.e., 120 and 160 mm/min for both CFSW and UAFSW. But the fall in the UTS was more dramatic for CFSW joints recording values of 80 MPa at a speed of 120 mm/min and 42 MPa at 160 mm/min, which means that joints had failed. This failure of joints at such high welding speeds is mainly because of the lack of time available for material to absorb heat and soften hence the
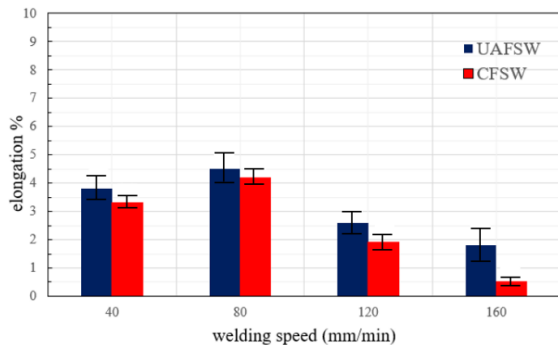
material flow is poor and severe defects are produced. On the other hand, the situation for UAFSW was much better as the UTS at a speed of 120 mm/min and 160 mm/min were 132 MPa and 121 MPa respectively. This performance of UAFSW joints compared to CFSW is evidence of the significant role the ultrasonic waves played in providing the material with more softening action.

Regarding the elongation%, as shown in Figure 5, there is a considerable reduction in the elongation % whether in CFSW or UAFSW compared to the base metal. This is because of the lower morphological homogeneity in CFSW and UAFSW, as different microstructural zones namely, SZ, TMAZ, and HAZ are formed which are morphologically different. A similar finding was reported by other researchers.

3. 3. Influence of Ultrasonic Vibration on Hardness   A comparison between the micro-hardness profile in CFSW and UVAFSW at different welding speeds is shown in Figures 6 and 7. In general, the micro-hardness profile resulting from FSW process is characterized by W-shape. Where the values of micro-hardness slightly decrease in the HAZ due to dissolution and coarsening of precipitates compared to the values at the SZ and then rise again until reaching its maximum value at the base metal.
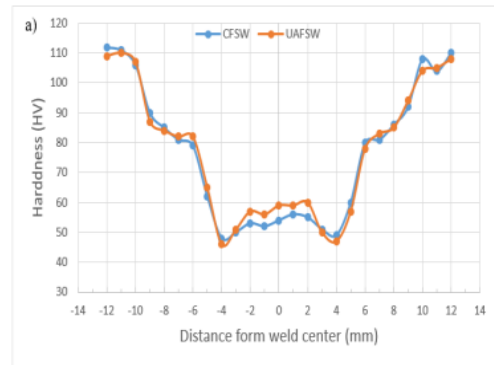
(a)
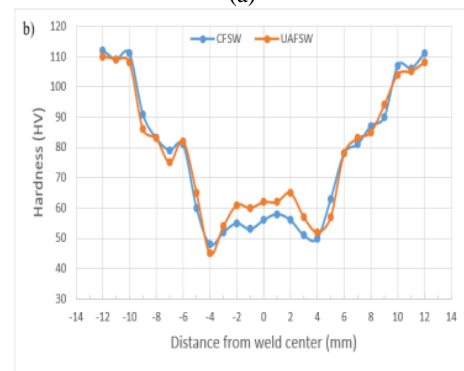
(b)

Figure 6. Comparison of microhardness for a) Samples A and E , b) Samples B and F

Figure 5. Comparison of elong% for CFSW and UAFSW

(a)

(b)
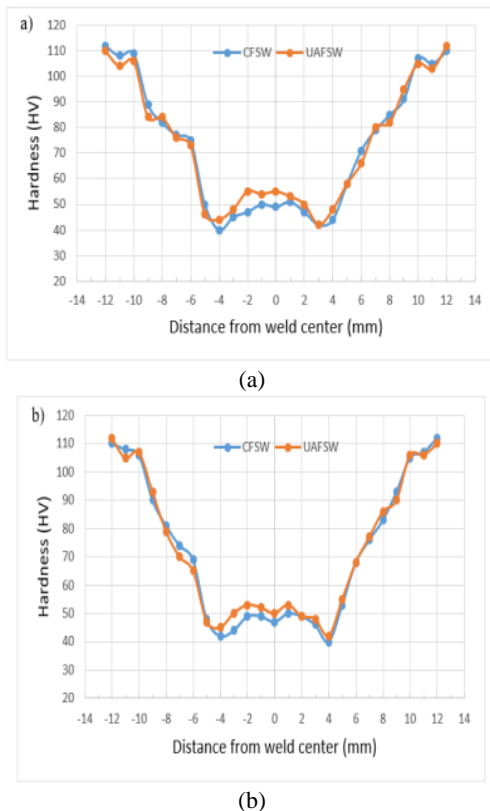
Figure 7. Comparison of microhardness for a) Samples C and G b) Samples D and H

As shown from figures the micro-hardness profiles for CFSW and UAFSW are close in most of the regions except the stirring zone, where the values of micro-hardness are higher in UAFSW than CFSW. This improvement in micro-hardness values in the stirring zone are predicted because of the grain refinement in the stirring zone.

3. 4. Influence of Ultrasonic Vibration on Microstructure Microstructure evolution is of great importance as it controls the properties of the weld joint. Many microstructural alterations happen during the FSW process because of the thermal cycles and plastic deformation. there are mainly three distinct regions in FS-welded joints, namely, stir zone (SZ), thermo-mechanically affected (TMAZ), and heat-affected zone (HAZ). In this section microstructure samples extracted from CFSW and UAFSW joints were prepared according to standard procedure and examined using light optical microscopy to find out the potentiality that ultrasonic vibration waves have on controlling the microstructure of the welded joints in terms of the grain size and weld formation.

3. 4. 1. The Microstructure of the Base Metal Firstly, the microstructure of the parent metal AA 6082-

T61 in the as-received status was viewed using LOM and SEM to determine the average grain size and examine the precipitate state as shown in Figures 8(a) and (b). The grain size for the base metal was found by applying the line intercept method. In this manner, image J software was utilized and average grain size of 14 μm was obtained. The hardening precipitates of type Mg_5Si_6 were revealed using SEM.

3. 4. 2. Microstructural Map of FS-Welded Joint To ensure the appropriateness of all preparation steps for microstructural analysis and thereby the clarity of all microstructural, a microstructural map was established using LOM as shown in Figure 9. All microstructural zones i.e., stir zone which has experienced an intense plastic deformation with very equiaxed fine grains, TMAZ with its distinguished elongated grains, and HAZ which has coarse grains were obtained obviously.

3. 4. 3. Influence of Ultrasonic Vibration on Different Microstructural Zones The influence of ultrasonic vibration waves on the grain size at various microstructural zones was investigated by comparing the microstructure of sample B which has been conventionally friction stir welded with sample F which has been ultrasonically assisted friction stir welded. Both samples are welded at the same welding condition of 800 rpm and 80 mm/min. Figures 10(a) and (b) presents the microstructures of samples B and F, respectively. Investigating the SZ of both samples showed a grain refinement due to the high plastic deformation in this region. The average grain sizes calculated were 3.8 μm and 2.9 μm for samples B and F, respectively. Thereby, it is clear that imposing ultrasonic vibration waves during the FSW process causes a grain size reduction by 23.6% at the stirring zone. This grain refinement action can be
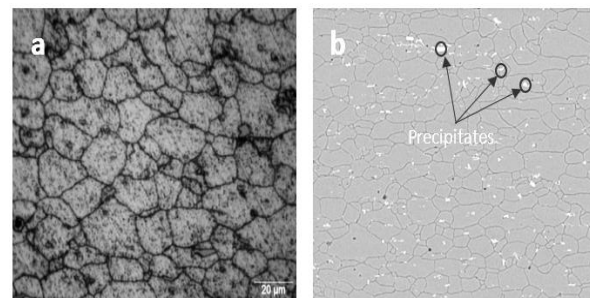
Figure 8. Microstructure of base metal using a) LOM, b) SEM

Figure 9. Microstructural map for FS-welded sample
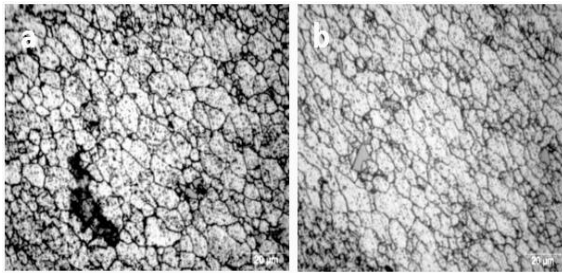
Figure 10. Microstructure of a) sample B at TMAZ, b) Sample F at TMAZ

mainly attributed to the acoustic softening phenomena furthering welding operation and Its role in improving plastic deformation [16]. From this finding, it is expected that the mechanical properties of UAFSW joints will be superior compared to CFSW according to Hall-Petch equation. These results agree with similar findings by other researchers [22].

The microstructure of the TMAZ at samples B and F was obtained as shown in Figures 11(a) and (b), respectively. The grain size of 7.8 μm and 7.6 μm in average, was calculated for samples B and F, respectively. Thereby, it can be stated that ultrasonic vibration waves do not have a significant influence on the grain size at the TMAZ.

The average grain size at the HAZ was also calculated for samples B and F after viewing their microstructure as shown in Figures 12(a) and (b). The average grain size of 14 μm and 14.1 μm was obtained for samples B and F, respectively. The two values are approximately equal and

hence we can demonstrate that ultrasonic vibration does not have any effect on the grain size at the HAZ.

3. 5. Influence of Ultrasonic Vibration on the Weld Formation   The weld formation at the stirring zone was examined at high welding speed to find out the role of ultrasonic vibration waves on the material flow. Hence, the microstructures of samples C and G which have been welded at a welding speed of 120 mm/min were viewed and compared as shown in Figures 13(a) and (b). At the SZ of sample C, which was conventional welded, a large defect of tunnel type was detected as shown in Figures 13(a). This defect mainly results from the low heat input, which is corresponding to high welding speed, leading to insufficient softening and improper material flow [23]. On the contrary, the microstructure of sample G which has been ultrasonically assisted during the FSW process is defect-free and onion rings which express the proper material flow are clear in Figures 13(b). This enhancement in the material flow when ultrasonic vibration was applied can be explained by the acoustic softening effect which is responsible for providing the FSW process with an additional amount of softening during the welding operation. Subsequently, it can be stated that ultrasonic vibration plays a critical role in eliminating some welding defects at the SZ due to the extra softening it provides [24]. The microstructure data, grain sizes, and a scatter of grains sizes are summarized in Table 4.

Figure 11. Microstructure of a) sample B at SZ, b) sample F at SZ
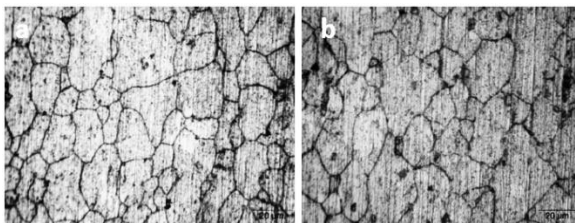
Figure 12. Microstructure of a) sample B at HAZ, b) Sample F at HAZ
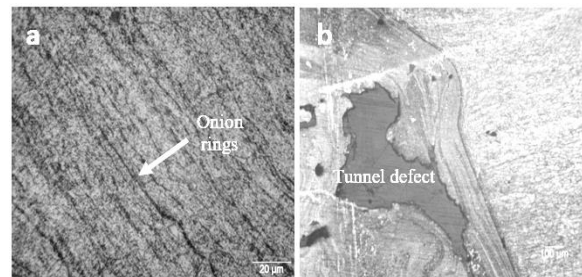
Figure 13. a) Free-defective microstructure at sample G, b) Tunnel defect in sample C

TABLE 4. The microstructure data and grain sizes

Specimen type	Average Particle size	Microstructure zone
Base Material	14μm	Through the sample
CFSW	3.8 μm	SZ
UAFSW	2.9 μm	
CFSW	7.8 μm	TMAZ
UAFSW	7.6 μm	
CFSW	14 μm	HAZ
UAFSW	14.1 μm	

4. CONCLUSIONS

In the present study, a microstructural investigation showed that integrating ultrasonic vibration with the FSW process can reduce the grain size at the stirring zone by 23 %. While ultrasonic vibration does not affect the grain size at the HAZ nor at the TMAZ. As a result of grain refinement at SZ, the strength of joints produced by the UAFSW process was higher than its counterparts made by CFSW. In addition, examining the weld formation showed that ultrasonic vibration acted a dominant role in enhancing the material flow and eliminating some specific weld defects at high welding speeds such as tunnel defect. The effect of ultrasonic vibration on the UTS is more profound at higher welding speeds, where acoustic softening can provide FSW process with additional softening and thereby, the material flow is improved. Ultrasonic vibration has helped also in improving the elongation percentage by 7%. On the contrary, at these high welding speeds, the weld appearance of conventional FS-welded joints contain large defects due to the low heat input, and fewer defects were detected when ultrasonic vibration was applied.

5. REFERENCES

1. Terje, M., Ove, K. and Øystein, G., "Modified friction stir welding", *International Patent, Appl. WO99039861*, (1999).

2. Smith, B.L., Saville, P.A., Mouak, A. and Myose, R.Y., "Strength of 2024-t3 aluminum panels with multiple site damage", *Journal of Aircraft*, Vol. 37, No. 2, (2000), 325-331.

3. Ahmadnia, M., Seidanloo, A., Teimouri, R., Rostamiyan, Y. and Titrashi, K.G., "Determining influence of ultrasonic-assisted friction stir welding parameters on mechanical and tribological properties of aa6061 joints", *The International Journal of Advanced Manufacturing Technology*, Vol. 78, No. 9, (2015), 2009-2024. doi: 10.1007/s00170-015-6784-0.

4. Mabrouk, O., El-Wazery, M. and El-Desouky, M., "Simulating ultrasonic vibration enhanced fsw process of aa6082 using finite element method", in IOP Conference Series: Materials Science and Engineering, IOP Publishing. Vol. 973, (2020), 012023.

5. Saha, R. and Biswas, P., "Current status and development of external energy-assisted friction stir welding processes: A review", *Welding in the World*, (2022), 1-33. https://doi.org/10.1007/s40194-021-01228-7

6. Gibson, B.T., Lammlein, D., Prater, T., Longhurst, W., Cox, C., Ballun, M., Dharmaraj, K., Cook, G. and Strauss, A., "Friction stir welding: Process, automation, and control", *Journal of Manufacturing Processes*, Vol. 16, No. 1, (2014), 56-73. http://dx.doi.org/10.1016/j.jmapro.2013.04.002

7. Padhy, G., Wu, C. and Gao, S., "Friction stir based welding and processing technologies-processes, parameters, microstructures and applications: A review", *Journal of Materials Science & Technology*, Vol. 34, No. 1, (2018), 1-38. https://doi.org/10.1016/j.jmst.2017.11.029

8. Zhou, L., Li, G., Liu, C., Wang, J., Huang, Y., Feng, J. and Meng, F., "Microstructural characteristics and mechanical properties of al–mg–si alloy self-reacting friction stir welded joints", *Science and Technology of Welding and Joining*, Vol. 22, No. 5, (2017), 438-445. http://dx.doi.org/10.1080/13621718.2016.1251733

9. Padhy, G., Wu, C. and Gao, S., "Auxiliary energy assisted friction stir welding–status review", *Science and Technology of Welding and Joining*, Vol. 20, No. 8, (2015), 631-649. http://dx.doi.org/10.1179/1362171815Y.0000000048

10. Ferrando, W.A., *The concept of electrically assisted friction stir welding (eafsw) and application to the processing of various metals*. 2008, Naval Surface Warfare Center Carderock Div Bethesda Md Survivability ….

11. Campanelli, S.L., Casalino, G., Casavola, C. and Moramarco, V., "Analysis and comparison of friction stir welding and laser assisted friction stir welding of aluminum alloy", *Materials*, Vol. 6, No. 12, (2013), 5923-5941. https://doi:10.3390/ma6125923

12. Mohan, D.G. and Gopi, S., "Induction assisted friction stir welding: A review", *Australian Journal of Mechanical Engineering*, (2018). https://doi.org/10.1080/14484846.2018.1432089

13. Bang, H., Bang, H., Jeon, G., Oh, I. and Ro, C., "Gas tungsten arc welding assisted hybrid friction stir welding of dissimilar materials al6061-t6 aluminum alloy and sts304 stainless steel", *Materials & Design*, Vol. 37, No., (2012), 48-55. doi. https://doi:10.1016/j.matdes.2011.12.018

14. El-Wazery, M., Mabrouk, O. and El Sissy, A., "Optimization of ultrasonic-assisted friction stir welded using taguchi approach", *International Journal of Engineering, Transactions A: Basics* Vol. 35, No. 1, (2022), 213-219. doi: 10.5829/ije.2022.35.01a.20

15. Liu, X., Wu, C. and Padhy, G., "Improved weld macrosection, microstructure and mechanical properties of 2024al-t4 butt joints in ultrasonic vibration enhanced friction stir welding", *Science and Technology of Welding and Joining*, Vol. 20, No. 4, (2015), 345-352. https://doi.org/10.1179/1362171815Y.0000000021

16. Padhy, G., Wu, C., Gao, S. and Shi, L., "Local microstructure evolution in al 6061-t6 friction stir weld nugget enhanced by ultrasonic vibration", *Materials & Design*, Vol. 92, (2016), 710-723. http://dx.doi.org/10.1016/j.matdes.2015.12.094

17. Zhong, Y., Wu, C.a. and Padhy, G., "Effect of ultrasonic vibration on welding load, temperature and material flow in friction stir welding", *Journal of Materials Processing Technology*, Vol. 239, (2017), 273-283. https://doi.org/10.1016/j.jmatprotec.2016.08.025

18. Gao, S., Wu, C. and Padhy, G., "Material flow, microstructure and mechanical properties of friction stir welded aa 2024-t3 enhanced by ultrasonic vibrations", *Journal of Manufacturing Processes*, Vol. 30, (2017), 385-395.

19. Warren, A., "Developments and challenges for aluminum--a boeing perspective", in Materials forum. Vol. 28, (2004), 24-31.

20. Krasnowski, K., Hamilton, C. and Dymek, S., "Influence of the tool shape and weld configuration on microstructure and mechanical properties of the al 6082 alloy fsw joints", *Archives of Civil and Mechanical Engineering*, Vol. 15, No. 1, (2015), 133-141. http://dx.doi.org/10.1016/j.acme.2014.02.001

21. Yang, C., Wu, C. and Shi, L., "Effect of ultrasonic vibration on dynamic recrystallization in friction stir welding", *Journal of Manufacturing Processes*, Vol. 56, (2020), 87-95. https://doi.org/10.1016/j.jmapro.2020.04.064

22. Zhou, H., Cui, H. and Qin, Q.H., "Influence of ultrasonic vibration on the plasticity of metals during compression process", *Journal of Materials Processing Technology*, Vol. 251, (2018), 146-159. http://dx.doi.org/10.1016/j.jmatprotec.2017.08.021

23. Kah, P., Rajan, R., Martikainen, J. and Suoranta, R., "Investigation of weld defects in friction-stir welding and fusion welding of aluminium alloys", *International Journal of Mechanical and Materials Engineering*, Vol. 10, No. 1, (2015), 1-10. doi: 10.1186/s40712-015-0053-8

24. Liu, X. and Wu, C., "Elimination of tunnel defect in ultrasonic vibration enhanced friction stir welding", *Materials & Design*, Vol. 90, (2016), 350-358. http://dx.doi.org/10.1016/j.matdes.2015.10.131

Persian Abstract

چکیده

فرآیند جوشکاری اصطکاکی اغتشاشی (FSW) هنوز در حال رشد است تا قابلیت‌های فرآیند را بهبود بخشد و بر اشکالات خاصی که در فرآیند با آن مواجه می‌شویم غلبه کند. سرعت‌های جوشکاری کم، بارهای جوشکاری بالا و گشتاور مورد نیاز بالا از محدودیت‌های اصلی این فرآیند هستند. استفاده از ارتعاش اولتراسونیک یکی از رویکردهای همه‌کاره‌ای است که برای مقابله با این مسائل پیشنهاد شده است. در این مقاله، یک مطالعه مقایسه‌ای بین فرآیند جوشکاری اصطکاکی اغتشاشی معمولی (CFSW) و فرآیند جوشکاری اغتشاشی اصطکاکی به کمک اولتراسونیک (UAFSW) انجام شد. هدف ارزیابی کمی و کیفی تأثیر امواج ارتعاشی اولتراسونیک بر کیفیت سطح جوش، استحکام کششی، میکروسختی، ریزساختار و تشکیل جوش اتصالات است. نتایج نشان داده‌اند که امواج ارتعاشی اولتراسونیک باعث عمل پالایش دانه در ناحیه همزن (SZ) و همچنین نقش مطلوب آن در افزایش خواص مکانیکی و از بین بردن عیوب جوش، به‌ویژه در سرعت جوشکاری بالا (۱۲۰ میلی‌متر در دقیقه) می‌شود. همچنین، کاهش قابل توجهی در درصد کشیدگی چه در CFSW و چه UAFSW در مقایسه با فلز پایه وجود دارد. این به دلیل همگنی مورفولوژیکی کمتر در مناطق مختلف ریزساختاری در CFSW و UAFSW است. با این حال، هیچ اثر عمیقی برای امواج مافوق صوت بر روی اندازه دانه در منطقه تحت تاثیر حرارت مکانیکی (TMAZ) یا منطقه متاثر از حرارت (HAZ) یافت نشد.

International Journal of Engineering

The Behaviour of Wave Propagation for Structural System Identification: A Comparative Study

B. Patel*, U. K. Dewangan

Department of civil engineering, National Institute of Technology, Raipur, India

P A P E R   I N F O

A B S T R A C T

The way a wave behaves, while propagating across a medium, varies with the wave type and the medium. So, knowledge of the behaviour of a wave in a system with a different form of damage, and behaviour of different types of waves in a particular system is an essential prerequisite for almost all activities in structural system identification and mainly for damage detection and localization of damage. This paper presents a comparative study of various wave propagations, that has been done by researchers in various structural systems. Further, a numerical model of an isotropic plate using finite element is created both with and without damage. The behaviour of waves has been studied. Finally, the comparative result is shown. This paper offers a new perspective for ongoing research by providing the most recent developments, difficulties, and prospects of wave propagation behaviours for damage detection and localization in the commonly used structural systems and structural elements. While propagating through different structural systems and components, the most used waves, which are (a) Shear wave, (b) Rayleigh wave, (c) Ultrasonic wave and (d) Lamb wave, have been thoroughly investigated. Along with several difficult problems for future growth, the summarized observations are provided.

doi: *10.5829/ije.2022.35.12c.05*

1. INTRODUCTION

A wave is a form of disturbance that is carried forward by the particles of the system through vibration. During wave propagation, only energy is transferred and not particles. As, the behaviour of waves changes with change in medium, this property has been used by researchers for system identification. This method is called, "Wave Propagation based System Identification". During 19th century, to determine the presence of damage on train wheels, wheel-tappers generated the waves by tapping a railroad wheel with a hammer. They determine the presence of damage based on the sound waves produced by the wheel. The various rail irregularities, in the wheel-rail system, have also been analyzed by Yang et al. [1].

The vibration based structural system identification, for damage identification and localization, has also been used by many researchers. But, not all cases can be adequately assessed using this method [2]. When damage starts occurring and further when it grows, the stiffness is reduced and the stability of the structure is also affected. Also, if the change in stiffness is small, the change in natural frequencies is small. In that case, the vibration based technique is not very efficient [3]. Also, the Timoshenko cantilever beam supported by spring was examined by Aydin et al. [4]. According to the authors, the different beam vibrations will result in varied distributions of elastic supports supported by the beams. Internal forces can occasionally exceed yield limits, which is significant for damage. Also, the sensitivity of the behaviour parameters could be used for the damage assessment. For the same beam, the optimum locations and the amounts of the springs were investigated for the first and second modes [5]. This technique may be used for finding the damage location. When damage is far from the support as in the case of the cantilever beam, the vibration based feature may not detect the damage accurately. Golafshani et al. [6] have also studied the vibration feature in the system.

Corresponding Author Institutional Email:
bpatel.phd2018.ce@nitrr.ac.in (B. Patel)

In metallic and composite constructions, wave propagation has been very effective for damage detection and localisation. So, it can also be used in various other structural systems such as trusses, multi-storey frames, bridges etc. In the previous studies, it was observed that in many cases, the wave packet overlap, due to which the identification of damage signal becomes more complex. The diffraction wave packets expand in the time domain. Consequently, the crack imaging result based on the signals presents a reasonably low resolution. Also, the wave's multimodal behaviour, dispersion, scattering and attenuation have an impact on damage signature. As a result, it is more difficult to use the wave technique. But with the right knowledge of the wave's properties and behaviour, the right choice of transducers, and signal processing, this complexity can be minimized. Hence, a broad classification has been provided for various forms of waves in section 2. For better understanding of how different types of waves behave, while propagating through different structural systems and components, the most commonly used waves, are (a) Shear wave, (b) Rayleigh wave, (c) Ultrasonic wave and (d) Lamb wave, which have been thoroughly investigated in section 3.

As, the objective of this paper is to study the behaviour of wave in a system with different form of damage, so for that total four different damage cases in a particular system were considered for numerical case studies in section 4. As per the literature, the behaviour of waves can be clearly seen in the plate, as compared to any other structural element. Also, in plate various forms of damage occur. So, for the numerical case study, the most common form of damage that can occur in the plate (damage in the form of hole, fatigue crack, near edge crack at 2 different locations) has been considered. The comparative result has been provided.

2. CLASSIFICATION OF WAVE

The broad classification of various types of waves, including waves that can be utilized for structural system identification.

2. 1. Depending upon the Motion of the Wave
Depending on the motion of the wave, it can be classified as mechanical waves, matter waves and electromagnetic waves.

The matter waves' wavelength is too tiny to have a noticeable practical effect on daily living. An atom's wavelength is roughly 3×10^{-11} metres. It is difficult to encapsulate a wavelength of this size in a structure. Electromagnetic wave does not require any medium for propagation. Both the magnetic and electric fields couple together to form this wave. These waves have been used by researchers for damage detection in metallic and composite materials. However, the generation of electromagnetic waves is not as simple as the generation of mechanical waves in a structural system. Thermal waves have also been used by many researchers for damage assessment. Parvez et al. [7] have shown that, as this wave is generated in the system, the temperature rises and this response is further quantified for building relation for damage assessment. The medium must have a minimal amount of friction between its particles as well as elasticity and inertia to produce mechanical waves. These waves can be refracted, diffracted and reflected. They could be alter in velocity at material discontinuity or when there are foreign particles inside the medium or on its surface. This characteristic will be useful in identifying damage and pinpointing the damage to a specific structural system or structural component.

2. 2. Depending upon the Dynamic Deformation of Particle
Waves can be elastic waves, plastic waves, or shock waves depending on how dynamic deformation in particle occurs.

Recent analyses of plastic wave profiles in metals like Beryllium30, Copper29, and Aluminum28 reveal viscous effects within the shock front and strength qualities at the Hugoniot state that are peculiar in behaviour and difficult to understand. Shock waves also require a medium to propagate, similar to the mechanical wave. Also, the medium required is elastic. But, the speed of propagation is faster than the local speed of sound. Elastic waves are the most commonly used, it can be further classified as:
1. Longitudinal wave/ P Wave
2. Transverse wave/ Distortional wave/ Secondary wave/ Shear wave/ S wave
3. Bending/ Flexural wave
4. Love wave
5. Stonley wave/ Interfacial wave
6. Rayleigh wave/ Surface wave

2. 3. Based on Region of Propagation
Waves can be further classified as Guided Waves and Bulk Waves, based on the region of propagation.

The bulk wave can be generated in an infinite homogenous body. This wave can propagate without getting interrupted by the boundaries or the interface. The guided wave is further classified as a lamb wave and ultrasonic wave. Lamb waves can be symmetric, asymmetric or have a combined mode.

3. VARIOUS WAVE PROPAGATION BEHAVIOUR IN STRUCTURAL SYSTEMS AND ELEMENTS

The way a wave behaves, while propagating across a medium, varies with the wave type and the medium. Therefore, understanding how various types of waves behave in a given system is a requirement for nearly all actions related to wave propagation based structural

health monitoring, mainly for system identification for various structural systems and structural elements. So, for the above, various literature review are presented in this section.

3. 1. Shear Wave   This wave is generated in a system that has shearing properties, such as solids. In the case of a shear horizontal wave, the particle of the medium executes a simple harmonic motion about its mean position in the direction perpendicular to the direction of propagation of the wave. If the layer interface is too close to the wavelength, it was impossible to discern between the body wave and the surface wave [8]. Mei et al. [9] mentioned in their research that, the shear horizontal waves were very sensitive to damage at the interface. Delamination in composites is considered here. These waves are mild dispersive in composites compared to the lamb wave, so they are simpler for damage diagnostic. This wave has been generated at the layer of a composite beam, with both ends clamped. The symmetric and asymmetric modes of lamb wave along with shear horizontal wave are generated in the system, the damage identification becomes complex in that case. Further, the pure shear horizontal wave has been generated that are non-dispersive and the wave packets are strong. The damage was successfully identified and located with an error of 3.7%. Nazeer et al. [10] have done the damage identification in the plate, having damage in the form of transverse cracks running along the bend and delamination in the bend. The shear mode in the bend is dispersive in comparison to the SH0 wave in a plate, and the curvature of the bend influences its wavefield properties. The scattering investigations revealed that, in contrast to inner surface cracks, the wave is more sensitive to outer surface fractures in the bend as frequency increases, because there is transverse shear tension at the bend. Choi et al. [11] have also used the MIRA, a shear-wave based ultrasonic system of low frequency (20–100 kHz) multifunctional phased array, which is used to detect damage in concrete related structures. Damage in the form of the changes that occurred in adhesion property at the interfacial adhesion was considered [12]. Further, the damage assessment in an isotropic plate with thickness crack was done by using the shear horizontal guided wave mode [13]. Rajagopal and Lowe [13] have shown that the shear horizontal guided wave gets scattered at the crack location in an isotropic plate. Hashemi and Ghasem Alaskari [14] have also studied the behaviour of shear waves in a laterally complex medium. They have taken the displacement vector of shear waves in two different orientations and showed that this will be best suited for dynamic cases.

3. 2. Rayleigh Wave   Masserey and Fromme [15] have shown that it can be interpreted as the superposition of the first anti-symmetric and symmetric Lamb mode.

These are also sensitive to extremely small cracks. The wave alters its behaviour even at a 120 μm size crack. Wang et al. [16] have considered damage in the form of crack, that is present near the surface, in any homogeneous, isotropic and elastic system. The wave showed a change in behaviour at the crack length, that are smaller than the wavelength of the Rayleigh Wave. Also, damage identification is more accurate in such cases. Cook and Berthelot [17] have considered the damage in the form of fatigue crack, on the surface of the flat bar specimen. A small amount of wave gets reflected at the notch, and also at the growing fatigue crack. Both the wave signals interfered. The amplitude of the reflected wave signal of the notch is much larger than that of the fatigue crack. That property is used to identify the damage. If the wavelength is smaller than the radius of curvature then it can not detect the little distortion. Zeng et al. [18], considered the inclined surface crack in an aluminium plate. When the wave reaches the inclined defect, it splits into two parts. Thus, these waves can only be employed for the identification of near-surface fractures and flaws, according to the aforementioned literature.

3. 3. The Ultrasonic Guided Wave   This wave can be generated in the cantilever beam. Damage may be in the form of crack, discontinuity or the presence of a foreign particle. All of these cases create change in the medium. So, in this region, the velocity of the wave is affected, if scatters, refracts or diffracts. Hence, the wave signal when compared with the baseline signal indicate the existence and location of the damage. Arundas and Dewangan [19] have used the ultrasonic pulse velocity test to find the crack location in a cantilever beam. Mu et al. [20], have done the real-time performance of health monitoring in ocean platform. Carbon Steel, Q235, of 500 mm (length) × 500 mm (width) × 5 mm (thickness) was taken for damage assessment. Damage is in the form of a hole of 2 mm in depth with a 3 mm diameter. Initially, when there was no damage, there is no reflected wave, so all the wave packets at the sensors are the same. When a wave comes across the damage, the signal scatters, resulting in the formation of minor wave packets, as shown in Figures 4(a) and 4(b) [20]. Mu et al. [21] have given a damage localization approach based on diffracted wave property of the ultrasonic wave. In this paper, Carbon Steel, Q235, of 1250 mm (length) × 1250 mm (width) × 2 mm (thickness) is taken for analysis. Damage is in the form of a fatigue crack. When the wave reaches the damage region, it gets reflected, scattered and diffracted. When the obstruction's size is far less than the sound wave's wavelength, it still propagates as it would in the absence of the obstacle, hence damage could not be captured in such case. The sound wave diffracts around the obstruction and propagates to the other side of the obstacle if the obstacle length is similar to the

wavelength and is primarily reflected and the region behind the obstruction is silent when the obstacle's size is significantly larger, hence in these two conditions the damage affect wave signal. Also, the ultrasonic guided wave propagation method was utilized by Malik, and Chinchilla [22] to detect and locate damage in a composite beam. The damage is defined as delamination and transverse crack. Delamination was located between the 2nd and 3rd layers of the beam. The exact damage location was 0.45 meters, but the Bayesien inverse problem methodology has given 0.4494 meters. Thus, the deviation was only 0.13%. Further, on a 6.4 m tube, by El Mountassir et al. [23], they have carried out the damage identification and localization using a sparse estimating technique. The actual position of damage was at 3 meters but this technique estimated at 3 meters $\pm$ 0.41 mm. Here, $\pm$ 0.41 mm is the error of localization. Structural system when discretized to the higher order finite element, the ultrasonic wave was able to capture the damage, which was reported by Schmicker et al. [24]. This wave can also capture the damage caused by improper manufacturing, in carbon fibre reinforced plastic rods, that are used in gliders [25]. Also, the ultrasonic wave propagation technique for damage detection can be used in the polycrystalline medium stated by Adithya et al. [26].

3. 4. Lamb Wave   Guided waves have been widely employed in the structural health monitoring and system identification of composite constructions, because of their long-distance propagation in complicated structures with low energy loss. Staszewski et al. [27] presented a damage detection methodology for composites based on active and passive approach. Lamb waves were used for online monitoring. However, there is propagation complexity of these waves which results in difficult analysis and interpretation. Requirements for baseline measurements are mainly the problem. Ng and Veidt [28] have conducted the numerical case study on the laminate composite square plate of 0.250 mm and thickness of 0.0016 mm. Damage is modelled as through-hole. In the output, the out-of-plane displacement of waves is shown on the plate. The demonstration of lamb wave propagating in all directions was seen at 15.8 µs. Further, at 26.8 µs and 36.8 µs, the scattering of the wave at the through-hole has been observed. Now, the signal with damage and undamaged case, are combinely plotted to identify the presence of damage. This plot has represented the presence of the damage. Mishra et al. [29] have shown the displacement along the y-direction of the beam in crack identification.

4. NUMERICAL CASE STUDY

4. 1. Finite Element Model   In this section, the finite element model of a plate having a density of 2500

Kg/m^3, Young's modulus of elasticity 62 GPa and Poisson's ratio 0.33 is modelled in ABAQUS CAE. The length of the plate is 100 mm, and the width of 100 mm has a thickness of 1 mm. To study the behaviour of a wave in a system with different forms of damage four most common forms of damage are considered in a particular system.
Case 1: Damage in the form of a hole
Case 2: Damage in the form of fatigue crack
Case 3: Damage in the form of crack near bottom edge
Case 4: Damage in the form of crack near the right edge
The simulation model of the initial state and all four damage cases are shown in Figures 1(a), 1(b), 1(c), 1(d) and 1(e), respectively.

4. 2. Simulation of Finite Element Model   An impulse signal, which is applied as concentrated force(CF3) in normal direction on exciter node to generate lamb wave is shown in Figure 2. The wave field model of the initial state is shown in Figure 3. and for all four damage cases are shown in Figure 4 to 7.

4. 3. Analysis of Simulation Result   In all the damaged model and the initial model, the exciter S1 is actuated, and the sensor S2 collect the wave motion. The signals collected by the sensor are shown in Figure 3 to
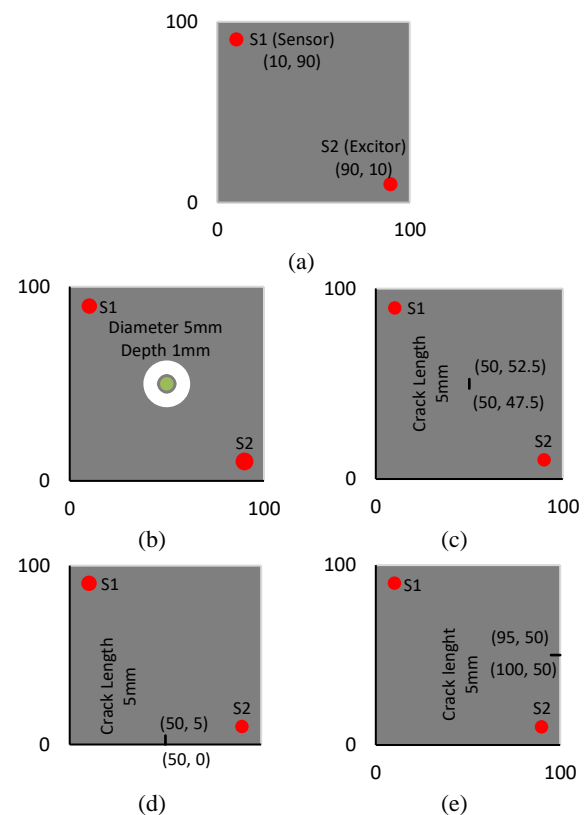
Figure 1. Simulation model of (a) Initial state (b) Damage state in Case 1 (c) Damage state in Case 2 (d) Damage state in Case 3 (e) Damage state in Case 4
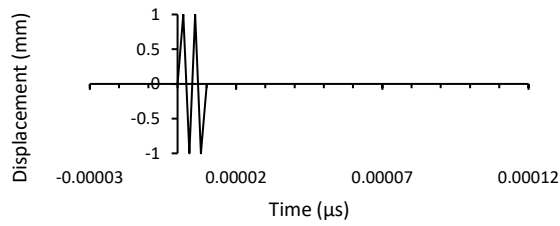
Figure 2. Impulse signal applied on the exciter
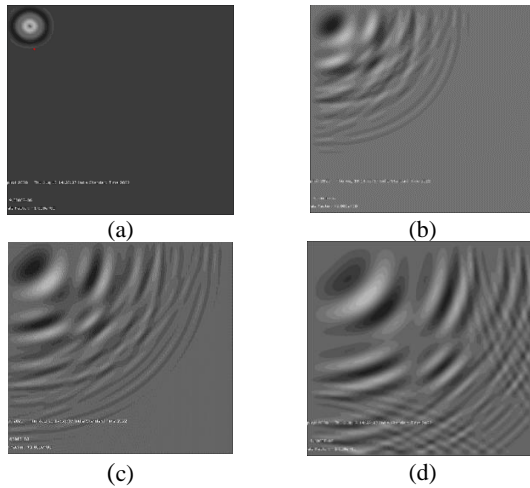
Figure 3. Wave field of baseline model at (a) 9μs, (b) 48μs, (c) 66μs, (d) 96μs
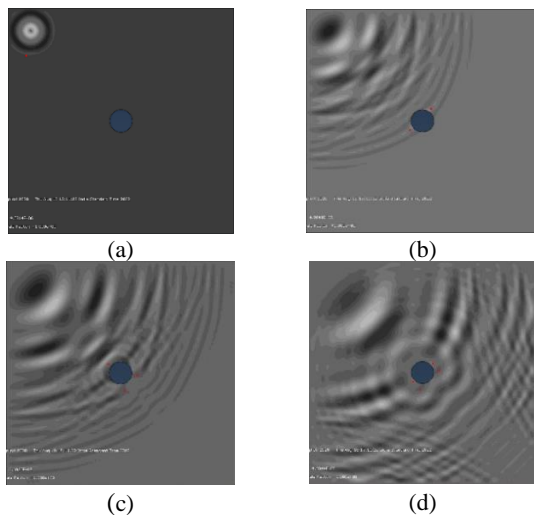
Figure 4. Wave field of damage model at (a) 9μs, (b) 48μs, (c) 66μs, (d) 96μs

Figure 5. Wave field of damage model, at (a) 9μs, (b) 48μs, (c) 66μs, (d) 96μs
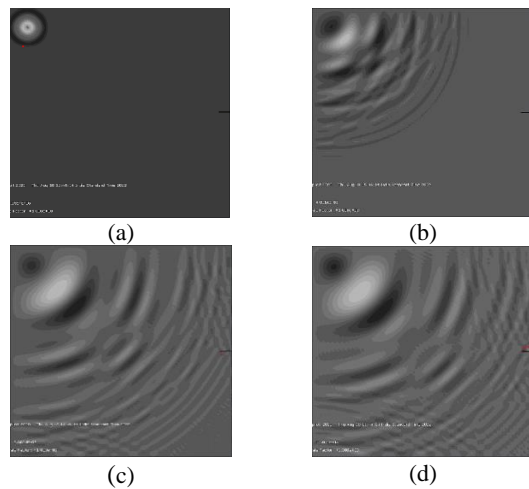
Figure 6. Wave field of damage model, at (a) 9μs, (b) 48μs, (c) 66μs, (d) 96μs
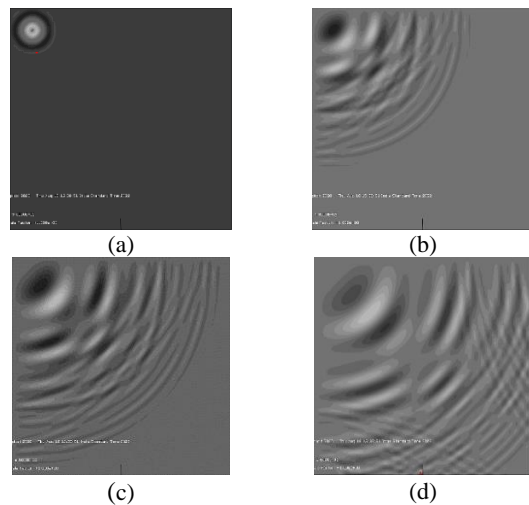
Figure 7. Wave field of damage model, at (a) 9μs, (b) 48μs, (c) 66μs, (d) 96μs

Figure 7. Initially, the wave has not reached the damage location, when the signal was collected by S2. So, it is visualized that the wave packets in all five models shown in Figures 3(a), 4(a), 5(a), 6(a), and 7(a) are identical in shape. The wave pattern at 48 μs, in Figures 6(b) and 7(b) is still the same as that of initial stage Figure 3(b), this is because the wave has not reached the damage portion.

Whereas, the wave when interacting with the damage case 1 and case 2, as shown in Figures 4(b) and 5(b); it is observed that, it gets reflected in this region. Due to this, the phase change occurs and the intensity of the wave is also affected. The wave field at this time interval when compared with the initial model, will provide the existence of damage. Further at time 66 µs (approximately) the minor wave packet formation is observed, which appears only in the damage stage and not in the initial stage. As shown in Figures 4(c) and 6(c) is due to phase change. The red mark is shown in figures is clearly showing the phase change. Further, when the wave reaches the boundary of the plate, then again due to phase change the wave packets are formed at each boundary. After some time all the wave packets are merged. If the sensor capture signal at this interval the complex wave signal may not give an accurate result. If there is a crack at the edge, then the sensor must be present near it. At the crack tip, the wave pattern is affected, and also it forms another wave packet.

In the following section, the signal of initial and damage state is plotted combinely, for the following case:
Case 1: Combine signal of initial state and damage in the form of a hole.
Case 2: Combine signal of initial state and damage in the form of fatigue crack
Case 3: Combine signal of initial state and damage in the form of crack near the right edge
Case 4: Combine signal of initial state and damage in the form of crack near the bottom edge

In all the graphs, it can be visualized that the signal of the initial stage and damage signal is initially overlapping. Only there is a uniform variation in magnitude in fatigue and hole in Figures 8(a) and 8(b). Although this variation is different in both damage cases, the pattern is similar. At the time interval, approximately between 78 µs to 90 µs the magnitude of both signals of Figures 8(a) and 8(b) are showing variation which can be due to some change in the model, that may be due to the presence of damage. The signal in this region is showing variation because it is affected by the difference between the initial and the damage model. The location of both fatigue crack and hole as damage is the same. This is the reason for the variation in the signal at the same time interval. Thus it can be remarked that if the location of the damage is the same then the signal may show variation at a particular time interval irrespective of the type of damage.

If the crack is present near the bottom edge then at the time interval between 55 µs to 78.7 µs (approximately) as shown in Figure 8(d), the signal of damage is not overlapping with the initial stage signal. Thus it can be remarked that it is due to the existence of some damage. If the crack is present near edge of the system, it is observed that the magnitude of the signal due to the crack is showing uniform decrease in comparison to the initial
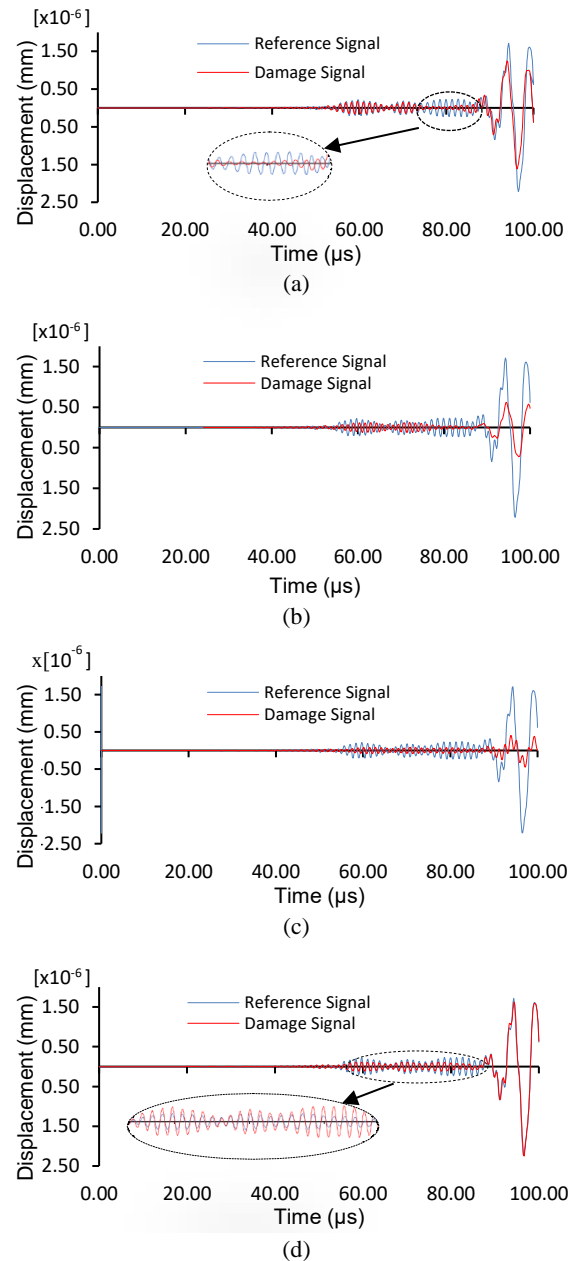
Figure 8. The signal of initial and damage state are plotted combinely for (a) Case1 (b) Case2 (c) Case3 (d) Case4

stage signal. As the crack is present far from the sensor near the edge, so the wave reflected at the boundary and the crack are combinedly showing in the signal. Due to this complexity sensor is not able to detect the variation accurately, hence for such a case the infinite boundary condition could provide a better solution.

5. FINAL REMARKS

Damage if present in the purview of the sensor will only change the behaviour of the wave. Also, the finite system

produces wave packets due to reflection at the boundaries, which when combined with the signal of the damage portion, will create a complex signal. Hence infinite boundaries could provide better results. Also, if the location of the damage is the same, then the signal may show variation at a particular time interval irrespective of the type of damage. Only the magnitude will vary. Each damage is creating its own wave packet, this could vary the signal.

Shear wave is commonly studied for monitoring composite structures, periodically layered composite structures with defects and adhesively bonded joints and plate like structures such as laminated composite plates. These waves are very mild dispersive in composites compared to the lamb wave, so they are simpler for damage diagnostic. The wave is more sensitive to outer surface fractures in the bend as frequency increases. The wave gets scattered at the crack location. In comparison, Rayleigh wave has been used for damage detection in metallic, civil structures, geo-materials and geophysical problems in literature. It involves mostly the propagation of single wave mode and a nearly non-dispersive nature. This wave alters its behaviour even at 120 μm size crack, hence they are also sensitive to extremely small cracks. Also, the wave travels to a very large extent as the speed is independent of the frequency. It easily propagates in the system containing a curved surface portion, with very little distortion if the wavelength is smaller than the radius of curvature. This wave can be used for the detection of near-surface cracks and defects. The ultrasonic wave can propagate through bounded structural media, such as thin plates and shells bounded by stress-free surfaces, composite beams, tubes, and rods. But, the bounded configuration of the waveguide often results in multi-modal, dispersive and attenuation, due to which the signal becomes more complex. In addition, the waves are reflected by the discontinuities and boundaries, leading to the cluttering of the response Thus, analysis and implementation of this wave propagation of guided wave and their interaction with damage are more complex. The above phenomena often camouflage the damage signature. Which can be sorted out through a proper selection of transducers, a good understanding of the wave characteristics, and signal processing schemes. Lamb wave propagates through thin plates and shells bounded by stress-free surfaces. Also, it can travel as an integral part of an aircraft. But, a major hindrance to the use of Lamb wave for SHM of real-life structures is the complexities associated with the multi-modal nature of Lamb wave propagation. In order to lower the complexities, the frequency of excitation is kept below the cut-off frequencies of the higher Lamb wave modes. The consequence is a decrease in sensitivity to detect minute damages of size smaller than the wavelength of excitation. At higher frequency or in thicker plates, Lamb wave gets converted to Rayleigh wave propagation.

6. REFERENCES

1. Yang, H., Chen, Z. and Zhang, H., "Vibration of train-rail-bridge interaction considering rail irregularity with arbitrary wavelength", *International Journal of Engineering, Transactions A: Basics*, Vol. 28, No. 4, (2015), 516-522. doi: 10.5829/idosi.ije.2015.28.04a.04

2. Patel, B. and Dewangan, U., "Damage detection techniques to identify the unknown damage parameters from the structural response data in beam: A review", *Recent Trends in Civil Engineering*, (2021), 175-183. doi: 10.1007/978-981-15-5195-6_13.

3. Ramadas, C., Balasubramaniam, K., Joshi, M. and Krishnamurthy, C., "Detection of transverse cracks in a composite beam using combined features of lamb wave and vibration techniques in ann environment", *International Journal on Smart Sensing and Intelligent Systems*, Vol. 1, No. 4, (2008), 970. doi: 10.21307/ijssis-2017-331.

4. Aydin, E., Dutkiewicz, M., Öztürk, B. and Sonmez, M., "Optimization of elastic spring supports for cantilever beams", *Structural and Multidisciplinary Optimization*, Vol. 62, No. 1, (2020), 55-81. doi: 10.1007/s00158-019-02469-3.

5. Aydın, E., Öztürk, B. and Dutkiewicz, M., "Determination of optimal elastic springs for cantilever beams supported by elastic foundation", Proceedings of 24th International Conference Engineering Mechanics 2018 (Svratka, Czech Republic, 2018), (2018), 33-36, doi: 10.21495/91-8-33.

6. Tabeshpour, M.R., Golafshani, A.A. and SEYF, M., "The effect of added mass fluctuation on heave vibration of tlp", *International Journal of Engineering*, Vol. 18, No. 3, (2005).

7. Parvez M, M., Shanmugam, J., Sangeetha, M. and Ghali, V., "Coded thermal wave imaging based defect detection in composites using neural networks", *International Journal of Engineering, Transactions A: Basics*, Vol. 35, No. 1, (2022), 93-101. doi: 10.5829/ije.2022.35.01a.08.

8. Akal, T., "Acoustics in marine sediments", *Encyclopaedia of Ocean Sciences*, (Second Edition) (2001) 75-91. doi: 10.1016/B978-012374473-9.00316-7.

9. Mei, H., Haider, M.F., James, R. and Giurgiutiu, V., "Pure s0 and sh0 detections of various damage types in aerospace composites", *Composites Part B: Engineering*, Vol. 189, (2020), 107906. doi: 10.1016/j.compositesb.2020.107906.

10. Nazeer, N., Ratassepp, M. and Fan, Z., "Damage detection in bent plates using shear horizontal guided waves", *Ultrasonics*, Vol. 75, (2017), 155-163. doi: 10.1016/j.ultras.2016.11.020.

11. Choi, P., Kim, D.-H., Lee, B.-H. and Won, M.C., "Application of ultrasonic shear-wave tomography to identify horizontal crack or delamination in concrete pavement and bridge", *Construction and Building Materials*, Vol. 121, (2016), 81-91. doi: 10.1016/j.conbuildmat.2016.05.126.

12. Castaings, M., "Sh ultrasonic guided waves for the evaluation of interfacial adhesion", *Ultrasonics*, Vol. 54, No. 7, (2014), 1760-1775. doi: 10.1016/j.ultras.2014.03.002.

13. Rajagopal, P. and Lowe, M., "Scattering of the fundamental shear horizontal guided wave by a part-thickness crack in an isotropic plate", *The Journal of the Acoustical Society of America*, Vol. 124, No. 5, (2008), 2895-2904. doi: 10.1121/1.2982410.

14. Ghasem, A.M. And Hashemi, S.J.A., "Shear-wave dynamic behavior using two different orientations", *International Journal of Engineering, Transactions A: Basics*, Vol. 20, No. 3, (2007), 293-300.

15. Masserey, B. and Fromme, P., "Surface defect detection in stiffened plate structures using rayleigh-like waves", *Ndt & E International*, Vol. 42, No. 6, (2009), 564-572. doi: 10.1016/j.ndteint.2009.04.006.

16. Wang, C., Balogun, O. and Achenbach, J.D., "Scattering of a rayleigh wave by a near surface crack which is normal to the free surface", *International Journal of Engineering Science*, Vol. 145, (2019), 103162. doi: 10.1016/j.ijengsci.2019.103162.

17. Cook, D. and Berthelot, Y., "Detection of small surface-breaking fatigue cracks in steel using scattering of rayleigh waves", *Ndt & E International*, Vol. 34, No. 7, (2001), 483-492. doi: 10.1016/S0963-8695(00)00080-3.

18. Zeng, W., Qi, S., Liu, L. and Yao, Y., "Research on laser-generated rayleigh waves with angled surface crack by finite element method", *Optik*, Vol. 181, (2019), 57-62. doi: 10.1016/j.ijleo.2018.11.105.

19. Arundas, P. and Dewangan, U., "Prediction of crack locations using non destructive tests", *Indian Journal of Science and Technology*, Vol. 9, No. 34, (2016), 1-6. doi: 10.17485/ijst/2016/v9i34/95491.

20. Mu, W., Sun, J., Xin, R., Liu, G. and Wang, S., "Time reversal damage localization method of ocean platform based on particle swarm optimization algorithm", *Marine Structures*, Vol. 69, (2020), 102672. doi: 10.1016/j.marstruc.2019.102672.

21. Mu, W., Sun, J., Liu, G. and Wang, S., "High-resolution crack localization approach based on diffraction wave", *Sensors*, Vol. 19, No. 8, (2019), 1951. doi: 10.3390/s19081951.

22. Malik, M.K., Chinchilla, S.C., Chronopoulos, D., Chiachio, J. and Essa, Y., "Ultrasonic guided-wave based system identification for beams", (2019). doi: 10.12783/shm2019/32371.

23. El Mountassir, M., Mourot, G., Yaacoubi, S. and Maquin, D., "Damage detection and localization in pipeline using sparse estimation of ultrasonic guided waves signals", *IFAC-PapersOnLine*, Vol. 51, No. 24, (2018), 941-948. doi: 10.1016/j.ifacol.2018.09.688.

24. Schmicker, D., Duczek, S., Liefold, S. and Gabbert, U., "Wave propagation analysis using high-order finite element methods: Spurious oscillations excited by internal element eigenfrequencies", *Technische Mechanik-European Journal of Engineering Mechanics*, Vol. 34, No. 2, (2014), 51-71. doi: 10.24352/UB.OVGU-2017-053.

25. Raišutis, R., Kažys, R., Žukauskas, E., Mažeika, L. and Vladišauskas, A., "Application of ultrasonic guided waves for non-destructive testing of defective cfrp rods with multiple delaminations", *Ndt & E International*, Vol. 43, No. 5, (2010), 416-424. doi: 10.1016/j.ndteint.2010.04.001.

26. Adithya, R., Shivaprasad, S., Balasubramaniam, K. and Krishnamurthy, C., "Finite element modelling of elastic wave propagation in polycrystalline media", in Proceedings of the Indian National Seminar & Exhibition on Non-Destructive Evaluation NDE., (2016), 15-17.

27. Staszewski, W., Mahzan, S. and Traynor, R., "Health monitoring of aerospace composite structures–active and passive approach", *composites Science and Technology*, Vol. 69, No. 11-12, (2009), 1678-1685. doi: 10.1016/j.compscitech.2008.09.034.

28. Ng, C.-T. and Veidt, M., "A lamb-wave-based technique for damage detection in composite laminates", *Smart Materials and Structures*, Vol. 18, No. 7, (2009), 074006. doi: 10.1088/0964-1726/18/7/074006

29. Mishra, S., Kumar, A., Mishra, R. and Sharma, S., "Structural health monitoring and propagation of lamb waves to identification of crack", *Materials Today: Proceedings*, Vol. 2, No. 4-5, (2015), 1833-1840. doi: 10.1016/j.matpr.2015.07.122.

Persian Abstract

چکیده

موج نوعی اختلال است که توسط ذرات یک سیستم از طریق ارتعاش به جلو منتقل می شود. نحوه رفتار موج، در حین انتشار در یک محیط، با نوع موج و محیط متفاوت است. بنابراین، آگاهی از رفتار موج در یک سیستم با اشکال مختلف آسیب، و رفتار انواع امواج در یک سیستم خاص، پیش نیازی ضروری برای تقریباً تمام فعالیت‌ها در شناسایی سیستم ساختاری و عمدتاً برای تشخیص و مکان‌یابی آسیب است. از آسیب این مقاله به بررسی تطبیقی انتشار امواج مختلف می‌پردازد که توسط محققان در سیستم‌های سازه‌ای مختلف انجام شده است. علاوه بر این، یک مدل عددی از یک صفحه همسانگرد با استفاده از المان محدود هم با و هم بدون آسیب ایجاد می‌شود. رفتار امواج مورد مطالعه قرار گرفته است. در نهایت، نتیجه مقایسه ای نشان داده شده است. این مقاله با ارائه جدیدترین پیشرفت‌ها، مشکلات و چشم‌انداز رفتارهای انتشار موج برای تشخیص آسیب و محلی‌سازی در سیستم‌های ساختاری و عناصر ساختاری رایج، دیدگاه جدیدی را برای تحقیقات در حال انجام ارائه می‌دهد. در حین انتشار از طریق سیستم‌ها و اجزای مختلف ساختاری، پرمصرف‌ترین امواج که عبارتند از: الف) موج برشی، ب) موج ریلی، ج) موج اولتراسونیک و د) موج بره به طور کامل مورد بررسی قرار گرفته‌اند. همراه با چندین مشکل دشوار برای رشد آینده، مشاهدات خلاصه ارائه شده است.

Stern Flap Application on Planing Hulls to Improve Resistance

U. Budiarto[a], S. Samuel*[a], A. A. Wijaya[a], S. Yulianti[a], K. Kiryanto[a], M. Iqbal[b]

[a] Department of Naval Architecture, Faculty of Engineering, University of Diponegoro, Semarang, Indonesia
[b] Department of Naval Architecture, Ocean, and Marine Engineering, University of Strathclyde, Glasgow, UK

P A P E R I N F O	*A B S T R A C T*
	Drag is one of the main factors in improving fuel efficiency. Various study in regards to improve drag performance of a planing hull amongst them is a stern flap. The main parameters to design a stern flap are span length and angle of stern flap. The stern flap works by changing pressure distribution over the ship's bottom and creating a lift force on the stern transom part. This study aims to analyze the behavior of stern flap in variations of span length and angle of stern flap towards drag performance of Fridsma hull form. Finite Volume Method (FVM) and Reynolds-Averaged Navier - Stokes (RANS) are used to predict the hull resistance during simulations. Results show that shear drag is very sensitive towards the total drag value, proving that shear drag valued at least 60% of the total drag in each planing hull multi-phase characteristics phase. Stern flap with 58% of hull breadth span length installed at 0° is considered the most optimal, reducing 10.2% of total drag, followed by 18% displacement reduction. In conclusion, the stern flap effectively improves the Fridsma hull's total drag and its components on $0.89 < \mathrm{Fr} < 1.89$.

NOMENCLATURE

$y+$	Boundary layer thickness	d_i	Vertex's displacement
L	Ship's length	n	Number of vertices
Re	Reynold's number	subjc_j^2	Basis constant
C_f	Friction coefficient	r_{ij}	Magnitude between two vertices
Δt	Time steps	λ_j	Expansion coefficient
U	Ship speed	α	Constant value
Fr	Froude number	Δ	Displacement
LCG	Longitudinal center of gravity	B	Breadth of the ship
VCG	Vertical center of gravity	T_{AP}	Draft of the ship
I_{yy}	Momen inertia at y axis	τ_o	Trim angle
I_{zz}	Momen inertia at z axis		

1. INTRODUCTION

Planing hull has very complex characteristics, especially during high-speed performance. Due to cost-related issues, the need to improve resistance performances of a planing hull emerges. Planing hulls have also been one of the most challenging problems for the naval architecture community as large hull motions complicate hydrodynamic calculations and hull optimization [1].

There has been a great deal of research towards saving devices to increase ship performance. Examples include microbubble injection method, stern wedges, tunnel stern, stern flap, and stepped hull. Yaakob [2] studied stern flap effect on a planing hull, resulting in 7.2% reductions in total drag.

Planing hulls are considered suitable to apply stern flap. That corresponds to the pressure drag value on the hull's bottom at a tangential angle between hulls and the water surface [3]. A boat or ship can be categorized as

*Corresponding Author Institutional Email: samuel@ft.undip.ac.id (S. Samue)

planing hull if its Froude Number values at $(Fr) \geq 1 - 1.2$ [4]. Experimental research was conducted by Fridsma [5] using simple geometry to predict planing hull type. This research was then broadly used by researchers worldwide to perform numerical computational verifications. Studies on the mesh density of the Fridsma hull have been reported to ensure accurate results [6]. Recent research on Fridsma hull is concerned with hull modification. Spray strip application can reduce the deflection of the spray wash to reduce the wet surface on the hull. Recent research on Fridsma hull related to spray strip modification has been reported to reduce the deflection effect of spray wash. Using the CFD approach, spray strips on Fridsma hull can reduce the total drag [7].

In 2014, Ghadimi et al. [8] stated that a stern flap could reduce Effective Horsepower (EHP) values of a propulsion machine of a planing hull. Ghassemi et al. [9] used Savitsky equations to determine the stern flap usage efficient dimension. The optimal angle of stern flap depends on the size of the hull itself.

Technology development in numerical analysis has been one factor that encourages researchers to conduct numerical analysis-based studies. Numerical analysis of planing hull ships is considered less accurate than displacement hulls [10]. There are methods used in numerical analysis, such as Finite Volume Method (FVM), Finite Element Method (FEM), Finite Difference Method (FDM), and analytic-experiment [11]. Based on the literature mentioned above, the Finite Volume Method (FVM) is the most used method to solve fluid dynamics problems. Turbulence modeling is served in k-ε and Volume of Fluid (VOF) to represent the water and air phases. The RANSE method is used to calculate the turbulent free-surface flow around the stepped planing hull [12].

The present study aims to understand the effect of span length and angle of stern flap on total drag and its components in a planing hull, especially Fridsma hull form. Drag components such as trim, heave, and displacement provide good insight into stern flap effect on a planing hull. The results of our suggestion on ship drag components will increase the shear drag component. Stern flap application will reduce shear drag experienced by the hull.

The component studied is the ship's response to stern flap installation. Resistance components, shear resistance, and pressure resistance are shown in this study. Installation of stern flap causes resistance reduction, followed by heave, trim, and displacement.

This paper summarizes the effect of stern flap technology on ship resistance. The installation of a stern flap can change the flow of water underneath the transom area; therefore, resistance is reduced, and speed is increased. The principles behind the stern flap are the lift force and the pressure distribution change under the

transom area. In addition, the stern flap tends to change the flow underneath the hull to be laminar flow. One of the approaches in stern flap study is CFD-based numerical simulation. This method is based on RANS principles to display turbulent flows. CFD approach is carried out by implementing finite volume method and calculated with morphing mesh method. Validation will then be based on Fridsma experimental study. This study aims to fill the gap of previous research in stern flap modeling in calm water conditions. By simulating stern flap installed planing hull with different span lengths and angle of stern flap. This study provides a better understanding of the changes in ship performances caused by stern flap.

This study explains the effect of the stern flap on ship dynamics, including heave and trim. The effect of span length and angle on the ship's performance will then be obtained. It is expected that the result of this study can help naval architects design planing hulls with lower resistance and higher fuel efficiency. These steps are carried out to achieve the global target of reducing fossil fuel emission rates.

2. MATERIALS AND METHOD

2. 1. Fridsma Hull Form   This research uses experimental data of Fridsma hull form as a benchmark and stern flap application. Experimental hull data used in the study is shown in Table 1 and Figure 1.

TABLE 1. Fridsma hull form main dimension [5]

Parameter	Unit	Value
L/B	-	5
L	m	1.143
B	m	0.229
T_{AP}	m	0.081
LCG from AP	m	0.457
VCG from keel	m	0.067
τ_o	Degree	1.569
B	Degree	20
Δ	Kg	10.890
$I_{yy} = I_{zz}$	Kg.m^2	0.235
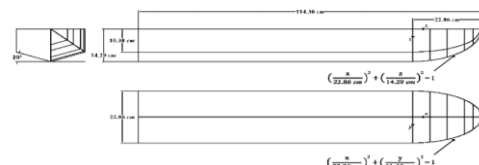
Figure 1. Fridsma hull form

2. 2. Stern Flap   The present study will analyze the effect of span length and angle of stern flap on ship resistance. The visualization of stern flap configurations is shown in Figure 2.

Span length will be based on ship breadth (B), as shown in Figure 3. Stern flap are installed at three different angles; they are 0°, 5°, dan 7°.

2. 3. Numerical Modelling   This study represents fluid simulation using the star CCM code. The solver is based on FVM to discretize the Navier-Stokes equation and SIMPLE algorithm to couple the pressure and velocity equations. A SIMPLE type algorithm (Semi Implicit Method for Pressure Linked Equations) is also called a predictor-corrector approach, the non-linear governing equations are solved a poisson equation for pressure [13].

The Dynamic Fluid Body Interaction (DFBI) module is employed to solve the vessel's dynamic motion, which allows the solver to analyze hull movements under the influence of fluid forces and moments. There are two degrees of freedom in the heave and pitch directions. Visualization of the fluid domain and boundary conditions used during this study are shown in Figure 4. The setup is referred to the ITTC recommendation [14] and detailed information on the numerics used.
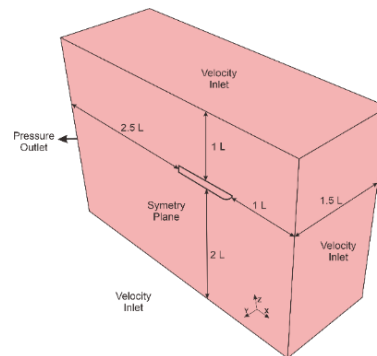
Figure 4. Fluid domain and boundary conditions

The quality of the mesh does affect the quality of the numerical results. In the mesh with sufficient fineness, it shows a better level of accuracy compared to the coarse mesh quality. Grid skewing and grid stretching important contributing factors to the loss in nominal accuracy of the solution. Local refinement is applied to a mapped mesh using feature edges, boundary regions, or volume shapes to maximize the accuracy.

This research explores the mesh density variations. This is carried out to give more details about the sensitive areas of physics characteristic definition around the hull. Mesh density will affect computation time; therefore, mesh density study is carried out with an expectation to increase the calculation's accuracy. Morphing mesh is used as the meshing method. Morphing meshworks based on interpolation between two shapes, morphing will need two model shapes consisting of the source shape and target shape, transformations can occur directly from the source shape towards the target shape. In this case, the whole ship hull can be transformed parametrically using the main dimension. Morphing mesh is convenient for relatively complex motions, while larger deformation requires new cells to be formed to maintain high-quality mesh. The morphing mesh method needs special treatment from the moving nodes to control the accuracy of derivative space and time-stepping scheme.

Morphing mesh and chimera grid (overset) are considered the most efficient meshing method in the numerical analysis of a planing hull [15]. Morphing mesh is more suitable to implement because it is more efficient in computation resources. The morphing grid method requires special treatment for moving cells to control the accuracy of the time-step scheme conducted during simulations. The locality of the B-spline coefficients and the parallelization scheme make this method more scalable for parallel computing, thereby potentially reducing computational costs [13]. Simulation using morphing grid mesh is carried out by interpolating specific fluid flow variables. Such interpolations are used to move cells from meshes using the Radial Basis Functions (RBF) method [16], a more
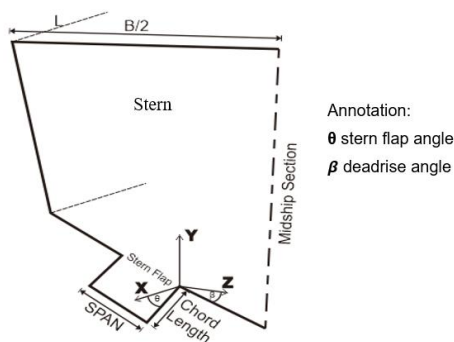
Figure 2. Stern flap parameter
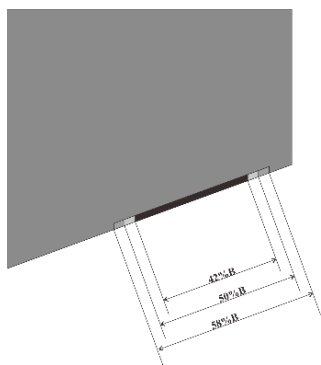
Figure 3. Configuration of stern flap

detailed discussion of RBF can be seen in literature [17, 18]. To be able to produce an interpolation field, it is necessary to solve system equations using control vertices and specific mesh displacements; for every i vertex, with d displacement, the equation is stated as:

$$d_i = \sum_{j=1}^{n} \lambda_j \sqrt{r_{ij}^2 + c_j^2 + \alpha} \qquad (1)$$

Computational domain and boundary conditions are defined based on ITTC Recommendations [14], as explained in Figure 4.

The present work investigates the use of the wall y+ as a guide in determining the right grid arrangement and corresponding turbulence models. Figure 5 shows the value of y+ between 60-70. Y+ wall functions are used to increase the accuracy of the simulations. Based on paractical guide line, the desired range of y+ value recommended between 45-60. Y+ value calculations based on ITTC are stated in Equation (2):

$$\frac{y}{L} = \frac{y^+}{R_e \sqrt{\frac{C_f}{2}}} \qquad (2)$$

Time-step is the time interval between iteration calculations in numerical simulations. The lower the time step, the more iteration calculations and the more time used in a simulation. Time-step used in the present study is 0,005 seconds. This study referred to the ITTC as an international standard that provides recommendations for predicting drag resistance using numerical and experimental methods [14] and referred to the user manual [13], shown in Equation (3):

$$\Delta t \, ITTC = 0.005 \sim 0.01 \frac{L}{U} \qquad (3)$$

3. RESULTS AND DISCUSSION

3. 1. Validation and Benchmark   Previous research has studied mesh independency by using the same ship model [6]. Within those research, mesh independency characteristics are studied using five grid variations consisting of 0.48 M, 0.89 M, 1.44 M, 2.33 M, and 2.99 M, as shown in Figure 6. Froude Number 1.79 is simulated on each grid size. In that study, a high accuracy value of convergence was obtained on 2.33 M

and 2.99 M grid sizes. However, the 2.99 M grid takes a relatively long time to finish each iteration calculation. Therefore, grid 2.33 M was chosen because the time is relatively shorter and shows good convergence values. The ideal mesh for numerical simulation of the stable planing problem is determined through a mesh analysis. The independency of the mesh resolution was verified using five grid meshes with cell numbers of 0.48 M, 0.89 M, 1.44 M, 2.33 M, and 2.99 M, respectively. Studies have been carried out on this topic to demonstrate the level of accuracy on high-speed vessel. A Froude value of 1.79 was used for mesh analysis. According to numerical simulation findings, the number of cells 2.3 M and 2.99 M have reliable outcomes. As a result, for the remainder of the CFD simulations, grid mesh 2.3 M was used.

To validate the results of numerical simulations, Fridsma's experimental data with L/B = 5, LCG = 0.6L from AP is used. Simulations are conducted with 800 K-900 K meshes, mainly concentrated on the water surface and hull region to obtain more accurate results. Simulations are carried out with STAR CCM+ in deep and calm water conditions. Simulations will grant Y and Z axis motions freedom to obtain trim and sinkage results.

The numerical simulations of bare hull show a discrepancy between the obtained numerical and Fridsma's experimental data. This also occurred during studies conducted by Wheeler et al. [19]. What caused the discrepancy between experimental and computational studies is the difference between each hull's center of gravity.

Figure 5. Y+ value at the bottom
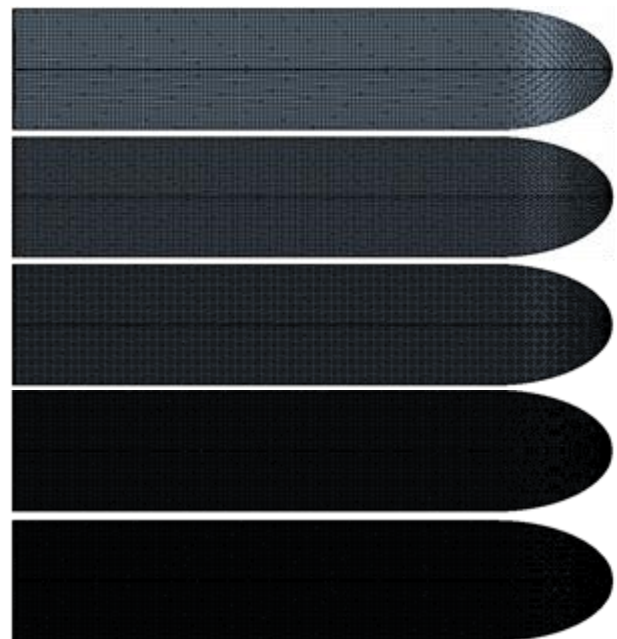
Figure 6. Grid size

In this study, different Centre of Gravity (CG) positions might occur between experimental study and numerical simulations using CFD. This will cause a discrepancy between both results. However, the result shows a similar pattern between experimental data and the data obtained from numerical simulations, and the discrepancy is not that significant. Therefore, it is still considered acceptable. Our statements follow several studies carried out by Mousaviraad et al. [20]. It is stated that the change in location of CG causes a significant influence on resistance and trim values. They also changed the CG position to obtain better and more accurate results. A study carried out by Sukas et al. [1] also showed the CG position between the experimental and numerical simulation. In this study, the CG position is similar to experimental data, even though it shows a different CG position from experimental data when the ship is not moving.
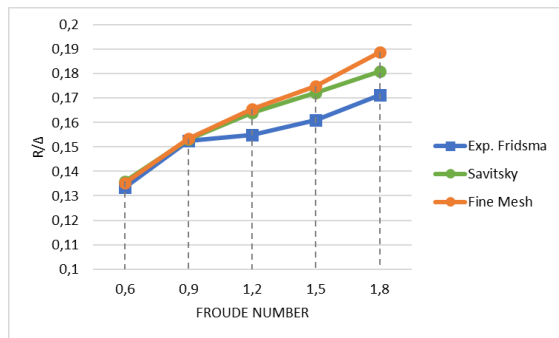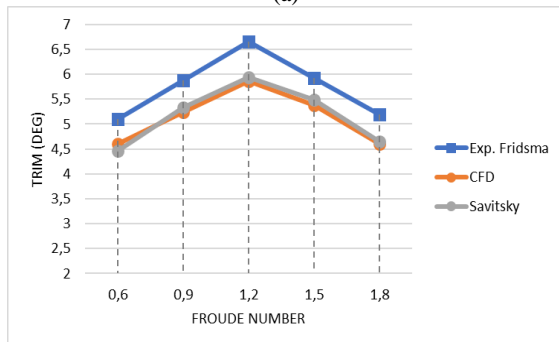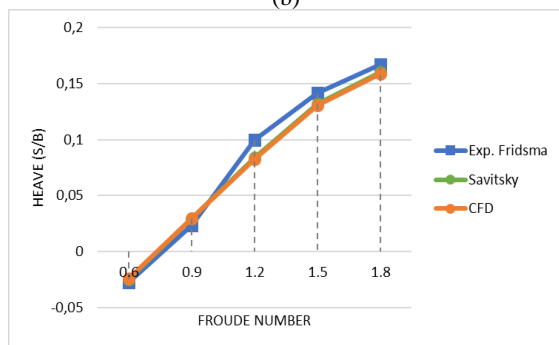
Other than the difference between the presented model centre of gravity, Numerical Ventilation Problem (NVP) can cause such discrepancy, especially during high speed (Fr>1.0). A study regarding Numerical Ventilation Problem on Fridsma hull form with overset grid method carried out by Samuel [21] shows that during Fr 1.2 – 1.8, there is a significant inaccuracy of obtained numerical analysis results caused by Numerical Ventilation Problem.

The average discrepancy between experimental data and numerical analysis drag, dynamic trim, and heave was less than 9%, 4%, 10.5%, as explained in Figure 7; similar validation results between numerical and experimental methods. Studies also occurred in a study carried out by Nourghassemi [22]. He stated that such discrepancy is acceptable and that the presented model can predict the hydrodynamic performance of planing craft. Bakhtiari et al. [12] also obtained 10% average result errors and stated that such result shows good agreement with experimental results.

3. 2. Results   Obtained numerical analysis on total drag for every Froude Number with shear drag and pressure drag as its components are shown in Figures 8, 9, and 10.

The simulation results show a reduction in total drag and components from every flap model compared to bare hull in every Froude Number. One of the main factors in the total drag of a planing hull is hydrodynamic forces. During the high-speed phase, hydrodynamic forces that work during high-speed increase. Because of the increasing hydrodynamic forces, the ship's displacement also changes. Hydrodynamic forces also significantly affect the total resistance of a high-speed vessel. This is different from the ship's characteristics during the low-speed phase. During the low-speed phase, hydrostatic forces are more dominant than hydrodynamic forces; therefore, the change in displacement value is not significant.

Figure 11 shows compositions of total drag in every phase of Fridsma hull form. Fr 0.6 represents the hull's displacement mode, Fr 0.9 represents the hump region or transitional phase between displacement and planing

(a)

(b)

(c)

Figure 7. Validation results for resistance, heave, and trim
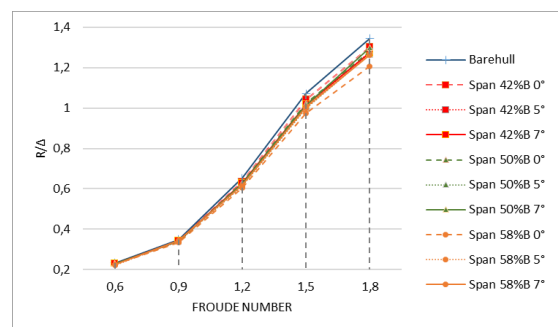
Figure 8. Total drag comparison
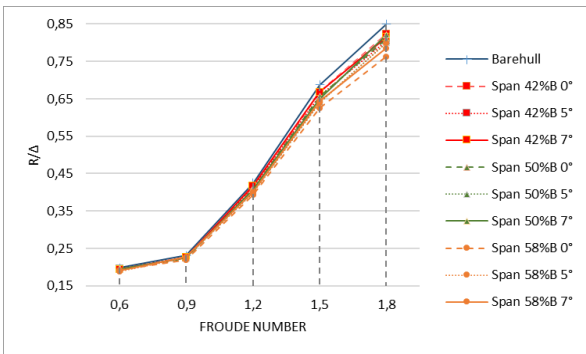
Figure 9. Shear drag comparison
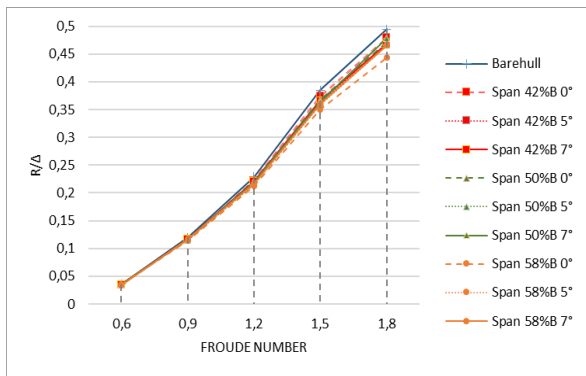
Figure 10. Pressure drag comparison
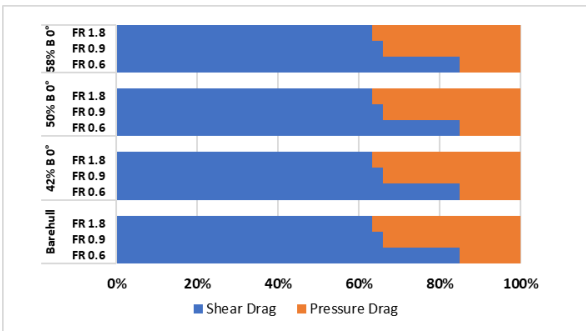
Figure 11. Total drag components

hull, and Fr 1.8 represents the full planing phase. Stern flap with 58%B span installed at 0° towards water surface shows 4.9% reduction in hump resistance. The result obtained from the simulation is similar to a study carried out by Zou et al. [23] on stern flap influence on double-stepped planing hull shows that stern flap played a positive role towards resistance reduction Fr < 3.94, reducing 4.9% on hump resistance.

There is a difference in R/Δ between validation and results of this study. Different R/Δ is because the benchmark uses constant displacement valued at 10, 68 kg, while the present study calculates each

displacement's differences in every Froude Number. Data regarding displacement changes in every model is shown in Figure 12. The drag results of each stern flap model are reduced by reducing displacement, one of the main components of drag calculations, especially in planing conditions. Changes in displacement values are caused by the hull's trim and heave value. Obtained trim angle predictions are shown in Figure 13. The obtained trim prediction shows that stern flap can significantly reduce trim experienced by Fridsma hull form. Besides trim, heave is also one of the main factors in calculating ship displacement. Figure 14 shows the heave predictions of each model.

Heave predictions also show significant heave reductions in each model compared to bare hull on Fr > 1. The study conducted by Zou et al. [23] showed similar results regarding trim angle and heave or sinkage reduction. The stern flap positively affects trim angle and sinkage in every observed Froude Number [23].

The stern flap will change the pressure distribution on hull's bottom. As observed in Figure 15, the part where stern flap is installed to the hull showed a high-pressure area, raising the stern and reducing the trim, and heave, which in return the total drag is reduced.
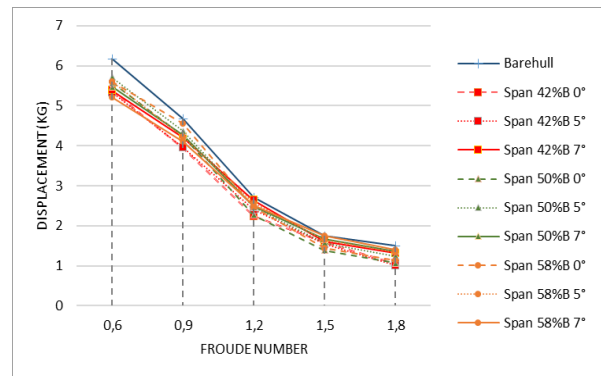
Figure 12. Displacement comparison
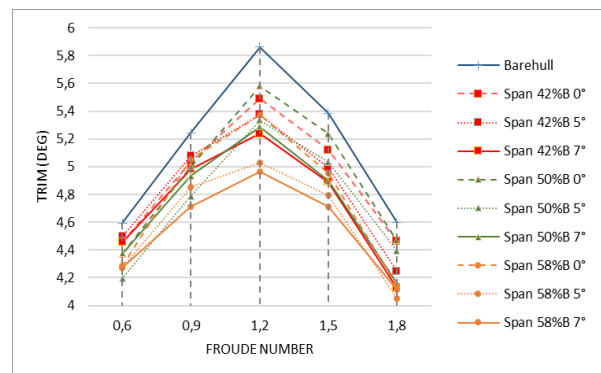
Figure 13. Trim angle comparison
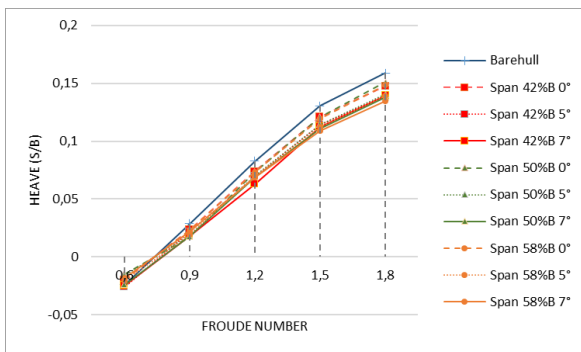
Figure 14. Heave comparison
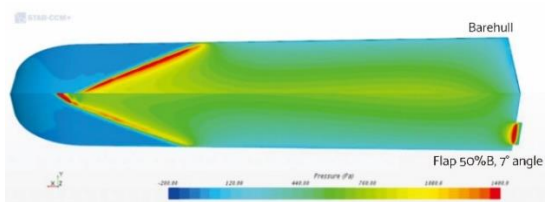
Figure 15. A Pressure Distribution Comparison Between Bare hull and Model with 50%B 7°

4. CONCLUSION

Simulation results show that stern flap application positively influences total drag on Fr 0.89 – 1.78 of Fridsma hull form. On top of that, obtained results showed that stern flap can improve the drag components experienced by Fridsma hull form, such as pressure drag and shear drag. Improvement in total drag and its components is followed by reducing displacement, with trim angle and heave value as its components. Flap with 58% of Hull Breadth as its span length shows the most optimal results compared to other flap models, reducing 10.2% of total drag and 18% displacement compared to bare hull.

5. ACKNOWLEDGEMENT

6. REFERENCES

1. Sukas, O.F., Kinaci, O.K., Cakici, F. and Gokce, M.K., "Hydrodynamic assessment of planing hulls using overset grids", *Applied Ocean Research*, Vol. 65, (2017), 35-46. doi: 10.1016/j.apor.2017.03.015.

2. Yaakob, O., Shamsuddin, S. and Koh, K.K., "Stern flap for resistance reduction of planing hull craft: A case study with a fast crew boat model", *Jurnal Teknologi*, (2004), 43–52-43–52. doi: 10.11113/jt.v41.689.

3. Savitsky, D., "Hydrodynamic design of planing hulls", *Marine Technology and SNAME News*, Vol. 1, No. 04, (1964), 71-95.

4. Faltinsen, O.M., "Hydrodynamics of high-speed marine vehicles, Cambridge university press, (2005).

5. Fridsma, G., *A systematic study of the rough-water performance of planing boats*. 1969, Stevens Inst of Tech Hoboken NJ Davidson Lab.

6. Fathuddiin, A. and Samuel, S., "Meshing strategi untuk memprediksi hambatan total pada kapal planing hull", *Jurnal Rekayasa Mesin*, Vol. 12, No. 2, (2021), 381-390.

7. Trimulyono, A., Manik, P. and Chrismianto, D., "A numerical study of spray strips analysis on fridsma hull form", *Fluids*, Vol. 6, No. 11, (2021), 420. doi: 10.3390/fluids6110420.

8. Ghadimi, P., Loni, A., Nowruzi, H., Dashtimanesh, A. and Tavakoli, S., "Parametric study of the effects of trim tabs on running trim and resistance of planing hulls", *Advances in Shipping and Ocean Engineering*, Vol. 3, No. 1, (2014), 1-12. doi.

9. Ghassemi, H., Bahrami, H., Vaezi, A. and Ghassemi, M.A., "Minimization of resistance of the planing boat by trim-tab", *International Journal of Physics*, Vol. 7, No. 1, (2019), 21-26. doi: 10.12691/ijp-7-1-4.

10. Tagliafierro, B., Mancini, S., Ropero-Giralda, P., Domínguez, J.M., Crespo, A.J. and Viccione, G., "Performance assessment of a planing hull using the smoothed particle hydrodynamics method", *Journal of Marine Science and Engineering*, Vol. 9, No. 3, (2021), 244. doi: 10.3390/jmse9030244.

11. Yousefi, R., Shafaghat, R. and Shakeri, M., "High-speed planing hull drag reduction using tunnels", *Ocean engineering*, Vol. 84, (2014), 54-60. doi: 10.1016/j.oceaneng.2014.03.033.

12. Bakhtiari, M., Veysi, S. and Ghassemi, H., "Numerical modeling of the stepped planing hull in calm water", *International Journal of Engineering, Transactions B: Applications,* Vol. 29, No. 2, (2016), 236-245. doi: 10.5829/idosi.ije.2016.29.02b.13.

13. Siemens, P., "Software: Star-ccm+ user guide− version 13.06", *Siemens PLM Software, Texas*, (2018).

14. ITTC, *Practical guidelines for ship cfd applications*. 2011, 26th ITTC Executive Committee Rio de Janeiro, Brazil.

15. De Marco, A., Mancini, S., Miranda, S., Scognamiglio, R. and Vitiello, L., "Experimental and numerical hydrodynamic analysis of a stepped planing hull", *Applied Ocean Research*, Vol. 64, (2017), 135-154. doi: 10.1016/j.apor.2017.02.004.

16. Dashtimanesh, A., Esfandiari, A. and Mancini, S., "Performance prediction of two-stepped planing hulls using morphing mesh approach", *Journal of Ship Production and Design*, Vol. 34, No. 03, (2018), 236-248. doi: 10.5957/JSPD.160046.

17. Gumerov, N.A. and Duraiswami, R., "Fast radial basis function interpolation via preconditioned krylov iteration", *SIAM Journal on Scientific Computing*, Vol. 29, No. 5, (2007), 1876-1899.

18. Faul, A., Goodsell, G. and Powell, M., "A krylov subspace algorithm for multiquadric interpolation in many dimensions", *IMA Journal of Numerical Analysis*, Vol. 25, No. 1, (2005), 1-24.

19. Wheeler, M.P., Matveev, K.I. and Xing, T., "Validation study of compact planing hulls at pre-planing speeds", in Fluids Engineering Division Summer Meeting, American Society of Mechanical Engineers. Vol. 51562, (2018), V002T009A009.

20. Mousavirad, S.J., Schaefer, G. and Korovin, I., "An effective approach for neural network training based on comprehensive

learning", in 2020 25th International Conference on Pattern Recognition (ICPR), IEEE., (2021), 8774-8781.

21. Kim, D.J., Fathuddiin, A. and Zakki, A.F., "A numerical ventilation problem on fridsma hull form using an overset grid system", in OP Conference Series: Materials Science and Engineering. Vol. 1096, (2021), 012041.

22. Nourghassemi, H., Taghva, H., Molyneux, D. and Ghassemi, H., "Numerical hydrodynamic performance of the stepped planing

craft and its step height effect (research note)", *International Journal of Engineering*, *Transactions A: Basics,* Vol. 32, No. 4, (2019), 602-607. doi: 10.5829/ije.2019.32.04a.19.

23. Zou, J., Lu, S., Jiang, Y., Sun, H. and Li, Z., "Experimental and numerical research on the influence of stern flap mounting angle on double-stepped planing hull hydrodynamic performance", *Journal of Marine Science and Engineering*, Vol. 7, No. 10, (2019), 346. doi: 10.3390/jmse7100346.

Persian Abstract

چکیده

درگ یکی از عوامل اصلی در بهبود بهره وری سوخت است. مطالعات مختلف در رابطه با بهبود عملکرد درگ بدنه هواپیما در میان آنها یک فلپ استرن است. پارامترهای اصلی برای طراحی فلپ استرن طول دهانه و زاویه فلپ استرن می باشد. فلپ عقب با تغییر توزیع فشار در کف کشتی و ایجاد نیروی بالابر در قسمت گذرگاه عقب کار می کند. این مطالعه با هدف تجزیه و تحلیل رفتار فلپ استرن در تغییرات طول دهانه و زاویه فلپ استرن نسبت به عملکرد درگ فرم بدنه فریدما انجام شده است. روش حجم محدود (FVM) و رینولدز میانگین ناویر – استوکس (RANS) برای پیش‌بینی مقاومت بدنه در طول شبیه‌سازی استفاده می‌شود. نتایج نشان می‌دهد که کشش برشی نسبت به مقدار کشش کل بسیار حساس است، و ثابت می‌کند که پسا برشی حداقل ٦٠ درصد از کشش کل را در هر فاز ویژگی‌های چند فازی بدنه برنامه‌ریزی ارزش دارد. فلپ استرن با ٥٨٪ طول دهانه عرض بدنه نصب شده در ٠ درجه بهینه ترین در نظر گرفته می شود و ١٠.٢٪ از کشش کل را کاهش می دهد و به دنبال آن ١٨٪ کاهش جابجایی را به دنبال دارد. در نتیجه، فلپ عقب به طور موثر کشش کل بدنه Fridsma و اجزای آن را در ١.٨٩ > Fr > ٠.٨٩ بهبود می بخشد.

International Journal of Engineering

Inrush Current Reduction by a Point-on-wave Energization Strategy and Sequential Phase Shifting in Three-Phase Transformer

A. Yahiou*[a], H. Mellah[a], A. Bayadi[b]

[a] Department of Electrical Engineering, Faculty of Sciences and Applied Sciences, University of Bouira, Bouira, Algeria
[b] Department of Electrical Engineering, Faculty of Technology, University of Sétif-1, Sétif, Algeria

P A P E R   I N F O

A B S T R A C T

The main goal of this work is the mitigation of inrush current in a three-phase transformer. This inrush current appears when energizing a no-load or lightly loaded transformer. It can reach very high values and can cause failures in the electrical system. The control strategy is achieved by considering the value of the residual flux when the transformer is de-energized as well as by respecting the phase shifting between the three phases. To measure the inrush current, an experimental configuration with a data acquisition system using dSPACE 1104 card was developed and is presented in this paper. A technique to control the circuit breaker for energizing a 2 kVA three-phase transformer without the appearance of inrush current was also tested and applied in the experimental setup. The specific contribution of this work is that this technique is applied in the measurements with a thorough investigation of the residual flux. The proposed technique achieved complete elimination of the inrush current.

doi: 10.5829/ije.2022.35.12c.07

NOMENCLATURE

ϕ	Iron core flux	v	Applied voltage
λ	Linkage flux.	λr	Residual linkage flux.
i_l	Reactive magnetizing current.	t_{close}:	Closing time
λ_{max}	Maximum linkage flux	V_{max}	Maximum voltage.
ω	Angular pulsation.	n1 :n2	Transformation ratio
it	Total magnetizing current	ir	Active magnetizing current

1. INTRODUCTION

Inrush current is a phenomenon that appears during the energization of an unloaded transformer in a power system. Due to the high value of the first peak of this inrush current, which sometimes reaches the value of the short circuit current [1]. It is necessary to conduct an investigation and analysis under several constraints and conditions in order to predict the protection system intended for the transformer. For this purpose, several analytical and numerical methods have been developed, as reported in literature [2- 4]. To mitigate and eliminate these transient currents in single or three-phase transformers, many techniques have been proposed in the

literature. Cano-González et al. [5] conducted a comparative analysis of four of these strategies that depend on whether the residual flux can be measured and whether independent-pole-operated or three-pole-operated circuit-breakers are used. The work carried out by Brunke et al. [6, 7] have considered to be one of the first studies presented in the field of inrush current reduction in single or three-phase transformers, both in simulation and measurement. The technique is based on three strategies: a rapid, delayed, and simultaneous closing strategy taking into account the residual flux. To increase the value of the transient inductance, as well as to reduce the inrush current. Cheng et al. [8] presented a new approach where they modified the transformer coil

*Corresponding Author Institutional Email:
abdelghani.yahiou@univ-bouira.dz (A. Yahiou)

distribution. Arand et al. [9], Abdulsalam, and Xu [10], Abdelsalam and Abdelaziz [11] and Cui et al. [12] suggested a simple technique by the insertion of a resistance between the neutral of the transformer and the ground, taking into account the sequential energization of the three phases. Using an existing photovoltaic generator. Xu et al. [13] investigated the mitigation of the transient inrush current; the technique was based on applying the opposite flux with taking the switching instant into consideration. A method for isolating the neutral of a three-phase transformer using controlled switching was presented by Cano-González et al. [14]. The method takes the residual flux into consideration and respects the phase shifting between the three phases. To be able to protect the load for daily switching and reduce the interaction with other relays in transformers, several methods were proposed by Schramm et al. [15]. In addition, a strategy based on placing resistances before energization with the transformer was presented. The resistances are inserted in parallel with the circuit breakers. The effect of the resistance is controlled by opening and closing the circuit breaker: if the circuit breaker is open, the current passes through the resistances, while if it is closed, the resistances have no effect. Based on the state space equation to represent the equivalent circuit, Rudez et al. [16] have chosen a format to solve the differential equations. Moreover, they presented a consistent study for deriving the eigenvectors and self-values. They also investigated the effect of energizing a fully loaded transformer (application of transient regime), with the presence of transformers under constant operation (i.e. with no transient regime) and compared the measurement results obtained using WAMS (Wide Area Monitoring System) with those obtained through simulations. To reduce the inrush current levels in the transformer and its effects on the electrical system, Pontt et al. [17] used a technique based on the transformer tap changer to increase the impedance value of the transformer winding.

Gamji et al. [18] presented a method to reduce the inrush current using the modified transient current limiter (MTCL), which overcomes the drawbacks of the conventional transient current limiter (TCL) during normal operating mode. The proposed MTCL gives lower current/voltage THD and power losses. This approach minimizes the cost by operating one limiting reactor instead of two. The performance of the method was tested experimentally and also by PSCAD/EMTDC simulation. The efficacy of the method was confirmed by comparing the results obtained with MTCL with those obtained with TCL. Ebadi et al. [19] simulated 510 different cases of inrush current in order to study the REF relay maloperation under inrush current conditions.

To measure the inrush current in a three-phase transformer, a laboratory experimental setup with an acquisition system (dSPACE card) is detailed and

presented in this article. The technique presented and proposed by Yahiou et al. [20, 21] has exploited to reduce the three-phase transformer transient current. This technique is based on Faraday's law to estimate the magnetic flux waveform via the voltage waveform, then the value of residual flux at the de-energizing moment (the circuit breaker is open) is estimated. The main contribution of the present work is the exploitation of the method previously proposed by Yahiou et al. [20, 22], using a single phase transformer, to reduce the inrush current in three-phase transformers, where the residual flux value and the optimal time to close the circuit breaker for only the first phase (U) are calculated. For the other phases (V and W), the previous calculations are used. Thus, the optimal time to close the circuit breaker for the phases V and W is also calculated by adding the phase shifting ($2*\pi/3$), without calculating each one separately. The technique was applied to real-time measurements.

2. FLUX AND INRUSH CURRENT RELATIONSHIP

Figure 1 depicts the appearance of unloaded current when energizing a transformer, either in the steady state or in the transient state and its relation with the magnetic flux waveform. It is clear that the existence of a residual flux value at the instant of energization of the transformer leads to an inrush current peak (with values that can be ten times greater than the nominal current). In the steady state, i.e. when the transformer is energized without the appearance of this transient current, there is only the magnetizing current.

3. MATERIALS AND METHOD

3. 1. Laboratory Configuration and Measurement Proceedings
Construction of References The measurement setup is shown in Figure 2. A three-phase voltage source with
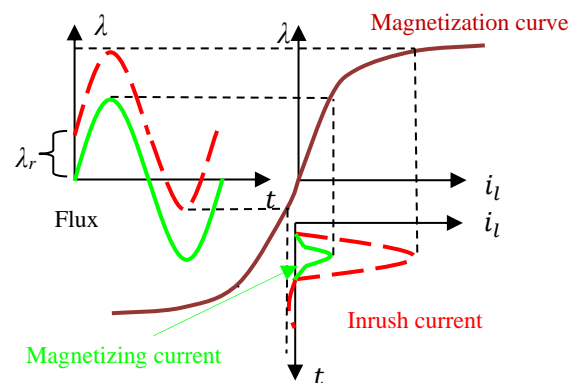
Figure 1. Flux Vs Magnetizing current of the unloaded transformer (transient and steady state)

220 V AC supplies the 2 kVA three-phase transformer. The current sensor and voltage probe are used to measure the magnetizing current waveforms and the applied voltage, respectively. The waveforms are acquired using the data acquisition system (dSPACE 1104 card connected to the computer with the Control Desk software) and by a digital oscilloscope simultaneously. The storage, data acquisition, control, and analysis were performed under the MATLAB environment and using the dSPACE experimental software, as shown in Figure 3, which shows the Control Desk interface developed.

These measurement experiments complement the work conducted in the same research field and reported in literature [22].

In the steady state, the voltage value is gradually increased from zero until the nominal voltage value for the transformer primary side, which is rated at 220 volts, while the secondary side remains in an open circuit. Figure 4 portrays the steady state current waveform for the 2 kVA transformer. For the transient case, three breakers are used to energize the three-phase transformer. The voltage value is fixed at 220 Volts. The current waveforms are recorded via the acquisition system, after giving a random impulse to the breaker to close at the desired moment.
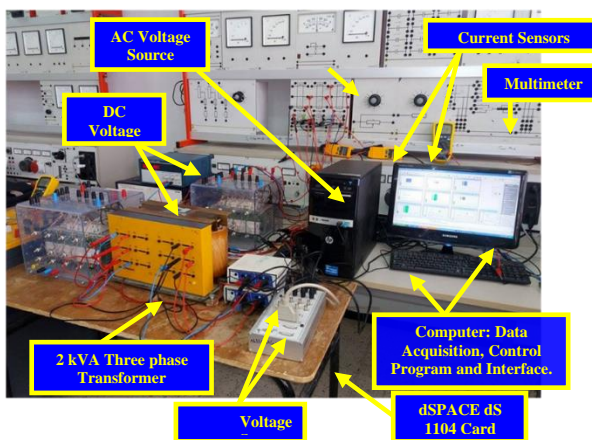
Figure 2. Measurement setup
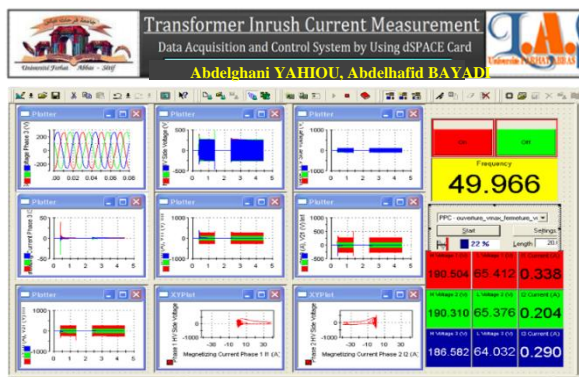
Figure 3. Data acquisition interface (Control Desk)
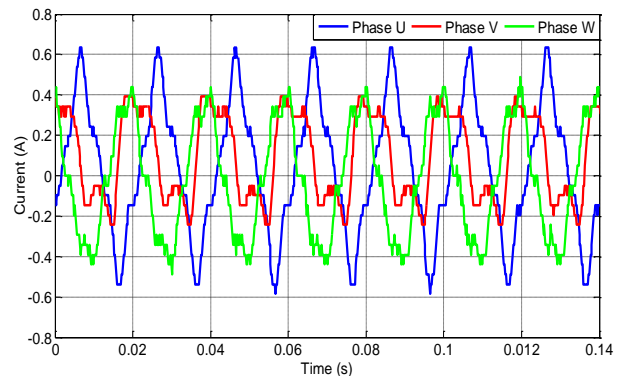
Figure 4. Magnetizing current (steady state)

The measured inrush current waveform of the three-phase transformer is shown in Figure 5.

As shown in Figure 5, the magnetizing current value in the transient state is much higher than the current value in the steady state, especially in the first peak where it can reach the value of the short-circuit current, and then there is a gradual decrease of this current until it reaches the value of the steady state value after a few seconds.

As the inrush current can create failures in the transformer (protection relays) as well as affect the quality of the service in the power system (voltage), ongoing research in the field seeks to reduce this inrush current. The method proposed here to achieve this is detailed in the following section.

3. 2. Controlled Energization to Mitigate Inrush Current   The technique proposed in this article to reduce three-phase transformer inrush current is presented in this section. The technique, modeled with MATLAB, was applied in the laboratory measurement setup, and the results demonstrated its effectiveness. The mitigation technique is mainly based on computing the optimal closing instant and considering the point-on-wave voltage waveform just for the first phase U. It is sufficient to calculate the residual flux for the phase U, and for the other phases (V and W), it is sufficient to add only the phase shifting between them and the phase U.
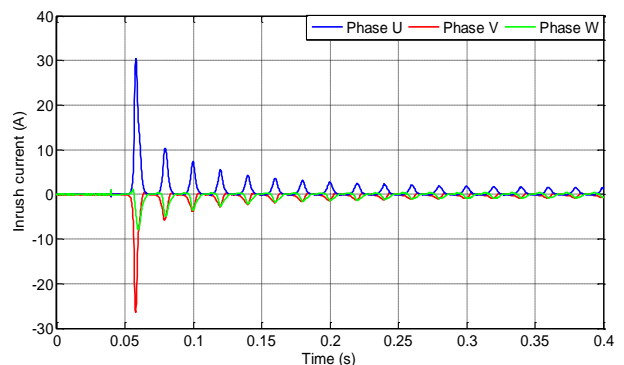
Figure 5. Magnetizing inrush current (transient)

3. 2. 1. Principle of the Control Procedure   The main goal of this section is to detail the procedure for opening and closing the circuit breaker. The first energization of the three-phase transformer is done randomly (the circuit breaker is closed). This closing lasts for a well-defined period, then the three-phase transformer is de-energized randomly (circuit breaker open). Finally, the circuit breaker is closed a second time (transformer re-energization), this time not randomly, but applying the control technique that takes into consideration the magnetic flux data for the latest opening of the breaker, i.e. point-on-wave of the primary voltage of phase U.

This procedure is repeated several times (5 times) to ensure that the technique gives similar results for the same conditions on the voltage wave point, i.e., good elimination of the inrush current for the three phases whatever the operating conditions of the transformer (Figure 6).

3. 2. 2. Control Technique in Equation   In a magnetic circuit wound by a coil and as in a transformer, there is proportionality between the iron core flux ϕ and the voltage v applied to the winding. Therefore, considering that the voltage is sinusoidal, and by considering Faraday's law, it is possible to write:

$$v(t) = V_{max} \, sin(\omega t) = n_1 \frac{d\phi}{dt} = \frac{d\lambda}{dt} \tag{1}$$

where:
V_{max} is the maximum value of the voltage and λ is the flux. The integration of Equation (1) gives:

$$\lambda(t) = \int V_{max} \sin(\omega t)dt = -\frac{V_{max}}{\omega}\cos(\omega t) + K \tag{2}$$

At the closing moment of the breaker, the flux value is the residual flux λ_R. Therefore, it is possible to write Equation (2) as follows:

Figure 6. Explanation of the circuit breaker closing and opening procedure

$$\lambda_R = -\frac{V_{max}}{\omega}\cos(\omega t_{cl-opt}) + K \tag{3}$$

Considering that, at two instants t_{cl-opt} and top, the value of λ_R has a constant and equal value, the constant K becomes equal to:

$$K = \lambda_R + \frac{V_{max}}{\omega}\cos(\omega t_{cl-opt}) \tag{4}$$

Equation (2) becomes:

$$\lambda(t) = -\frac{V_{max}}{\omega}\cos(\omega t) + \frac{V_{max}}{\omega}\cos(\omega t_{cl-opt}) + \lambda_R \tag{5}$$

To eliminate the transient current, it is necessary to compensate the residual flux value by the flux value at the closing moment, i.e., the total flux becomes the flux of the steady state (the flux waveform does not move as was the case of what is shown in red color in Figure 1)

$$\lambda(t) = -\frac{V_{max}}{\omega}\cos(\omega t) \tag{6}$$

This means that:

$$\lambda_R + \frac{V_{max}}{\omega}\cos(\omega t_{cl-opt}) = 0 \tag{7}$$

The optimal instant of energization can be calculated as follows:
If $\lambda_R < 0$:

$$t_{f-opt\,1} = -\frac{1}{\omega}\arccos\left(\frac{\lambda_R}{\lambda_{max}}\right) \tag{8}$$

Else:

$$t_{f-opt\,2} = \frac{1}{\omega}\left[\arccos\left(\frac{\lambda_R}{\lambda_{max}}\right) + 1\right] \tag{9}$$

The relationship between the flux λ and the applied voltage v at the commanded closing instant and the opening moment of the breaker is well explained graphically in Figure 7. It is as summed that the time between opening and closing is not very large so that there is no change in the residual flux value in the two moments.

The flowchart of the different steps in the control technique is given in Figure 8. Equation (7) is the essential basis of this inrush current mitigation technique.

3. 2. 3. Measurement Steps and Real-time Application of the Control Technique   To estimate the flux waveform and to control the circuit breaker, a control and measurement plan was carried out as explained in Figure 9. A detailed clarification of the strategy is given in the following steps:

1) Fixing the voltage source to a value of 220 V, which represents the nominal voltage value for the primary side of the three-phase transformer, the current and voltage waveforms are captured and recorded via the acquisition system.

Figure 7. Voltage-flux relationship for optimal switching on

2) The Phase-Locked Loop (PLL) is used to synchronize the signal of the measurement voltage and the sinusoidal signal of the simulation under MATLAB. The PLL helps us to know the zero crossing moment for the voltage signal. The three breakers receive a pulse to close at this time (zero crossing), without considering the flux value at this closing moment.

3) Using the integration tool of such a signal, it is possible to obtain the flux waveform of the phase U through the voltage signal for the same phase.

4) The flux value when the circuit breaker opens is taken as a residual flux value for phase U.

5) The circuit breakers of phases V and W open later than the circuit breaker of phase U.

6) Execution of the MATLAB program on the Control Desk interface at the same time, i.e., synchronization (estimation of the optimal instant to close the circuit breaker of phase U).

7) The circuit breakers of phases V and W close optimally later than the circuit breaker of phase U.

8) The steps are repeated to confirm the validity of the technique and that whatever the point on the voltage wave it gives the same results. In addition, it is necessary to sweep the entire voltage wave, from 0 at 2π with a pitch of $1/6$.

Figures 9, 10, and 11 display the procedure of the residual flux estimation, the method for calculating the optimal closing moment, and the explanatory scheme of the sequential closing of the three circuit breakers.

In this study, the residual flux was calculated for only one column (the column of phase U), and from that the optimal time to close the circuit breaker for phase U was calculated. To this point, we added the phase shifting of $2*\pi/3$ and $4*\pi/3$ for an optimal closing of the circuit breakers for phases V and W respectively. Hence, the residual flux for other columns was not calculated.
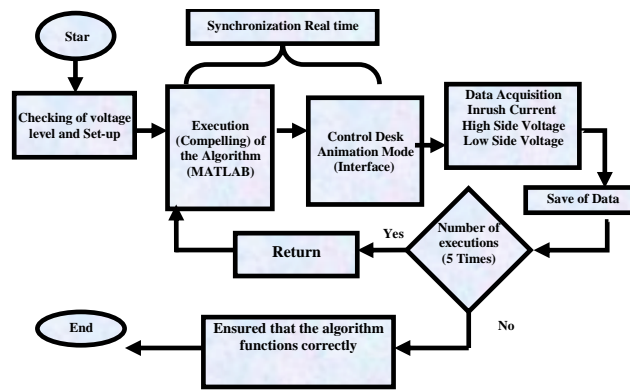
Figure 8. Data acquisition system and control strategy steps
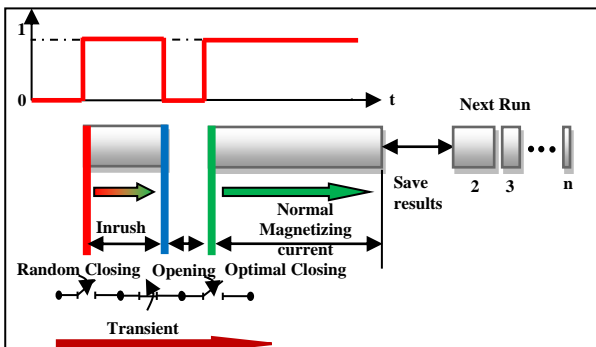
Figure 9. Flux measurement and Control strategy

4. RESULTS

Figures 12 and 13 display the experimental results with the application in real time of the proposed strategy. Initially, the three-phase transformer is switched on. After the three-phase transformer is de-energized, at the opening moment of the breaker, the value of the residual flux is computed. Lastly, the transformer is switched on again by closing the breaker, but not in a random way, since here, the program interferes to calculate the optimal time to close the breaker in such a way that the inrush current does not occur. This concerns phase U. As for the
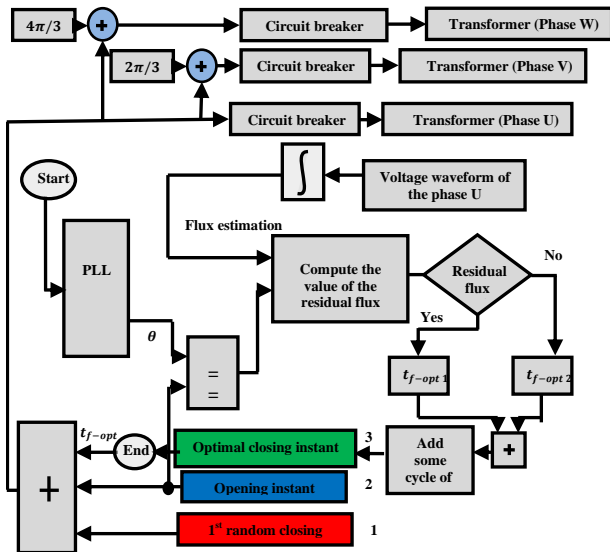
Figure 10. Flow chart of the control strategy and flux estimation

opening and closing instants of the breakers for phases V and W, they are equal to the opening and closing instants of the breaker for phase U plus the values $\frac{2\pi}{3}$ and $\frac{4\pi}{3}$ respectively, without calculating the instants in terms of residual flux for both phases U and W.

As explained earlier, the angle value α is changed on the voltage wave with a step of $\frac{\pi}{6}$, starting from the value 0 to the target of 2π and the results are shown in Figures 12 and 13 are for the values of the angle $\alpha = \frac{\pi}{2}$ and $\alpha = 0$, respectively.

5. DISCUSSION

The experimental results, presented in Figures 12 and 13, show that there is a complete fade-out of the three-phase transformer inrush current upon application of the technique proposed in this article. As anticipated, when the three-phase transformer is first switched on, high values of the inrush current occur, due to the random impulse given to the breaker to close at any time without calculating the appropriate and optimal instant, and whatever the angle (α) value.

On the other hand, when the three-phase transformer is switched on the second time using the proposed technique, which calculates the optimal moment for closing the breaker, it is noticeable that there is no occurrence of the inrush current (only of the magnetizing current), because the circuit breaker is closed at the same point of the voltage wave as where it was opened. This proves the efficacy of the proposed technique to control and mitigate the inrush current for three-phase transformers.

Figure 11. Explanatory scheme of the sequential phase energization
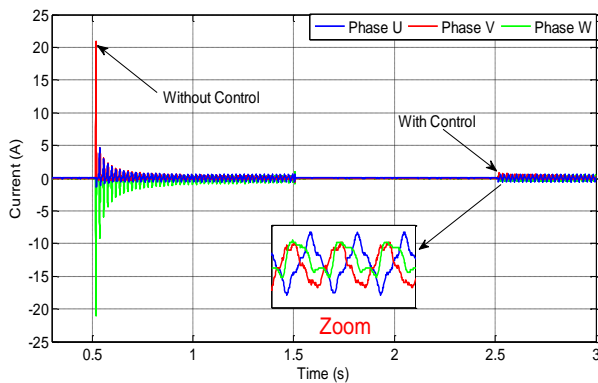
Figure 12. Inrush current mitigation with a point on voltage waveform angle $\alpha = \frac{\pi}{2}$.
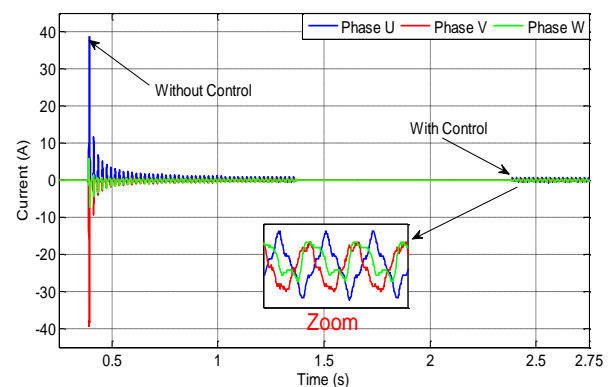
Figure 13. Inrush current mitigation with a point on voltage waveform angle $\alpha = 0$

6. CONCLUSION

In the work summarized in this article, a control technique was proposed to reduce and eliminate the transient regime when a three-phase transformer is switched on. The proposed algorithm is based mainly on a strategy of compensating the residual flux value of the first phase U in the three-phase transformer core by the instantaneous value of the flux at the closing instant of the breaker.

This technique was tested in the laboratory measurement configuration in real-time using the data acquisition system (dSPACE card). The results obtained demonstrate the reliability of the control technique. Moreover, it also enables the optimal closing moment of the breaker to be obtained more rapidly without complicating the calculations. It is also sufficient to calculate the instant just for one phase U and then to calculate the instant for the phases V and W with respect to U.

The proposed technique resulted in a complete mitigation of the inrush current. The technique was applied herein the experiment with a good investigation of the residual flux.

In future work, we intend to apply the proposed technique to reduce and eliminate the transient current resulting from the interaction between three-phase transformers, one of them exposed to the transient regime (energization) while the others are already energized (Sympathetic phenomenon).

7. LIST OF ABBREVIATIONS

dSPACE: Digital Signal Processing and Control Engineering
ControlDesk: dSPACE experiment software for seamless ECU development.
WAMS: Wide Area Monitoring System
AC: Alternative Current
DC: DirectCurrent

8. REFERENCES

1. Steurer, M., Frohlich, K., "The impact of inrush currents on the mechanical stress of high voltage power transformer coils", *IEEE Transactions on Power Delivery,* Vol. 17, No. 1, (2002),155–160. doi: 10.1109/61.974203

2. Bertagnolli, G., "The ABB Approach to Short-circuit Duty of Power Transformers", *ABB Trasformatori, 3nd Edition* (2007). file:///C:/Users/pc/Downloads/kupdf.net_2007-abb-short-circuit-duty-of-power-transformers.pdf

3. Specht, T. R.,"Transformer Magnetizing Inrush Current", *Transactions of the American Institute of Electrical Engineers,* Vol. 70, No. 1, (1951), 323–328. doi: 10.1109/T-AIEE.1951.5060409.

4. Holcomb, J. E., "Distribution Transformer Magnetizing Inrush Current", *Transactions of the American Institute of Electrical*

Engineers. Part III: Power Apparatus and Systems, Vol. 80, No. 3, (1961), 697-702. doi: 10.1109/AIEEPAS.1961.4501117

5. Cano-González, R., Bachiller-Soler, A., Rosendo-Macías, J. A., Álvarez-Cordero, G., "Controlled switching strategies for transformer inrush current reduction: A comparative study", *Electric Power Systems Research*, Vol. 145, (2017), 12-18. doi: 10.1016/j.epsr.2016.11.018

6. Brunke, J. H., Frohlich, K. J., "Elimination of transformer inrush currents by controlled switching. I. Theoretical considerations", *IEEE Transactions on Power Delivery*, Vol. 16, No. 2,(2001), 276-280. doi: 10.1109/61.915495

7. Brunke, J. H.,K. Frohlich, J., "Elimination of transformer inrush currents by controlled switching. II. Application and performance considerations",*IEEE Transactions on Power Delivery*, Vol. 16, No. 2,(2001), 281-285. doi: 10.1109/61.915496

8. Cheng, C.-K., Liang, T.-J., Chen, J.-F., Chen, S.-D., Yang, W.-H., "Novel approach to reducing the inrush current of a power transformer", *IEE Proceedings - Electric Power Applications*, Vol. 151, No. 3, 289-295, (2004). DOI: 10.1049/ip-epa:20040223

9. Arand, S. J., Saeedi, M., Masoudi, S., "Transformer Inrush Current Mitigation Using Controlled Switching and Magnetic Flux Shunts", *International Journal of Energy and Power Engineering,* Vol. 2, No. 2, (2013), 46-53. doi: 10.11648/j.ijepe.20130202.13

10. Abdulsalam, S. G., Xu, W., "A Sequential Phase Energization Method for Transformer Inrush Current Reduction-Transient Performance and Practical Considerations", *IEEE Transactions on Power Delivery,* Vol. 22, No. 1, (2007), 208-216. doi: 10.1109/TPWRD.2006.881450

11. Abdelsalam, H. A., Abdelaziz, A. Y., "A New Strategy for Selection of Switching Instant to Reduce Transformer Inrush Current in a Single-phase Grid-connected Photovoltaic System", *Electric Power Components and Systems*, Vol. 43, No. 11, (2015), 1297-1306. doi: 10.1080/15325008.2015.1027424

12. Cui, Y., Abdulsalam, S. G., Chen, S., Xu, W., "A Sequential Phase Energization Technique for Transformer Inrush Current Reduction— Part I: Simulation and Experimental Results", *IEEE Transactions on Power Delivery*, Vol. 20, No. 2, (2005), 943-949. doi: 10.1109/TPWRD.2004.843467

13. Xu, W., Abdulsalam, S. G., Cui, Y., Liu, X., "A Sequential Phase Energization Technique for Transformer Inrush Current Reduction—Part II: Theoretical Analysis and Design Guide", *IEEE Transactions on Power Delivery*, Vol. 20, No. 2, (2005), 950-957. doi: 10.1109/TPWRD.2004.843465.

14. Cano-González, R., Bachiller-Soler, A.,Rosendo-Macías, J. A., Álvarez-Cordero, G., "Inrush current mitigation in three-phase transformers with isolated neutral", *Electric Power Systems Research,* Vol. 121, (2015), 14-19. doi: 10.1016/j.epsr.2014.11.031

15. Schramm, S., Sihler, C., Rosado, S., "Limiting Sympathetic Interaction Between Transformers Caused by Inrush Transients", International Conference on Power System Transients (IPST2011), Delft, Netherlands, (2011).https://www.ipstconf.org/papers/Proc_IPST2011/11IPST 053.pdf

16. Rudez, U., Mihalic, R., "Sympathetic inrush current phenomenon with loaded transformers", *Electric Power Systems Research,* Vol. 138, (2016), 3-10. DOI: 10.1016/j.epsr.2015.12.011

17. Pontt, J., Rodriguez, J., San-Martin, J., Aguilera, R., "Mitigation of Sympathetic Interaction between Power Transformers Fed by Long over Head Lines Caused by Inrush Transient Currents", *IEEE Industry Applications Annual Meeting,* (2007), 1360-1363. DOI: 10.1109/07IAS.2007.211.

18. Ganji, M., Bigdeli, M., Azizian D., "Mitigation Transformer Inrush Current Using Modified Transient Current Limiter", *International Journal of Engineering, Transactions B:*

Applications, Vol. 32, No. 5, (2019), 701-709. doi: 10.5829/ije.2019.32.05b.12

19. Ebadi, A., Hosseini, S. M., Abdoos, A. A., "A New Restricted Earth Fault Relay Based on Artificial Intelligence", *International Journal of Engineering, Transactions B: Basics,* Vol. 32, No. 1, (2019), 62-70. doi: 10.5829/ije.2019.32.01a.08

20. Yahiou, A., Bayadi, A., Babes, B., "Modified method for transformer magnetizing characteristic computation and point-on-wave control switching for inrush current mitigation", *International Journal of Circuit Theory and Applications,* Vol. 47, No. 10, (2019), 1664-1679. doi: 10.1002/cta.2682.

21. Yahiou, A., Bayadi, A., Babes, B., "Point on Voltage Wave Switching for Sympathetic Inrush Current Reduction", International Conference on Applied Smart Systems (ICASS), Médéa, Algeria, 2018, 1-4. doi: 10.1109/ICASS.2018.8651972.

22. Yahiou, A., Bayadi, A., "Data Acquisition System for Magnetizing Inrush Current Measurement in Three Phase Transformer", International Conference on Electrical. Engineering and Automatic Control (ICEEAC), Sétif, Algeria, (2013). Available on: https://www.researchgate.net/publication/330221741_Data_Acq uisition_System_for_Magnetizing_Inrush_Current_Measuremen t_in_Three_Phase_Transformer.

Persian Abstract

چکیده

هدف اصلی این کار کاهش جریان هجومی در ترانسفورماتور سه فاز است. این جریان هجومی هنگام روشن کردن یک ترانسفورماتور بدون بار یا با بار کم ظاهر می شود. می تواند به مقادیر بسیار بالایی برسد و باعث خرابی در سیستم الکتریکی شود. استراتژی کنترل با در نظر گرفتن مقدار شار باقیمانده هنگامی که ترانسفورماتور قطع می شود و همچنین با رعایت تغییر فاز بین سه فاز به دست می آید. برای اندازه گیری جریان هجومی، یک پیکربندی آزمایشی با یک سیستم اکتساب داده با استفاده از کارت dSPACE 1104 توسعه داده شد و در این مقاله ارائه شده است. تکنیکی برای کنترل قطع کننده مدار برای انرژی دادن به یک ترانسفورماتور سه فاز ۲ کیلوولت آمپر بدون جریان هجومی نیز آزمایش و در تنظیمات آزمایشی اعمال شد. سهم ویژه این کار این است که این تکنیک در اندازه‌گیری‌ها با بررسی کامل شار باقیمانده به کار می‌رود. تکنیک پیشنهادی به حذف کامل جریان هجومی دست یافت.

International Journal of Engineering

Crosswalk Utilization by Pedestrian: Perception versus Reality - Case Study of New Delhi

F. Haque*, F. A. Kidwai

Jamia Millia Islamia, Department of Civil Engineering, New Delhi, India

P A P E R I N F O	*A B S T R A C T*
	Pedestrian safety at signalized intersections is a major cause of concern all over the world. Properly marked crosswalk enhances the safety of pedestrians as it is a well recognized crossing location by drivers. However a large number of accidents are reported at intersections predominantly due to the violation behavior of pedestrians. This study aims at understanding the crosswalk utilization behavior of pedestrians at urban signalized intersections. Data was collected through video recording and a questionnaire survey. Significant variables were identified and modelled using binomial logistic regression. Pedestrian personal level factors were found to significantly affect crosswalk compliance. Discrepancies were identified between perception and reality, suggesting that variation exists between what people say and what they practice in reality. The findings from this study suggest that a perception based study may not be as reliable as an observational study. The findings have both theoretical as well as practical implications and would certainly help the policy makers and designers in enhanced understanding of pedestrian behavior at urban signalized intersections.

1. INTRODUCTION

Road accidents have become a major concern globally and particularly in emerging economies. Every year, approximately 1.35 million people die due to road accidents costing most countries about 3% of their GDP [1]. India being a developing country is no exception to this global predicament. To put into context India ranks second in terms of incidences of road accident fatalities globally [2]. The accident records from within the country report the occurrence rate of road accidents at 53 per hour and on an average 17 lives are lost per hour. The situation is alarming in million plus population Indian cities as these cities accounted for 11.5 % of the total fatalities. Delhi had the highest number of accidental death followed by Chennai in 2017 [3]. Pedestrians are the most vulnerable road users and ultimate sufferers of road accidents. Road accident fatalities involving pedestrians account for about 22% of the total fatalities worldwide [4]. Accident statistics from China report that

pedestrian fatalities in traffic accidents are as high as 30% [5]. The share of fatal pedestrian road crashes in India was 13.8% in 2017 which is 3.4% more than the previous year whereas for Delhi it is almost 40% [3].

The probability of pedestrian crashes is high at intersections due to its typical nature in which a common space is shared among various road users. One recent study has highlighted that pedestrian crashes at intersections are associated with a higher probability of severe and fatal injuries [6]. Many of these accidents happen while crossing the road. In the past few years urban signalized and uncontrolled intersections in India have become accident hot-spots as more than 60% of pedestrian fatalities occurred there [3, 7]. Pedestrians violating the signal or not crossing the road along the designated crosswalks are considered as violation behaviors. Several studies have reported frequent violation behaviors by pedestrians as the leading cause of such accidents [8]. Compared to other road users, the behavior of pedestrians is quite unpredictable. They have

*Corresponding Author Institutional Email: faizanul26@gmail.com (F. Haque)

higher freedom to choose their path and are bounded by fewer laws. Several studies have been performed to understand pedestrians' road crossing behavior at signalized intersections more specifically their violation behavior. Studies have reported several internal as well as external factors affecting pedestrians' crossing decisions at intersections.

Pedestrian personal attributes such as gender and age group were reported as significant factors affecting violation behavior. Male pedestrians have higher violation and risk taking tendencies than females. Contrary to this, female pedestrians are more sensitive to risk perception and provide less preference to cross the road during the red phase [9, 10]. In a study in China it was reported that males were found to comply more with traffic rules [11]. Females also consider waiting for more safer crossing opportunities [12]. Older pedestrians are found to be the most law-abiding whereas young adults have more frequent violation behavior [9, 11].

Researchers have also focused on other personal factors such as group size, effect of other pedestrians and crossing speed. Single or smaller groups of pedestrians have higher whereas larger group sizes have lower violation tendency [13]. Pedestrians are more likely to show unsafe behavior if they observe others doing the same. Further presence of children and other pedestrians who wait for the walk sign, increases the tendency to wait for pedestrian green signal [14, 15]. Pedestrians' crossing speed is a crucial parameter for designing pedestrian facilities. The HCM 2000 and the existing manual of the Indian Road Congress, suggests considering pedestrian walking speed as 1.2 m/s for design purposes [16, 17]. Pedestrian crossing speed is highly subjective to the pedestrian's demographic and crossing behavior. Higher crossing speed was reported for pedestrians with violation behavior, males and smaller groups as compared to their counter parts [8, 18, 19].

An important location specific factor that notably affects the safe crossing behavior of pedestrians, is the presence of properly marked crosswalks at signalized intersections. The safety potential is great at properly marked zebra crossings as a majority of crossings occur at these locations. An early study in Scandinavian countries reported that the absence of crosswalks significantly increases the pedestrian dangerous behaviors [20]. Signalized intersections with properly marked crosswalks are very attractive and well identified site by pedestrians to cross the road and help to channelize pedestrian traffic [21]. In a study conducted in Delhi it was found that zebra crossing is preferred as it is perceived to be safe [22]. Pedestrians decision is also influenced by many factors such as comfort level, convenience to cross and safety [23].

The appalling data indicates the unfortunate state of road safety, predominantly the plight of the most vulnerable road users in emerging economies. Pedestrian behavior is stochastic and modelling their behavior is often a challenging task. The behavior of pedestrians, especially in developing countries is different from that of other countries. While several attempts have been made to study pedestrian behavior in developed countries. It requires more attention and understanding in developing countries such as India. Studies have focussed mainly on "reactive approach" (crash data analysis) rather than "proactive approach" (perception and behavior analysis) to assess pedestrian safety at signalized intersections. In light of the above discussions the primary aim of this study is to understand pedestrians' crosswalk utilization behavior at urban signalized intersections. Further this study aims at analyzing the discrepancy between pedestrians' perception and reality for crosswalk utilization.

2. METHODOLOGY

The major steps involved in this study are: (1) site selection (2) data collection- video recording and questionnaire survey (3) data extraction and compilation (4) analysis and results.

2. 1. Site Selection   Reconnaissance survey of several signalized intersections in New Delhi was performed initially and two intersections were finalized considering various physical, vehicular and pedestrian factors.   Site 1 is 4-legged and has mixed land use patterns consisting of college, offices, commercial establishment and open spaces. Site 2 is 3-legged and predominantly industrial area with few residential dwellings. Both sites have substantial pedestrian and vehicular traffic and are spatially well apart. Site pictures are shown in Figure 1.

2. 2. Data Collection   Video recording technique was used to record pedestrian road crossing behaviour [24]. Data such as pedestrian's crosswalk compliance, gender, age group, group size and technological distractions were successfully captured. Data was collected on week days with normal weather conditions. Two or more cameras were installed as per the site conditions to cover the entire section of the study sites. The field of view and height of the cameras were adjusted to cover the ends of the carriageway including sidewalks and medians, crosswalks with a few meters distance on both sides and signal phases. Video recordings were carried out during morning (9-10 AM) and evening (5-6 PM) hours without disturbing the normal traffic flow. The placements of cameras were not noticed by the pedestrians thus their naturalistic and actual behaviours were recorded. Further to compare the actual behavior of pedestrians

(a)

(b)

Figure 1. (a) Broad View of Site 1 (b) Broad View of Site 2

with their perceived behavior, a response based face to face questionnaire survey was also conducted simultaneously along with video recordings. The moment pedestrians crossed the road; volunteers approached and requested them to participate in the survey. A comprehensive questionnaire was prepared by studying previous relevant literature. Data was collected by using printed as well as Google forms. The questions were clearly explained to respondents and their responses were recorded. Question related to their crosswalk compliance behavior was asked. Respondents' gender, age, education and employment status were also obtained.

The observed pedestrians and questionnaire respondents belong to the same population (study sites) and both the samples were collected at study locations simultaneously. In total 552 pedestrians were observed out of which, 309 pedestrians participated in the survey resulting in a response rate of about 56%. The difference in the sample size of video data and questionnaire exits because all of the observed pedestrians were not willing to participate in the questionnaire survey. Some of the previous studies have adopted a similar methodology [11, 25].

2. 3. Data Extraction   The data from video recordings were extracted manually using AVS Video Editor Software. Recordings were played in ultra slow motion and frame by frame images were watched to extract the required data. In total, 552 pedestrian data were extracted with complete information. Data were coded and entered into excel sheets for further analysis.

Gender is categorized into "Male (0) and Female (1)". Since the exact age of a pedestrian cannot be found from video, it is estimated by grouping them into "Young (0), Middle (1) and Old age (2) groups". Group size is defined as pedestrian crossing alone "Single (0), Pair (1) and More than two (2)". Technological distraction is defined as "Yes (1)", if a person was clearly observed using mobile, talking over the phone and using head phones or else "No (0)". Pedestrian crosswalk compliance behavior (CCB) is "Yes (1)" if s/he crosses the road using a strip of road which includes crosswalk plus the area up to a distance of 0.5 m on either side of the crosswalk. A distance of 0.5m on either side of the crosswalk was included in CCB to include those pedestrians who cross in large groups and some of them are not exactly on the crosswalk but very close to it [11]. Crossing the road at any other location other than this strip would be considered as crosswalk non compliance, "No (0)". CCB at study sites is shown in Figure 2.

The data from the questionnaire form were extracted, coded and entered into an excel sheet. Incomplete or erroneous responses were excluded from further analysis. A total of 309 responses with complete information were successfully recorded. Gender and age group were coded similarly. Pedestrian education levels were collected into four categories- "Uneducated or Nil (0), Primary school (1), Secondary school (2) and Graduate and above (3)". Employment status consists of five categories- "Unemployed (0), Job (1), Self Employed (2), Student (3) and Home Maker (4)". To assess the utilization of crosswalk question, "Where do you generally cross the road at signalized intersection?" was asked. The response categories were "At any convenient location at intersection (0), Away from intersection (1), Crosswalks (2) and between vehicles stopped at signal (3)".

(a)

(b)
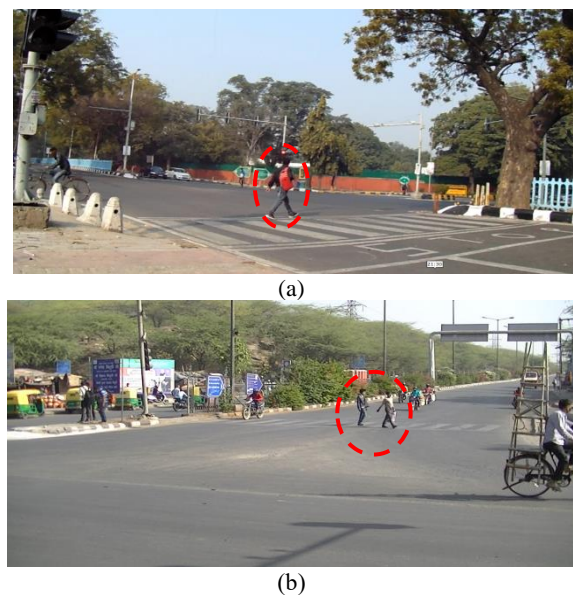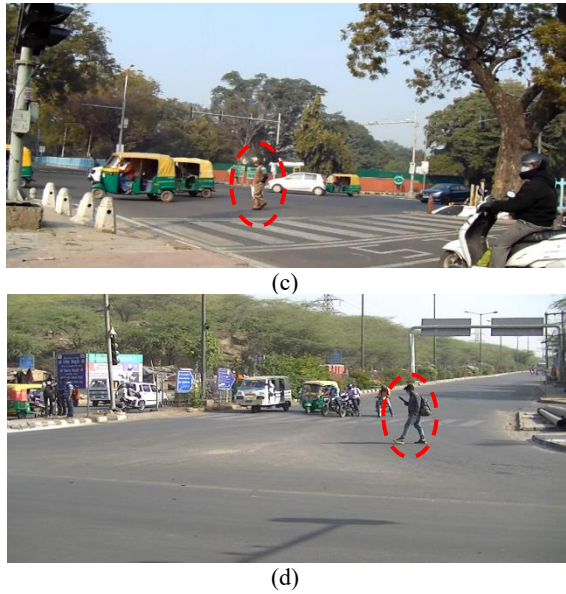
Figure 2. (a) CCB-Yes Site 1 (b) CCB-Yes Site 2 (c) CCB-No Site 1 (d) CCB-No Site 2

2. 4. Analysis and Modeling   Initially descriptive statistics are performed for the variables from video data to have a brief inference of sample distribution. Concise information about pedestrian characteristics and behaviour related to crosswalk compliance is obtained. To identify significant variables, Chi-square hypothesis test is performed to ascertain significant association between categorical variables using IBM SPSS Statistics 22. If p-value is less than 0.05 then it supports the alternate hypothesis that significant difference exists within groups in terms of crosswalk compliance. Finally, pedestrian CCB model is developed using statistically significant variables. A pedestrian has only two choices while crossing the road, whether or not to cross the road using crosswalk. Therefore, a binary logistic regression model is used to predict binary responses from categorical predictor variables [26].

The probability of selecting an alternative (compliance/non compliance) is based on a linear combination function (utility function) expressed as follows:

$$U_i = \beta_0 + \beta_1 x_{1,i} + \beta_2 x_{2,i} + \beta_3 x_{3,i} + \dots \beta_N x_{N,i} \qquad (1)$$

$$P(i) = \frac{e^{U_i}}{1+ e^{U_i}} \qquad (2)$$

where U_i = the utility of choosing alternative i, i = the alternative (compliance/non compliance), N = number of independent variables, β_0 = model constant, and β_N = coefficients of predictor variables, x= predictor variables that determine the probability of outcome of alternatives and $P(i)$= probability of pedestrian compliance. Descriptive analysis is performed for questionnaire data as well. Crosswalk utilization of respondents is compared

with gender, age group, education level and employment status. Finally, the results between perception and observation were compared.

3. RESULTS AND DISCUSSION

3. 1. Obsevational Study   The descriptive statistic of video data is shown in Figure 3. The sample has a major share of male and young pedestrians. Concerning group size, most of the pedestrians crossed the road alone followed by pairs and larger groups. Small percentages (5.62%) of pedestrians were found to be technologically distracted while crossing the road. Overall only 28.8% were observed to show crosswalk compliance behavior. The CCB at sites 1 and 2 were found to be 27.56% and 29.76%, respectively. Such low CCB can be due to the fact that, either the pedestrians fail to realize the importance of zebra or the wrong placement of zebra crossings [27]. Further chi-square test shows that statistically significant differences exist among gender (p= 0.037), age group (p=0.003), group size (p=0.048) and distracted pedestrian (p=0.029) with regards to CCB.

To have a comprehensive understanding of factors affecting pedestrian's crosswalk utilization, regression model is developed. Binary logistic regression model is developed to predict CCB using gender, age group, group size and technological distraction as explanatory variables. From the total data 80% of the sample is used for model development and the remaining 20% for model validation. The BL model outcomes are shown in Table 1. The model accuracy is found to be 70.7% and 73.1% for training and validation data, respectively. Hosmer and Lemeshow test which is used to assess the predictive performance of the model, is found to be insignificant (p=0.807) suggesting that that model has considerable predictive capability [28].

From the model results it can be inferred that gender is positively but weakly associated with CCB. Odds ratio or Exp(B) is slightly more than 1 suggesting that the odds of crosswalk compliance is a rather high for females as compared to males. The result is in line with previous findings [9, 10] but contradicts the result
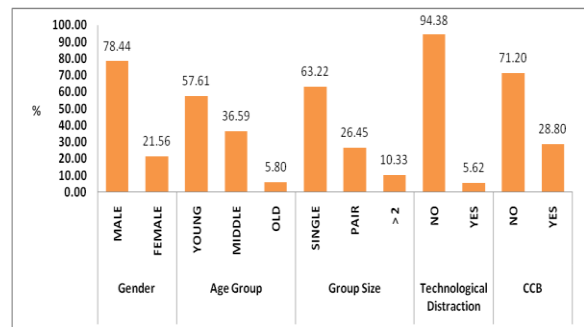
Figure 3. Descriptive Statistics from Video Data

TABLE 1. BL Model Outcomes for CCB

Variables	B	Std. Error	Exp(B)	p-value
Constant	-0.989	0.180	0.372	0.000
Gender	0.008	0.256	1.008	0.037
Age Group	0.181	0.175	1.198	0.003
Group Size	0.127	0.161	1.135	0.048
Technological Distraction	-1.068	0.630	0.344	0.029
Model Summary				
Sample	Training - 444 ; Validation - 108			
Log Likelihood	531.077			
Cox & Snell Pseudo R^2	0.013			
Nagelkerke Pseudo R^2	0.019			
Hosmer and Lemeshow Test χ^2	3.760 (p-value = 0.807)			
Model Accuracy	Training - 70.7% ; Validation - 73.1%			

obtained in China where males showed more compliance behavior [11]. Males have more risk-taking tendencies and have a negative attitude towards rules and regulations whereas females are more sensitive to risk perception and prefer compliance behavior. The result is also contradictory to previous results where gender failed to yield any significant association with compliance behavior [25].

Pedestrian's age group is positively and moderately related to crosswalk utilization at signalized intersection. Odds ratio is found to be 1.198 which means that the odds of compliance are less for younger pedestrians as compared to middle or old age. The compliance rate of old age pedestrians is about 5% more than middle age. Overall elderly pedestrians are the most compliant and young adults are the least. The results complement the past studies where similar behavior was observed [11]. The above findings conclude that old age pedestrians are associated with an increased level of compliance and law abidance. Older pedestrians suffer from reduced mobility, sensory and cognitive skills and thus prefer to cross slowly only when safer crossing opportunities are available. The presence of properly marked crosswalk enhances the safety perception of elderly pedestrians as it is a well recognised crossing location by drivers. Various other studies failed to establish any significant relation between pedestrians' age and crossing behavior [13, 18].

As in previous studies [13] this study also has a similar conclusion regarding the effect of group size on compliance behavior. As compared to individual pedestrians the crosswalk compliance is more for larger groups. Single pedestrian has higher noncompliance than that of a platoon due to freedom from platoon and directional effects [18]. The more the pedestrians wait at an intersection the more number of pedestrians join them and the larger the group size the less likely is the violation behavior. Such behavior can be explained based on conformity psychology. Similar conformity tendency behavior has been reported in many studies [14, 29]. The CCB for pedestrians crossing in pairs is found to be the highest as compared to others.

Technological distraction includes talking and texting on mobile and listening to music while crossing. The model result suggests that it is negatively and strongly associated with CCB. The CCB for non-distracted pedestrians is 30.3% whereas for distracted pedestrians it is only 12%. So technological distraction is associated with reduction in CCB and is in line with past findings [30]. Use of mobile phones causes cognitive distractions thereby reducing safety [31]. Mobile phone usage is also intimately related to the crossing performance of pedestrians. Text distraction is associated with least crossing performance and most impairment followed by talking and listening to music while crossing [32]. Technological distraction is significantly associated with situational awareness. Pedestrians using mobile phones are less likely to look left-right before and during crossing [9].

3. 2. Questionnaire Survey Study
The descriptive statistic of questionnaire survey data is shown in Figure 4. The distribution of respondents with respect to gender and age is similar to observational data. The sample consists of a large proportion of male and young respondents. In terms of education level and employment status the sample has a mixed distribution. It can be observed that a large share of respondents is secondary school educated and job holders. About 52.7% of respondents said to use the crosswalk to cross the road at signalized intersections and a fourth of respondents cross at any convenient location.

The variation in road crossing behavior concerning gender, age, education level and employment status are shown in Figure 5. Within gender an equal proportion of male and female respondents use crosswalk to cross the road at signalized intersection. As compared to males more females choose convenient location to cross the road, suggesting that females prefer more comfort and convenience. Crosswalk utilization is the most for young followed by middle and elderly respondents. On the contrary significant number of old age respondents cross road at any convenient location. Old pedestrians suffer from lack of mobility, so they might face hardship in walking an additional distance to crosswalk locations; hence prefer to cross the road as per their comfort and
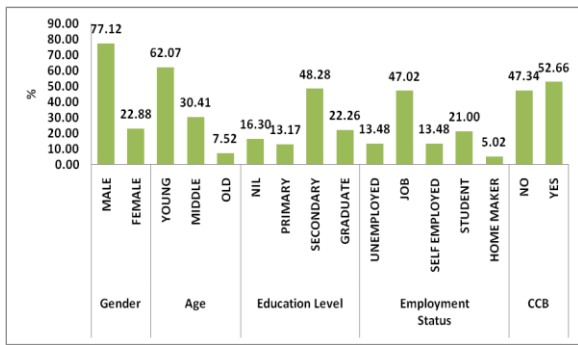
Figure 4. Descriptive Statistics from Questionnaire Survey
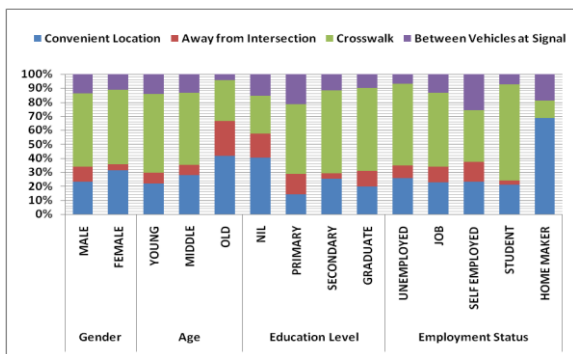
Figure 5. Road Crossing Behaviors for Gender, Age, Education and Employment

convenience. Education is found to have a significant effect on crosswalk compliance as higher education level is associated with an increase in crosswalk compliance. The result is similar to the results obtained in Mumbai [33]. In terms of employment status most crosswalk compliance is reported from students and least from home makers. Students are well aware of the safety implications of crosswalks whereas home maker might not be frequent visitors at signalized intersection and are not much aware hence cross the road at any convenient location.

3. 3. Perception versus Reality   In view of above outcomes no significant correlation is found between perception and reality. There exists a gap between what people say and what they actually practice. Since only three variables (gender, age and crosswalk compliance) are common in video and questionnaire data, so a comparison is made considering these variables. During the observational survey only 28.8% of pedestrians used the crosswalk, whereas 52.7% of respondents revealed using a crosswalk at signalized intersections. Crosswalk compliance regarding gender and age from perception and reality data is shown in Table 2. Crosswalk compliance rate for males and females is similar in perception as well as reality. But overall both males and females reported to be more compliant while in reality it is not so. In respect to age group large differences are

TABLE 2. Crosswalk Compliance: Reality versus Perception

Variable	Category	Crosswalk Compliance (%)	
		Observation	Perception
Gender	Male	29.14	52.44
	Female	29.79	53.42
Age	Young	27.38	56.06
	Middle	31.10	51.55
	Old	35.71	29.17

observed between perception and reality. Younger pedestrians were observed to be the least crosswalk compliant whereas they reported toward a much higher side. On the contrary old age pedestrians were observed to be most compliant but they reported to be less compliant. Overall, it is concluded that in all cases except for old age, pedestrians responded to be more crosswalk compliant than they practice.

The discrepancy between perceptions and reality could be explained as follows. Pedestrian movements were recorded without making them aware; thus, showing their actual behavior. On the contrary questionnaire survey was conducted face to face with pedestrians. Although pedestrians were aware that none of their personal details are collected and it is purely for academic research, still some might feel that the information might be used against them. Pedestrians' responses might also be affected by their mood. Further it is a common human psychology to portray oneself as good, in front of others.

Although perception based approach for assessment of pedestrian safety at signalized intersections is a crucial proactive approach, it suffers from certain limitations. Differences might exist between actual and perceived risks [34, 35]. A lot of variations exist between what people say and what they actually do [27]. In addition, it should be noted that although pedestrian perceptions are important, they may not highly correlate with actual safety considerations. Finally, it suffers from social attraction bias where respondents give favourable responses which might not reflect their actual behavior or feelings. In light of the above discussions, perception based study might not portray the reality, resulting in misleading conclusions. So, it is recommended that additional analysis to be performed to establish a relationship between perceived and actual behaviors.

4. CONCLUSIONS

The present study aimed to analyze pedestrian crosswalk compliance behavior at urban signalized intersections. Data was collected using video recordings and a response based questionnaire survey.

Significant variables were analyzed and modelled using the binary logistic regression technique. Finally differences between reality and perception were assessed. Based on the above findings the following important conclusions are made:

- Female, elderly and larger groups have higher odds whereas technologically distracted pedestrians have lower odds of crosswalk compliance.
- Higher level of education is associated with an increase in crosswalk compliance behavior.
- Large differences exist between what people say and what they actually practice. So perception based study should not be solely used for decision making as it might have misleading outcomes.

Based on the valuable findings, the present study has practical as well as theoretical applications. This study has added useful insights about pedestrian behavior in the existing state of art. It highlighted the fact that even though marked crosswalks are safer locations to cross the road, but failed to attract the pedestrians to use them. The low CCB suggests that pedestrians are not much aware of the importance of crossing the road at designated crosswalks. Further proper placement of crosswalks might significantly increase crosswalk compliance. So to increase the CCB and ultimately increase pedestrian safety at intersections, pedestrian facilities should be suitably designed particularly catering to the needs of elderly pedestrians. As far as possible, crosswalks should be placed along major pedestrian crossing paths to increase CCB. Pedestrians should be made aware of the consequences of distracted walking. Since education is associated with an increased level of CCB, road safety education at various levels and awareness campaigns should be conducted. As there exists a gap between reality and perception, a questionnaire based study should be used in conjunction with an observational study for decision making. The outcomes of this research would help policy makers and other stake holders in better understanding of pedestrian crosswalk utilization behaviour. Further it would guide them to take intervention measures to reduce violations and increase safety at signalized intersections.

The present study considered only the effect of pedestrian level factors to assess crosswalk compliance behavior. Various other external factors such as traffic characteristics, built environment and intersection geometry might also affect CCB. Data was collected from two intersections with a limited sample size. In the future more intersections may be included and analysis may be performed considering the effects of other factors as well.

5. REFERENCES

1. World Health Organization. *Global status report on road safety*. Geneva.

2. International Road Federation. *World Road Statistics 2017*. Geneva.

3. Transport Research Wing. *Road accidents in India-2017*. MoRTH,Government of India. New Delhi , India.

4. Zhang, W., Wang, K., Wang, L., Feng, Z., and Du, Y. "Exploring Factors Affecting Pedestrians' Red-Light Running Behaviors at Intersections in China." *Accident Analysis and Prevention*, Vol. 96, (2016), 71-78. https://doi.org/10.1016/j.aap.2016.07.038

5. Ni, Y., Cao, Y., and Li, K. "Pedestrians' Safety Perception at Signalized Intersections in Shanghai." In *Transportation Research Procedia,* Vol. 25, 1955-1963. Elsevier B.V.,https://doi.org/10.1016/j.trpro.2017.05.222

6. Nasri, M., Aghabayk, K., Esmaili, A., and Shiwakoti, N. "Using ordered and unordered logistic regressions to investigate risk factors associated with pedestrian crash injury severity in Victoria, Australia." *Journal of Safety Research*, Vol. 81, (2022), 78-90. https://doi.org/10.1016/j.jsr.2022.01.008

7. Priyadarshini, P., and Mitra, S. "Investigating Pedestrian Risk Factors Leading to Pedestrian Fatalities in Kolkata City Roads." *Transportation in Developing Economies*, Vol. 4, No. 1, (2018), 1. https://doi.org/10.1007/s40890-017-0054-9

8. Zaki, M. H., and Sayed, T. "Automated Analysis of Pedestrians' Nonconforming Behavior and Data Collection at an Urban Crossing." *Transportation Research Record: Journal of the Transportation Research Board*, Vol. 2443, No. 1, (2014), 123-133. https://doi.org/10.3141/2443-14

9. Aghabayk, K., Esmailpour, J., Jafari, A., and Shiwakoti, N. "Observational-based study to explore pedestrian crossing behaviors at signalized and unsignalized crosswalks." *Accident Analysis and Prevention*, Vol. 151, (2021), 105990. https://doi.org/10.1016/j.aap.2021.105990

10. Mukherjee, D., and Mitra, S. "A comprehensive study on factors influencing pedestrian signal violation behaviour: Experience from Kolkata City, India." *Safety Science*, Vol. 124, (2020). https://doi.org/10.1016/j.ssci.2020.104610

11. Ren, G., Zhou, Z., Wang, W., Zhang, Y., and Wang, W. "Crossing behaviors of pedestrians at signalized intersections: Observational study and survey in China." *Transportation Research Record*, Vol. 2264, No. 1, (2011), 65-73. https://doi.org/10.3141/2264-08

12. Tiwari, G., Bangdiwala, S., Saraswat, A., and Gaurav, S. "Survival analysis: Pedestrian risk exposure at signalized intersections." *Transportation Research Part F: Traffic Psychology and Behaviour*, Vol. 10, No. 2, (2007), 77-89. https://doi.org/10.1016/j.trf.2006.06.002

13. Dommes, A., Granié, M. A., Cloutier, M. S., Coquelet, C., and Huguenin-Richard, F. "Red light violations by adult pedestrians and other safety-related behaviors at signalized crosswalks." *Accident Analysis and Prevention*, Vol. 80, (2015), 67-75. https://doi.org/10.1016/j.aap.2015.04.002

14. Yagil, D. "Beliefs, motives and situational factors related to pedestrians' self-reported behavior at signal-controlled crossings." *Transportation Research Part F: Traffic Psychology and Behaviour*, Vol. 3, No. 1, (2000), 1-13. https://doi.org/10.1016/S1369-8478(00)00004-8

15. Yang, J., Deng, W., Wang, J., Li, Q., and Wang, Z. "Modeling pedestrians' road crossing behavior in traffic system micro-simulation in China." *Transportation Research Part A: Policy and Practice*, Vol. 40, No. 3, (2006), 280-290. https://doi.org/10.1016/j.tra.2005.08.001

16. Transportation Research Board. *Highway Capacity Manual*. National Research Council, Washington, DC. Washington,D.C.

17. Indian Road Congress. *Guidelines on Design and Installation of Road Traffic Signals. (IRC-93)*. New Delhi , India.

18. Marisamynathan, and Perumal, V. "Study on pedestrian crossing

behavior at signalized intersections." *Journal of Traffic and Transportation Engineering (English Edition)*, Vol. 1, No. 2, (2014), 103-110. https://doi.org/10.1016/S2095-7564(15)30094-5

19. Muley, D., Kharbeche, M., Alhajyaseen, W., and Al-Salem, M. "Pedestrians' Crossing Behavior at Marked Crosswalks on Channelized Right-Turn Lanes at Intersections." In *Procedia Computer Science*, Vol. 109C, 233-240. Elsevier B.V. https://doi.org/10.1016/j.procs.2017.05.339

20. Ekman, L., and Hyden, C. *Pedestrian safety in Sweden (No. FHWA-RD-99-091)*. University of North Carolina, Chapel Hill.

21. Akin, D., and Sisiopiku, V. P. "Pedestrian crossing compliance characteristics at-grade signalized crosswalks: case study in a downtown-university campus environment." *Transportation Research Board Annual Meeting*, (2007), 1-18.

22. Rankavat, S., and Tiwari, G. "Pedestrians perceptions for utilization of pedestrian facilities - Delhi, India." *Transportation Research Part F: Traffic Psychology and Behaviour*, Vol. 42, , (2016), 495-499. https://doi.org/10.1016/j.trf.2016.02.005

23. Al Bargi, W. A., David Daniel, B., Prasetijo, J., Md Rohani, M., and Mohamad Nor, S. N. "Crossing Behaviour of Pedestrians Along Urban Streets in Malaysia." In MATEC Web of Conferences, Vol. 103, 1-10. https://doi.org/10.1051/matecconf/201710308003

24. Bargegol, I., Najafi Moghaddam Gilani, V., and Jamshidpour, F. "Relationship between Pedestrians' Speed, Density and Flow Rate of Crossings through Urban Intersections (Case Study: Rasht Metropolis) (RESEARCH NOTE)." *International Journal of Engineering, Transactions C: Aspects*, Vol. 30, No. 12, (2017), 1814-1821. https://doi.org/https://dx.doi.org/10.5829/ije.2017.30.12c.00

25. Demiroz, Y. I., Onelcin, P., and Alver, Y. "Illegal road crossing behavior of pedestrians at overpass locations: Factors affecting gap acceptance, crossing times and overpass use." *Accident Analysis and Prevention*, Vol. 80, (2015), 220-228. https://doi.org/10.1016/j.aap.2015.04.018

26. Haque, F., and Kidwai, F. A. "Modeling Pedestrian Compliance Behavior at an Urban Signalized Intersection." *Journal of the Eastern Asia Society for Transportation Studies*, Vol. 14, (2021), 1334-1348. https://doi.org/https://doi.org/10.11175/easts.14.1334

27. Ibrahim, N. I., Karim, M. R., and Kidwai, F. A. "Motorists and pedestrian interaction at unsignalised pedestrian crossing." In *Eastern Asia Society for Transportation Studies*, Vol. 5, 120-125.

28. Hosmer, D. W., Lemeshow, S. A., and Sturdivant, R. X. Applied Logistic Regression (3rd ed.). New York: Wiley.

29. Zhou, R., Horrey, W. J., and Yu, R. "The effect of conformity tendency on pedestrians' road-crossing intentions in China: An application of the theory of planned behavior." *Accident Analysis & Prevention*, Vol. 41, No. 3, (2009), 491-497. https://doi.org/10.1016/j.aap.2009.01.007

30. Russo, B. J., James, E., Aguilar, C. Y., and Smaglik, E. J. "Pedestrian behavior at signalized intersection crosswalks: Observational study of factors associated with distracted walking, pedestrian violations, and walking speed." *Transportation Research Record*, Vol. 2672, No. 35, (2018), 1-12. https://doi.org/10.1177/0361198118759949

31. Hatfield, J., and Murphy, S. "The effects of mobile phone use on pedestrian crossing behaviour at signalised and unsignalised intersections." *Accident Analysis and Prevention*, Vol. 39, No. 1, (2007), 197-205. https://doi.org/10.1016/j.aap.2006.07.001

32. Jiang, K., Ling, F., Feng, Z., Ma, C., Kumfer, W., Shao, C., and Wang, K. "Effects of mobile phone distraction on pedestrians' crossing behavior and visual attention allocation at a signalized intersection: An outdoor experimental study." *Accident Analysis and Prevention*, Vol. 115, (2018), 170-177. https://doi.org/10.1016/j.aap.2018.03.019

33. Marisamynathan, S., and Vedagiri, P. "Modeling pedestrian crossing behavior and safety at signalized intersections." *Journal of Transportation Research Board*, Vol. 2672, No. 31, (2018), 76-86. https://doi.org/10.1177/0361198118759075

34. Schneider, R. J., Ryznar, R. M., and Khattak, A. J. "An accident waiting to happen: A spatial approach to proactive pedestrian planning." *Accident Analysis and Prevention*, Vol. 36, No. 2, (2004), 193-211. https://doi.org/10.1016/S0001-4575(02)00149-5

35. Rankavat, S., and Tiwari, G. "Pedestrians risk perception of traffic crash and built environment features - Delhi, India." *Safety Science*, Vol. 87, (2016), 1-7. https://doi.org/10.1016/j.ssci.2016.03.009

Persian Abstract

چکیده

ایمنی عابران پیاده در تقاطع های علامت دار یکی از دلایل اصلی نگرانی در سراسر جهان است. خط عابر پیاده با علامت گذاری مناسب ایمنی عابران پیاده را افزایش می دهد زیرا این محل عبور و مرور توسط رانندگان به خوبی شناخته شده است. با این حال تعداد زیادی از تصادفات در تقاطع ها عمدتاً به دلیل رفتار تخلف عابران پیاده گزارش می شود. این مطالعه با هدف درک رفتار استفاده از عابر پیاده در تقاطع‌های علامت‌دار شهری انجام شده است. داده ها از طریق فیلمبرداری و پرسشنامه جمع آوری شد. متغیرهای مهم با استفاده از رگرسیون لجستیک دو جمله ای شناسایی و مدل سازی شدند. فاکتورهای سطح شخصی عابر پیاده به طور قابل توجهی بر رعایت عابر پیاده تأثیر می گذارد. تفاوت‌هایی بین ادراک و واقعیت شناسایی شد، که نشان می‌دهد بین آنچه مردم می‌گویند و آنچه در واقعیت عمل می‌کنند تفاوت وجود دارد. یافته های این مطالعه نشان می دهد که یک مطالعه مبتنی بر ادراک ممکن است به اندازه یک مطالعه مشاهده ای قابل اعتماد نباشد. یافته‌ها هم مفاهیم نظری و هم کاربردی دارند و مطمئناً به سیاست‌گذاران و طراحان در درک بهتر رفتار عابر پیاده در تقاطع‌های علامت‌دار شهری کمک می‌کنند.

International Journal of Engineering

Numerical Investigations of Damage Behaviour at the Weld/Base Metal Interface

S. Talouti*[a], D. Benzerga[a], H. Abdelkader[b]

[a] LSCMI, University of Sciences and Technology of Oran, Mechanical Department, Oran, Algeria
[b] Univ. Artois, IMT Lille Douai, Junia, Univ. Lille, ULR 4515, Laboratoire de Génie Civil et géo Environnement (LGCgE), Béthune, France

P A P E R I N F O	*A B S T R A C T*
	In the present paper, the numerical modelling to predict the interface damage of weld defect in a steel pipeline was studied. This work focused on determination of the maximum operating pressure and the characterisation of mechanical behaviour at a weld-base metal interface. The operating pressure can fluctuate leading to the phenomenon of fatigue and consequently to the failure of pipeline. Experimental investigations were carried out using non-destructive test (NDT) in order to locate and determine size of defects. A bilinear interface decohesion model is used to simulate the damage behaviour considering a stress-relative displacement laws. Numerical simulations based on the finite element method were used to study the influence of size defects and young's moduli ratio on the operating pressure as well as interfacial damage between the weld and base metal. The obtained results showed that the interface damage depending on shape and material properties of defects has an impact on pipeline safety and integrity. *doi: 10.5829/ije.2022.35.12c.09*

1. INTRODUCTION

Weld defect is one of the most significant threats to onshore pipelines that can have consequences for environment due to the dangerousness of transport fluids. These macro-defects result from the micro-defects growth due to internal pressure [1-3]. Micro-defects are incorporated during the welding procedure. There are many types of welding defects that affect the performance of a product such as incomplete penetration (or lack of penetration), porosity, cluster porosity, incomplete fusion, suck back, cracks, undercut, slag, etc. Inspection of welded joints may be done using destructive methods (such as tension, shear, or bending tests) or non-destructive methods. The non-destructive testing methods that are typically used for the inspection of weldments include visual inspection, dye penetrant inspection, magnetic particles inspection, radiography and ultrasonic inspection [4]. Eshtayeh et al. [5] have shown that the digital image correlation (DIC) method can be successfully and easily used as a non-destructive inspection tool for detecting internal defects in welded joints which cannot be detected using visual inspection.

The DIC method is capable of detecting the existence of different types of welding defects such as incomplete penetration, incomplete fusion, slag inclusion, cluster porosity, and such back as well as the apparent linear size of the defect.

Deivanai and Soni [6] concluded that the NDT can be applied on all type of materials including composite materials and allowed to identify surface subsurface and internal defects ensuring quality of materials and joining processes without destroying them. The effect of defect on toughness behaviour of pipeline steels is studied by Vijay Kumar Dalla [7] using facture and failure analysis. The authors showed that fracture toughness is reduced by 68 % due to influence of microstructure. Pipeline failure also depends on cycling loading due to the operating pressure of the fluids and corrosion [8-10]. Many methods have addressed accessing fatigue life performance, like empirical model using a safe-life approach, fracture mechanics method, and statistical based on probability models [11-13]. Damage by pitting corrosion of the surface areas of the local oil and gas pipelines was identified and numerically analysed by Maruschak et al. [14, 15]. They concluded that the

* Corresponding author Email: *said.talouti@yahoo.com* (S. Talouti)

decrease of the structural strength of oil and gas pipelines is due to reduction of the cross section, caused by corrosion; softening because of stress relaxation; formation of defects, such as micro cracks; and fragility influenced by hydrogen action. Also, they demonstrated that increase in fatigue crack length is accompanied by the increase in the size of plastic deformation zone near the crack tip that makes the transition from the quasi-brittle failure to the fatigue one with the formation of fatigue striations. It is known that crack initiation and propagation can be occurred at the weld defect and base metal interface. Debonding of the interface is one of an undesirable failure mechanism. This paper presents the analysis of numerical modelling based on the indirect use of fracture mechanics to determine the behaviour of weld defect – pipeline interface. The model is based on NDT method to detect metallurgical defects that could represent a potential source of damage. Both approaches, NDT and numerical, offer an alternative to the destructive methods such as hydrostatic test to predict the interface damage that causes failure of pipeline.

Our study focuses on the interface damage of a weld defect which is supposed to have a spherical shape, embedded in a matrix of a micro-alloyed steel gas pipeline. The interface model assumes a bilinear softening behaviour of the interfacial provided with stress-relative displacement laws. This work is carried out using the finite element code (ANSYS) in association with a house program to simulate decohesion at the interface (inclusion/matrix) and its effect on the macroscopic behaviour of the structure.

2. NUMERICAL MODELING

Gas pipelines are obtained by welding operations from sheets. The molten pool created during welding operation is characterized by a very complex thermophysical processes involving thermal, convective, chemical and electromagnetic phenomena depending on the nature of the process used [11]. These convection movements of the liquid or gaseous metal significantly influence the shape of the weld bead and the heat transfers can induce defects such as inclusions or porosities. These defects are generally too small to be detectable by the non-destructive method, called NDT [12]. Generally, failure results from the germination, growth and coalescence of defects at the microscopic scale. These cavities originate from inclusion/matrix decohesion [13, 15]. The model used for the numerical simulations is composed of an incompressible matrix and a cavity possibly filled by a spherical inclusion. The matrix represents the representative elementary volume of a pipe in which the defect is embedded. This matrix is supposed to be elastoplastic, whereas the material which constitutes the inclusion can be purely elastic in the case of rigid defects

or elastoplastic in the case of ductile defects. The inclusion that represents the defect is initially assumed to be perfectly spherical [16]. The matrix behaviour subjected to an internal pressure is studied under a pure tension loading [17, 18]. Due to the symmetry, only a quarter of body is modelled. The following boundary conditions were chosen: constraints on one side of the matrix – inclusion and an applied displacement on the other side, as shown in Figures 1 and 2.

Taking into account the symmetry of the structure, we mesh only a quarter of model. The structure has been discretized using a four-node quadrilateral element mesh for both matrix and inclusion, as shown in Figure 3. The inclusion is assumed to have a spherical shape embedded in a matrix of X65 pipeline steel. The displacement was imposed in the tangential direction due to the value of the tangential stress (hoop stress) which is equal to the double of the axial and radial stress ($\sigma_{hoop} = 2\sigma_{axial} = 2\sigma_{radial}$).

The main inclusions present in X65 steel of this study are the tungsten and copper inclusions coming from the TIG and MIG welding process, respectively [19, 20].

The proposed interfacial damage model is considered as a two dimensional entity, taking into account two decohesion modes which ensure traction stress σ_n and shear stress t_n [21, 22]:
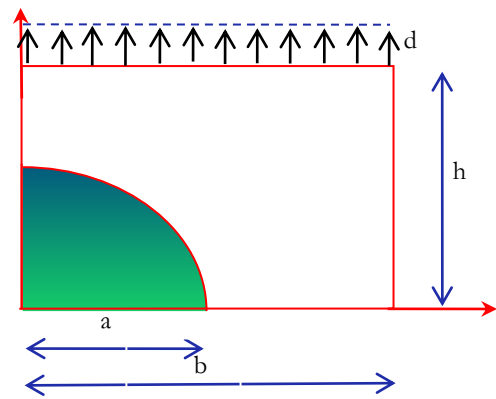
Figure 1. Weld defect as an inclusion and matrix model
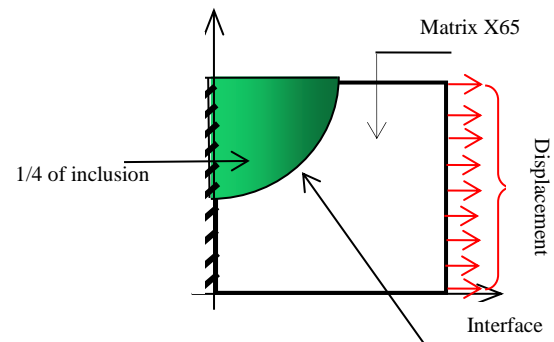
Figure 2. Applied boundary conditions
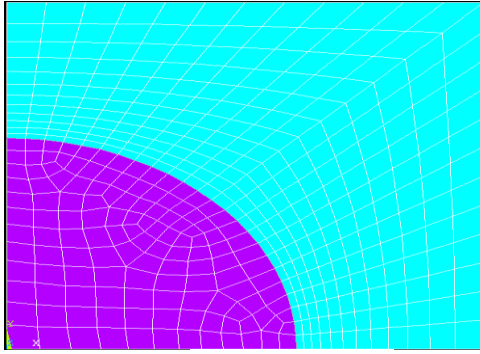
Figure 3. Finite element model

$$\left(\frac{\sigma_{\mathrm n}}{\hat\sigma_{\mathrm n}}\right)^2 + \left(\frac{t_{\mathrm n}}{\hat t_{\mathrm n}}\right)^2 = 1 \qquad \text{for} \qquad \sigma_n > 0 \tag{1}$$

$\hat\sigma_n$ et $\hat t_n$ are the ultimate traction and shear strengths of the interface, respectively. By introducing an evolution law of the ultimate stress $\hat\sigma_n$

$$\left(\sigma_{\mathrm n}\right)^2 + \left(\frac{\hat\sigma_{\mathrm n}}{\hat t_{\mathrm n}}\right)^2 \left(t_{\mathrm n}\right)^2 = \left(\hat\sigma_{\mathrm n}\right)^2 \quad \Rightarrow$$

$$\left[\sigma_{\mathrm n} \quad t_{\mathrm n}\right]\begin{bmatrix} 1 & 0 \\ 0 & \left(\frac{\hat\sigma_{\mathrm n}}{\hat t_{\mathrm n}}\right)^2 \end{bmatrix}\begin{bmatrix} \sigma_{\mathrm n} \\ t_{\mathrm n} \end{bmatrix} = \left(\hat\sigma_{\mathrm n}\right)^2 \tag{2}$$

The interface behaviour can be described by a bilinear relationship between the traction and relative displacement (see Figure 4)

The interface model (Equation (1)) is reconsidered as a plasticity criterion with softening:

$$\sqrt{\sigma^T A \sigma} - \hat\sigma_n(u) = f(\sigma) - \hat\sigma_n(u) = 0 \ \text{ for } \ \sigma_n > 0 \tag{3}$$

with

$$u = \langle \delta - \delta_0 \rangle$$
$$\langle x \rangle = \begin{cases} x \ if \ x \geq 0 \\ 0 \ if \ x < 0 \end{cases} \tag{4}$$
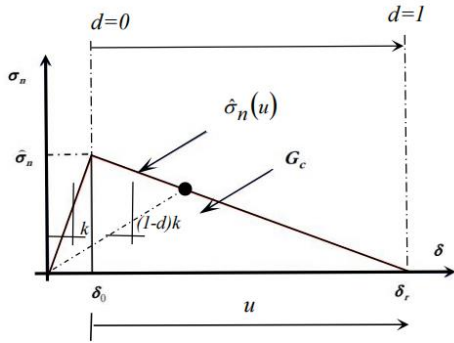
Figure 4. Bilinear interface decohesion model

δ represents the relative interfacial displacement.

Considering a bilinear behaviour of the interface [23] See Figure 4, the term $\hat\sigma_n(u)$ can be expressed as follows:

$$\hat\sigma_n(u) = \hat\sigma_n(1 - \omega u) \qquad \text{with} \quad \omega > 0 \tag{5}$$

The parameter ω is derived from critical energy G_C that represents the surface under the curve (Figure 4) [24]:

$$\omega = \frac{\hat\sigma_n e}{2G_C} \tag{6}$$

e denotes the thickness of the interface.

The relationship (3) shows that when $f(\sigma)$ reaches the threshold $\hat\sigma_n$ ($\delta = \delta_0$ corresponds to $u = 0$ and u will be calculated from the relationship 5). At this moment, we have an initiation of the decohesion at the interface. The decohesion is complete when $\hat\sigma_n(u)$ reaches a zero value for interfacial displacement ($\delta = \delta_r$) threshold of total decohesion and opened surfaces are completely free of stresses.

To develop an interface model damage, it is assumed that the mechanical behaviour of the interface $(\hat\sigma_n - \delta)$ follows the law described in Figure 4, where $\delta = \delta_0$ et $\delta = \delta_r$ correspond to the displacements obtained for the maximum stress $\hat\sigma_n$ and at the final rupture of the interface when the stress vanishes. A damage variable can be expressed as follows [25-27]:

$$d = \begin{cases} 0 \Leftarrow \delta \leq \delta_0 \\ \dfrac{\hat\sigma_n - \hat\sigma_n(u)}{\hat\sigma_n} \Leftarrow \delta_0 < \delta < \delta_r \\ 1 \Leftarrow \delta > \delta_r \end{cases} \tag{7}$$

Taking into account the damage, the behaviour of the interface is given by the following relations:

$$\begin{Bmatrix} \sigma_n \\ \tau_n \end{Bmatrix} = \begin{bmatrix} (1-d)k_n & 0 \\ 0 & (1-d)k_t \end{bmatrix}\begin{Bmatrix} \delta_n \\ \delta_t \end{Bmatrix} \tag{8}$$

where k_n and k_t are the stiffnesses of the interface in the normal and tangential direction. d_n and d_t are the interfacial relative displacements (see Figure 4). To illustrate the progression of interfacial decohesion, when $d = 1$ describes total decohesion which means that the absolute value of the interlaminar stress vector is reduced to zero.

3. APPLICATION OF THE METHOD

Recent developments in digital image processing and computer vision have enabled the introduction of a new automated vision system for the detection and evaluation of gas pipeline weld defects from radiographic films. This new system makes it possible to detect welding

defects and estimate the necessary information such as the length, width, area, orientation, angle and perimeter of the defects. It offers many advantages such as eliminating the need for image interpretation by specialist inspectors and the ability to enhance captured images so that defects appear much clearer (see Figure 5) [28].

Among the welding defects, taken within the framework of this study, the inclusions of tungsten and copper resulting from the processes of welding TIG and MIG respectively. Tungsten particles embedded in welds (Generally GTAW only) are very hard and can cause very intense local residual stresses. These defects come from too small tungsten electrodes, too high and amperage, AC balance on +, Upslope too high, electrode tip not snipped, electrode dipped into the weld pool or touched with the fill rod, electrode split. These tungsten inclusions are detected by x-ray and show up as bright particles since they are much denser than the steel (see Figure 6).
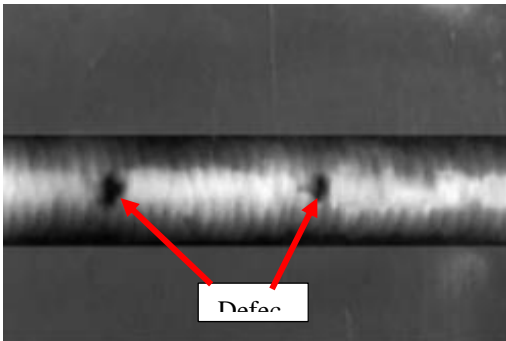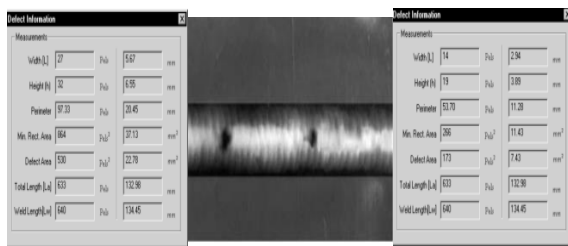
Figure 5. Captured radiographic image [24]
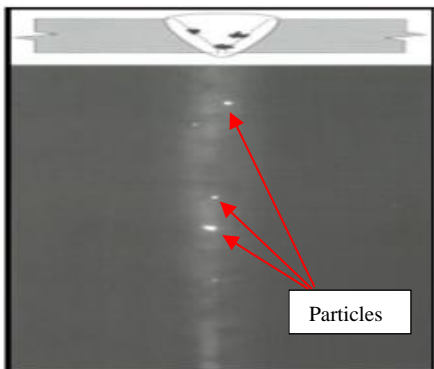
Figure 6. Tungsten inclusions

It can also happen that copper inclusions enter the weld pool. This is the case when copper welding consumables come into contact with the weld pool, or when the copper gas nozzle comes into contact with the weld pool or the seam preparation side. Copper inclusions are extremely difficult to detect with non-destructive testing. These inclusions cause embrittlement of the weld. The previously developed decohesion model has been translated into APDL language and implemented in the ANSYS finite element code. The interface was modelled using the CZM interface element [29]. Interface surfaces are represented by a special set of interface elements or contact elements. In the case of CZM, decohesion is treated as a progressive phenomenon in which cohesive tensile separation takes place across a cohesive zone. The extension of this cohesive zone in front of the crack tip is modelled using the tensile separation laws (also called the cohesion law) which links the cohesive stress to the separation in the process zone. First, we studied the effect of Young's modulus of the inclusion on the macroscopic behaviour of the structure. In a second step, the effect of inclusion size was considered to highlight this parameter on the global behaviour of the structure. The defects are embedded in a matrix of API 5L X65 pipeline steel [30] (see Table 1).

To highlight the effect of mechanical resistance of the inclusion on the macroscopic behaviour, we have examined several ratios: Young's modulus of the inclusion / Young's modulus of the matrix (E_{in}/E_{mat}).
In the case of a ratio ($E_{inc}/E_{mat}=0.7$), Figure 7(a) shows that the deformation of matrix and inclusion is homogeneous and the decohesion is small compared with the ratio $E_{inc}/E_{mat} =3.5$ in Figure 7(b). In this Figure 7(b), the decohesion is important at the tops of the inclusion; this is due to the rigidity of the tungsten inclusion; the deformation is inhomogeneous. This shows that the decohesion is more important for a hard inclusion ($E_{inc}/E_{mat} =3.5$) than a ductile inclusion ($E_{inc}/E_{mat}=0.7$). This behaviour leads to anisotropic damage at the interface.

Figure 8 shows the effect of inclusions of different resistances on the macroscopic behaviour. We clearly see the effect of Young's moduli of the defect, i.e. of the inclusion, on the macroscopic level. When the inclusion is hard with a high elastic modulus, the initiation of its interfacial damage occurs for lower stress levels compared to softer inclusions (Figure 8). It should be noted, after initiation of damage (critical zone), that the curves representing the hard inclusions are characterized by a strain hardening more important than the ductile

TABLE 1. API 5L X65 mechanical properties

Young's modulus	Poisson's ratio	Yield strength	Tensile strength
210 (GPa)	0.3	450 (MPa)	535 (MPa)
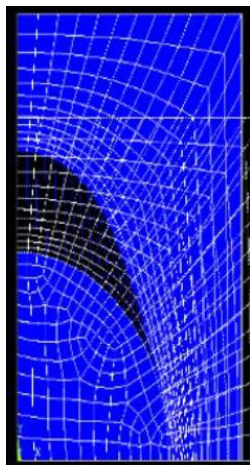
(a) Inclusion of tungsten
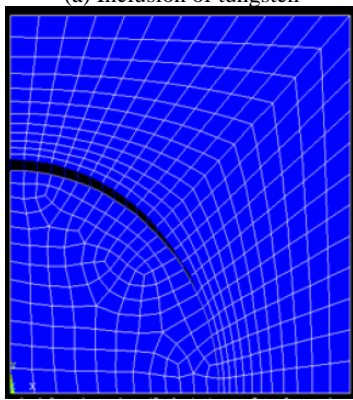
(b) Inclusion of copper

Figure 7. Damage behaviour at matrix-inclusion interface
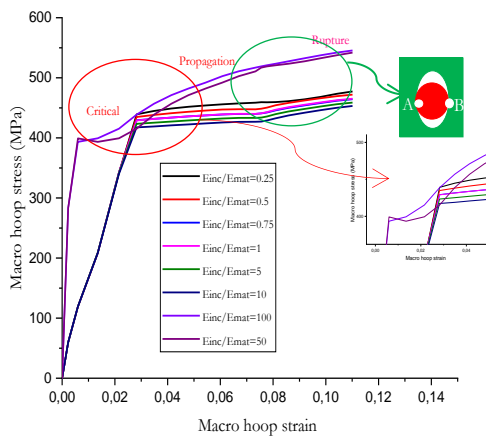
Figure 8. Effect of inclusion strength on macroscopic behaviour

inclusions. This can be explained by the great resistance that a hard inclusion opposes to zones A and B when it is subjected to the compression caused by the matrix during

external static loading. This behaviour leads to anisotropic damage at the interface. The effect of dynamic loading on changes in the mechanical properties and crack resistance of the pipe steel has been studied by Chausov et al. [31].

Figure 9 shows the effect of defect strength (Young's modulus of inclusion) on interfacial damage pressure. It can be noted, from Figure 7, the decohesion is higher for hard inclusions ($E_{incl}/E_{mat} > 2$) causing failure of structure if hydrostatic test is performed. From a ratio E_{incl}/E_{mat} higher than 5, defects cannot withstand fluctuations of operating pressure as function of time. The defect of tungsten with a ratio equal to 3.5 (TIG welding) cannot withstand the hydrostatic test.

The propagation can cause the variation of the operating pressure. While in the case of copper defect (MIG welding) with a ratio equal to 0.7, the structure can withstand to the hydrostatic test.

Figure 10 highlights the influence of defect size on the interfacial damage between the inclusion and the X65 matrix. This figure shows the behaviour of copper and
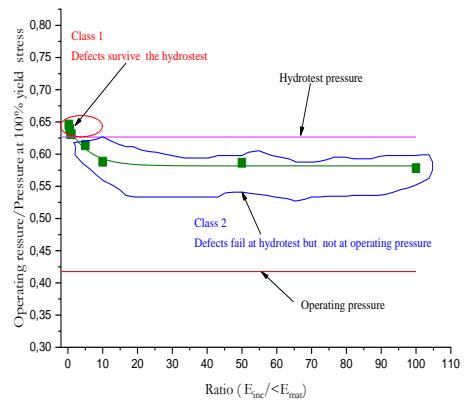
Figure 9. Interfacial damage pressure values for inclusion of radius 5µm
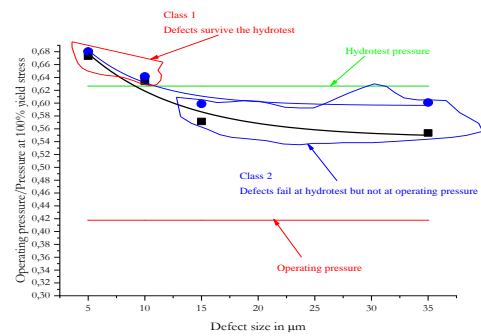
Figure 10. Interfacial damage pressures for tungsten and copper defects

tungsten defects for different sizes. It is observed that at small size defect, the operating pressure is high due to the toughness of inclusion, but at greater size defect, the operating pressure is small because of the ductility of inclusion. In conclusion, we can say that the damage of matrix – inclusion interface occurs rapidly for a hard inclusion than for a ductile inclusion.

4. CONCLUSION

In the present work, numerical simulation associated with NDT method has shown that it could replace destructive methods such as hydrostatic test to predict the failure of pipeline. Numerical results using interface model have been presented to predict the damage process at a matrix weld defect interface. This damage model was based on the indirect use of fracture mechanics considering a softening stress-relative displacements law. Different size defects and young's moduli ratios were used and a numerical predicted was developed to separate the failure and safe zones for damage of matrix - weld defect interface. For lower young's moduli and size defect ratios, no failure of structure was observed if hydrostatic test is performed. An excessive rise young's moduli and size defect ratios has not an impact on the rupture of structure. Not only the elastoplastic properties of the affected material (degradation of elastic moduli, decrease in elastic limit, etc.), but there is also a significant softening effect on the macroscopic behavior as well as anisotropy. The results obtained show that the rigid interfaces fail rapidly, while the soft interfaces, in spite of a weakening effect of the material, have a slow fail.
This approach, numerical modelling associated with NDT method, will certainly be more economic than hydrostatic test.

5. REFERENCES

1. Adjogbe, S., Okoronkwo, C., Oguoma, O., Igbokwe, J. and Okwu, M., "Investigation of the effect of hydrostatic pressure testing on the microstructure of carbon steel pipeline material", *AASCIT Journal of Materials*, Vol. 4, No. 3, (2018), 58-65.

2. Matta, L., "Collective effects of leakage, temperature changes, and entrapped air during hydrostatic testing", in Pipeline Pigging and Integrity Management Conference., (2017).

3. Bulatovic, S., Aleksic, V. and Milovic, L., "Failure of steam line causes determined by ndt testing in power and heating plants", *Frattura ed Integrità Strutturale*, Vol. 7, No. 26, (2013), 41-48. doi: 10.3221/IGF-ESIS.26.05.

4. Khan, M.I., "Welding science and technology, New Age International, (2007).

5. Eshtayeh, M., Hijazi, A. and Hrairi, M., "Nondestructive evaluation of welded joints using digital image correlation", *Journal of Nondestructive Evaluation*, Vol. 34, No. 4, (2015), 1-12. doi: 10.1007/s10921-015-0310-z.

6. Deivanai, S. and Soni, M., "Non destructive testing and analysis of friction stir welded aluminium alloy 2024 pipes", *Materials Today: Proceedings*, Vol. 56, (2022), 3721-3726. https://doi.org/10.1016/j.matpr.2021.12.470

7. Dalla, V.K., "Experimental investigation of fracture behavior and microstructure of api 5lx60 line pipe", *Materials Today: Proceedings*, Vol. 56, (2022), 595-608. https://doi.org/10.1016/j.matpr.2021.12.149

8. Adjogbe, A., Okoronkwo, C., Igbokwe, J., Ezurike, O. and Oguoma, O., "The impact of hydrostatic pressure test on the interstitial strength of mild-steel pipeline material", *Indian Journal of Science and Technology*, Vol. 12, (2019), 43. doi: 10.17485/ijst/2019/v12i43/144730.

9. Balamuralikrishnan, R., Krishnamurthy, B. and AlHarthy, M.N., "Destructive and non-destructive testing methods for condition monitoring of concrete elements", *Journal of Multidisciplinary Engineering Science and Technology*, Vol. 4, No. 6, (2017).

10. Foorginejad, A., Taheri, M. and Mollayi, N., "A non-destructive ultrasonic testing approach for measurement and modelling of tensile strength in rubbers", *International Journal of Engineering, Transactions C: Aspects,* Vol. 33, No. 12, (2020), 2549-2555. doi: 10.5829/ije.2020.33.12c.16.

11. Bilat, A.-S., "Estimation du risque de rupture fragile de soudures de pipelines en aciers à haut grade: Caractérisation et modélisation", Paris, ENMP, (2007),

12. Allouti, M., "Etude de la nocivité de défauts dans les canalisations de transport de gaz tels les éraflures, les enfoncements ou leurs combinaisons", Université Paul Verlaine-Metz, (2010),

13. Ramière, I., Masson, R., Michel, B. and Bernaud, S., "Un schéma de calcul multi-échelles de type éléments finis au carré pour la simulation de combustibles nucléaires hétérogènes", in 13e colloque national en calcul des structures., (2017).

14. Maruschak, P., Prentkovskis, O. and Bishchak, R., "Defectiveness of external and internal surfaces of the main oil and gas pipelines after long-term operation", *Journal of Civil Engineering and Management*, Vol. 22, No. 2, (2016), 279-286. doi: 10.3846/13923730.2015.110067.

15. Maruschak, P., Panin, S., Stachowicz, F., Danyliuk, I., Vlasov, I. and Bishchak, R., "Structural levels of fatigue failure and damage estimation in 17mn1si steel on the basis of a multilevel approach of physical mesomechanics", *Acta Mechanica*, Vol. 227, No. 1, (2016), 151-157. https://doi.org/10.1007/s00707-015-1420-5

16. Czarnota, C., "Endommagement ductile des matériaux métalliques sous chargement dynamique-application à l'écaillage", Université de Metz, (2006),

17. Regad, A., Benzerga, D., Berrekia, H., Haddi, A. and Chekhar, N., "Repair and rehabilitation of corroded hdpe100 pipe using a new hybrid composite", *Frattura ed Integrità Strutturale*, Vol. 15, No. 56, (2021), 115-122. doi: 10.3221/IGF-ESIS.56.09

18. Berrekia, H., Benzerga, D. and Haddi, A., "Behavior and damage of a pipe in the presence of a corrosion defect depth of 10% of its thickness and highlighting the weaknesses of the asme/b31g method", *Frattura ed Integrità Strutturale*, Vol. 13, No. 49, (2019), 643-654. doi: 10.3221/IGF-ESIS.49.58

19. Gupta, M., Shukla, S.K., Sharma, V.K. and Kumar, H., "Effect of tig and mig welding on microstructural and mechanical properties: Astate of art", *International Journal of Applied Engineering Research*, Vol. 13, No. 9, (2018), 83-90.

20. Chaht, F.L., Mokhtari, M. and Benzaama, H., "Using a hashin criteria to predict the damage of composite notched plate under traction and torsion behavior", *Frattura ed Integrità Strutturale*, Vol. 13, No. 50, (2019), 331-341. doi: 10.3221/IGF-ESIS.50.28.

21. Benzerga, D., Haddi, A., Seddak, A. and Lavie, A., "A mixed-mode damage model for delamination growth applied to a new

woven composite", *Computational materials science*, Vol. 41, No. 4, (2008), 515-521. doi: 10.1016/j.commatsci.2007.05.022.

22. Orangi, R., Mansourian, H., Bina, K. and Rabbanifar, S., "Vulnerability assessment of steel structures in district 12 of mashhad city and prioritizing the welding defects using the analytic hierarchy process", *International Journal of Engineering*, Vol. 31, No. 6, (2018), 877-885. doi: 10.5829/ije.2018.31.06c.03.

23. Li, S., Zhang, L., Sun, Q. and Tengfei, M., "Numerical simulation method study of rock fracture based on strain energy density theory", *Frattura ed Integrità Strutturale*, Vol. 13, No. 47, (2019), 1-16. doi: 10.3221/IGF-ESIS.47.01.

24. Wagner, W. and Gruttmann, F., "Delamination growth analysis of composite panels", *Revue Européenne des Eléments*, Vol. 13, No. 8, (2004), 915-929. doi: 10.3166/reef.13.915-929.

25. Wu, Q. and Wang, Y., "Experimental detection of composite delamination damage based on ultrasonic infrared thermography", *International Journal of Engineering, Transactions B: Applications* Vol. 27, No. 11, (2014), 1723-1730. doi: 10.5829/idosi.ije.2014.27.11b.10.

26. Sprenger, W., Gruttmann, F. and Wagner, W., "Delamination growth analysis in laminated structures with continuum-based 3d-shell elements and a viscoplastic softening model", *Computer Methods in Applied Mechanics and Engineering*, Vol. 185, No. 2-4, (2000), 123-139. doi: 10.1016/S0045-7825(99)00255-8.

27. Saboori, B. and Moshrefzadeh-sani, H., "A continuum model for stone-wales defected carbon nanotubes", *International Journal of Engineering*, Vol. 28, No. 3, (2015), 433-439. doi: 10.5829/idosi.ije.2015.28.03c.13.

28. Gobbi, G., Colombo, C. and Vergani, L., "A cohesive zone model to simulate the hydrogen embrittlement effect on a high-strength steel", *Frattura ed Integrità Strutturale*, Vol. 10, No. 35, (2016), 260-270. doi: 10.3221/IGF-ESIS.35.30.

29. Shafeek, H., Gadelmawla, E., Abdel-Shafy, A. and Elewa, I., "Assessment of welding defects for gas pipeline radiographs using computer vision", *NDT & e International*, Vol. 37, No. 4, (2004), 291-299. doi: 10.1016/j.ndteint.2003.10.003.

30. Benzerga, D., "Burst pressure estimation of corroded pipeline using damage mechanics", in Conference on Multiphysics Modelling and Simulation for Systems Design, Springer., (2014), 481-488.

31. Chausov, M., Maruschak, P., Pylypenko, A. and Sorochak, A., Effect of impact-oscillatory loading on the variation of mechanical properties and crack resistance of pipe steel, in Degradation assessment and failure prevention of pipeline systems. 2021, Springer.189-201.

Persian Abstract

چکیده

تست های هیدرواستاتیک پس از تحقق تاسیسات مشمول مقررات از جمله: سازه های متمرکز، لوله ها، لوله کشی، تجهیزات استاتیک، مخازن تحت فشار، مخازن و غیره از اهمیت بالایی برخوردار است. بازرسی جوش ها اغلب با آزمایش هیدرواستاتیک با فشار ۱.۵ برابر فشار سرویس تضمین می شود و در حضور ضروری نماینده ARH (مرجع تنظیم کننده هیدروکربن ها) انجام می شود. تجهیزات تحت فشار تحت بازرسی NDT (تست غیر مخرب) برای تأیید اجرای صحیح جوش ها و آزمایش هیدرواستاتیک برای تأیید یکپارچگی آنها قرار می گیرند. تکنسین ها با محدودیت های زیادی در جداسازی تجهیزات مواجه می شوند تا آن ها را در اختیار بخش تست هیدرواستاتیک قرار دهند. بنابراین کاملاً واضح است که آزمایشات هیدرواستاتیکی یک ناراحتی واقعی برای مدیریت سازه های جوش داده شده است. هدف از این کار نشان دادن این است که تکنیک‌های بازرسی NDT با شبیه‌سازی‌های عددی می‌تواند یک راه‌حل جایگزین برای جایگزینی آزمایش‌های هیدرواستاتیکی باشد. برنامه ای در APDL در کد Ansys برای شبیه سازی وابستگی رابط (شامل/ماتریس) و تأثیر آن بر رفتار ماکروسکوپی سازه توسعه یافته و پیاده سازی شده است.

International Journal of Engineering

Journal Homepage: www.ije.ir

Structural and Optical Properties of Bismuth-doped ZnO Nanoparticles Synthesized by Co-precipitation

C. Sermsrithong, P. Jaidaew, C. Promjantuk, P. Buabthong*

Physics and General Science Program, Faculty of Science and Technology, Nakhon Ratchasima Rajabhat University, Bangkok, Thailand

A B S T R A C T

Bismuth-doped zinc oxide (ZnO) nanoparticles can serve as efficient photocatalysts for various reactions. Herein, we synthesized and discussed the growth mechanisms of Bi-doped ZnO nanoflakes using co-precipitation with Bi concentrations ranging from 0 to 3 %. The resulting ZnO were hexagonal nanosheets with diameters ranging from 80 nm (ZnO) to 200 nm (ZnO: Bi 3%). The dominant crystal structure matches hexagonal wurtzite with a small presence of Bi_2O_3 diffraction peaks. The estimated crystallite sizes range from ~ 33 nm to ~ 45 nm, indicating multiple crystalline regions in each nanoflake. Nevertheless, as sheet resistance monotonically decreases with the Bi concentration, the higher number of grain boundaries likely has a lower effect on the conductivity compared to an increase in free carriers and larger grain size in the samples with higher Bi concentration. The bandgap decreases from ~ 3.13 eV to ~ 2.96 eV, likely due to the shrinkage effect from electron-electron or electron-impurity interaction that lowers the conduction band of ZnO.

doi: 10.5829/ije.2022.35.12c.10

NOMENCLATURE

D	Crystallite size	λ	Wavelength of the X-ray
θ	Diffracting angle	β	Full-width half-max of the diffracting peak

1. INTRODUCTION

Zinc oxide (ZnO) has been one of the most versatile materials with applications ranging from optoelectronics to photocatalysis. Among different forms of ZnO, nanoparticles can provide a higher surface area, which increases the number of active sites for the reactions compared to thin films or other 2D bulk surfaces, particularly useful for catalytic applications [4]. ZnO nanoparticles have been prepared by various techniques, including sol-gel method [5], electrophoretic deposition [6], hydrothermal methods [7], thermal decomposition [8, 9], chemical vapor deposition [10], and co-precipitation [11]. Co-precipitation is considered one of the most straightforward and affordable techniques due to its minimal setup and fewer chemical precursors involved in the process; while also allowing for

incorporating dopants to vary the electronic properties [12].

Since the surface area of the nanoparticles can highly influence the catalytic performance, different morphologies of the ZnO nanoparticles have been investigated, including nanorods [13], nanospheres [9], nanoplates [14], and nanowires [15]. In particular, ZnO nanosheets have been reported to exhibit better catalytic performance because of their higher number of polar facets [16, 17], which would likely be beneficial to reactions in aqueous solutions.

In addition, to further improve the photocatalytic activity of the ZnO nanoparticles, dopants are typically introduced to increase the absorption as well as potentially enhance the charge transfer on the surface. Particularly, bismuth has been used in catalytic applications, either as the cation in mixed oxide catalysts [18], or the dopant [3]. Bi dopant has been reported to

Corresponding Author Institutional Email: pakpoom.b@nrru.ac.th
(P. Buabthong)

lower the bandgap of ZnO nanocatalysts [19] and accelerate the interfacial electron transfer process, thus enhancing the photocatalytic activity under UV illumination [3]. Nevertheless, the growth mechanisms of Bi-doped ZnO nanosheet using co-precipitation is still not well investigated.

Herein, we present an investigation of the structural and optical properties of Bi-doped ZnO nanoparticles using a simple co-precipitation technique. Specifically, the procedure was optimized to produce hexagonal ZnO nanosheets. We also further discuss the formation mechanisms of these particles as well as the possible factors affecting the optoelectronic properties of the ZnO samples.

2. MATERIALS AND METHODS

All chemicals were used as received, including zinc acetate hydrate ($Zn(CH_3COO)_2 \cdot 2H_2O$, AR Grade), bismuth nitrate pentahydrate ($BiN_3O_9 \cdot 5H_2O$, AR Grade), sodium hydroxide (NaOH, AR Grade), ethanol (C_2H_6O). Deionized water with a resistivity $\rho > 18$ M$\Omega \cdot$cm was used for the dilution processes. The zinc precursors were prepared using 0.5M of zinc acetate hydrate. For the dopant, bismuth nitrate pentahydrate was introduced to the zinc solution ranging from 0 to 3 wt% weighed using a high-precision digital scale with a sensitivity of 0.001 g, then rigorously mixed at room temperature for 15 min.

To initiate the co-precipitation process, 2.5M NaOH was gradually dropped into the zinc-bismuth solution while continuously stirring until the mixture reached pH = 13. The pH was monitored using a pH meter with a sensitivity of pH = 0.01, and the value was allowed to stabilize for 30 s after each NaOH addition. The solution was kept stirred for 15 min at room temperature. The precipitate was rigorously rinsed with DI water, vacuum dried, and rinsed again with ethanol before annealed at 80°C for 8 hours, then heated at 550°C for 2 hours to form zinc oxide nanoparticles.

The samples were then characterized for their optical and structural properties. Scanning electron micrographs (SEMs) were obtained with a Carl Zeiss AURIGA at an accelerating voltage of 3.00 kV with a working distance of 7.5 mm. X-ray Diffractometry (XRD) was performed using Bruker D2 Phaser with a Cu Kα monochromator with an x-ray wavelength of 1.54060 Å using 2θ angles ranging from 10° to 90°. UV-Vis spectrometer was utilized to obtain the absorption spectra at the wavelength ranging from 200 nm to 1000 nm.

For sheet resistance measurement, the nanoparticles were screen painted onto 1x1 cm glass slides and were characterized using Jandel RM3-AR four-point probe with an operating current of 10 mA.

3. RESULTS AND DISCUSSION

As-synthesized ZnO nanoparticles were first inspected for surface morphology. Figures 1(a)-1(f) show the SEM images of ZnO samples with bismuth concentration of (a) 0 %, (b) 1 %, (c) 1.5 %, (d) 2 %, (e) 2.5 % and (f) 3 %. In all concentrations, the ZnO nanoparticles were formed into hexagonal nanoflakes, showing higher contrast, and sharper morphology as the bismuth concentration increased, with the average flake diameter ranging from 80 nm (ZnO) to 200 nm (ZnO: Bi 3%). The hexagonal shape of the particle is likely due to the preferred deposition along the *a*-axis of the ZnO lattice as supposed to the other common nanorod where the deposition would be preferred along the *c*-axis. Only the local structure and the facet of the particles were assumed to have any effects on the growth orientation. The transport of the precursor ion could potentially affect the growth, but were assumed to have a minimal influence in this environment. This preferential deposition along the *a*-axis can most likely be attributed to the strong local environment (pH = 13) around the initial nucleation site of the particle, where the excess OH$^-$ leads to the formation of zinc hydroxide complex $Zn(OH)_4^{2-}$ from the Zn^{2+}, that was dissociated from the zinc acetate hydrate precursor. The negatively charged zinc hydroxide complex was then repelled from the negative surface of ZnO along the *c*-axis (100) orientation, thus resulting in more prominent 2D hexagonal flakes. This preferential growth on the 2D
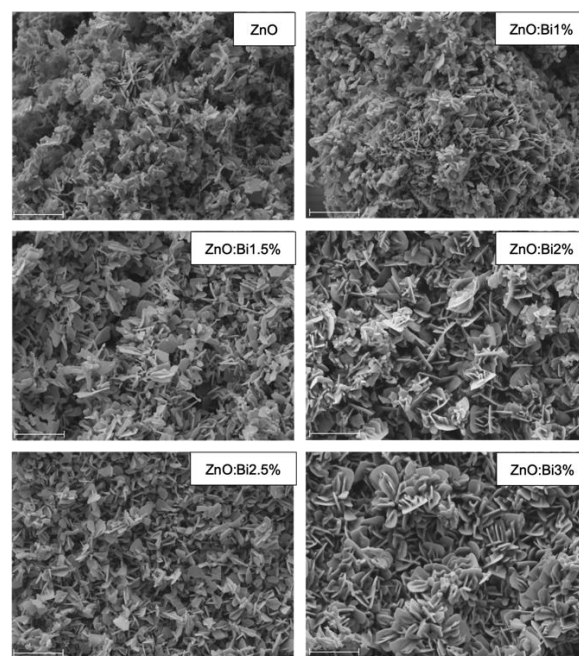
Figure 1. Scanning electron micrographs of ZnO with Bi concentration ranging from 0% to 3%, with the scalebar representing 1 µm

plane is also likely more observable in the co-precipitation technique, where the deposition mechanisms rely heavily on diffusion and adsorption of the precursors.

In addition, larger hexagonal flakes and the shaper 2D morphology were observed as higher Bi concentration was introduced. The positively charged Bi^{3+} from the bismuth nitrate precursor likely creates a more favorable local deposition environment at the ZnO sites, assisting the oxidation of the zinc hydroxide complex around the edge of the nanosheet. This preferred deposition can also be observed from having less residual deposition in other orientations in the samples with lower Bi concentration (Figure 1: ZnO and ZnO: Bi1%).

Figure 2 shows XRD patterns of the as-prepared Bi-doped ZnO nanoparticles with different Bi concentrations. The peaks at $2\theta=\sim27.5°$ and $\sim33.2°$ represent the Bi_2O_3 peaks which can be observed in all samples except ZnO with no Bi dopant [20]. The main diffracting peaks were observed for the (100), (002), and (101) orientation of wurtzite ZnO at $2\theta = 31.8°$, $34.6°$, and $36.4°$, respectively, with the remaining peaks corresponding to the (102), (110), (103), and (112) orientation [21]. The locations of the diffraction peaks match precisely with the standards as well as the ZnO particles with different morphology and different preparation techniques [9]. The intensities of the diffraction peaks are all comparable even with increasing Bi concentration, indicating that the amount of the Bi dopant in the lattice is not sufficient to have any effect on the overall crystal structure of the ZnO host. The intensity of the (002) peak is comparable to that of (100), suggesting growth along the planar axis, [22] which is in good accord with the observed morphology (Figure 1).

Table 1 summarizes the crystallite size (D) estimated from the XRD pattern (Figure 2) using Scherrer's equation:

$$D = \frac{0.94\lambda}{\beta \cos\theta} \qquad (1)$$

TABLE 1. Estimated crystallite size using Scherrer's equation

ZnO:Bi (%)	Crystalline size (nm)
0	33.58
1	41.79
1.5	41.95
2	42.06
2.5	42.53
3	44.65

where λ is the x-ray wavelength, β is the full-width half max (FWHM), and θ is the Bragg diffraction angle. The crystallite size monotonically increases with the Bi concentration, agreeing with more favorable deposition environment under the presence of Bi^{3+} cation. Nevertheless, the crystallite size is still substantially smaller than the size of each hexagonal nanoflake (Figure 1), suggesting that each flake may consist of multiple crystallites. Moreover, the average diameter of the flake increases by more than twice from ~ 80 nm to ~ 200 nm, while the estimated crystallite size increases from ~ 33 nm to ~ 45 nm, indicating that new nucleation sites on each nanosheet could be developed during the deposition, especially on the larger flakes and higher Bi concentration.

In addition, the distribution of the crystalline region in the sample also has a strong influence on the resistance. Since electronic conduction relies predominantly on the transport of free carriers in the sample, larger grain size typically leads to lower sheet resistance, while grain boundaries between multiple crystallites usually increase the sheet resistance. Figure 3 shows the sheet resistance of the ZnO nanoparticles with different Bi concentrations. The measured resistance monotonically decreases from $\sim 58 \ \Omega$ sq^{-1} in an undoped ZnO to $\sim 20 \ \Omega$ sq^{-1} in the 3%-doped ZnO. The reduction in sheet resistance with higher Bi concentration is likely

Figure 2. X-ray diffractometry patterns of Bi-doped ZnO with Bi concentration 0% to 3%
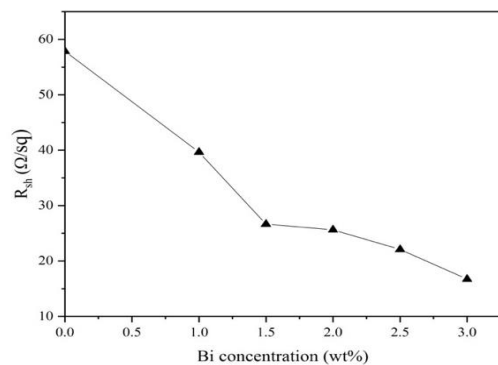
Figure 3. Sheet resistance of the ZnO nanoparticles as a function of Bi concentrations

due to an increase in free electrons from Bi^{3+} donors in the lattice. Although the conductivity was previously reported to decrease at specific Bi concentrations because of the segregation of Bi atoms at the grain boundaries [23], the monotonic decrease in the observed resistance suggests that the Bi concentration used in this experiment is still low or the grain boundary resistance is negligible at this scale.

The absorbance of the nanoparticles was measured with the wavelength sweeping from 350 nm to 800 nm, shown in Figure 4, which gradually increases and peaks at ~ 370 nm for all samples, then slowly decreases to the baseline. Similar peak positions at ~ 370 nm have also been observed in other study as the hexagonal wurtzite phase [24]. These absorbance spectra were then used to calculate the bandgap of the ZnO samples with Tauc relation [25]:

$$\alpha h v = E(h v - E_g)^{\frac{1}{2}} \qquad (2)$$

where α is the optical absorption coefficient from Figure 4, $h v$ is the photon energy, E_g is the bandgap, E is a fitting constant, and the power of $\frac{1}{2}$ indicating direct bandgap transition of ZnO. Figure 5(a) shows the example Tauc plot using the absorption from the undoped ZnO sample, with the straight line extrapolated from the right regime of the curve and the x-intercept of this line representing the derived bandgap of the material. Figure5(b) shows the calculated bandgap with varying Bi
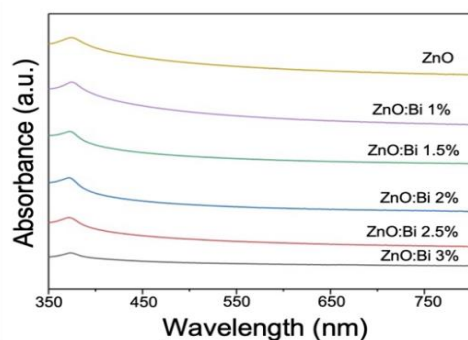
Figure 4. Absorbance of the ZnO nanoparticles as a function of wavelength
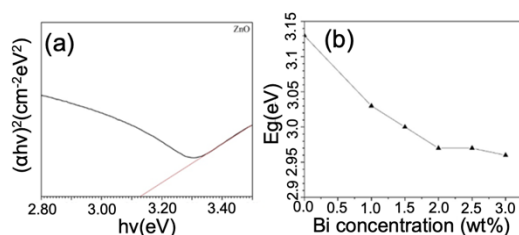
Figure 5. (a) Tauc plot of ZnO nanoparticles and (b) Bandgap of the ZnO nanoparticles as a function of Bi concentrations

concentration, where the bandgap decreases sharply from 0 % to 2 %, then remains relatively constant between 2 % to 3 %. The decrease can primarily be attributed to the shrinkage effect, which results in a lowering of the conduction band due to the net attractive interaction between electron-electron and electron-impurity interaction. Nevertheless, the more minor change after 2% dopant is likely due to fluctuation that comes from both the broadening of the valence band as well as the lowering of the conduction band [26–28].

4. CONCLUSIONS

Bi-doped ZnO nanoparticles were successfully prepared using co-precipitation using minimal laboratory setup. The morphology of the nanoparticles reveals that hexagonal nanosheets were produced, mostly by maintaining high alkalinity of the solution, with the average diameter increasing from 80 nm to 200 nm with higher Bi concentration. The wurtzite structure was observed, with the average crystallite size ranging from ~ 33 nm to ~ 45 nm, suggesting multiple crystalline regions in each nanoflake. Nevertheless, grain boundary resistance likely has minimal effect on the conductivity of the free carriers in these particles, as the sheet resistance decreases monotonically with the dopant concentration. The decrease in the optical bandgap with higher Bi concentration is likely due to the shrinkage effect from the electron-electron and electron-impurity interaction that leads to the lowered conduction band. However, the decrease of the bandgap gradually diminishes as the Bi concentration is > 2 %. These results show co-precipitation as a viable technique to synthesize Bi-doped ZnO nanosheets that exhibit optoelectronic and structural properties similar to those prepared using more sophisticated techniques. Nevertheless, further precise optimization of the electronic properties such fine-tuning the absolute band edge positions might require a more advance technique such as chemical vapor deposition.

5. ACKNOWLEDGMENT

6. REFERENCES

1.   Lokhande, B. J., and Uplane, M. D. "Structural, optical and electrical studies on spray deposited highly oriented ZnO films." *Applied Surface Science*, Vol. 167, No. 3-4, (2000), 243-246. https://doi.org/10.1016/S0169-4332(00)00533-X

2. Kang, Y., Yu, F., Zhang, L., Wang, W., Chen, L., and Li, Y. "Review of ZnO-based nanomaterials in gas sensors." *Solid State Ionics*, Vol. 360, (2021), 115544. https://doi.org/10.1016/j.ssi.2020.115544

3. Chandraboss, V. L., Natanapatham, L., Karthikeyan, B., Kamalakkannan, J., Prabha, S., and Senthilvelan, S. "Effect of bismuth doping on the ZnO nanocomposite material and study of its photocatalytic activity under UV-light." *Materials Research Bulletin*, Vol. 48, No. 10, (2013), 3707-3712. https://doi.org/10.1016/j.materresbull.2013.05.121

4. Siddiqi, K. S., ur Rahman, A., Tajuddin, and Husen, A. "Properties of Zinc Oxide Nanoparticles and Their Activity Against Microbes." *Nanoscale Research Letters*, Vol. 13, No. 1, (2018), 141. https://doi.org/10.1186/s11671-018-2532-3

5. Vaezi, M. R., and Zameni, M. "Synthesis of zinc oxide nanostructured thin film by sol-gel method and evaluation of gas sensing properties." *International Journal of Engineering, Transactions B: Applications*, Vol. 27, No. 5, (2014), 757-762. https://doi.org/10.5829/idosi.ije.2014.27.05b.11

6. Lommens, P., van Thourhout, D., Smet, P. F., Poelman, D., and Hens, Z. "Electrophoretic deposition of ZnO nanoparticles, from micropatterns to substrate coverage" *Nanotechnology*, Vol. 19, No. 24, (2008), 245301. https://doi.org/10.1088/0957-4484/19/24/245301

7. Bulcha, B., Leta Tesfaye, J., Anatol, D., Shanmugam, R., Dwarampudi, L. P., Nagaprasad, N., Bhargavi, V. L. N., and Krishnaraj, R. "Synthesis of Zinc Oxide Nanoparticles by Hydrothermal Methods and Spectroscopic Investigation of Ultraviolet Radiation Protective Properties." *Journal of Nanomaterials*, Vol. 2021, (2021), 1-10. https://doi.org/10.1155/2021/8617290

8. Hajiashrafi, S., and Motakef Kazemi, N. "Preparation and evaluation of ZnO nanoparticles by thermal decomposition of MOF-5." *Heliyon*, Vol. 5, No. 9, (2019), e02152. https://doi.org/10.1016/j.heliyon.2019.e02152

9. Darezereshki, E., Vakylabad, A. B., and Yousefi, M. "Chemical process of synthesizing zinc oxide (ZnO) with nanorod and spherical morphologies." *International Journal of Engineering, Transactions B: Applications*, Vol. 34, No. 8, (2021), 1888-1897. https://doi.org/10.5829/ije.2021.34.08b.10

10. Reuge, N., Bacsa, R., Serp, P., and Caussat, B. "Chemical Vapor Synthesis of Zinc Oxide Nanoparticles: Experimental and Preliminary Modeling Studies." *The Journal of Physical Chemistry C*, Vol. 113, No. 46, (2009), 19845-19852. https://doi.org/10.1021/jp9070955

11. Purwaningsih, S. Y., Zainuri, M., Triwikantoro, T., Pratapa, S., and Darminto, D. "Structural, optical and defect state analyses of ZnO nanoparticle films." *International Journal of Engineering, Transactions B: Applications*, Vol. 33, No. 5, (2020), 852-860. https://doi.org/10.5829/IJE.2020.33.05B.17

12. Priscilla, S. J., Judi, V. A., Daniel, R., and Sivaji, K. "Effects of Chromium Doping on the Electrical Properties of ZnO Nanoparticles." *Emerging Science Journal*, Vol. 4, No. 2, (2020), 82-88. https://doi.org/10.28991/esj-2020-01212

13. Wang, T. X., and Lou, T. J. "Solvothermal synthesis and photoluminescence properties of ZnO nanorods and nanorod assemblies from ZnO_2 nanoparticles." *Materials Letters*, Vol. 62, No. 15, (2008), 2329-2331. https://doi.org/10.1016/j.matlet.2007.11.083

14. Jang, J. S., Yu, C.-J., Choi, S. H., Ji, S. M., Kim, E. S., and Lee, J. S. "Topotactic synthesis of mesoporous ZnS and ZnO nanoplates and their photocatalytic activity." *Journal of Catalysis*, Vol. 254, No. 1, (2008), 144-155. https://doi.org/10.1016/j.jcat.2007.12.010

15. Ding, Y., and Wang, Z. L. "Structures of planar defects in ZnO nanobelts and nanowires." *Micron*, Vol. 40, No. 3, (2009), 335-342. https://doi.org/10.1016/j.micron.2008.10.008

16. Hsu, Y.-K., Lin, Y.-G., and Chen, Y.-C. "Polarity-dependent photoelectrochemical activity in ZnO nanostructures for solar water splitting." *Electrochemistry Communications*, Vol. 13, No. 12, (2011), 1383-1386. https://doi.org/10.1016/j.elecom.2011.08.016

17. Sun, J., Cao, J., and Jiang, X. "Preparation and photoelectric properties of Bi doped ZnO nanoarrays." *Journal of Alloys and Compounds*, Vol. 896, (2022), 162801. https://doi.org/10.1016/j.jallcom.2021.162801

18. Araujo Scharnberg, A. R., Carvalho de Loreto, A., and Kopp Alves, A. "Optical and Structural Characterization of Bi2FexNbO7 Nanoparticles for Environmental Applications." *Emerging Science Journal*, Vol. 4, No. 1, (2020), 11-17. https://doi.org/10.28991/esj-2020-01205

19. Singh, B. K., and Tripathi, S. "Influence of Bi concentration on structural and optical properties of Bi doped p-type ZnO thin films prepared by sol-gel method." *Journal of Materials Science: Materials in Electronics*, Vol. 27, No. 3, (2016), 2360-2366. https://doi.org/10.1007/s10854-015-4033-9

20. Oudghiri-Hassani, H., Rakass, S., al Wadaani, F. T., Al-ghamdi, K. J., Omer, A., Messali, M., and Abboudi, M. "Synthesis, characterization and photocatalytic activity of α-Bi_2 O_3 nanoparticles." *Journal of Taibah University for Science*, Vol. 9, No. 4, (2015), 508-512. https://doi.org/10.1016/j.jtusci.2015.01.009

21. Arefi, M. R., and Rezaei-Zarchi, S. "Synthesis of Zinc Oxide Nanoparticles and Their Effect on the Compressive Strength and Setting Time of Self-Compacted Concrete Paste as Cementitious Composites." *International Journal of Molecular Sciences*, Vol. 13, No. 4, (2012), 4340-4350. https://doi.org/10.3390/ijms13044340

22. Ebrahimifard, R., Abdizadeh, H., and Golobostanfard, M. R. "Controlling the extremely preferred orientation texturing of sol-gel derived ZnO thin films with sol and heat treatment parameters." *Journal of Sol-Gel Science and Technology*, Vol. 93, No. 1, (2020), 28-35. https://doi.org/10.1007/s10971-019-05157-2

23. Chouikh, F., Beggah, Y., and Aida, M. S. "Optical and electrical properties of Bi doped ZnO thin films deposited by ultrasonic spray pyrolysis." *Journal of Materials Science: Materials in Electronics*, Vol. 22, No. 5, (2011), 499-505. https://doi.org/10.1007/s10854-010-0167-y

24. Wahab, R., Ansari, S. G., Kim, Y. S., Song, M., and Shin, H.-S. "The role of pH variation on the growth of zinc oxide nanostructures." *Applied Surface Science*, Vol. 255, No. 9, (2009), 4891-4896. https://doi.org/10.1016/j.apsusc.2008.12.037

25. Makuła, P., Pacia, M., and Macyk, W. "How To Correctly Determine the Band Gap Energy of Modified Semiconductor Photocatalysts Based on UV-Vis Spectra." *The Journal of Physical Chemistry Letters*, Vol. 9, No. 23, (2018), 6814-6817. https://doi.org/10.1021/acs.jpclett.8b02892

26. Auvergne, D., Camassel, J., and Mathieu, H. "Band-gap shrinkage of semiconductors." *Physical Review B*, Vol. 11, No. 6, (1975), 2251-2259. https://doi.org/10.1103/PhysRevB.11.2251

27. Yildiz, A., Ozturk, E., Atilgan, A., Sbeta, M., Atli, A., and Serin, T. "An Understanding of the Band Gap Shrinkage in Sn-Doped ZnO for Dye-Sensitized Solar Cells." *Journal of Electronic Materials*, Vol. 46, No. 12, (2017), 6739-6744. https://doi.org/10.1007/s11664-017-5778-0

28. Keskenler, E. F., Aydın, S., Turgut, G., and Doğan, S. "Optical and Structural Properties of Bismuth Doped ZnO Thin Films by Sol-Gel Method: Urbach Rule as a Function of Crystal Defects." *Acta Physica Polonica A*, Vol. 126, No. 3, (2014), 782-787. https://doi.org/10.12693/APhysPolA.126.782

Persian Abstract

چکیده

نانوذرات اکسید روی دوپ شده با بیسموت (ZnO)می توانند به عنوان فوتوکاتالیست کارآمد برای واکنش های مختلف عمل کنند. در اینجا، ما مکانیسم‌های رشد نانوفلکه‌های اکسید روی دوپه‌شده را با استفاده از رسوب همزمان با غلظت‌های بی از ۰ تا ۳ درصد سنتز و مورد بحث قرار دادیم. ZnO حاصل، نانوصفحات شش ضلعی با قطرهای ۸۰ نانومتر (ZnO)تا ۲۰۰ نانومتر (ZnO: Bi 3%)بود. ساختار کریستالی غالب با ورتزیت شش ضلعی با حضور کمی از قله های پراش Bi₂O₃ مطابقت دارد. اندازه کریستالیت تخمین زده شده از ۳۳ نانومتر تا ٤٥ نانومتر متغیر است که نشان دهنده چندین ناحیه کریستالی در هر نانوفلکه است. با این وجود، از آنجایی که مقاومت ورق به طور یکنواخت با غلظت Bi کاهش می یابد، تعداد بیشتر مرزهای دانه احتمالاً تأثیر کمتری بر هدایت در مقایسه با افزایش حامل های آزاد و اندازه دانه بزرگتر در نمونه های با غلظت Bi بالاتر دارد. فاصله باند از ~ eV ۳.۱۳ به ~ eV ۲.۹٦ کاهش می یابد، که احتمالاً به دلیل اثر انقباض ناشی از برهمکنش الکترون–الکترون یا الکترون–ناخالصی است که نوار رسانایی ZnO را کاهش می دهد.

International Journal of Engineering

Effects of Inflation Pressure and Wall Thickness on Gripping Force of Semi-Cylindrical Shaped Soft Actuator: Numerical Investigation

D. Doreswamy[a], S. S. Menon[a], J. M. D'Souza[a], S. K. Bhat[*b]

[a] Department of Mechatronics, Manipal Institute of Technology, Manipal Academy of Higher Education, Manipal, Karnataka, India
[b] Department of Mechanical and Manufacturing Engineering, Manipal Institute of Technology, Manipal Academy of Higher Education, Manipal, Karnataka, India

A B S T R A C T

Soft robotics using Pneumatic Network actuators (Pneu-Net) is a developing field that has a promising future for variety of applications involving delicate operations such as biomedical assistance. The interaction between geometry and the performance of the actuator is an important topic which has been studied by many researchers in this field. However, there is a lack of investigation on the relationship between gripping capability and geometrical parameters of soft actuators. Especially, there is a need to shed more light on the effects of wall thicknesses on the gripping force developed. In the present study, a semi-cylindrical chambered PneuNet soft actuator is numerically investigated to evaluate the effects of pressure and wall thickness variations on its performance characteristics. The results revealed that increasing the restraining layer thickness (RLT) aids the bending capability of the actuator whereas increasing the chamber wall thickness reduces it. Therefore, maximum bending of the actuator is achieved at the combinations of minimum wall thickness and maximum RLT. At these geometrical configurations of maximum bending, the deformation-pressure relationships followed a sigmoidal function and tended towards linearity with increasing wall thickness and decreasing RLT. The gripping force showed an exponential increase with increasing working pressures and wall thicknesses. The maximum gripping force increased cubically with increasing wall thicknesses at their respective maximum working pressures, which was modeled using a polynomial regression model (R^2=99.79%).

doi: 10.5829/ije.2022.35.12c.11

1. INTRODUCTION

Robotics is a vast area that caters to various domains and applications including automobile engineering, biomedical engineering, and so on. Conventionally, the robots are made up of rigid materials which are suited for handling hard materials. These robots can be used to perform robust and intensive tasks. However, they are not applicable for tasks that require a soft and feather touch or need to interact with delicate organisms or objects in their workspace. Such gentle tasks can be taken up by robots made up of soft, rubber-like materials. A wide array of applications is possible for such robots, such as medical and exploration fields where the traditional robots cannot be easily employed because of the rigid

connections and joints that they are made up of. Also, soft robots can be applied to work alongside humans without causing any harm to those working in proximity. For instance, honeycomb structures can provide a larger deformation with a relatively lesser quantity of material. Further, different types of materials can be utilized according to the load carrying capability and usability criteria of the soft robots. It is observed that there are various methods of actuation that can be used in accordance with the use case and the materials used [1].

Soft robotics can be utilized for various biomedical applications, and can assist in sensitive and intricate surgical procedures while reducing the human induced errors [2]. Wearable soft robots can be developed to aid in the rehabilitation process providing a much better

*Corresponding Author Institutional Email: sk.bhat@manipal.edu (S. K. Bhat)

recovery rate and long-term usage. A wide variety of soft actuators have been developed for biomedical applications [3]. Soft robots that mimic human organs need to be made of compliant materials which respond to natural stimuli [2]. Various combinations of materials and actuation methods can be used to solve certain types of use cases. Apart from the complex applications such as mimicking human organs and animal motions, soft robots can also perform picking and placing operations. Zheng et al. [4] developed a soft robot inspired by the water animal, Ascidian, capable of performing pick-and-place operations such as drug-release tasks in millimeter scale. Such robots can be used for exploration and interaction with different organisms. Several gripping technologies exist which can be used for simple cases [5]. It is observed that the most common method of actuation is by application of air or fluidic pressure in the internal chambers of the actuators, which are known as Pneumatic Networks or PneuNets [6]. The major point of focus of the present study is to develop a gripper using soft materials that be used to pick-and-place sensitive objects without damaging them.

One of the most fascinating use cases of Pneumatic Networks is the creation of rehabilitation gloves that are used for fine movements of the hands during physiotherapy after a serious injury. It is observed that the use of soft robots provides a more comfortable and quicker recovery than the traditional rigid methods. The finger-like structure consists of internal chambers that can be filled with fluid or air. As the fluidic pressure increases through the tubular structures, the finger-like structure begins to bend, aiding in the bending of the human hands of the user undergoing physiotherapy. This type of therapy is used to regain the lost motion of fingers after serious injuries. Numerous grippers are being tested and compiled to obtain the required characteristics with a large variety of possible actuations [5]. Pneumatically operated grippers have been explored for industrial applications to increase productivity of transporting operations [7-9]. Researchers have developed advanced control systems and machine learning based tools for biomedical applications and for enhancing the learning process of students in educational institutes [10,11].

Numerous materials can be used to create soft robots as explained in works conducted by Rossiter et al. [12], Shen et al. [13], Manti et al. [14] and Wu et al. [15]. The actuation methods can be modified based on material properties as discussed by Hughes et al. [16] and Bira et al. [17]. The materials used can define the use case and the limits of the robot. This has been realized and optimized in the works introduced by Mosadegh et al. [18] and Yan et al. [19]. The most common materials used for PneuNet based soft grippers are usually elastomers and they have a wide range of applications as seen in research conducted by Zhou and Li [20], Liu et al. [21]. For simulations and analyses, these materials are considered as hyperelastic materials. Hyperelastic materials exhibit nonlinear stress-strain relationships and tend to retain their shape after the removal of external forces and can undergo numerous loading and unloading cycles without undergoing plastic deformation.

The structure of the actuator chamber plays an important role on the nature of deformations exhibited in literature [7,22,23]. The major mode of actuation that is being developed and in focus for actuation in the present paper is the pneumatic network with reference to works conducted by Honarpardaz [24]. These consist of multiple pneumatic chambers that can be in series or parallel connection to each other. On application of pneumatic pressure in these chambers, it expands applying pressure on the restraining layer causes a bending motion, which is used to actuate and carry out the gripping mechanism. The restraining layer can consist of a different material or can be implemented by increasing the thickness of the layer [25]. The absence of this restraining layer causes the actuator to expand radially and laterally without undergoing bending. The geometry and the size of the internal pneumatic chamber define the bending and gripping force of the developed gripper [26]. Also, the direction of expansion is majorly defined by the geometry of the individual chambers.

From the literature review on geometrical aspects of soft actuators it is observed that, comparatively fewer studies have investigated the semi-cylindrical shaped actuators [27-30]. Among these studies, Tan et al. [28] and Wang et al. [30] experimentally measured the forces generated by the soft gripppers. However, as per the best information of the authors, the effects of restraining layer thicknesses on the gripping force generation has not been investigated. In this perspective, the gripping force and deformation characteristics of soft actuators can be modified by varying the wall thicknesses and the pneumatic actuation pressure. Thus, the present study focused on the numerical investigation of a semi-cylindrical silicone-based soft actuator by varying each parameter individually while keeping the remaining parameters constant to understand the effect of the corresponding parameter on its deformation characteristics. Based on the results obtained with the variations of the parameters, a suitable configuration of the parameters can be chosen depending on the application where the soft robot is being employed. Further, the working pressure for such robots and the critical pressure above which they may malfunction can also be determined. Thus, the present study aims to arrive at a comprehensive understanding of the characteristics of a semi-cylindrical silicone-based soft actuator. Based on these results, a suitable actuator can then be developed in a robust and systematic manner according to the deformation characteristics and the gripping force requirements of specific applications.

2. MATERIALS AND METHODS

2. 1. Hyperelastic Material Model For the simulation and analysis of the soft robotics structures, the materials are considered as hyperelastic in nature. These materials deform and later with the removal of the pressure return to their original shape, i.e., they do not undergo any plastic deformation. They can undergo such deformation cycles numerous times without undergoing permanent deformations. Various hyperelastic material models can be used to predict the stress-strain curve closely to the original curve [31]. Selection of a hyperelastic model involves a choice between complexity of models with higher number of material parameters which help in precise fitting to experimental data and on the other hand simple models with stable and acceptable results with reasonable accuracy. Compared to other models, Yeoh model is found to be efficient in this regard because of its simplicity, smaller number of material parameters and ability to describe multi-axial deformation behaviors [32]. In the present study, the 2nd order Yeoh hyperelastic model was used for the simulations [33] as shown in Equation (1).

$$W = \sum_{i=1}^{2} C_i (I_1 - 3)^i + D[compression\ term] \qquad (1)$$

where, W is the strain-energy potential, I_1 is the first invariant of the right Cauchy-Green deformation tensor, and C_i are the material constants. By assuming incompressibility of the material, the compression term is taken to be null. The order of series expansion can be done based on the number of terms required to represent the experimental deformation characteristics. The material constants of the Yeoh 2nd order model used in the present numerical investigation with the constant values stated in Table 1 [34]. Using the strain-energy expression of Equation (1), the stress-strain relationship under uniaxial loading can be obtained as follows [30].

$$\sigma = \sum_{i=1}^{n} 2C_i \cdot i \cdot (\lambda - \lambda^{-2}) \cdot (\lambda^2 + 2\lambda^{-1} - 3)^{i-1} \qquad (2)$$

where, σ is the Cauchy stress developed, λ is the ratio of deformed length to actual length (1+nominal strain). By substituting the constants in Table 1 in Equation (2), a graph of stress vs strain is plotted (Figure 1). It is observed that with an increase in strain, the rate at which the stress is developed increases.
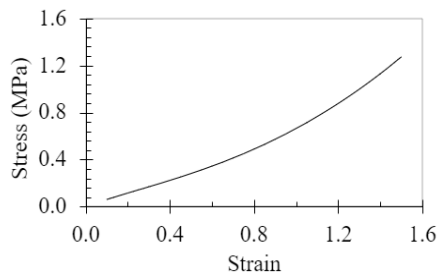
Figure 1. Stress-strain relationship with the Yeoh model

TABLE 1. Material constants of Yeoh model [29]

Constant	Values (MPa)
C_1	0.11
C_2	0.02
D	0

2. 2. Modeling of the Computational Domain and Boundary Conditions As discussed in the Introduction, actuator geometries govern the nature of deformation exhibited the actuators. The "semi-cylinder chamber" type of actuator was chosen for the present study (Figure 2) because of its tendency to curl and bend under the action of pressure through its chambers. The gripping action aimed to be obtained is achieved by curling around an object. The boundary conditions applied are shown in Figure 2. The actuator is considered to be fixed at one end and free at the other end. A static pressure is applied on all the internal faces of the chambers, which is varied between 100 kPa and 350 kPa in the analyses (Figure 2).

Figure 3 shows the details of the geometrical parameters which were varied during the analysis, i.e., the restraining layer thickness (RLT) and wall thickness ((D-d)/2). The total length of the gripper unit (L) measured between the inner faces is kept constant at 150 mm. Table 2 presents the different combinations of dimensions that were considered. The outer radius (D/2) of the structure varies from 8.5 mm to 11.5 mm with a gradual increase of 1 mm. It is observed that with an increase in the wall thickness, the gaps decrease as the total length of the internal chamber remains constant.
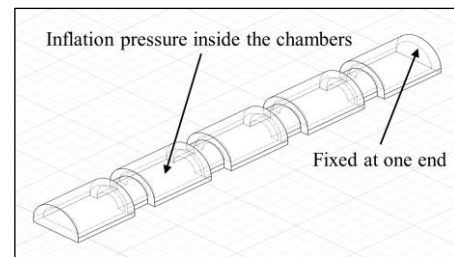
Figure 2. Boundary conditions on the semi-cylindrical actuator gripping unit
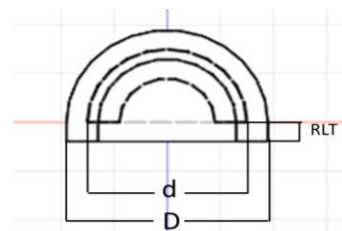
Figure 3. Geometrical parameters varied in the analysis

TABLE 2. Parametric variations of the dimensions (mm)

Sl. no.	L	RLT	d/2	D/2	(D-d)/2
1	150	5	7.5	8.5	2
2	150	5	7.5	9.5	3
3	150	5	7.5	10.5	4
4	150	5	7.5	11.5	5
5	150	2.5	7.5	10	2.5
6	150	5	7.5	10	2.5
7	150	7.5	7.5	10	2.5
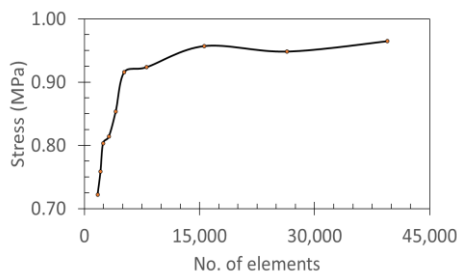
Figure 4. No. of elements vs stress developed

2. 3. Grid-Independence Study The computational domain is discretized using second-order tetrahedral elements. To identify the optimum size of the elements for the numerical analyses, the grid-independence study is conducted. For this purpose, the numerical model is simulated at a pressure of 100 kPa while the element size is varied until a result is obtained which is independent of further refinement of mesh sizing. It is observed from Figure 4 that the results do not show significant difference above 15,000 elements. Thus, the element size for this case, i.e., 0.15 mm was chosen for further numerical analyses which was found to be the optimum mesh size for obtaining satisfactory results.

2. 4. Gripping Force Evaluation The gripping force has to be modulated based on the required application as discussed by Wang et al. [36, 37] and Cacucciolo et al. [38]. The bending of the actuator is postulated to be along the side of the restrain layer [39]. On application of the inflating pressure, the gripping actuator unit undergoes deformation. For this end, the gripping actuator unit (placed on top of the rigid block, shown in Figure 5) is placed on a solid, rigid block made up of structural steel (Figure 5), and the inflating pressure is applied on the actuator. The force generated by the actuator's bottom surface is measured as the resultant reaction force developed at the bottom surface of the rigid block. A methodology (Figure 6) has been proposed in this study to measure the gripping force which is generated by the gripping unit.
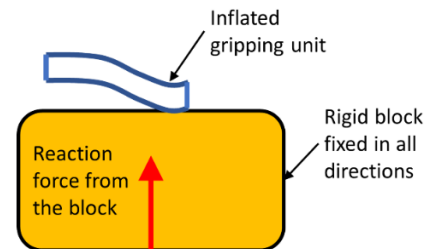
Figure 5. Schematic of FEA for gripping force evaluation
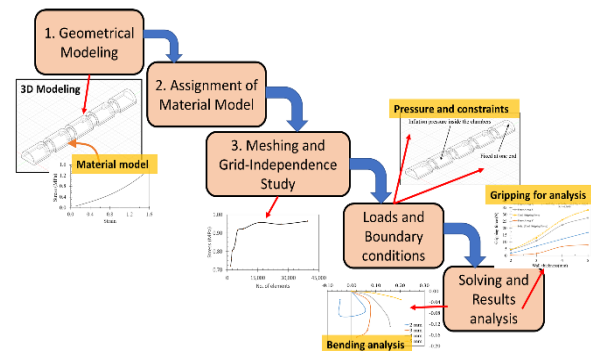
Figure 6. Research methodology of the present study

3. RESULTS AND DISCUSSION

3. 1. Effect of Pressure on Deformation of The Actuator Pneumatic networks operate by deforming on the application of different values of internal pressures. It can be postulated that on increasing the internal pressure the deformation of the structure increases. However, wall thickness and RLT play a key role in deciding the extent and nature of deformation observed. Figures 7(a) and 7(b) show the variations of bending profiles of the actuator with changes in wall thickness and RLT, respectively. It is observed that increasing RLT leads to increased bending whereas increasing the wall thickness leads to reduction in the bending of the actuator. This is because, wall thickness increases the rigidity of the layer; thereby reducing the amount of bending. Thus, a higher RLT and lower wall thickness is advisable for the required gripping mode of the actuator.

Figures 8(a) and 8(b) show the changes in total deformation of the actuator with increase in inflating pressures. In case of variation of wall thickness, the relationship between maximum deformation and pressure is inversely proportional. Thus, it can be inferred that with an increase in the wall thickness the total deformation values decrease proportionally. It is also noted that an increase in wall thickness decreases the nonlinearity of the deformation-pressure relationship. Notably, at 2 mm wall thickness, the total deformation variation follows a sigmoidal curve, and with an increase
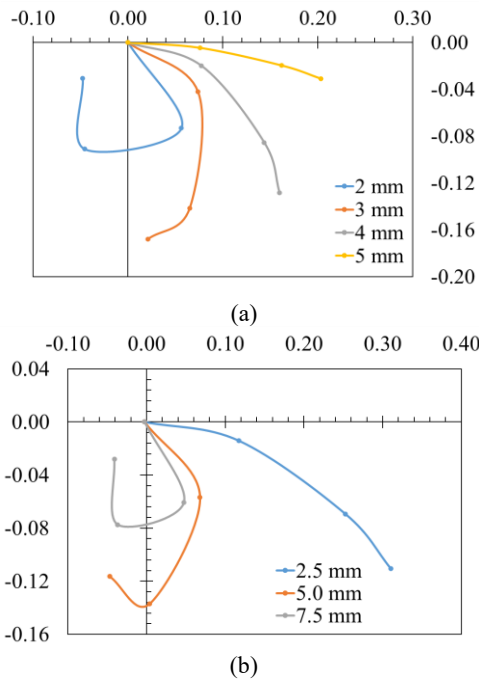
Figure 7. Bending profiles for varying (a) wall thickness and (b) RLT
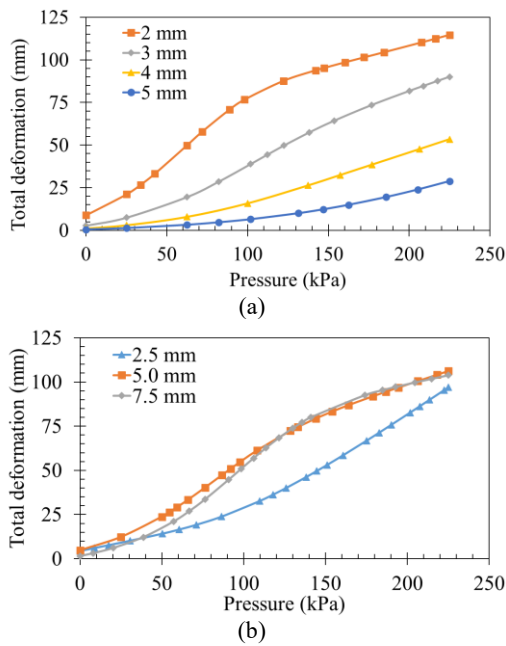
Figure 8. Total deformation results for variations of (a) wall thickness and (b) RLT

in the thickness, the curve becomes closer to a linear profile. Thus, it can be deduced that with higher wall thicknesses, the geometry becomes bulky leading to increase in the effect of geometry of the structure compared to the effect of material nonlinearity of the soft material.

With an increase in RLT, the total deformation increased until the RLT of 7.5 mm. However, this result does not provide a complete description of its deformation behavior. It is observed that an increase in RLT results in increased bending whereas an increase in wall thickness leads to an increase in radial expansion of the gripping unit. Therefore, to attain the curling motion for the gripping actuation, radial expansions and longitudinal expansions have to be minimized and bending actuation should be maximized. Notably, at 5 and 7.5 mm RLT, the total deformation variation follows a sigmoidal curve, and with a decrease in RLT, the nonlinearity of the deformation-pressure curve decreases. As RLT reduces, the effect of expanding flexible wall increases which augments the effect of the nonlinear nature of the material to the forefront by reducing the bulkiness of the geometrical structure.

3. 2. Effect of Pressure on Strain Variations
With the increase in the internal pressure the actuator is made to expand, resulting in a change in strain values. The internal pressure is increased from 0 kPa to 225 kPa in a quasi-static manner. For various pressure levels, strain values were recorded and plotted as shown in Figures 9(a) and 8(b). Since, strain is an absolute quantity normalized with respect to the initial dimension of an object, in both the cases of an increase in wall thickness and RLT, it is observed that strain decreases with addition of material. This is because, with the addition of material the average stiffness of the actuator increases; thereby reducing the average strains. Our analysis revealed that the average stresses also follow a similar tendency as average strains.
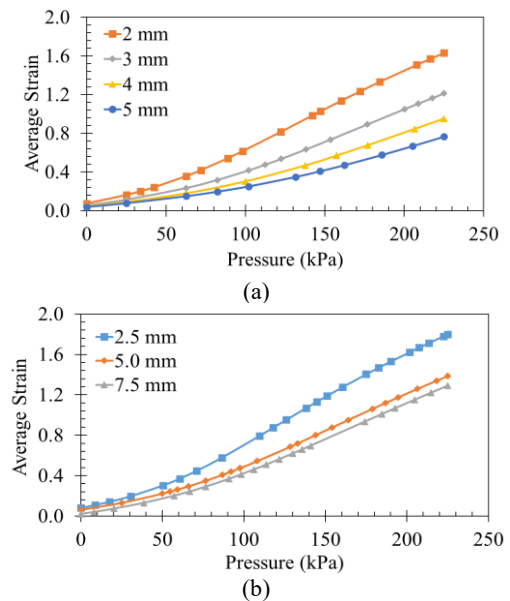
Figure 9. Effect of pressure on average strain for variations of (a) wall thickness and (b) RLT

3. 3. Effects of Pressure and Thickness on the Gripping Force Developed by the Actuator

Figure 10(a) shows the effect on gripping force as the chamber wall thickness increases while keeping a constant base layer thickness (RLT) of 5mm. From the obtained results it can concluded that with an increase in wall thickness, higher working internal pressure can be employed for the gripping actuation, leading to higher gripping forces. The gripping force tends to follow an exponential law, increasing with the increase in working internal gripping force and wall thickness. The maximum gripping force achieved in the simulations were around 35 N at 300 kPa pressure for 5 mm thick RLT. In an experimental study of human thumb inspired semi-cylindrically shaped soft actuator, Wang et al. [30] reported a comparable gripping force between 30 N – 40 N having a nonlinear variation with respect to actuation pressure as observed in Figure 9(a). Although the shapes of their internal chamber were different, the forces were in the same order as in the present study. Further, Chatterjee et al. [40] fabricated a human finger inspired actuator in the shape of a hollow semi-cylindrical tube, in which they observed a force generation of around 1.2 N at an actuation pressure of 30 kPa, which is again in the range of results in the present paper at the same pressure level.

For a better understanding of the effect of wall thicknesses, the force values are evaluated at a common pressure of 100 kPa and RLT of 5 mm and depicted as shown in Figure 10b. From this result it is noted that with an increase in wall thickness from 2 mm to 5 mm, the gripping force increases and becomes saturated at 5 mm thickness. This saturation can be accounted for by an increase in the pressure requirements for actuation with increased wall thicknesses. As wall thickness increases, the pressure applied, i.e., 100 kPa, is comparatively low to produce higher gripping forces. Since, an actuator with higher thickness can bear higher pressures, it develops higher gripping forces as depicted in Figure 9(a).

Figure 10(c) illustrates the maximum gripping force developed by the gripping unit by curling around it at their maximum bearable internal pressures. Force vector components along the three major axes, X, Y, and Z, are plotted. The effective gripping force developed by the actuator has been plotted and a regression equation is developed. The developed cubic polynomial regression model has an R^2 value of 99.79%. It is observed that with an increase in wall thicknesses, the working pressure and maximum gripping force increases nonlinearly. This variation of the gripping force tends to follow a sigmoidal nature of curve. Similar trends of the nonlinear gripping force variations (sigmoidal variation) has been observed in the study conducted by Wang et al. [30].

3. 4. Effects of Geometric Parametric Variations on Maximum Stresses and Strains
Two types of
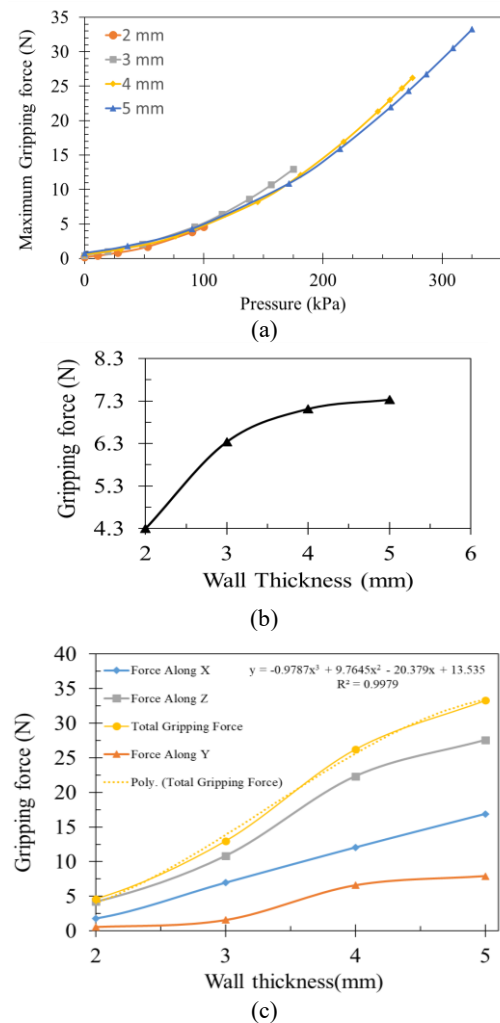
Figure 10. Gripping force variations with (a) varying pressures and wall thicknesses, (b) constant pressure of 100 kPa and (c) different wall thicknesses and corresponding maximum working pressures

parametric variations in the geometrical dimensions were considered for the present paper while keeping the remaining dimensional details constant. The geometry that is considered is a semi-cylindrical internal chamber. The flat part of the geometry is considered the restraining or base layer. The thickness of this layer is varied from 2.5 mm to 7.5 mm with an increment of 2.5 mm, by keeping the chamber wall thickness constant at 2.5 mm. The second type of geometrical variations considered is by keeping the base layer or restrain layer constant at 5 mm and varying the chamber wall thickness from 2 mm to 5 mm with an increment of 1 mm. The working internal pressures considered during these parametric variations were different to understand the effect of actuation pressure on the deformation characteristics. To further understand the effects of the parametric variations on the strain and stress states of the actuator, Figures 10

and 11, respectively, are shown. The Figures 11 and 12 are plotted at constant pressures of 225 kPa and 150 kPa, respectively.

Chamber wall thickness and RLT are the key factors that affect the stress developed. Figure 11 shows the relationships between the chamber wall thickness and RLT with maximum stresses developed in the actuator.

As the thicknesses increase the stress developed by the model decreases at a constant pressure. However, it needs to be noted that with increasing thicknesses, the

(a)

(b)
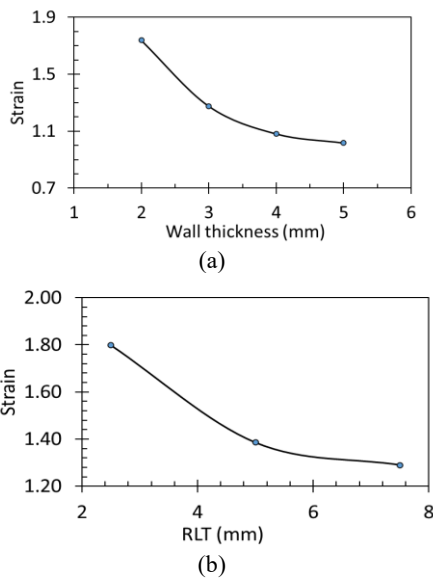
Figure 11. Effect of variations in (a) wall thickness and (b) RLT on maximum strain developed in the actuator

(a)

(b)
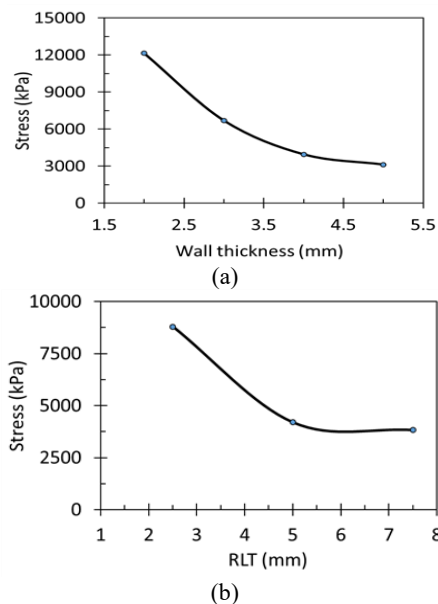
Figure 12. Effect of variations in (a) wall thickness and (b) RLT on maximum stresses developed in the actuator

working pressure of the actuator increases thereby increasing actual maximum pressures experienced by the actuators during their operations. As postulated earlier in case of Figure 8, the stresses and strains follow a declining trend with increase in the thickness of the material.

From the effects of geometric parametric variations, it can be observed that the maximum stresses and strains developed on the chamber walls and restraining layer thickness increases with increasing working pressures. Thus, using thinner walls or restraining layers will result in more portable gripping units that require less working pressure to attain the same deformation. However, the RLT has a positive effect on the bending capability of the actuator as shown in Figure 7. Thus, a tradeoff has to be made between RLT and the stresses the actuator may be subjected to during its working conditions. The developed actuator has potential applications such as smart harvesting of delicate agricultural produce (such as tomatoes) [40, 41] and biomedical assistance to the elderly [42-44].

The present study does have certain limitations. Since, in the current work, the effect of dynamic loading scenarios have not been simulated and the focus was only on static response of the actuator, the inertial effects (effect of gravity) has not been considered in the analysis. The effect of friction between the object and the grabber has not been considered in the present analyses. This will lead to underestimation of the gripping forces developed. Hence, this is a scope for future work.

4. CONCLUSIONS

The numerical analysis of the novel curling semi-cylindrical actuator revealed its capability to curl into a complete 360° and thus producing a robust gripping force distribution for holding delicate objects with precision. Based on the study on the effects of pressure and thickness variations on the performance of semi-cylindrical pneumatic soft actuator, the following conclusions are drawn:

- Increasing wall thickness leads to increased radial expansion and decreased bending whereas increasing the RLT increases the bending capability of the actuator. Complete curling of the actuator is achieved for two combinations of wall thickness and RLT: (2 mm, 5 mm) and (2.5 mm and 7.5 mm), respectively.

- The deformation-pressure relationship at 2 mm wall thickness and 5 mm RLT follow a sigmoidal curve and with increasing wall thicknesses the nonlinearity decreases. With decreasing RLT from 5 mm to 2.5 mm the deformation-pressure relationship become close to a linear function.

- The gripping force increases exponentially with an increase in applied pressure as well as both wall thickness and RLT due to the increase in working pressure capability with increasing thicknesses.
- For a common actuating pressure, the gripping force is seen to saturate at a certain thickness, while for the maximum working pressure the gripping force increases nonlinearly. A third-order polynomial model is developed to represent the relationship between wall thickness and total gripping force developed at the maximum operating pressures, which showed an R^2=99.79%, valid for the range: 2 mm $\leq$ wall thickness $\leq$ 5 mm and 2.5 mm $\leq$ RLT $\leq$ 7.5 mm.

5. ACKNOWLEDGEMENT

6. REFERENCES

1. El-Atab, N., Mishra, R.B., Al-Modaf, F., Joharji, L., Alsharif, A.A., Alamoudi, H., Diaz, M., Qaiser, N. and Hussain M.M. "Soft Actuators for Soft Robotic Applications: A Review" *Advanced Intelligent Systems*, Vol. 2, (2020), 2000128. doi: 10.1002/aisy.202000128

2. Cianchetti, M., Laschi, C., Menciassi, A. and Dario, P. "Biomedical applications of soft robotics" *Nature Reviews Materials*, Vol. 3, (2018), 143-153. doi: 10.1038/s41578-018-0022-y

3. Hsiao, J., Chang, J-Y. and Cheng, C.M. "Soft medical robotics: clinical and biomedical applications, challenges, and future directions" *Advanced Robotics*, Vol. 33, No. 21, (2019), 1099-1111. doi: 10.1080/01691864.2019.1679251

4. Zheng, S., Park, T., Hoang, M.C., Go, G., Kim, C-S., Park, J-O., Choi, E. and Hong A. "Ascidian-Inspired Soft Robots That Can Crawl, Tumble, and Pick-and-Place Objects" *IEEE Robotics and Automation Letters*, Vol. 6, No. 2, (2021), 1722-1728. doi: 10.1109/LRA.2021.3059621

5. Terrile, S., Argüelles, M. and Barrientos, A. "Comparison of Different Technologies for Soft Robotics Grippers" *Sensors*, Vol. 21, (2021), 3253. https://doi.org/10.3390/s21093253

6. Wang, J., Fei, Y. and Pang, W. "Design, Modeling, and Testing of a Soft Pneumatic Glove with Segmented PneuNets Bending Actuators" *IEEE/ASME Transactions on Mechatronics*, Vol. 24, No. 3, (2019), 990-1001. doi: 10.1109/TMECH.2019.2911992

7. Savkiv, V., Mykhailyshyn, R., Duchon, F., Prentkovskis, O., Maruschak, P. and Diahovchenko, I. "Analysis of Operational Characteristics of Pneumatic Device of Industrial Robot for Gripping and Control of Parameters of Objects of Manipulation." *Transbaltica XI: Transportation Science and Technology*, Transbaltica 2019. Lecture Notes in Intelligent Transportation and Infrastructure. Springer, (2020). 504-510. doi: 10.1007/978-3-030-38666-5_53

8. Savkiv, V., Mykhailyshyn, R., Duchon, F. and Maruschak, P. "Justification of Influence of the Form of Nozzle and Active

9. Surface of Bernoulli Gripping Devices on Its Operational Characteristics" *Transbaltica XI: Transportation Science and Technology*, Transbaltica 2019. Lecture Notes in Intelligent Transportation and Infrastructure. Springer, (2020). 263-272. doi: 10.1007/978-3-030-38666-5_28

9. Savkiv, V., Mykhailyshyn, Maruschak, P., Kyrylovych, V., Duchon, F. and Chovanec, L. "Gripping Devices of Industrial Robots for Manipulating Offset Dish Antenna Billets and Controlling Their Shape" *Transport*, Vol. 36, No. 1, (2021), 63-74. doi: 10.3846/transport.2021.14622

10. Poolsawad, K., Songkram, N., Piromsopa, K. and Songkram, N. "Teachers' Perception for Integrating Educational Robots and Use as Teaching Assistants in Thai Primary Schools" *Emerging Science Journal*, Vol. 4, (2020), 127-140. doi: 10.28991/esj-2021-SP1-09

11. Iswanto, I., Ma'arif, A., Raharja, N.M., Hariadi, T.K. and Shomad, M.A. "Using a Combination of PID Control and Kalman Filter to Design of IoT-based Telepresence Self-balancing Robots during COVID-19 Pandemic" *Emerging Science Journal*, Vol. 4, (2020), 241-261. doi: 10.28991/esj-2021-SP1-016

12. Rossiter, J., Walters, P. and Stoimenov, B. "Printing 3D dielectric elastomer actuators for soft robotics" In Electroactive Polymer Actuators and Devices (EAPAD) 2009, 7287, (2009). https://doi.org/10.1117/12.815746

13. Shen, Z., Chen, F., Zhu, X., Yong, K-T. and Gu, G. "Stimuli-responsive functional materials for soft robotics" *Journal of Materials Chemistry B*, Vol. 8, (2020), 8972-8991. doi: 10.1039/D0TB01585G

14. Manti, M., Hassan, T., Passetti, G. and D'Elia, N., Laschi, C., Cianchetti M. "A Bioinspired Soft Robotic Gripper for Adaptable and Effective Grasping" *Soft Robotics*, Vol. 2, No. 3, (2015), 107-116. doi: 10.1089/soro.2015.0009

15. Wu, S., Hu, W., Ze, Q., Sitti, M. and Zhao, R. "Multifunctional magnetic soft composites: a review" *Multifunctional Materials*, Vol. 3, (2020), 042003. doi: 10.1088/2399-7532/abcb0c

16. Hughes, J., Culha, U., Giardina, F., Guenther, F., Rosendo, A. and Iida, F. "Soft Manipulators and Grippers: A Review" *Frontiers in Robotics and AI*, Vol. 3, (2016), 69. doi: 10.3389/frobt.2016.00069

17. Bira, N., Dhagat, P. and Davidson J.R. "A Review of Magnetic Elastomers and Their Role in Soft Robotics" *Frontiers in Robotics and AI*, Vol. 7, (2020), 588391. doi: 10.3389/frobt.2020.588391

18. Mosadegh B., Polygerinos, P., Keplinger, C., Wannstedt, S., Shepherd, R.F., Gupta, U., Shim, J., Bertoldi, K., Walsh, C.J. and Whitesides G.M. "Pneumatic Networks for Soft Robotics that Actuate Rapidly" *Advanced Functional Materials*, Vol. 24, (2014), 2163-2170; doi: 10.1002/adfm.201303288

19. Yan J., Zhang, X., Xu, B. and Zhao J. "Pneumatic Networks for Soft Robotics that Actuate Rapidly." *Soft Robotics*, Vol. 5, No. 5, (2017), 2163-2170. doi: 10.1089/soro.2017.0040

20. Zhou, W. and Li, Y. "Modeling and Analysis of Soft Pneumatic Actuator with Symmetrical Chambers Used for Bionic robotic Fish." *Soft Robotics*, Vol. 7, No. 2, (2018), 168-178. DOI: 10.1089/soro.2018.0087

21. Liu, X., Zhao, Y., Geng, D., Chen, S., Tan, X. and Cao C. "Soft Humanoid Hands with Large Grasping Force Enabled by Flexible Hybrid Pneumatic Actuators." *Soft Robotics*, Vol. 8, No. 2, (2020), 175-185. doi: 10.1089/soro.2020.0001

22. Chandler, J.H., Chauhan, M., Garbin, N., Obstein, K. and Valdastri, P. "Parallel Helix Actuators for Soft Robotic Applications." *Frontiers in Robotics and AI*, Vol. 7, (2020), 119. doi: 10.3389/frobt.2020.00119

23. Zhang J., Wang, T., Wang J., Wang, M.Y., Li B., Zhang, X.J. and Hong, J. "Geometric Confined Pneumatic Soft–Rigid Hybrid

Actuators" *Soft Robotics*, Vol. 7, No. 5, (2018), 574-582. doi: 10.1089/soro.2018.0157

24. Honarpardaz, M. "A methodology for design and simulation of soft grippers" *Simulation*, Vol. 97, No. 11, (2021), 779-791. doi: 10.1177/00375497211018743

25. Jing, X., Chen, S., Zhang, C. and Xie, F. "Increasing Bending Performance of Soft Actuator by Silicon Rubbers of Multiple Hardness" *Machines*, Vol. 10, (2022), 272. doi: 10.3390/machines10040272

26. Zhou, X., Majidi, C. and O'Reilly, O.M. "Soft hands: An analysis of some gripping mechanisms in soft robot design" *International Journal of Solids and Structures*, Vol. 64-65, (2015), 155-165. doi: 10.1016/j.ijsolstr.2015.03.021

27. Luo, M., Tao, W., Chen, F., Khuu, T.K., Ozel, S. and Onal, C.D. "Design improvements and dynamic characterization on fluidic elastomer actuators for a soft robotic snake" 2014 IEEE International Conference on Technologies for Practical Robot Applications, (2014), 1-16. doi: 10.1109/TePRA.2014.6869154

28. Tan, N., Gu, X. and Ren, H. "Design, characterization and applications of a novel soft actuator driven by flexible shafts" *Mechanism and Machine Theory*, Vol. 122, (2018), 197-218. doi: 10.1016/j.mechmachtheory.2017.12.021

29. Pranav, V.K., Prakash, A., Rajendran, A. and Sreedharan, P. "Design optimization and analysis of external corrugation and geometry of asymmetrical bellow flexible pneumatic actuator" *IOP Conf. Series: Materials Science and Engineering*, Vol. 1132, (2021), 012011. doi: 10.1088/1757-899X/1132/1/012011

30. Wang, Y., Kokubu, S., Zhou, Z., Guo, X., Hsueh, Y.H. and Yu, W. "Designing soft pneumatic actuators for thumb movements" *IEEE Robotics and Automation Letters*, Vol. 6, No. 4, (2021), 8450-8457. doi: 10.1109/LRA.2021.3105799

31. Marckmann, G. and Verron E. "Comparison of Hyperelastic Models for Rubber-Like Materials" *Rubber Chemistry and Technology*, Vol. 79, No. 5, (2006), 835-858. doi: 10.5254/1.3547969

32. Joshi, A., Kulkarni, A. and Tadesse, Y. "FludoJelly: Experimental Study on Jellyfish-Like Soft Robot Enabled by Soft Pneumatic Composite (SPC)" *Robotics*, Vol. 8, No. 4, (2019), 56. doi: 10.3390/robotics8030056

33. Yeoh, O.H. "Some Forms of the Strain Energy Function for Rubber" *Rubber Chemistry and Technology*, Vol. 66, (1993), 754-771. doi: 10.5254/1.3538343

34. Xavier, M.S., Fleming, A.J. Yong, Y.K. "Finite Element Modeling of Soft Fluidic Actuators: Overview and Recent

Developments" *Advanced Intelligent Systems*, Vol. 3, (2021), 2000187. doi: 10.1002/aisy.202000187

35. Rackl, M. "Material testing and hyperelastic material model curve fitting for Ogden, Polynomial and Yeoh models" In ScilabTEC 2015, Paris, France, (2015) http://dx.doi.org/10.13140/RG.2.2.29552.25600/1

36. Wang, Z., Or, K. and Hirai S. "A dual-mode soft gripper for food packaging" *Robotics and Autonomous Systems*, Vol. 125, (2020), 103427. doi: 10.1016/j.robot.2020.103427

37. Wang, Z., Kanegae, R. and Hirai S. "Circular Shell Gripper for Handling Food Products" *Soft Robotics*, Vol. 8, No. 5, (2020), 542-554. doi: 10.1089/soro.2019.0140

38. Cacucciolo, V., Shintake, J. and Shea H. "Delicate yet strong: characterizing the electro-adhesion lifting force with a soft gripper" In 2019 2nd IEEE International Conference on Soft Robotics (RoboSoft) COEX, Seoul, Korea, April 14-18, (2019), 108-113. https://doi.org/10.1109/ROBOSOFT.2019.8722706

39. Li H., Yao, J., Zhou, P., Chen, X., Xu, Y. and Zhao Y. "High-Load Soft Grippers Based on Bionic Winding Effect", *Soft Robotics*, Vol. 6, No. 2, (2018), 276-288. doi: 10.1089/soro.2018.0024

40. Reddy, A.S., Chembuly, V.V.M.J.S. and Rao, V.V.S.K. "Collision-free Inverse Kinematics of Redundant Manipulator for Agricultural Applications through Optimization Techniques" *International Journal of Engineering, Transactions A: Basics,* Vol. 35, No. 7, (2022), 1343-1354. doi: 10.5829/ije.2022.35.07a.13

41. Ishii, K., Matsuo, T., Takemura, Y., Sonoda, T., Nishida, Y., Yasukawa, S. and Fujinaga, T. "Tomato-Harvesting-Robot Competition Towards Smart Agriculture" The 2021 International Conference on Artificial Life and Robotics (ICAROB2021), (2021). https://doi.org/10.5954/ICAROB.2021.PS-1

42. Shahzad, K. and Khan, M.B. "Control of a Robotic Wheel-Chair Prototype for People with Walking Disabilities" *International Journal of Engineering, Transactions B: Applications*, Vol. 31, No. 5, (2018), 693-698. doi: 10.5829/ije.2018.31.05b.02

43. Sangdani, M.H. and Tavakolpour-Saleh, A.R. "Particle Swarm Optimization Based Parameter Identification Applied to a Target Tracker Robot with Flexible Joint" *International Journal of Engineering, Transactions B: Aspects*, Vol. 33, No. 9, (2020), 1797-1802. doi: 10.5829/ije.2020.33.09c.14

44. Saadat, M. and Garmsiri, N. "A New Intelligent Approach to Patient-cooperative Control of Rehabilitation Robots" *International Journal of Engineering, Transactions B: Aspects*, Vol. 27, No. 3, (2014), 467-474. doi: 10.5829/idosi.ije.2014.27.03c.15

Persian Abstract

چکیده

رباتیک نرم با استفاده از محرک‌های شبکه پنوماتیک (Pneu-Net) یک زمینه در حال توسعه است که آینده امیدوارکننده‌ای برای کاربردهای مختلف شامل عملیات ظریف مانند کمک‌های زیست پزشکی دارد. تعامل بین هندسه و عملکرد محرک موضوع مهمی است که توسط بسیاری از محققان در این زمینه مورد بررسی قرار گرفته است. با این حال، در مورد رابطه بین قابلیت چنگ زدن و پارامترهای هندسی محرک‌های نرم تحقیقی وجود ندارد. به ویژه، نیاز به روشن کردن تأثیرات ضخامت دیواره بر نیروی چنگ زدن ایجاد شده وجود دارد. در مطالعه حاضر، یک محرک نرم PneuNet محفظه‌ای نیمه استوانه‌ای به صورت عددی برای ارزیابی اثرات تغییرات فشار و ضخامت دیواره بر ویژگی‌های عملکردی آن مورد بررسی قرار گرفته است. نتایج نشان داد که افزایش ضخامت لایه بازدارنده (RLT) به قابلیت خمشی محرک کمک می کند در حالی که افزایش ضخامت محفظه آن را کاهش می دهد. بنابراین، حداکثر خمش محرک در ترکیب حداقل ضخامت دیواره و حداکثر RLT به دست می آید. در این پیکربندی‌های هندسی حداکثر خمش، روابط تغییر شکل–فشار از یک تابع سیگموئیدی پیروی می‌کنند و با افزایش ضخامت دیواره و کاهش RLT به سمت خطی شدن گرایش پیدا می‌کنند. نیروی چنگ زدن با افزایش فشار کاری و ضخامت دیواره افزایش نمایی را نشان داد. حداکثر نیروی گرفتن به صورت مکعبی با افزایش ضخامت دیواره در حداکثر فشار کاری مربوطه افزایش یافت که با استفاده از مدل رگرسیون چند جمله‌ای ($R^2 = 99.79٪$) مدل‌سازی شد.

International Journal of Engineering

Multi-Objective Vehicle Routing Problem for a Mixed Fleet of Electric and Conventional Vehicles with Time Windows and Recharging Stations

A. Mohammadbagher, S. A. Torabi*

School of Industrial Engineering, College of Engineering, University of Tehran, Tehran, Iran

PAPER INFO	*ABSTRACT*
	The vehicle routing problem as a challenging decision problem has been studied extensively. More specifically, solving it for a mixed fleet requires realistic calculation of the performance of electric and combustion vehicles. This study addresses a new variant of the vehicle routing problem for a mixed fleet of electric and combustion vehicles under the presence of time windows and charging stations. A bi-objective mixed-integer programming model is developed which aims at minimizing cost and pollution level concurrently. To accurately quantify travel quantities, such as fuel consumption, emission, and battery charge level, a set of realistic mathematical formulas are used. The model is first converted to a single-objective counterpart using the epsilon-constraint method and a simulated annealing algorithm is tailored to obtain Pareto optimal solutions. A discussion is also made on how the final solution can be selected from the Pareto frontier according to the design objectives. The presented framework can find a set of Pareto optimal solutions as a trade-off between cost and pollution objectives by considering different combinations of electric and combustion vehicles. It was shown that those solutions that involve more electric fleet than combustion fleet, lead to higher total costs and smaller emissions and vice versa.

Description	Notation	Description	Notation
0	Depot	q_i	Load of the vehicle at node i [kg]
u_0	Start depot node	e_i	The earliest beginning of service time in Node i [h]
u_{n+1}	End depot node	l_i	The latest beginning of service time in Node i [h]
C	Set of customers	s_i	Service time of each node [h]
F	Set of Recharging stations	τ_i	The actual start of service time for node i [h]
F'	Subset with repetition of recharging stations	u_i	Vehicle's current load when it enters node i [kg]
$N = C \cup F'$	Set of all nodes (customers+ recharging stations)	SOC_i	Vehicle SOC when it enters node i [kWh]
$N_0 = N \cup u_0$	Set of nodes with start depot	x_{ij}^k	the binary variable of a vehicle of type k that travel from node i to node j
$N_{n+1} = N \cup u_{n+1}$	Set of nodes with end depot	f_D	Driver wage [$/h]
V_E	Set of electric vehicles	f_Y	Battery recharging cost per energy [$/kWh]
V_{IC}	Set of internal combustion vehicles	f_L	Internal combustion fuel cost per liter of fuel [$/L]
$V = V_E \cup V_{IC}$	Set of all the vehicles	ΔE_{ij}^k	Battery discharge of a vehicle with type k when travels from node i to node j [kWh]
Q	Vehicle Load capacity [kg]	ΔL_{ij}^k	Fuel consumption of the vehicle with type k when travels from node i to node j [L]
k	Vehicle type	$f_{O,E}$	Operating cost of EVs per traveled distance [$/km]
t_{ij}	Travel time between two nodes i and j [hours]	$f_{O,IC}$	Operating cost of ICVs per traveled distance[$/km]
m_{ij}	Distance between two nodes i and j [km]	p_{ij}	The total emission of the vehicle when traveled from node i to node j [g]
g^k	Battery recharging time-rate [kWh/h=kW]	d_i	Node i demand [kg]
Y^k	battery capacity [kWh]	q_i	Load of the vehicle at node i [kg]
d_i	Node i demand [kg]		

Corresponding Author Institutional Email: satorabi@ut.ac.ir
 (S. A. Torabi)

1. INTRODUCTION

Massive consumption of fossil fuels by conventional internal combustion engine vehicles has caused numerous environmental problems including global warming and the energy crisis [1]. In the European Union (EU-27) report, greenhouse gas (GHG) emissions have decreased rapidly in recent years, reaching 24 % below 1990 levels and 31 % below 2020 levels. As a result, the EU has met its 2020 GHG reduction target [2]. Numerous studies in the context of vehicle routing problems (VRP) have considered environmental aspects of transportation systems through solving green VRPs (GVRPs), in which a fleet of alternative fuel vehicles (AFVs), including homogeneous and heterogeneous fleets, are considered. Homogeneous fleets contain vehicles that are all the same. While heterogeneous fleets which have been addressed by fewer than 15% of the relevant studies include different types of vehicles with different quantities such as capacity, operating costs, environmental effects, charging systems, battery capacity, and energy consumption [3]. Schneider et al. [4], Erdoğan and Miller [5] proposed the formulation of electric VRPs (EVRP) with a fleet of electric vehicles while considering time windows and battery recharging stations. Romet et al. [6] addressed a homogeneous autonomous electric vehicle routing problem with the depth-of-discharge (DOD) method to improve battery life and reduce costs of battery replacement. The DOD method showed an 18 times longer battery lifespan even though it increased the initial cost and battery capacity. Hiermann et al. [7], Macrina et al. [8] have addressed a mixed heterogeneous fleet of conventional and electric vehicles. Minimization of air pollution is another objective considered in some other works in GVRP. Bektaş and Laporte [9] solved an emission routing problem by minimizing the travel distance and greenhouse emissions, fuel consumption, and travel times. Zhou et al. [10] presented a multi-depot heterogeneous vehicle routing problem in which average risk and costs were reduced by 3.99% and 2.01%, respectively, with an acceptable risk compared to a half-open multi-depot homogeneous vehicle routing problem.

To calculate different quantities in GVRP (including but not limited to fuel consumption, emission, and battery energy consumption), different mathematical formulas have been utilized in the literature. Most of the works assumed that the energy consumption (i.e., fuel consumption of combustion fleet, and electrical energy of electric fleet) is a function of traveled distance [4, 5]. On the other hand, some other works are considered more realistic models. Davis and Figliozzi [11] assumed that energy consumption also depends on the average vehicle speed during the trip. Goeke and Schneider [12] and Perera [1] formulated a more complicated model of fuel

consumption that considers speed, road gradient, and vehicle load in the model structure. Goeke and Schneider [12] used data from Global Positioning System (GPS) to predict energy consumption in simulation environments. Sivagnanam et al. [13] utilized real GPS data to predict electricity consumption based on several factors, including vehicle locations, traffic, elevation, and weather data.

Most studies in GRVP have considered a single objective including traveled distance [5], cost [7, 14], emission [9] and fuel consumption [15, 16]. Sivagnanam, et al. [13] considered an extra objective of emission as a constraint on the solution space. To allow the evaluation of possible trade-offs between multiple objectives, some other works have formulated multi-objective optimization models. Ghannadpour and Zarrabi [17] considered customers' requirements for servicing as an extra objective in a multi-objective problem. Abad et al. [18] proposed a bi-objective model to minimize cost and fuel consumption. Androutsopoulos and Zografos [19] formulated and solved a bi-objective path-dependent VRP to minimize time and load. Goeke and Schneider [12] considered three objectives including the traveled distance, energy consumed, and total costs.

Considering two objectives of cost and emission for a mixed fleet of electric and combustion engines requires multi-objective optimization programming to allow an evaluation of possible trade-offs between different objectives. On the other hand, quantifying each objective requires evaluating different travel quantities, such as fuel consumption and emission. The travel quantities are dependent on various vehicle parameters and states, including size, mass, engine characteristics, vehicle speed, battery state of the charge (SOC), etc. which may change by the vehicle type, assigned route, current load, environmental conditions, etc. Therefore, the calculation of the travel quantities requires using realistic mathematical models. In this work, a novel multi-objective VRP for a mixed fleet of combustion and electric vehicles with the presence of time windows and recharging stations is formulated and solved. The main contributions of this work are as follows:

(I) A new variant of bi-objective VRPs with a fleet of mixed electric and conventional vehicles under the presence of recharging stations and time windows is formulated.

(II) A set of realistic mathematical formulas are used to accurately quantify required travel-dependent quantities, including fuel consumption, electric energy consumption, and emission.

The rest of this paper is organized as follows. In section 2, a mixed-integer formulation is proposed for the problem. Section 3 presents the solution procedure and the developed general optimization framework. Section 4 presents the results and discussion for a set of benchmark

instances. Finally, section 5 provides concluding remarks and future avenues for further research.

2. PROBLEM DESCRIPTION & FORMULATION

The targeted routing problem follows a classic VRP formulation with some additions including time windows and recharging stations. The problem is to start from a depot node u_0, serve a set of customers C once using a mixed fleet of vehicles with type K within acceptable time windows, and return to the node u_0, while a set of recharging stations F is available. The proposed Multi-Objective Vehicle Routing Problem for a Mixed Fleet of Electric and Conventional Vehicles with Time Windows and Recharging Stations (MF-EVRPTW) must satisfy the following additional conditions or assumptions:

- Each vehicle is fully recharged after visiting a recharging station.
- Every customer is visited exactly once
- Every route starts from and ends at the depot node u_0.

The goal of this paper is to propose and solve a multi-objective problem in which the two conflicting objectives of cost and emission are minimized.

The problem under study in this paper is an extension of work conducted by Schneider et al. [4], Hiermann et al. [20]. The proposed model seeks to find an optimal routing for a mixed fleet of EVs and ICVs under the minimization of cost and emission. The Nomenclature table summarizes different parameters and variables that are used in the model.

The optimization problem is formed as a mixed-integer program, which involves two objectives and multiple constraints. The first objective is to minimize the total cost as the summation of the driver cost, energy consumption cost, and operation cost, which is calculated as follows:

$$\text{minimize} \quad C = C_D + C_E + C_O =$$

$$f_D \left\{ \sum_{i \in N_0} \sum_{j \in N_{n+1}, i \neq j} (t_{ij} + s_i) x_{ij}^k + \right.$$
$$\left. \sum_{i \in F'} \sum_{j \in N_{n+1}, i \neq j} \left(\frac{(1 - SOC_i^k)Y^k}{g^k} \right) x_{ij}^k \right\} + \quad (1)$$
$$\sum_{k \in V_E} \sum_{i \in N_0, j \in N_{n+1}, i \neq j} (f_Y \Delta E_{ij} + f_{O,E} m_{ij}) x_{ij}^k +$$
$$\sum_{k \in V_{IC}} \sum_{i \in N_0, j \in N_{n+1}, i \neq j} (f_L \Delta L_{ij} + f_{O,IC} m_{ij}) x_{ij}^k$$

The second objective is to minimize the total emission of the fleet, which is calculated as follows:

$$\text{minimize} \quad P = \sum_{k \in V_{IC}} \sum_{i \in N_0, j \in N_{n+1}, i \neq j} p_{ij}^k . x_{ij} \quad (1)$$

Additionally, to satisfy the problem requirements, multiple constraints are considered.

$$x_{ij}^k \epsilon \{0,1\} \quad \forall k \epsilon V \ i \epsilon N_0, j \epsilon N_{n+1}, i \neq j \quad (3)$$

First of all, constraints (3) define the binary decision variables.

$$\sum_{k \in V} \sum_{j \in N_{n+1}, i \neq j} x_{ij}^k = 1 \quad \forall i \in C \quad (4)$$

$$\sum_{k \in V} \sum_{j \in N_{n+1}, i \neq j} x_{ij}^k \leq 1 \quad \forall i \in F' \quad (5)$$

$$\sum_{i \in N_{n+1}, i \neq j} x_{ji}^k - \sum_{i \in N_0, i \neq j} x_{ij}^k = 0 \ ; \ \forall j \in N, \forall k \in V \quad (6)$$

There are multiple constraints regarding visiting the nodes; constraints (4) ensure that every customer is visited by one vehicle exactly once. Constraints (5) enforce that a recharge station does not necessarily need to be visited. Constraints (6) guarantee that the number of incoming arcs into a node is equal to the number of outgoing arcs from it.

$$e_i \leq \tau_i \leq l_i \quad \forall i \in N_{0,n+1} \quad (7)$$

$$\tau_i + (s_i + t_{ij}) x_{ij}^k - l_0 (1 - x_{ij}^k) \leq \tau_j \quad \forall k \in V, \forall i \in \quad (8)$$
$$C, \forall j \in N_{n+1}, i \neq j$$

$$\tau_i + t_{ij} x_{ij}^k + \frac{(1 - SOC_i^k)Y^k}{g^k} - \left(l_0 + \frac{Y^k}{g^k} \right)(1 - x_{ij}^k) \leq \tau_j \quad (9)$$
$$\forall k \in V_E, \forall i \in F, \forall j \in N_{n+1}, i \neq j$$

Additionally, constraints (7)-(9) enforce the timing to visit nodes; constraint (7) ensures that the start of service time τ_i must be within the time window $[e_i, l_i]$ of node i; constraints (8) guarantee that for the start of service time of customer node j who is visited after node i must be later than the start of service time plus the service time of customer node i plus the travel time from node i to node j. Constraints (9) are the same as constraints (8) but for recharging stations; they consider the recharging time of EVs as a function of the remaining battery SOC when it enters a charging station. Note that to maximize the range of electric vehicles and to simplify the problem, the battery is enforced to be fully charged at the exit of recharging stations.

$$q_j^k \leq q_i^k - d_i x_{ij}^k + Q^k (1 - x_{ij}^k) \quad \forall k \in V, \forall i \in \quad (10)$$
$$N_0, \forall j \in N_{n+1}, i \neq j$$

$$0 \leq q_j^k \leq Q^k \quad \forall k \in V, \forall j \in N_{0,n+1} \quad (11)$$

There are some constraints regarding the load of the fleets. Constraints (10) ensure that a load of a vehicle in the node j depends on the initial load when visiting the previous node i plus the demand of node i. Constraints (11) enforce that a vehicle's load never exceeds the maximum capacity.

$$0 \leq SOC_j \leq SOC_i - \Delta SOC_{ij}^k . x_{ij}^k + (1 - x_{ij}^k) \quad \forall k \in \quad (12)$$
$$V_E, \quad \forall i \in N_0, \quad \forall j \in N_{n+1}, i \neq j$$

$$SOC_0^k = 1 \quad \forall k \in V_E \quad (13)$$

According to the SOC of batteries, constraints (12) ensure that the battery SOC at the next node j depends on

the SOC of node i plus battery discharge by traveling from node i to node j. Constraint (13) ensures that the battery is fully charged when exiting the depot.

3. SOLUTION PROCEDURE

According to the bi-objective constrained nature of the problem, we suggest a two-step solution method.

Step 1: Conversion to Single-objective Model
The epsilon-constraint method is used to obtain Pareto front solutions where the first objective function is considered as the main objective, and the second objective function is moved to the constraints of the problem:

$$\min C$$

s.t.

$$\sum_{k \in V} \sum_{i \in N_0, j \in N_{n+1}, i \neq j} P_{ij}^k \cdot x_{ij}^k \leq \varepsilon \qquad (14)$$

Constraints in $(4) - (3)$

Step 2: Unconstrained Formulation
Many constraints exist in the model (14) which bound the solution space. By using the penalty function method, the constraints are treated as soft constraints for two reasons; First, it increases the chance of finding a significantly better routing solution with some extra cost on some penalties, such as being late for a customer or putting some extra load on a vehicle. This brings the opportunity to the user to deal with trade-offs between violating some of the constraints while decreasing the overall cost or emission significantly. Second, it lets the simulated annealing (SA) method keep answers that are almost optimal but slightly violate some of the constraints; therefore, a neighborhood solution that does not violate a constraint is likely to be selected in later iterations of the SA algorithm, which leads to finding a better solution at the end of the optimization iterations. SA is a common metaheuristic local search algorithm known as one of the most preferred methods applied for solving VRPs. In SA algorithm, the annealing process involves heating metal, glass, or crystal alloys above their melting points and cooling them slowly to achieve perfect crystal structures. In metaheuristics, SA can escape the local optimum by using hill-climbing moves to decrease the temperature parameter and the probability of acceptance of a worse objective function. There are some papers that describe more details of this method [21]. Accordingly, the penalty functions associated with the constraints (14) are as follows:

$$CV = \operatorname*{mean}_{k \in V} \left\{ \max \left(\frac{\sum_{i \in c} q_i}{C_k} - 1 \right) \right\} \qquad (15)$$

$$TWV = \operatorname*{mean}_{i \in N_{n+1}} \left\{ \max \left(0, 1 - \frac{\tau_i}{e_i}, \frac{\tau_i}{l_i} - 1 \right) \right\} \qquad (16)$$

$$SOCV = \operatorname*{mean}_{i \in N_{n+1}} \{ \max(0, -SOC_i, SOC_i - 1) \} \qquad (17)$$

$$PV = \max \left(0, \left(\frac{p}{\varepsilon} - 1 \right) \right) \qquad (18)$$

in which CV, TWV, SOCV, and PV correspond to the constraints of the vehicle capacity, time windows, battery SOCs, and the epsilon, respectively. As a result, Equation (14) becomes an unconstrained problem with the following single objective function:

$$minimize\ Z = C(1 + \beta_1 PV + \beta_2 CV + \beta_3 TWV + \beta_4 SOCV) = \left(f_D \left\{ \sum_{i \in N_0} \sum_{j \in N_{n+1}, i \neq j} (\Delta t_{ij} + s_i) x_{ij}^k + \right. \right.$$
$$\sum_{i \in F'} \sum_{j \in N_{n+1}, i \neq j} \left(\frac{(1 - SOC_i^k) Y^k}{g^k} \right) x_{ij}^k \right\} +$$
$$\sum_{k \in V_E} \sum_{i \in N_0, j \in N_{n+1}, i \neq j} (f_Y \Delta E_{ij} + f_{O,E} m_{ij}) x_{ij}^k +$$
$$\sum_{k \in V_{IC}} \sum_{i \in N_0, j \in N_{n+1}, i \neq j} (f_L \Delta L_{ij} + f_{O,IC} m_{ij}) x_{ij}^k \right) \left(1 + \right.$$
$$\beta_1 \max \left(0, \left(\frac{p}{\varepsilon} - 1 \right) \right) + \beta_2 \operatorname*{mean}_{k \in V} \left\{ \max \left(\frac{\sum_{i \in c} q_i}{C_k} - 1, 0 \right) \right\} + \beta_3 \operatorname*{mean}_{i \in N_{n+1}} \left\{ \max \left(0, 1 - \frac{\tau_i}{e_i}, \frac{\tau_i}{l_i} - 1 \right) \right\} +$$
$$\left. \beta_4 \operatorname*{mean}_{i \in N_{n+1}} \{ \max(0, -SOC_i, SOC_i - 1) \} \right) \qquad (19)$$

where $\beta_1, \ldots, \beta_4$ denotes the weights associated with each penalty function. Note that all the penalty functions are designed to be between zero and one so all the weights can be chosen in the same order.

3. 1. Realistic Evaluation of Travel Information
To quantify the travel information, including fuel consumption, emission, and battery charge level, the models in ADVISOR are used [22]. ADVISOR contains realistic physics-based mathematical models for the vehicle's drivetrain components that can compute the performance of the vehicle in a driving scenario in the simulation environment accurately. Figure shows the ADVISOR model for the internal combustion engine drivetrain and electric drivetrains, respectively. Given the driving cycle as the input, ADVISOR estimates the fuel


Figure 1. Drivetrain Model of combustion (a) and electric (b) vehicles in ADVISOR [22]. The models in the simulation environments provide vehicle performance such as fuel combustion, electrical energy consumption, and emission

consumption, change in the battery state of the charge, and amount of emission, which are needed to evaluate the cost function in Equation (19).

$$d_{ij} = \int_0^{t_f} V(t)dt, \tag{20}$$

where t_f is the duration of the trip which is determined by the driving cycle.

The fuel consumption, emission, and state of charge are functions of the vehicle's parameters, including the vehicle's mass, the type of the drivetrain and its components as well as the initial condition of the vehicle at the start of the trip. The vehicle's mass can vary not only from one trip to another but also during a single trip due to unloading at customer nodes along a single trip. The drivetrain of the vehicle contains various components, which all influence the overall fuel consumption, emission, and battery SOC change. Finally, the vehicle's initial condition affects the entire performance of the vehicle over the driving cycle since it changes the working points of the drivetrain's components which result in different efficiency of each component.

To address the variability of the vehicle's performance in different conditions, the vehicle's model is simulated in ADVISOR in offline mode for a discrete multidimensional grid of different driving cycles, vehicle types, vehicle loads, and initial conditions. The result is a 3D tensor for fuel consumption denoted by ΔL, a 3D tensor for the emission denoted by P, and a 4D tensor for SOC change denoted by ΔSOC:

$$\Delta L = \Delta L(ij, K, L)$$
$$P = P(ij, K, L) \tag{21}$$
$$\Delta SOC = \Delta SOC(ij, K, SOC_0, L),$$

where ij is the route path (which determines the driving cycle), K is the vehicle's type, L is the vehicle's load during the trip, and SOC_0 is the initial state of the charge of the battery at the start of the trip. Note that the amount of emission is nonzero for the combustion fleet and it is zero for the electric fleet while the SOC change is only applicable to the electric fleet.

After constructing the multidimensional grid of Equation (21) offline, it is then used as the database during the vehicle routing optimization process. This is very beneficial since there is no need to run an ADVISOR simulation during the optimization loop of solving the routing problem, which can significantly reduce the computational load of the optimization problem.

Given the fact that the multidimensional grid in Equation (21) is discrete if a load of vehicles or state of charge of a vehicle is between two discrete values of the grid, a linear interpolation approach is used over the multidimensional grid to calculate the fuel consumption, emission and the SOC change of a trip from one node to another.

3. 2. SA Algorithm   The SA algorithm is tailored to find an optimal or near-optimal solution to the proposed VRP problem. The main advantage of SA is using exchange methods to produce new neighbors stochastically and search in a wider domain for better solutions to avoid being trapped in local extremums. The SA algorithm involves an outer loop for increasing initial temperature and an inner optimization loop. The iterative process continues until reaching the lowest limit of temperature or realizing the predetermined number of iterations.

3. 2. 1. Solution Vector Definition   The solution vector is defined as a vector of an ordered sequence of customers' ids. A delimiter technique is used within the solution vector to create the distinction between customers that are allocated to different vehicles. In addition to the customers, recharging stations need to be added to the solution vector. However, the required number of recharging stations is not known initially since they are not all mandatory to be visited according to the assumption of the problem. To select and place recharging stations along the customer route, a subset of stations is randomly placed along the customers' routes. Afterward, in each iteration, the number of recharging stations is reduced to avoid unnecessary visits to redundant recharging stations, until the best and most feasible solution vector is obtained.

3. 2. 2. SA Exchange Methods   In the SA process, the current solution vector needs to be replaced by its neighboring stochastically. Several different exchange methods can be implemented to generate neighborhoods. In this paper, four exchange methods, including swapping, insertion, reversion, and elimination, are used, where two index positions i, and j (i.e. two distinct numbers smaller than the length of the solution vector n where $i_1 < i_2 < n$) are randomly selected as the place in the solution vector to change the current solution vector under these four methods [23]. The swap operator is almost similarly to insertion whereas two distinct numbers change their position in the string vector. Inversion acts similar to the swap operator, except that in addition to swapping, it also puts the numbers between the two numbers reversely on the string vector. Due to the presence of a random insertion operator, the number of recharging stations added in each iteration of the algorithm may be surplus. For this reason, the removal operator was used such that with a low probability in each iteration of the algorithm, the number of recharging stations was reduced to end up with a lower cost while the solution remains feasible.

3. 2. 3. Overall Framework　　Figure 2 illustrates the proposed framework to solve the VRPs. According to this figure, the framework consists of three main layers; an offline layer (denoted in red) which calculates the required tensors of travel information by ADVISOR which are needed for the other layers; an outer optimization layer (denoted in yellow) that uses the ε-constraint approach to find the Pareto optimal solution; an inner optimization layer based on SA to find the optimal solution for each given ε. After reaching the SA stop condition for all values of epsilon, the Pareto frontier will be obtained as the final answer.

4. RESULTS AND DISCUSSION

In this section, the results of the proposed framework for solving the routing problem of a set of benchmark instances are presented. The benchmark instances are based on the Solomon modified data [4], which extends 56 VRPTW instances with a mixed fleet and recharging stations. To evaluate the solution method presented in this research, a sample problem of the transportation system has been set up. Table 1 summarizes the instances of the problem.

Accordingly, there are 15 customers with a time window between 0 to 8, 5 charging stations, and a fleet of 6 vehicles including 3 conventional and 3 electric vehicles. The algorithm was programmed in MATLAB and executed with the hardware of Intel(R) Core (TM) i7-3770K CPU, 3.5 GHz with 8 GB of RAM.

The mixed fleet contains two types of conventional and electric vehicles, including Navistar eStar Electric

TABLE 1. The details of the problem instances, including customers and recharging stations

Code	Type	Demand (kg)	Earliest starting	Latest starting	Service
			Time (hours)		
C01		100	0	8	0.25
C02		100	0	8	0.25
C03		200	0	8	0.5
C04		100	0	8	0.25
C05		100	0	8	0.25
C06		300	0	8	0.75
C07	Customers	100	0	8	0.25
C08		100	0	8	0.25
C09		100	0	8	0.25
C10		300	0	8	0.75
C11		200	0	8	0.5
C12		400	0	8	1
C13		300	0	8	0.75
C14		100	0	8	0.25
C15		100	0	8	0.25
S16		0	0	8	0
S17	Recharging stations	0	0	8	0
S18		0	0	8	0
S19		0	0	8	0
S20		0	0	8	0

Truck and ISUZU NKR 77- 5.2 Ton, whose specifications are summarized in Tables 2 and 3, respectively.

Table 4 includes all values of different cost parameters which are based on the research performed by Lin et al. [24], Feng and Figliozz [25]. Table 5 summarizes the economic data and assumptions of electric and conventional vehicles based on the work of [24], Feng and Figliozz [25].

Figure 2. The schematic diagram of the proposed optimization framework to solve the VRPs. There are three main layers; an offline layer (red) containing travel information provided by the advisor. An outer optimization layer (yellow) illustrated a Pareto optimal solution using an Epsilon constraint. An inner layer (blue) demonstrates the simulated annealing process

TABLE 2. Specification of Navistar eStar- Electric Truck [26]

Parameters	Amount
Net weight (kg)	3185
Load capacity (kg)	2313
Battery capacity (kWh)	80
Battery voltage (V)	300
Electric motor max power (kW)	70
Max range (km)	160
Air Drag Coefficient	0.5

TABLE 3. Specifications of Isuzu ELF truck N [27]

Parameters	Amount
Net weight (kg)	3185
Load capacity (kg)	2313
Engine capacity (CC)	3000
Max speed (km/h)	102
Tank capacity (L)	75
Air Drag Coefficient	0.7

TABLE 4. Considered cost parameters

Cost parameter	Description	Amount	Reference
f_D	Driver wage during working hours ($/h$)	16.43	
f_Y	Battery charging cost ($/kWh$)	0.12	[24]
f_L	Combustion fuel cost ($/L$)	1.03	
$f_{o,E}$	Electric vehicle operating cost ($/km$)	0.40	[25]
$f_{o,IC}$	Combustion vehicle operating cost ($/km$)	0.14	

TABLE 5. Economic data and assumptions of vehicles (maximal age=10 years, rate of interest=6.5%) [25]

Vehicle	Acquisition Cost ($)	Utilization (km/year)	Salvage value ($)
Navistar	149000	41840	58451
Isuzu	50000	41840	12803

In a real simulation, the real values can be taken into account, and the preferred output can be obtained using navigational and surveying equipment such as a Global Positioning System (GPS) to predict energy consumption and provide data based on the route of the vehicles in the simulation environments. Among 20 standard drive cycles that are selected as the benchmark, one is assigned randomly to every possible route between all the binary combinations of nodes. It is also assumed that the two types of vehicles in the fleet follow the same driving cycles between two nodes since the selected vehicle types fall in the same vehicle class with comparable specifications. The speed profiles of the selected driving cycles are presented in the appendix in Figure A1.

Table 6 summarizes the optimal hyperparameters of the SA method obtained by the Taguchi L16 method.

To obtain the Pareto front, the epsilon changes from 1500 to 0 with the step of 75. The obtained Pareto frontier points are shown in Figure 3. In this figure, the highest amount of costs and emissions belong to the lowest value of emissions (point 1) and costs (point 13), respectively.

In fact, it depicts the effectiveness of using a mixed fleet of electric and conventional vehicles. The routing associated with the Pareto frontier points is summarized in Table 7. According to this table, among the points that are in the Pareto frontier, the solution points that have less emission correspond to the routings in which more nodes are assigned to the electric vehicles.

On the other hand, the points that have more emissions correspond to the routings which involve using more combustion vehicles. To investigate the cost of the Pareto points in detail, Table 7 and Figure 4 summarize the break-down of the total cost, in terms of fuel consumption cost, the annual operating cost, driver of fuel consumption has increased with the increase in wages, the recharging cost, the cost of a battery kilowatt-hour, and the amount of emission. Accordingly, the cost number of combustion vehicles. The operating cost of the first Pareto point is higher than others, which means that more use of the electric fleet would result in more operational costs.

According to the priority of the design objectives, one can choose the final solution among the Pareto front points. If the cost is of the highest priority, using more combustion vehicles is more cost-effective compared to the electric fleet. On the other hand, with more priority on reducing the total emission, allocation of fewer combustion vehicles to customers is desirable.

According to the results, using more electric vehicles results in far less emissions, despite the total costs increase. The increase in the total costs is due to the increase in operating costs and the driver's wage. There is an increase in the total costs because the electric vehicle has traveled along the route for a longer period of

TABLE 6. Simulated Annealing hyper-parameters obtained by Taguchi L16 method

| SA parameters	Amount
Initial temperature	100
Iteration of each temperature	100
Temperature decrease factor	0.1
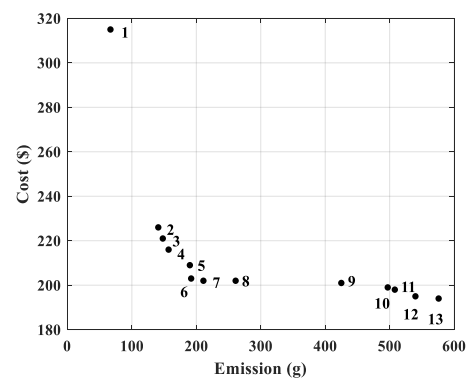
Figure 3. Pareto frontier solutions of the bi-objective routing problem

TABLE 1. Details of the Pareto frontier points. For each solution, combustion and electric fleets are assigned to different customers which results in different emissions and total costs

	Z_2	Z_1	Allocated customers					
Pareto Point	Emission (g)	Cost ($)	Combustion Fleet			Electric Fleet		
1	66.8	315	-	-	1	8-11-5-9-7-15-13-2-4	6-3-14	12-10
2	141	226	-	1	11-8	4-5-13-9-10-15-3-7	14-12-6-2	-
3	148	221	-	1	11	4-5-7-3-15-10-9-13-8	4-12-6-2	-
4	157	216	-	4	11-8	2	7-15-3-6-1-12-14-10-9-13-5	-
5	190	209	-	5-4	8	2-6-1-12-10-13-9-15-3-7	11-14	-
6	192	203	-	4	8	2-6-1-3-15-7-5-13-9-10-12-14	11	-
7	211	202	-	7	11	2-6-5-4	14-10-12-1-3-15-9-13-8	-
8	261	202	-	2	2-5-7	14-10-12-1-6-3-15-9-13-8	11	-
9	425	201	-	11	3-15-9-13-8	14-10-12-1-6-2	4-5-7	-
10	497	199	-	4-5-7-15-3	8-13-9	11	14-10-12-1-6-2	-
11	508	198	-	7	4-5-13-9-8	14-12-10-15-3-1-6-2	11	-
12	540	195	-	8-13-9-15-3	4-5-7	14-10-12-1-6-2	11	-
13	576	194	-	4-5-13-9-15-3-7	8	11	14-10-12-1-6-2	-
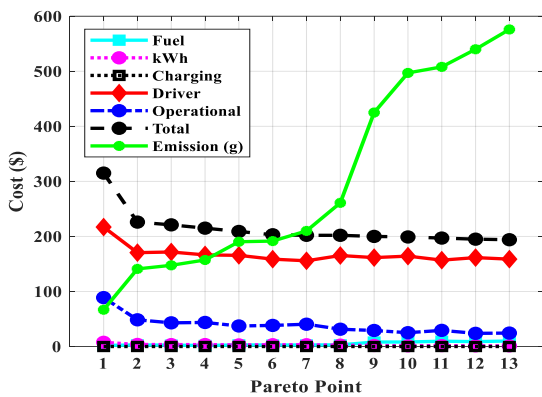
Figure 4. The breakdown of cost for the Pareto frontier points along with the emission

time (using the charging stations). Despite a decrease in the total cost, the number of conventional vehicles and emission increase along the route. A combination of the conventional and electric fleet can provide a solution that is balanced in terms of cost and emission. This can be achieved by selecting a middle point of the Pareto frontier, such as point 7 or point 8. In terms of cost, there is a small difference between these two points. This is because the operational cost of point 8 is less than point 7 while the driver cost is more (Figure 4 and Table 8).

The main difference between them is the amount of emission, which is due to the larger number of allocated combustion vehicles for point 8. Accordingly, one can select point 7 as the balanced final solution of the Pareto frontier.

TABLE 8. The cost breakdown and the emission values of the Pareto frontier solutions

Pareto Point	Fuel Cost ($)	Battery kWh Cost ($)	Charging Cost ($)	Driver wage ($)	Annual Operational Cost ($)	Total Cost ($)	Emission (g)
1	1.990	7.60	0	217	88.8	315	66.8
2	2.93	3.70	0	170.5	48.5	226	141.0
3	2.50	3.44	0	171.7	43.0	221	147.5
4	1.940	3.50	0	166.4	43.7	215	157.2
5	2.96	2.88	0	165.6	37.3	209	190.3
6	2.74	3.23	0	158.7	38.3	203	191.5
7	2.82	3.18	0	155.7	40.5	202	210
8	2.99	2.44	0	165.3	31.4	202	261
9	8.10	1.850	0	161.5	29.1	200	425
10	8.19	1.210	0	164.2	25.1	199	497
11	9.66	1.670	0	156.9	29.3	197	508
12	8.86	1.210	0	161.5	23.9	195	540
13	10.04	1.210	0	158.7	24.4	194	576

5. CONCLUSION

In this research, a new variant of the VRPs is formulated for a mixed fleet of vehicles to optimize cost and emission. Additionally, time windows and recharging stations were considered in the presented framework. In addition to considering the multi-objective nature of the routing problem, the proposed framework uses a set of realistic mathematical models to evaluate different travel quantities, including fuel consumption, change in the state of charge, and emission. To solve the resulting optimization model, the epsilon-constraint and simulated annealing methods were used. It was shown that those solutions that involve more electric fleet than combustion fleet, lead to higher total costs and smaller emissions and vice versa. Finally, a discussion was made on how the final solution can be selected from the Pareto frontier according to the design objectives.

Some improvements can be considered for future research. First, the electric fleet was always fully charged in this study. Therefore, taking partial charging into account can improve the results of this problem. This modified way may decrease the total cost of the electric fleet by lowering the charging cost and the driver cost. Second, based on the SA limitations, results may be improved using other well-known metaheuristic methods such as adaptive large neighborhood search. Furthermore, the proposed framework can be tested for a set of real instances to further investigate the effectiveness of the framework in practice.

6. REFERENCES

1. Perera, F., "Pollution from fossil-fuel combustion is the leading environmental threat to global pediatric health and equity: Solutions exist", *International Journal of Environmental Research and Public Health*, Vol. 15, No. 1, (2018), 16. https://doi.org/10.3390/ijerph15010016

2. Agancy, E.E. *Eu ghg emission inventory reported under the unfccc and the kyoto protocol*. 2022; Available from: https://www.eea.europa.eu/themes/climate/eu-greenhouse-gas-inventory.

3. Kucukoglu, I., Dewil, R. and Cattrysse, D., "The electric vehicle routing problem and its variations: A literature review", *Computers & Industrial Engineering*, Vol. 161, (2021), 107650. https://doi.org/10.1016/j.cie.2021.107650

4. Schneider, M., Stenger, A. and Goeke, D., "The electric vehicle-routing problem with time windows and recharging stations", *Transportation Science*, Vol. 48, No. 4, (2014), 500-520. https://doi.org/10.1287/trsc.2013.0490

5. Erdoğan, S. and Miller-Hooks, E., "A green vehicle routing problem", *Transportation Research Part E: Logistics and Transportation Review*, Vol. 48, No. 1, (2012), 100-114. https://doi.org/10.1016/j.tre.2011.08.001

6. Romet, P., Tabusse, R., Gechter, F., Aglzim, E.-H., Jemei, S., Bouquain, D. and Chrenko, D., "Autonomous electric vehicle routing problem using ant colony optimization with consideration

of the battery state-of-health", in 2021 IEEE 33rd International Conference on Tools with Artificial Intelligence (ICTAI), IEEE. Vol., (2021), 475-480. https://doi.org/10.1109/ICTAI52525.2021.00077

7. Hiermann, G., Hartl, R.F., Puchinger, J. and Vidal, T., "Routing a mix of conventional, plug-in hybrid, and electric vehicles", *European Journal of Operational Research*, Vol. 272, No. 1, (2019), 235-248. https://doi.org/10.1016/j.ejor.2018.06.025

8. Macrina, G., Laporte, G., Guerriero, F. and Pugliese, L.D.P., "An energy-efficient green-vehicle routing problem with mixed vehicle fleet, partial battery recharging and time windows", *European Journal of Operational Research*, Vol. 276, No. 3, (2019), 971-982. https://doi.org/10.1016/j.ejor.2019.01.067

9. Bektaş, T. and Laporte, G., "The pollution-routing problem", *Transportation Research Part B: Methodological*, Vol. 45, No. 8, (2011), 1232-1250. https://doi.org/10.1016/j.trb.2011.02.004

10. Zhou, Z., Ha, M., Hu, H. and Ma, H., "Half open multi-depot heterogeneous vehicle routing problem for hazardous materials transportation", *Sustainability*, Vol. 13, No. 3, (2021), 1262. https://doi.org/10.3390/su13031262.

11. Davis, B.A. and Figliozzi, M.A., "A methodology to evaluate the competitiveness of electric delivery trucks", *Transportation Research Part E: Logistics and Transportation Review*, Vol. 49, No. 1, (2013), 8-23. https://doi.org/10.1016/j.tre.2012.07.003.

12. Goeke, D. and Schneider, M., "Routing a mixed fleet of electric and conventional vehicles", *European Journal of Operational Research*, Vol. 245, No. 1, (2015), 81-99. https://doi.org/10.1016/j.ejor.2015.01.049

13. Sivagnanam, A., Ayman, A., Wilbur, M., Pugliese, P., Dubey, A. and Laszka, A., "Minimizing energy use of mixed-fleet public transit for fixed-route service", in Proceedings of the AAAI Conference on Artificial Intelligence. Vol. 35, (2021), 14930-14938. https://doi.org/10.1609/aaai.v35i17.17752

14. Macrina, G., Pugliese, L.D.P., Guerriero, F. and Laporte, G., "The green mixed fleet vehicle routing problem with partial battery recharging and time windows", *Computers & Operations Research*, Vol. 101, (2019), 183-199. https://doi.org/10.1016/j.cor.2018.07.012

15. Demir, E., Bektaş, T. and Laporte, G., "A review of recent research on green road freight transportation", *European Journal of Operational Research*, Vol. 237, No. 3, (2014), 775-793. https://doi.org/10.1016/j.ejor.2013.12.033

16. Kopfer, H.W., Schönberger, J. and Kopfer, H., "Reducing greenhouse gas emissions of a heterogeneous vehicle fleet", *Flexible Services and Manufacturing Journal*, Vol. 26, No. 1, (2014), 221-248. https://doi.org/10.1007/s10696-013-9180-9

17. Ghannadpour, S.F. and Zarrabi, A., "Multi-objective heterogeneous vehicle routing and scheduling problem with energy minimizing", *Swarm and Evolutionary Computation*, Vol. 44, (2019), 728-747. https://doi.org/10.1016/j.swevo.2018.08.012

18. Abad, H.K.E., Vahdani, B., Sharifi, M. and Etebari, F., "A bi-objective model for pickup and delivery pollution-routing problem with integration and consolidation shipments in cross-docking system", *Journal of Cleaner Production*, Vol. 193, (2018), 784-801. https://doi.org/10.1016/j.jclepro.2018.05.046

19. Androutsopoulos, K.N. and Zografos, K.G., "An integrated modelling approach for the bicriterion vehicle routing and scheduling problem with environmental considerations", *Transportation Research Part C: Emerging Technologies*, Vol. 82, (2017), 180-209. https://doi.org/10.1016/j.trc.2017.06.013

20. Hiermann, G., Puchinger, J., Ropke, S. and Hartl, R.F., "The electric fleet size and mix vehicle routing problem with time windows and recharging stations", *European Journal of*

Operational Research, Vol. 252, No. 3, (2016), 995-1018. https://doi.org/10.1016/j.ejor.2016.01.038

21. Alsumairat, N. and Alrefaei, M., "Solving hybrid-vehicle routing problem using modified simulated annealing", *International Journal of Electrical & Computer Engineering (2088-8708)*, Vol. 11, No. 6, (2021).

22. Markel, T., Brooker, A., Hendricks, T., Johnson, V., Kelly, K., Kramer, B., O'Keefe, M., Sprik, S. and Wipke, K., "Advisor: A systems analysis tool for advanced vehicle modeling", *Journal of Power Sources*, Vol. 110, No. 2, (2002), 255-266.

23. Vincent, F.Y., Redi, A.P., Hidayat, Y.A. and Wibowo, O.J., "A simulated annealing heuristic for the hybrid vehicle routing problem", *Applied Soft Computing*, Vol. 53, No., (2017), 119-132. https://doi.org/10.3390/ijerph15010016

24. Lin, J., Zhou, W. and Wolfson, O., "Electric vehicle routing problem", *Transportation Research Procedia*, Vol. 12, No., (2016), 508-521. https://doi.org/10.1016/j.trpro.2016.02.007

25. Feng, W. and Figliozzi, M.A., "Conventional vs electric commercial vehicle fleets: A case study of economic and technological factors affecting the competitiveness of electric commercial vehicles in the USA", *Procedia-Social and Behavioral Sciences*, Vol. 39, (2012), 702-711. https://doi.org/10.1016/j.sbspro.2012.03.141

26. Energy, U.S.D.o. *Navistar estar vehicle performance evaluation – cumulative*. 2014, August; Available from: https://www.nrel.gov/docs/fy14osti/61899.pdf.

27. Motors, I. *Isuzu introduces all-new elf truck(n-series) in japan*. 2006, December 13; Available from: https://www.isuzu.co.jp/world/press/2006/p_1213.html.

Appendix A:
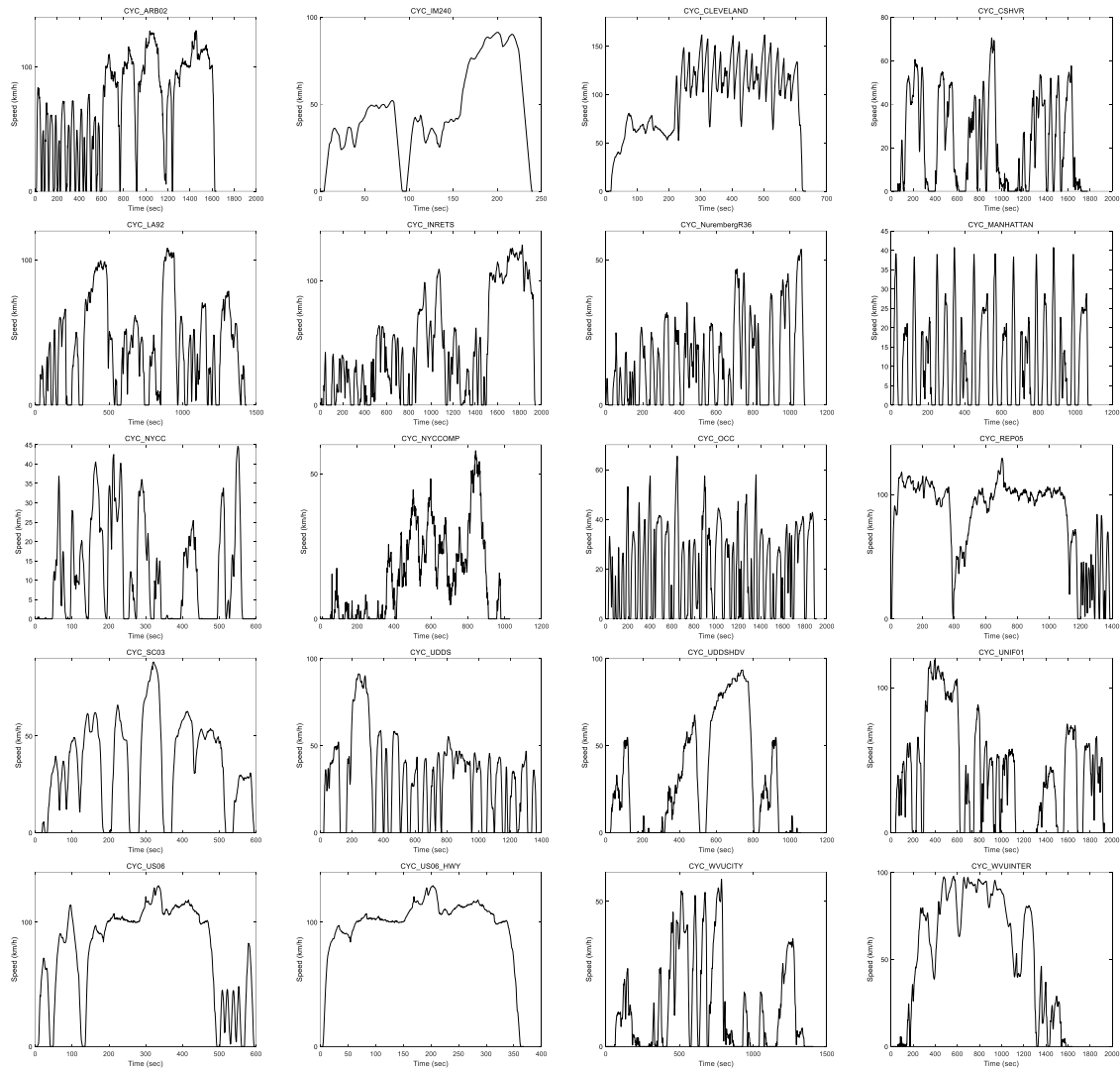
Figure A1. Speed profile of the driving cycles used for the problem instances

Persian Abstract

چکیده

حل مساله مسیریابی وسیله نقلیه، همچنان یک موضوع چالشی مورد مطالعه می باشد. به طور دقیقتر، حل مساله مسیریابی وسیله نقلیه تلفیقی نیازمند محاسبه واقع بینانه عملکرد ناوگان الکتریکی و احتراقی است. در این پژوهش مسئله مسیریابی وسیله نقلیه تلفیقی الکتریکی و احتراقی با در نظر گرفتن پنجره های زمانی و ایستگاه های شارژ بررسی شده است. مدل مسئله از نوع برنامه ریزی عدد صحیح مختلط دو هدفه با اهداف کمینه سازی مقدار هزینه و آلایندگی می باشد. مدل مسئله ابتدا با استفاده از روش محدودیت اپسیلون به مدل تک هدفه تبدیل شده و سپس، از یک الگوریتم شبیه سازی تبرید برای به دست آوردن نقاط بهینه پارتو استفاده شده است. به منظور تعیین دقیق کمیت مقادیر مرتبط با سفر مانند مصرف سوخت، آلایندگی و میزان شارژ باتری از مجموعه‌ای از فرمول‌های ریاضی استاندارد استفاده شده است. نتایج نشان می‌دهد چارچوب ارائه‌شده توانایی دستیابی به مجموعه‌ای از نقاط بهینه پارتو به عنوان تعادلی میان توابع هدف هزینه و آلایندگی با در نظر داشتن ناوگان ترکیبی الکتریکی و احتراقی را دارا می باشد.

Factors Affecting the Cathode Edge Nodulation in Copper Electrorefining Process

A. Ahmadi[a], S. Sheibani*[a], M. Mokmeli[a], S. M. J. Khorasani[b], N. S. Yaghoobi[c]

a School of Metallurgy and Materials Engineering, College of Engineering, University of Tehran, Tehran, Iran
b Process Control Unit, Khatoonabad Copper Refinery, Shahrebabak Copper Complex, Kerman, Iran
c Research and Development Center, Shahrebabak Copper Complex, Kerman, Iran

PAPER INFO	ABSTRACT

In this study the factors that are affecting the copper nodular growth on the cathode edge were investigated from metallurgical and operation point of view. Statistical analysis was performed to evaluate the effect of operational conditions on the nodular copper growth by characterization of the nodule-containing cathodes. Besides, the effects of defects on polymer edge strips as well as changes in weight and thickness of anodes on the formation of nodules were investigated. Electrochemical galvanostatic experiments were employed to study the effect of electrolyte additives and the distance between the anode and cathode on cathode surface quality. A relatively large porosities of about 50 µm were observed in the microstructure of the cathode edge nodules. In addition, few nodule samples that were taken was observed to have a higher concentration of Fe, Cd and Pb, up to 25 ppm. Low probability (1%) in the repeatability of the nodule formation over the same position on the edge strip was approved the insignificant effect of possible edge strip defects on nodulation. The large weight variation of anodes can cause the anode thickness variation by 10 mm and consequently alter the distance between the anode and the cathode. This was shown to cause formation of nodules at the cathode edge. The peaks that were observed in the cathodic potential curves in galvanostatic tests, were believed to be the sign of nodulation and therefore was investigated further using the optical microscopic images.

doi: 10.5829/ije.2022.35.12c.13

1. INTRODUCTION

Copper electrorefining is the final process of copper production. In this electrolytic process, impure copper (99.4-99.5%) as an anode, dissolves and electrodeposits on the surface of the cathode blank or starter sheet as pure copper cathode(>99.995%) [1,2]. Copper nodular growth as an unwanted phenomenon in copper electrorefining process, reduces the surface quality of the product and therefore its economic value [3,4]. Furthermore, the nodulation can causes an uneven distribution of the current density, a reduction in current efficiency, and hence, an increase in the operating cost of the refinery plant. Also, the short-circuiting caused by nodules adversely affect the current efficiency [5-7]. Copper nodular or dendritic growth is a complex phenomenon affected by different factors such as the physical parameters of a starter sheet or cathode blank and anode,

electrolyte additives and temperature, circulation condition and chemical composition of the anodic slimes [8]. The electrolyte additives are organic reagents that are added to the electrolyte to prevent nodulation and control the physical properties of the cathode [9]. Nodulation was attributed to several factors including: (i) the inclusion of slime particles on the surface of cathode, (ii) the local shortage of leveling additives (Cl$^-$, thiourea and gelatin), and (iii) the deformation of the stainless-steel starter sheets. It is believed that once a nodulated surface develops, the localized current density, and hence the copper deposition rate, increases abruptly resulting in the further rapid growth of the nodules. So far, investigations of the nodulation have mainly been focused on the different effective parameters causing the nodulation and mechanisms of the nodules' formation [10,11]. Most of the nodules are grown on the cathode surface due to the electrolyte impurities including Pb, Se, Te, Ag, Bi, As

Corresponding Author Institutional Email: ssheibani@ut.ac.ir
 (S. Sheibani)

and Sn [12,13]. Other types of nodules may grow due to the operational factors such as variation in the distance of anode and the cathode [14]. One of the factors that can change the distance between the anode and the cathode that caused the nodulation is the surface quality of the anode and its weight [15]. The anode weight variation, affects the distance between the anode and cathode which is significantly affected the process [16].

The use of new materials and new characterization techniques is considered a special approach in materials engineering that has been considered in recent years to solve challenges [17,18]. The galvanostatic technique may be used as a helpful tool in detecting the formation of nodules on the cathode surface during the copper electrodeposition process using the value of the starting electrolytic potential and monitoring the cathodic polarization peak on a potential-time curve [19]. In previous studies [2,20] a correlation between the above-mentioned factors and nodular growth at the cathode surface was proven. To the best knowledge of the authors, no reports have studied the conditions at which the nodules may grow on the cathode edge and edge strips. Besides, the mechanism of nodular growth on the cathode edges is not understood well. The cathode edge nodule is a common unwanted phenomenon that more or less is observed in any copper refinery; that was investigated in this study. In this work, it is proven that the anode and cathode configuration is an important factor that affects the nodulation. This will be shown by changing the cathode and anode distance where a small variation in a call configuration largely affects the current density distribution and consequently a growth of irregular crystals. The edge nodulation can cause problems during the copper production process such as damaging the refinery equipment and the polymer edge strips and therefore reduces the production efficiency. This study aims to reveal the nodulation mechanism of the edge side and to evaluate factors that may fortify the edge nodulation using the electrochemical tools.

2. EXPERIMENTAL PROCEDURE

Samples were used in this study were all taken from a refinery plant of Khatoonabad copper complex. At first, nodule-containing cathodes were marked and sampled, then various analyses were performed on samples both with and without nodules, as shown in Figure 1. The microstructure was studied using an optical microscope (OLYMPUS-BH2UMA), a stereo microscope (NSZ-806) and a FESEM (Cam-Scan MV2300). Besides, the chemical composition and impurity analysis was performed using ICP-MS (ELAN DRC-2-Perkin Elmer SCIEX). In addition, the effect of various operational factors such as possible defects in the polymer edge strip or cathode blank and the changes in a weight and

thickness of the anodes was statistically analyzed by taking different samples from the plant at different time intervals.

The nodules formation and growth was investigated using the galvanostatic technique. The electrolyte solution was made similar to Khatoonabad refinery plant. The electrolyte was made at a composition of 42 g.L^{-1} CuSO$_4$, 160 g.L^{-1} H$_2$SO$_4$, 40 mg.L^{-1} HCl, 4 mg.L^{-1} thiourea, and 11.5 mg L^{-1} gelatin. The electrolyte was preheated to 55 °C±0.5 °C. The current density used in the experiments was 500 A.m^{-2}. The deposition continued for 1 h without stirring. A commercially pure titanium plate (30×10×1 mm), a 316 stainless steel plate (30×12×3 mm) and anode copper plate (30×10×5 mm) from Khatoonabad were used as reference electrode, cathode and anode. The potential of the cathode surface relative to reference electrode was measured. Electrode surface preparation was performed using silicon carbide grinding papers following by cleaning, rinsing, and drying. The facial surface area of the cathode plate submerged in the electrolyte was 1.2 cm^2. All electrorefining experiments were performed at constant current densities using a rectifier (IPC SL20PRC). The galvanostatic tests were employed to investigate the effect of additives in the electrolyte as shown in Figures 2(a) and 2(b) and to investigate the effect of the anode and cathode arrangement on nodular formation. For this purpose, the effect of reducing the distance between the anode and cathode in various configurations were investigated (see Figure 2).
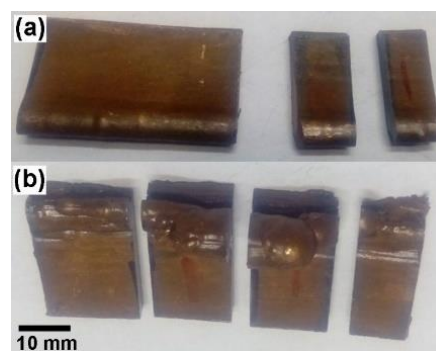

Figure 1. Samples of the cathode at different regions (a) without and (b) with nodules on the edge
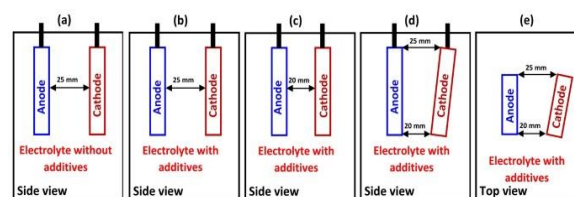

Figure 2. Position and distance of anode and cathode in the galvanostatic cell for experimental conditions of (a) T1, (b) T2, (c) T3, (d) T4 and (e) T5 experiments

3. RESULTS AND DISCUSSION

3. 1. Microstructure and Chemical Analysis of Nodules

Microscopic techniques have been used to examine and compare the microstructure of samples. Optical microscope and FESEM images of the cathode at different regions with and without nodules on the edge are shown in Figure 3. Comparison of the images for samples without and with nodules presented in Figures 3(a) and 3(b), respectively. That indicates the only noticeable difference to be the presence of relatively large porosities in a sample with nodules as shown in the optical and FESEM images in Figure 3(b). The size of the pores can easily reach up to 50 µm. Beside this large pore, both samples are contained very small porosities. This change in the microstructure can be caused by nodule formation or the cause of nodule formation, which will be further investigated.

Considering that the impurities can be a reason of nodule formation, the nodules at the cathode edge were sampled and analyzed. The chemical composition results are given in Table 1. The results showed similar values for most of the elements. However, for the few samples that were taken, differences in anlaysis of the three elements of Fe, Cd, and Pb was observed. The amount of Fe, Cd and Pb in the sample taken from the nodule was higher or equal to 22, 22 and 25 ppm, respectively; while for the sample without nodule were less than 1 ppm. This variation does not change the total concentration of the cathode and its deviation form cathode grade 1. The level of impurities that was proved to be the source of nodulation and was reported in the previous research [13], is much higher than the values found in the present study. For example, in presence of Pb up to 80 ppm, no nodule was observed in the cathode [13]. Therefore, it might be concluded that the presence of impurities at levels observed in the present study is not the main reason for nodule formation. It should be noted that this analysis is dependent on the number of analyzed samples.

TABLE 1. ICP analysis results of the sample without and with nodules (wt.%)

Element	Sample without nodules	Sample with nodules
Cu	99.995	99.992
Ag	0.005	0.001
Ba	0.0001<	0.0001<
Co	0.0001<	0.0001<
Fe	0.0001<	0.0022
Mg	0.0001<	0.0001<
Pb	0.0001<	0.0025
P	0.0001<	0.0001
Si	0.0001<	0.0001<
Ti	0.0001<	0.0001<
Al	0.0001<	0.0001<
Bi	0.0001<	0.0001
Cr	0.0001<	0.0001<
Mn	0.0001<	0.0001<
Se	0.0001<	0.0001<
Cd	0.0001<	0.0022
Sn	0.0001<	0.0001<
V	0.0001<	0.0001<
As	0.0001<	0.0001<
Ca	0.0001<	0.0001<
K	0.0001<	0.0001<
Mo	0.0001<	0.0001<
Ni	0.0001<	0.0001<
Ga	0.0001<	0.0001<

One of the possible reasons for nodule formation at the cathode edge could be similar to the conventional nodules formation and due to the accumulation of impurities at the cathode edge. As a result, the reason for accumulation of impurities in this particular area must be determined. Beside impurity distribution, other factors such as operational factors should be studied.

3. 2. Effect of Operational Factors on Nodular Growth

In this section and according to the results obtained in Table 2, the effect of operational factors on the formation of nodules at the cathode edge was investigated. In this regard, the effect of factors that disrupt the current density distribution was investigated. These possible factors are as follows:

3. 2. 1. Physical Defects in the Polymer Edge Strip or Cathode Starter Sheets

To investigate the effect of possible defects in the polymer edge strip or

Figure 3. Optical microscope and FESEM images of the cathode at different regions (a) without and (b) with nodules on the edge

cathode blank, the repeatability of nodule formation at marked locations of cathodes were evaluated.

This was performed on 60 cathodes of Khatoonabad copper refinery. For this purpose, the cathode blank were carefully marked at the nodulation place. After cathode stripping, the cathode blank were placed back in the electrolyte cell for another 10 days. The position of nodules at the edge of the cathodes was then determined and the repeatability of the nodule formation in each cathode and at the same position was monitored. The statistical results are summarized in Figure 4. The repeatability of nodule formation for a second time in a similar cathode blank was found to be 25%. The probability of recurrence of nodule formation in the similar position of a cathode blank was however below 4% (1 of 60 cases). Nodules in the remaining 21% were occurred elsewhere at the cathode edge. From these results, the conclusion can be drawn that nodulation on the polymer edge strip is not due to physical defects. Because if the defect in the edge strip caused nodule formation, the probability of repeating of nodule formation in the same previous position should be higher. For this reason, other possible factors were examined.

3. 2. 2. Changes in Weight and Thickness of Anodes Possible effect of changes in the anode weight and thickness on nodulation at the cathode edge, was studied by monitoring the weight distribution of 4000 anodes that is shown in Figure 5. The average anode weight was observed to be 346 kg. The minimum and maximum weights are 338 and 373 kg, respectively. In this analysis, the allowable number of changes in the weight of the anodes relative to the average weight was important. Previous research [18, 21] showed that the maximum tolerance up to ±10 kg have been accepted. The weight change can cause a thickness change of up to ±5 mm, depending on the dimensions of the anode. Considering the dimensions of the anodes used in Khatoonabad copper refinery, the relationship between thickness versus anode weight is shown in Figure 5. It can be seen the allowable range of weight change that results in a thickness change of less than 1 mm is about ±5 Kg. This range of weight change is shown on the


Figure 5. Distribution diagram of anodes weight. The inset shows the anode thickness versus anode weight

weight distribution diagram in Figure 5 with a dashed line.

As a result, approximately 15% of the anodes weigh is out of the acceptable range, and about 1% of the anodes weigh more than 20 kg of the average weight. This large weight difference can lead to a change in anode thickness up to 10 mm. It should be noted that this weight change often does not cause a uniform change in anode thickness. This change in the thickness of anodes is equal to a large change in the distance between the anode and the cathode in the cell, which can cause a change in the current density of the none uniform surfaces and nodule formation.

In Figure 6, the thickness of above-mentioned anodes were measured at different positions of the anode (top, bottom, left and right). In Figure 6 the thickness varies at different positions of an anode and as the weight of the anode increases, the thickness difference increases. For example, in the anode weighing 373 kg, the difference between the left and right side of the anode is 9 mm. This difference in thickness will change the distance between the anode and the cathode. For this reason, the current density will be different in these two positions. This phenomenon, especially at the beginning of the process, can cause anode passivation or nodular growth on the cathode in a position with smaller distance difference.


Figure 4. Results of the repeatability of nodule formation at a specific position on the cathode starter sheets
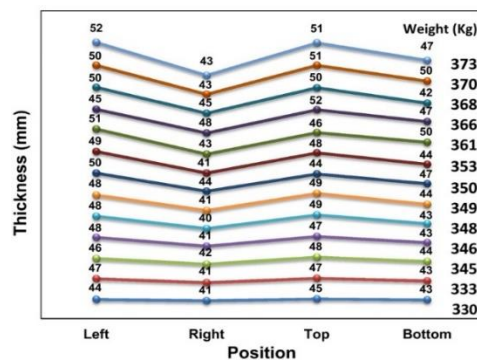
Figure 6. Changes of anode thickness in its various positions (left, right, top and bottom)

Previous research [18, 21] showed that a 5 mm local reduction in the distance between the anode and cathode can increase the current density by up to 20% locally. The distance at the anode edges is therefore a reason for nodule formation at the left side cathode edges.

3. 3. Galvanostatic Tests Results   According to the previous section observation, galvanostatic tests were performed to investigate the effect of nodule formation factors in a laboratory scale. According to the anode and cathode arrangement presented in Figure 2, the cathodic potential curves versus time were generated and showed in Figure 7. No peaks were observed for the arrangement b, T2 experiment, while two or three peaks are seen for other arrangements. In each peak, the cathodic potential decreases by approximately 40 to 60 mV. The presence of the peak in the cathodic potential curve is an indication of current unbalance during the deposition process. Based on the previous research [19, 20, 22], this current unbalance can be attributed to the nodular growth at cathode surface or edges. This means that for a test where additives is not used (T1 experiment), and for tests the cathode and anode have not normal arrangement, reducing the distance between the anode and the cathode from 25 to 20 mm (T3 experiment), either from the bottom (T4 experiment) or the lateral side (T5 experiment) have caused peak generation and possibly conditions for nodule formation. It should be noted that T2 experiment was developed similar to the industrial cell condition. A comparison of the T1 and T2 curves shows that the presence of additives in electrolyte increases the cathodic potential during the experiment [5, 6, 23].

The surface quality of cathodes formed at different conditions of galvanostatic tests was studied using an optical microscopic image shown in Figure 8. Images with higher magnifications from area 1 and 2 (shown in white rectangles) are shown at the right-hand side. Relatively smooth and homogeneous deposit without nodular growth was produced under T2 arrangement; as shown in Figure 8(b). However, in the absence of electrolyte additives (T1 experiment), the quality of deposit was not uniform and nodules were formed at the surface and edges of cathode; as shown in Figure 8(a). The additive role in improving cathode quality was verified in many previous studies [23, 24]. Additives promote the plating of smooth, dense copper deposits with minimal impurities. The effects of uniformly reducing the distance between the anode and cathode from 25 to 20 mm (T3 experiment), either from the bottom side (T4 experiment) or the lateral side (T5 experiment) is shown in Figures 8(c), 8(d) and 8(e), respectively. Reducing the distance has led to the formation of different types of nodules on the surface or on the edge. The results from the experiments indicate the importance of anode and cathode configuration in the

cell. To produce a smooth cathode without nodules it is necessary to have a uniform distribution of current density over the entire cathode surface.
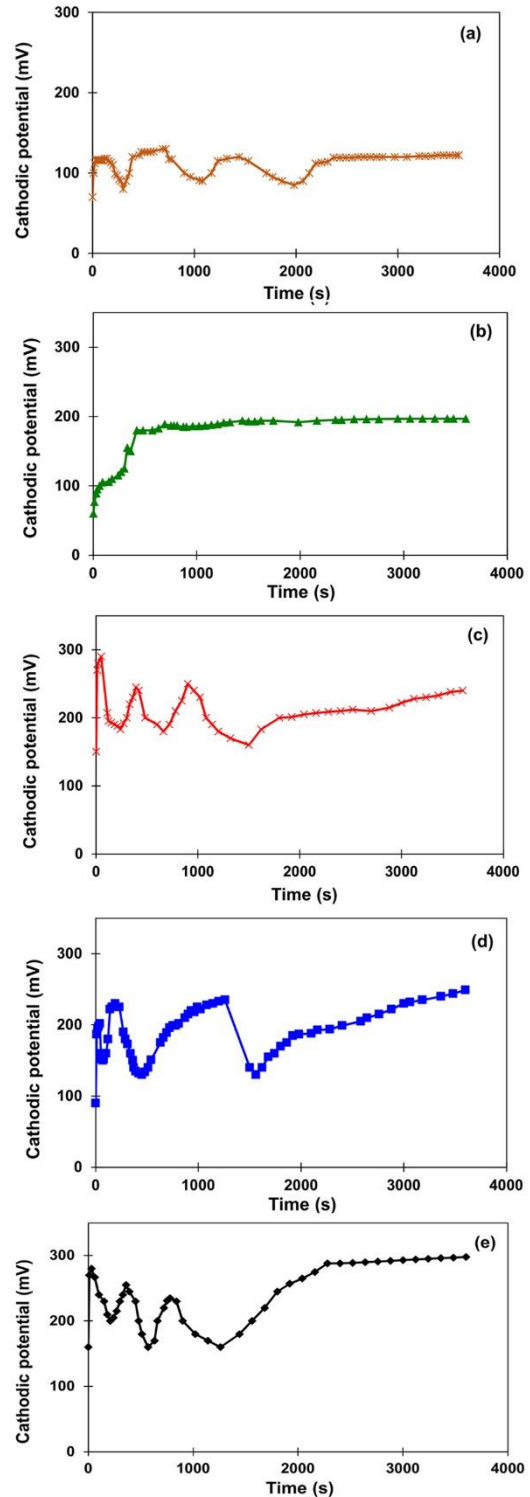

Figure 7. Cathodic potential curves versus time for (a) T1, (b) T2, (c) T3, (d) T4 and (e) T5 experiments
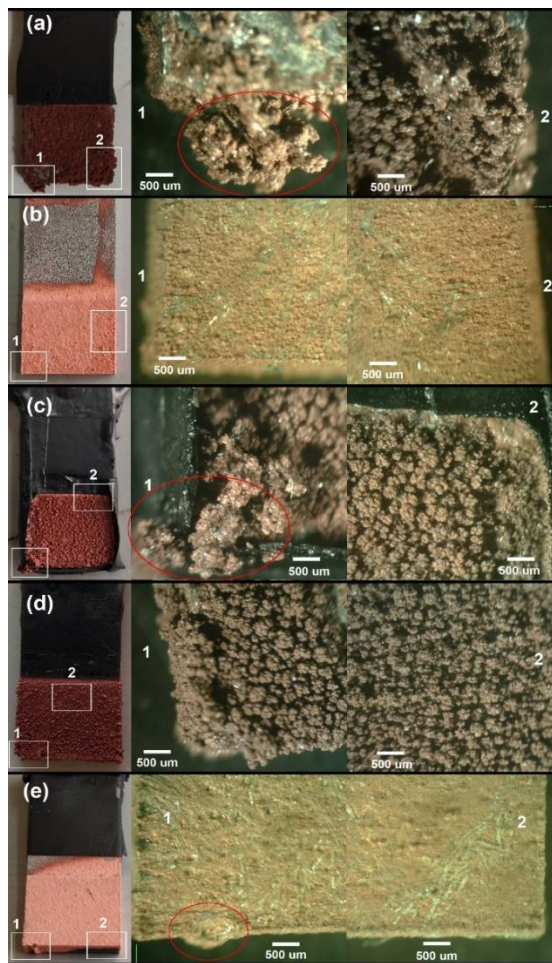
Figure 8. Optical images from the cathode surface for (a) T1, (b) T2, (c) T3, (d) T4 and (d) T5 experiments

To reach this objective, it is important to provide a constant distance between the anode and the cathode. It is also necessary to control the distance during the electrolysis operation. Ohmic electrolyte resistance, is dependent to the electrode distance and geometry. Different anode-cathode configuration with the consequence of variation in a current density resulted in irregular crystal growth and dendrite formation. Nodules on the edge were marked with a red oval in Figures 8(a), 8(c) and 8(e). The presence of peaks in the cathodic potential diagrams is consistent with nodule formation on cathode. In conclusion, changing the distance between the anode and the cathode not only caused the formation of nodules at the cathode edge but also at the cathode surface.

4. CONCLUSION

In this research, edge nodulation of the copper cathode was studied at Khatoonabad copper refinery.

Investigation was conducted by looking into the galvanostatic experiments to investigate the nodular growth during electrorefining process. The main results are as follows:

1. The optical and FESEM images showed that the main microstructural difference between the nodule and nodule-free regions is the presence of relatively large porosities with diameter of up to 50 µm.

2. The difference between the chemical composition of the noduled area and nodule-free area for the samples taken was observed to be higher for Fe, Cd and Pb in the noduled samples. This change was not caused devation of total concentration from cathode grade 1.

3. The repeatability of nodule formation in a similar position of a starter sheet was found 4%. Hence, nodule formation was not due to the physical defects in the polymer edge strip or stainless-steel cathode blank.

4. A large weight difference can lead to a change in a thickness of anode and therfore be a source of nodule.

5. The galvanostatic test showed that reducing the distance between the anode and the cathode can cause the formation of nodules at the cathode edge and cathode surface. This is parallel with the presence of peaks observed in the cathodic potential experiments.

6. Changes in anode weight and consequently the thickness of the anodes can shorten the local distance between the anode and the cathodeand a reason for nodule formation at the cathode edges.

5. ACKNOWLEDGMENTS

6. REFERENCES

1. Schlesinger, M.E., Sole, K.C., Davenport, and W.G., Extractive Metallurgy of Copper. Oxford: Elsevier Science, (2011).

2. Shojaei, M.R., Khayati, G.R., Assadat Yaghubi, N., Bagheri Sharebabaki, F., and Khorasan, S.M.J., "Removing of Sb and As from Electrolyte in Copper Electrorefining Process: A Green Approach." *International Journal of Engineering, Transactions C: Aspects,* Vol. 34, No. 3, (2021), 700-705. doi: 10.5829/ije.2021.34.03c.14.

3. Khazaei Feizabad, M.H., Khayati, G.R., Kafi Hernashki, R., Khorasani, and S.M.J., "Modeling and Optimization of Charge Materials Ranges in Converter Furnace with Enhanced Passivation Time in Copper Electrorefining Process: A Mixture Design Approach." *International Journal of Engineering, Transactions A: Basics*, Vol. 34, No. 4, (2021), 966-975. doi: 10.5829/ije.2021.34.04a.23.

4. Behagh, A.M., Fadaei Tehrani, A., Salimi Jazi, and H. R., Behagh, O., "Simulation of Nickel Electroforming Process of a Revolving Part Using Finite Element Method." *Iranian Journal of Materials Science and Engineering,* Vol. 12, No. 1, (2015), 20-27. doi: 10.22068/ijmse.12.1.20

5. Dutrizac, J.E., and Chen, T.T., "A Mineralogical Study of Nodulated Copper Cathodes." 4th International Conference Copper 99-Cobre 99, Volume III-Electrorefining and Electrowinningof Copper, The Minerals, Metals & Materials Societ, (1999), 383-403.

6. Xu, J., Ren, W., Lian, Z., Yu, P., and Yu, H., "A Review: Development of the Maskless Localized Electrochemical Deposition Technology." *The International Journal of Advanced Manufacturing Technology*, Vol. 110, (2020), 1731-1757, doi: 10.1007/s00170-020-05799-5.

7. Aqueveque, P., Wiechmann, E., and Burgos, R.P., "Short-Circuit Detection for Electrolytic Processes Employing Optibar Intercell Bars." *IEEE Industry Applications*, Vol. 45, (2009), 1225-1231. doi: 10.1109/07IAS.2007.267.

8. Muhlare, T.A., and Groot, D., "The Effect of Electrolyte Additives on Cathode Surface Quality during Copper Electrorefining." *Journal of the Southern African Institute of Mining and Metallurgy*, Vol. 111, No. 5, (2011), 371-378 .

9. Andersen, T.N., Budd, R.D., and Strachan, R.W., "A Rapid Electrochemical Method for Measuring the Concentration of Active Glue in Copper Refinery Electrolyte Which Contains Thiourea." *Metallurgical Transactions B*, Vol. 7, No. 3, (1976), 333-338. doi: 10.1007/BF02652702.

10. Moskalyk, R.R., and Alfantazi, A.M., "Nickel Laterite Processing and Electrowinning Practice." *Minerals Engineering*, Vol. 15, No. 8, (2020), 593-605. doi: 10.1016/S0892-6875(02)00083-3

11. Andersen, T.N., Pitt, C.H., and Livingston, L.S., "Nodulation of Electrodeposited Copper Due to Suspended Particulate." *Journal of Applied Electrochemistry*, Vol. 13, No. 4, (1983), 429-438. doi: 10.1007/BF00617517.

12. Fischer, H., "Aspects of Inhibition in Electrodeposition of Compact Metals II: Effects of Morphological Interface Inhibition." *Electrodeposition and Surface Treatment*, Vol. 1, No. 4, (1973), 319-337. doi: 10.1016/0300-9416(73)90038-2.

13. Fischer, H., "Aspects of Inhibition in Electrodeposition of Compact Metals: I. Effects of Electrochemical Iinhibition." *Electrodeposition and Surface Treatment*, Vol. 1, No. 3, (1973), 239-251. doi: 10.1016/0300-9416(73)90017-5.

14. Mubarok, Z., Filzwieser, I., and Paschen, P., "Electrochemical and Metallographic Characterization of Inhibitor Variation in Copper Refining Electrolysis." European Metallurgical Conference, EMC 2005, Dresden, Germany, (2005).

15. Mubarok, Z., Filzwieser, I., and Paschen, P., "Dendritic Cathode Growth during Copper Electrorefining in the Presence of Solid Particles." European Metallurgical Conference, EMC 2005, Dresden, Germany, (2005).

16. Filzwieser, I. "The Analysis and Mathematical Modelling of the Parameters Influencing Cathodic Deposits in Copper Refining Electrolysis." PhD Thesis, Montanuniversität Leoben, Department fur Metallurgie, 2005.

17. Saindane, U.V, Soni, S., and Menghani, J.V., "Dry Sliding Behavior of Carbon-based Brake Pad Materials." *International Journal of Engineering, Transactions B: Applications*, Vol. 34, No. 11, (2021), 2517-2524. doi: 10.5829/ije.2021.34.11b.14.

18. Saindane, U.V, Soni, S., and Menghani, J.V., "Friction and Wear Performance of Brake Pad and Optimization of Manufacturing Parameters using Grey Relational Analysis." *International Journal of Engineering, Transactions C: Aspects*, Vol. 35, No. 3, (2022), 552-559. doi: 10.5829/ije.2022.35.03C.07.

19. Lafront, A.M., Veilleux, B., and Ghali, E., "Galvanostatic and Microscopic Studies of Nodulation during Copper Electrolysis." *Journal of Applied Electrochemistry*, Vol. 32, No. 3, (2002), 329-337. doi: 10.1023/A:1015589725641.

20. Safizadeh, F., Lafront, A.M., Ghali, E., and Houlachi, G., "An Investigation of the Influence of Selenium on Copper Deposition During Electrorefining Using Electrochemical Noise Analysis." *Hydrometallurgy*, Vol. 111-112, (2011), 29-34. doi: 10.1016/j.hydromet.2011.09.008.

21. Moskalyk, R.R., Alfantazi, A., Tombalakian, A.S., and Valic, D., "Anode Effects in Electrowinning." *Minerals Engineering*, Vol. 12, No. 1, (1999), 65-73. doi: 10.1016/S0892-6875(98)00120-4

22. Pearson, T., and Dennis, J., "Effect of Pulsed Reverse Current on the Structure and Hardness of Copper Deposits Obtained from Acidic Electrolytes Containing Organic Additives." *Surface and Coatings Technology*, Vol. 42, No. 1, (1990), 69-79. doi: 10.1016/0257-8972(90)90115-S.

23. Ke, B., Hoekstra, J.J., Sison, B.C., and Trivich, D., "Role of Thiourea in the Electrodeposition of Copper." *Journal of the Electrochemical Society*, Vol. 106, No. 5, (1959), 382-388.

24. Lakshmanan, V.I., Mackinnon, D.J., and Brannen, J.M., "The Effect of Chloride Ion in the Electrowinning of Copper." *Journal of Applied Electrochemistry*, Vol. 7, No. 1, (1977), 81-90. doi: 10.1007/BF00615534.

Persian Abstract

چکیده

در این مطالعه، عوامل موثر بر رشد ندولار مس روی لبه کاتد از دیدگاه متالورژی و عملیاتی بررسی شده است. به منظور ارزیابی اثر شرایط عملیاتی روی رشد ندولار مس، تحلیل آماری روی کاتدهای دارای ندول انجام شده است. همچنین، تاثیر عیوب روی نوار لبه پلیمری و تغییرات وزن و ضخامت آندها بر تشکیل ندول مطالعه شده است. به منظور مطالعه تاثیر افزودنی‌های الکترولیت و فاصله بین آند و کاتد بر روی کیفیت سطح کاتد، از آزمایش‌های گالوانواستاتیکی الکتروشیمیایی استفاده شده است. تخلخل‌های نسبتا درشت با اندازه حدود ۵۰ میکرون در میکروساختار مربوط به ندول‌های لبه کاتد مشاهده شد. علاوه بر این، نتایج نشان داد که نمونه‌های ندول گرفته شده حاوی مقادیر بیشتری از آهن، کادمیم و سرب تا ۲۵ ppm بود. احتمال کم (٪۱) در تکرار تشکیل ندول در موقعیت یکسان روی نوار لبه بیانگر آن بود که تاثیر عیوب نوار لبه بر تشکیل ندول ناچیز است. تغییرات وزنی زیاد در آندها منجر به تغییرات ضخامت تا ۱۰ mm شده و لذا تغییر فاصله بین آند و کاتد را به دنبال دارد. این موضوع تشکیل ندول‌ها در لبه کاتد را باعث می‌شود. پیک‌های مشاهده شده در منحنی‌های پتانسیل کاتدی در آزمون‌های گالوانواستاتیکی می‌تواند به دلیل تشکیل ندول باشد که با استفاده از تصاویر میکروسکپی نوری مورد ارزیابی بیشتر قرار گرفته است.

International Journal of Engineering

A New Multilevel Inverter Based on Harvest of Unused Energies for Photovoltaic Applications

S. J. Salehi, M. A. Shmasi-Nejad*, H. R. Najafi

Department of Electrical and Computer Engineering, University of Birjand, Birjand, Iran

A B S T R A C T

In multilevel inverters, unused energies are created due to the asynchronous use of the input DC sources. when the input DC sources are replaced by renewable systems such as photovoltaic arrays, some of the input energies remain unused. This paper presents a new multilevel inverter topology that can harvest the unused energies and return them to another output which leads to the harvest of the maximum input energy. The harvest of maximum energy (HME) based multilevel inverter structure consists of two terminals. One is connected to AC-load and another is joined to DC-load or rechargeable batteries. Another merit of the proposed multilevel inverter is that the number of its switches is comparable to other structures where unused energies cannot be harvested. Selective harmonic elimination (SHE) has been used as the switching strategy in the proposed multilevel structure. To verify the performance of the HME-based multilevel inverter topology, the experimental results for a type seven-level inverter were performed by the TMS320F28379D DSP.

doi: 10.5829/ije.2022.35.12c.14

1. INTRODUCTION

In comparison with two-level inverters, multilevel inverters (MLI) have been rapidly developed by researchers due to lower total harmonic distortion (THD), lower switching frequency, the smaller size of the filter, and lower dv/dt stress on the load. They have been rapidly used in photovoltaic systems [1-8]. The MLI are classified to three main groups: neutral-point clamped (NPC) [9, 10], flying capacitor (FC) [11, 12] and cascaded H-bridge (CHB) topologies [13, 14]. In NPC and FC structures, the clamped diodes and capacitors are responsible for transmitting the input voltage to constitute the N-level voltage at the output, respectively. The main advantage of these topologies is that they require only one isolated DC source. However, to achieve higher voltage levels, they need a high number of semiconductor devices (switches and diodes) and passive elements. Another drawback of NPC and FC topologies is that the neutral point voltage is unbalanced. However, many researchers have reported several improved

structures to overcome such limitation; but, there are still a high number of semiconductor devices in their topologies [15-17]. The CHB multilevel inverters are suitable for reactive power compensators, battery chargers, photovoltaic systems, electrical vehicles, and so on. Unlike the NPC and FC topologies, the CHB structure acted in asymmetric mode (inequality of input DC-sources) to achieve a number of higher voltage levels. The most important disadvantage of the CHB topology is that there are several isolated DC sources in its structure [18, 19]. Recently, the switched-source (SS) and switched-capacitor (SC) based topologies have been introduced by researchers which reduced the number of semiconductor devices [20-24]. In the SS topologies, we can obtain structures with a very low number of switches. This reduces drastically switching losses, cost, and volume of the drive system. However, there are several DC sources in this structure. The SC multilevel inverters can behave as the boost converter. So, the SC multilevel inverters can be used for applications such as photovoltaic systems that produce a low voltage on their

Corresponding Author Institutional Email: mshamsi@birjand.ac.ir
(M. A. Shamsi-Nejad)

inputs. They can generate a number of high voltage levels at the output with a small number of DC sources. It can be concluded from the above discussion, that in the CHB, SS, and SC topologies, to achieve the number of high voltage levels and low THD on the load, they need a number of high input DC sources. This subject leads to the appearance of unused energies in the multilevel inverters. For more understanding, according to Figure 1, consider the seven-level SS-based multilevel inverter that has been introduced by Prabaharan et al. [25].

First, assume that the switching state equals $(S_1S_2T_1T_2T_3T_4=101010)$ and the current commutation paths are accords with the arrow lines shown in Figure 1a. In this condition, the input DC source u_1 is transferred to the load. Right at this moment, the input DC-source u_2 is unemployed. Moreover, according to Figure 1b, in the switching state $(S_1S_2T_1T_2T_3T_4=011010)$, when the input DC source u_2 is transmitted to the load, the input DC source u_1 is unemployed. Therefore, in multilevel inverters which contain several input DC sources, there are moments when some or all of the DC sources remain unused. It means that, if the input DC sources u_1 and u_2 are replaced by the photovoltaic systems, some of the

input energies will not be used by the inverter. In this paper, a new multilevel inverter is introduced so that it can harvest the unused energies and return them to another load which leads to the harvest of maximum input energy. It is obvious that the proposed topology must have the least number of semiconductor devices. For this reason, Prabaharan et al. [25] the inverter which is shown in Figure 1, is selected as the base structure for this purpose. To evaluate the performance of the HME-based multilevel inverter, the selective harmonic elimination (SHE) technique is selected as the switching strategy. The SHE is a low switching frequency strategy that provides us with low switching losses [26-29]. In summary, the benefits and properties of the proposed multilevel inverter can be listed as follows:

- The proposed HME-based multilevel inverter can harvest the maximum energy which could not be harvested by previous multilevel inverters.
- In the proposed topology, the number of switches is comparable to other structures.
- The SHE method is selected as the switching strategy.
- The proposed multilevel inverter can be implemented by an experimental setup.

2.   PROPOSED   HME-BASED   MULTILEVEL INVERTER

2. 1. Seven-level Structure   The proposed seven-level HME-based inverter is shown in Figure 2. However, it can be generalized to N-level configuration. As shown in Figure 2, the HME-based multilevel inverter consists of two terminals AB and XY which are connected to AC and DC load, respectively. It should be noted that the XY terminal is responsible for transferring the unused energies that did not previously exist on Prabaharan's inverter in Figure 1. The semiconductor
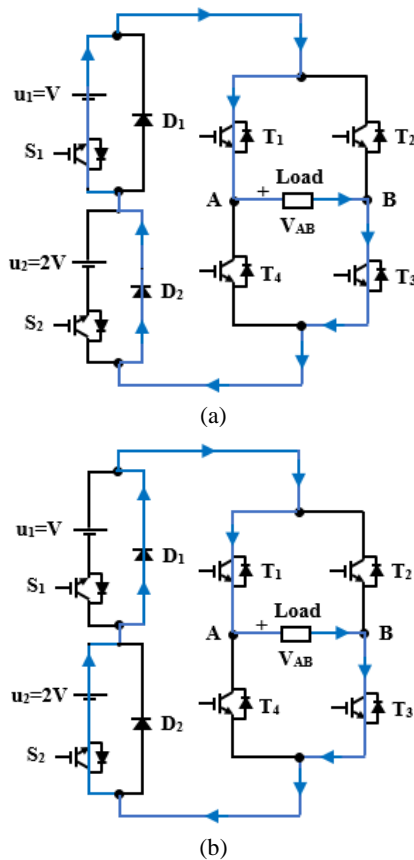

Figure 1. Introduced seven-level SS-based multilevel inverter by Prabaharan et al. [25]. (a) $S_1S_2T_1T_2T_3T_4=101010$), (b) ($S_1S_2T_1T_2T_3T_4=011010$)
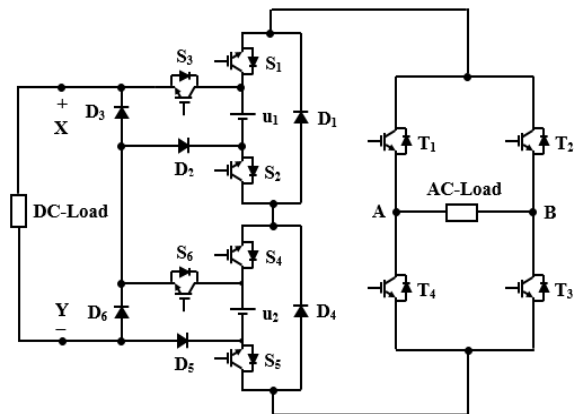

Figure 2. Proposed seven-level HME-based inverter with $u_1=V$ and $u_2=2V$

devices $(S_1 S_2 S_4 S_5 D_1 D_4)$ and $(S_3 S_6 D_2 D_3 D_5 D_6)$ are arranged to transfer the power to the AB and XY terminals, respectively. They are configured in the new structure so that there is no common current path between the two terminals. For instance, when the S_3 is turned on, $(S_1 S_2)$ is turned off and D_3 is reverse biasing. In this condition, the DC-source voltage u_1 is transferred to the XY terminal through D_2 and S_3 devices.

At this moment, D_1 is direct biasing and it can conduct the current to the AC load in the AB terminal. The switching states of the seven-level HME-based inverter have been listed in Table 1. As shown in Table 1, there are seven switching states for producing seven-level of voltage in the output. The switches $(S_1 S_2)$ and

$(S_4 S_5)$ are logically NOT the switches S_3 and S_6, respectively. In addition, the diodes D_1 and D_2 (also D_4 and D_5) can simultaneously be turned on and off. So, it is guaranteed that there is no common current between the AB and XY terminals. The commutation pathways according to switching states have been depicted in Figure 3. For example, in Figure 3(b), the DC-sources $u_1 = V$ and $u_2 = 2V$ are simultaneously transferred to the XY and AB terminals for DC and AC loads, respectively. In this condition, the $V_{AB} = +2V$ and $V_{XY} = +V$. In Figures 3(e), 3(f) and 3(g), according to the activating of T_2 and T_4 in the H-bridge section, the sign of V_{AB} is negative. The other switching modes in Figure 3 are analyzed according to Table 1.

TABLE 1. The switching states of proposed seven-level HME-based inverter

S_1	S_2	S_3	S_4	S_5	S_6	T_1	T_2	T_3	T_4	V_{AB}	V_{XY}
1	1	0	1	1	0	1	0	1	0	+3V	0
0	0	1	1	1	0	1	0	1	0	+2V	+V
1	1	0	0	0	1	1	0	1	0	+V	+2V
0	0	1	0	0	1	1	0	1	0	0	+3V
1	1	0	0	0	1	0	1	0	1	-V	+2V
0	0	1	1	1	0	0	1	0	1	-2V	+V
1	1	0	1	1	0	0	1	0	1	-3V	0

(a)

(b)

(c)

(d)

(e)

(f)

(g)
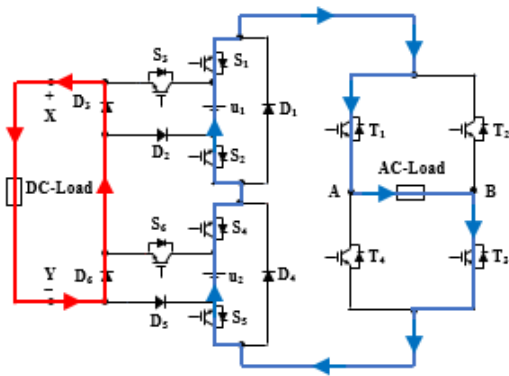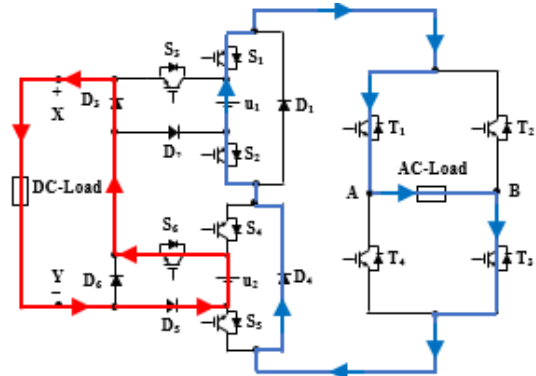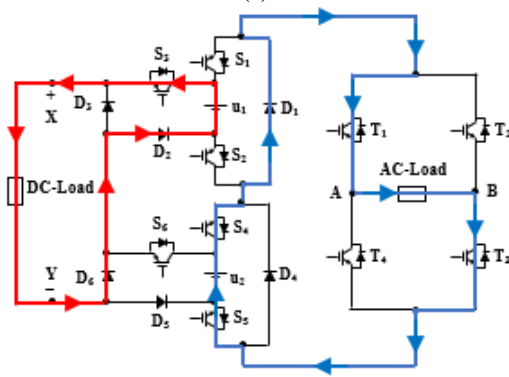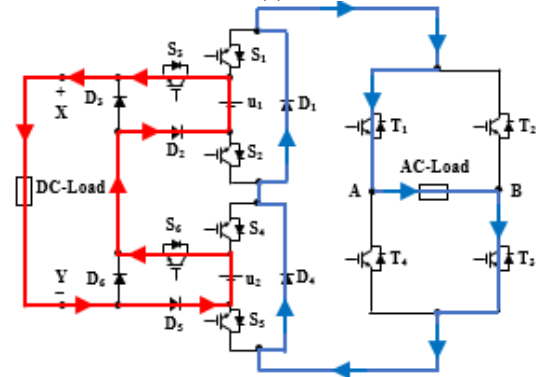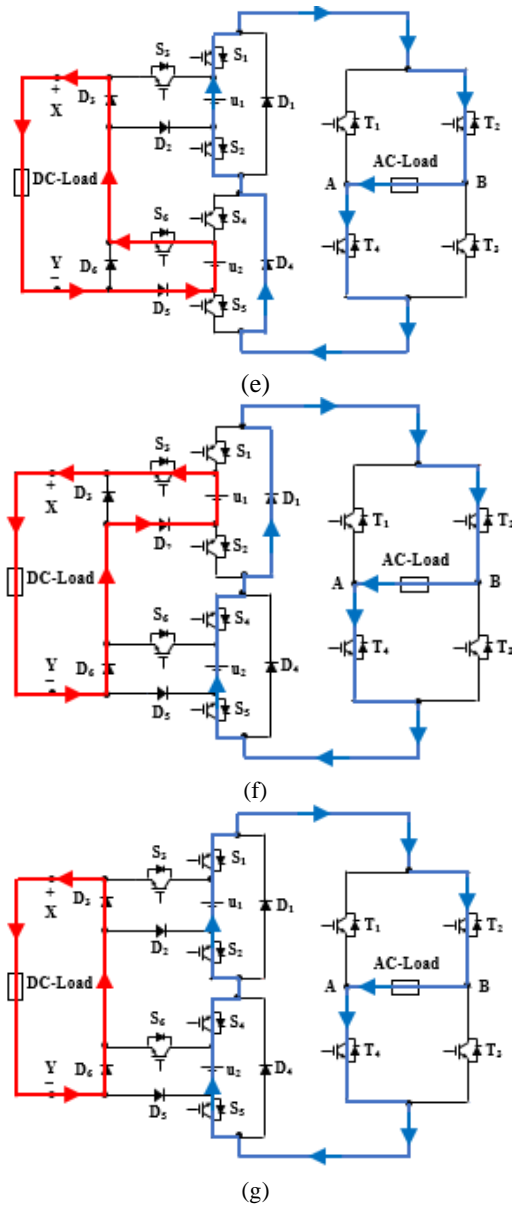
Figure 3. Schematic of switching states for generating different voltage levels on AC and DC loads with $u_1=V$ and $u_2=2V$. (See Table 1): (a) State 1 for $V_{AB}=+3V$ and $V_{XY}=0V$. (b) State 2 for $V_{AB}=+2V$ and $V_{XY}=+V$. (c) State 3 for $V_{AB}=+V$ and $V_{XY}=+2V$. (d) State 4 for $V_{AB}=0V$ and $V_{XY}=+3V$. (e) State 5 for $V_{AB}=-V$ and $V_{XY}=+2V$. (f) State 6 for $V_{AB}=-2V$ and $V_{XY}=+V$. (g) State 7 for $V_{AB}=-3V$ and $V_{XY}=0V$

It should be noted that, for decreasing the voltage ripple, we can consider a capacitor on the output XY terminal. However, in this work, to accurate calculation of the used and unused energy, we decided that it does not consider.

2. 2. Generalized HME-based Multilevel Inverter
An N-level structure can be implemented in modular

form by serializing the several units of the HME-based multilevel inverter which is shown in Figure 4.

It should be noted that the terminal XY is unipolar which can generate the voltage in forming of multilevel. In symmetric mode ($u_1 = u_2 = \ldots = u_n$), the number of switches (N_{sw}) and the number of generated voltage levels on the terminals AB ($N_{level,AB}$) and XY ($N_{level,XY}$) can be calculated as follows:

$$\begin{cases} N_{sw} = \dfrac{3N_{level,AB}+5}{2} \\ N_{level,AB} = 2n+1 \\ N_{level,XY} = n+1 \end{cases} \tag{1}$$

where n is the number of units.

In asymmetric mode, by considering the pattern of DC-sources voltage as ($u_1=V$, $u_2=2V$, $u_3=3V,\ldots$, $u_n=nV$), the number of switches and voltage levels can be formulated as follows:

$$\begin{cases} N_{sw} = \dfrac{3}{2}\sqrt{4N_{level,AB}-3}+\dfrac{5}{2} \\ N_{level,AB} = n^2+n+1 \\ N_{level,XY} = \dfrac{n^2+n+2}{2} \end{cases} \tag{2}$$

Although, there are multiple voltage patterns in the asymmetric mode for achieving the number of high


(a)

(b)
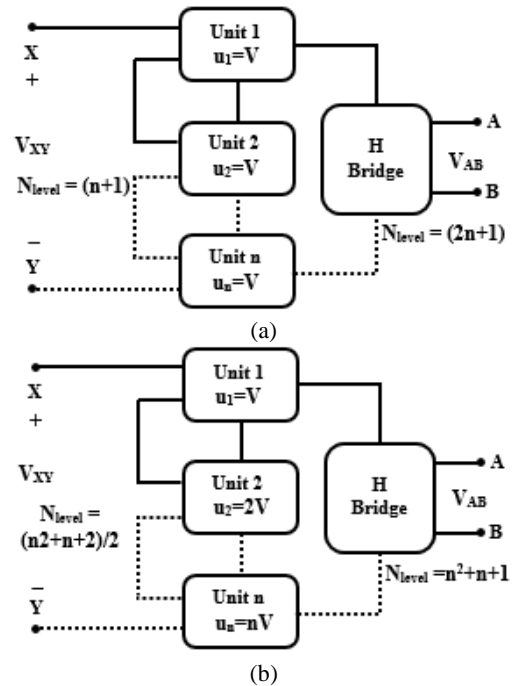
Figure 4. Generalizing of the proposed HME-based multilevel inverter to the N-level structure. (a) Symmetric mode and (b) Asymmetric mode

voltage levels such as (u_1=V, u_2=2V, u_3=4V,…, u_n=2^{n-1}V), they increase the total standing voltage (TSV) of some switches that are not appropriate.

3. COMPARISON OF THE HME-BASED MULTILEVEL INVERTER WITH OTHER TOPOLOGIES

It should be noted that harvesting maximum energy requires the use of a large number of switches. However, the proposed inverter is comparable to other structures that cannot absorb these energies. Table 2 shows the number of switches for six different multilevel inverters. In Table 2, the inverter is a multilevel inverter type of switched-source that has been introduced by Babaei and Hosseini [24]

Figure 5 shows the curve of the number of switches in terms of the number of voltage levels for multilevel inverters listed in Table 2. Any curve that has a lower slope means fewer switches in its structure. For example, in symmetric mode, as shown in Figure 5(a), to achieve a 50-level voltage in the inverter output, 28, 54, 78 and 96 switches are required for the Prabaharan, Babaei, HME and CHB topologies, respectively. Also, in asymmetric mode, according to point M shown in Figure 5(b), the HME-based multilevel inverter has a smaller number of switches than the CHB topology for voltages above 21 levels. So, the proposed HME-based multilevel inverter is comparable to other multilevel inverter topologies.

4. CALCULATION OF THE TRANSFERRED ENERGY TO THE TERMINAL XY

In this section, the transferred energy to terminal XY is calculated. This is the same unused energy in

TABLE 2. The number of switches in several multilevel inverter topologies

Type of Multilevel inverter	Number of switches in symmetric mode	Number of switches in asymmetric mode
NPC [9, 10]	$2\left(N_{level}-1\right)$	-----------
FC [11, 12]	$2\left(N_{level}-1\right)$	-----------
CHB [13]	$2\left(N_{level}-1\right)$	$2\sqrt{4N_{level}-3}-2$
Babaei and Hosseini [24]	$N_{level}+3$	$\sqrt{4N_{level}-3}+3$
Prabaharan et al. [25]	$\dfrac{\left(N_{level}+7\right)}{2}$	$\dfrac{1}{2}\sqrt{4N_{level}-3}+\dfrac{7}{2}$
Proposed HME	$\dfrac{\left(3N_{level}+5\right)}{2}$	$\dfrac{3}{2}\sqrt{4N_{level}-3}+\dfrac{5}{2}$
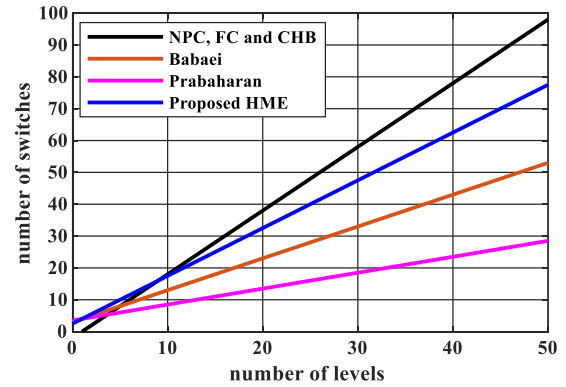
(a)
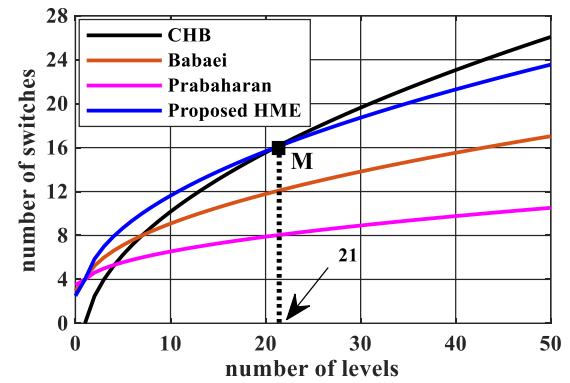
(b)

Figure 5. Comparison of the proposed HME-based multilevel inverter with other topologies. (a) Symmetric mode and (b) Asymmetric mode

conventional multilevel inverters such as Babaei and Hosseini [24], Prabaharan et al. [25], etc.

For this purpose, the SHE method is considered as a switching strategy due to its staircase manner and easy analysis. Here, for facilitating the equations, it is assumed that the load is pure resistive in both terminals AB and XY. Figure 6 shows the voltage waveforms in terminals AB and XY in the proposed seven-level HME-based inverter under the SHE switching strategy. In Figure 6, V_{dcm} and (α_1, α_2, α_3) are the smallest voltage level on the loads and switching angles, respectively. For calculating the transferred energy to the terminal XY, it should be integrated from the power. According to the in-phase of voltage and current in terminal XY, the transferred energy to the terminal XY (E_{XY}) can be written as follows:

$$E_{XY} = \int_0^t V_{XY}(t)I_{XY}(t)d(t) =$$

$$\int_0^{\alpha_1} 3V_{dcm}\frac{3V_{dcm}}{R}dt + \int_{\alpha_1}^{\alpha_2} 2V_{dcm}\frac{2V_{dcm}}{R}dt \qquad (3)$$

$$+......+ \int_{\pi-\alpha_1}^{\pi} 3V_{dcm}\frac{3V_{dcm}}{R}dt$$
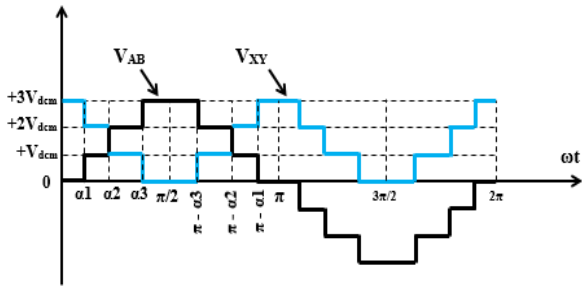
Figure 6. The voltage waveforms in terminals AB and XY under the SHE switching strategy, according to Table 1

**Figure 7.** The energy manner in terminal XY with increasing the number of voltage levels

Figure 8. The experimental setup

where $V_{XY}(\omega t)$ and $I_{XY}(\omega t)$ are the instantaneous voltage and current in terminal XY, respectively.

Moreover, R is the resistance of DC load. By solving equation 3, in one complete cycle ($t=2\pi$), the E_{XY} is obtained as follows:

$$E_{XY} = \frac{2V_{dcm}^2}{R}\left(10\alpha_1 + 6\alpha_2 + 2\alpha_3\right) \qquad (4)$$

Equation (4) describes the unused energy in a seven-level inverter under the SHE switching strategy which can be harvested by the proposed HME-based inverter in the terminal XY. It can be generalized to the N-level conditions as follows:

$$
\begin{aligned}
E_{XY,N_{level}} = \frac{2V_{dcm}^2}{R}[&\left(2N_{level}-4\right)\alpha_1 \\
&+\left(2N_{level}-8\right)\alpha_2 \\
&+\left(2N_{level}-12\right)\alpha_3 \\
&+......+2\alpha_{\frac{N_{level}-1}{2}}]
\end{aligned}
\qquad (5)
$$

Now, assume that there is a relationship between switching angles as $\alpha_k = k\alpha_1$ $\left(\alpha_2 = 2\alpha_1, \alpha_3 = 3\alpha_1,...\right)$ which is close to the real conditions. By defining P_0 as $P_0 = \left(V_{dcm}^2 / R\right)\alpha_1$, the curve E_{XY}/P_0 in terms of the number of voltage levels can be depicted in Figure 7. By comparing the real and linear curves in Figure 7, it can be seen that as the number of inverter voltage levels increases (with increasing the number of DC inputs), the unused energy increases with nonlinear behavior. So, the harvest of maximum energy at a high number of voltage levels is more important than the inverters with a low number of voltage levels.

5. EXPERIMENTAL RESULTS

The introduced HME-based seven-level inverter can be implemented as illustrated in Figure 8.

The experimental setup consists of a TMS320F28379D DSP as the processor, a gate driver, the proposed HME-based multilevel inverter, several R-

L loads, two 1/7 Ω series resistance as the current sensors, and multiple power supplies. In the gate driver circuit, the HCPL-3120 is used as both a DSP ground isolator and a switch driver. Moreover, in this circuit, two 74HC245 buffers are applied to prevent the current consumption by the DSP. The important point about the gate driver circuit is that the gate driver power supply ground should only be connected to the negative terminal of DC-source u_1 (see Figure 2). To select the switches and diodes, it should be noted that, in the experimental works, due to limitations in DC-link power supplies, the selected switches and diodes should have a low voltage drop. For this reason, the switches and diodes in our setup have been chosen as IRG41BC30S IGBTs and MBRF20100CT Schottky diodes, respectively.

In our experimental implementation, the values of DC-sources u_1 and u_2 are selected as 50v and 100v, respectively. For obtaining different values of DC-source voltage, they can be variable by two high current buck-boost converter modules. Figure 9 shows the inverter output voltages V_{AB} and V_{XY} with constant pure resistive load Z=50 Ω under various modulation indexes. According to a selection of DC sources as u_1=50v and u_2=100v, the maximum voltage level of both V_{AB} and V_{XY} was expected to be 150v (V=50v, 2V=100v, 3V=150v) but as shown in Figure 9(a), it is equal to 140v. This is due to the voltage drop across the switches and diodes. In Figure 9(b), as was expected, by reducing the modulation index, the width of the largest voltage AB

(a)

(b)
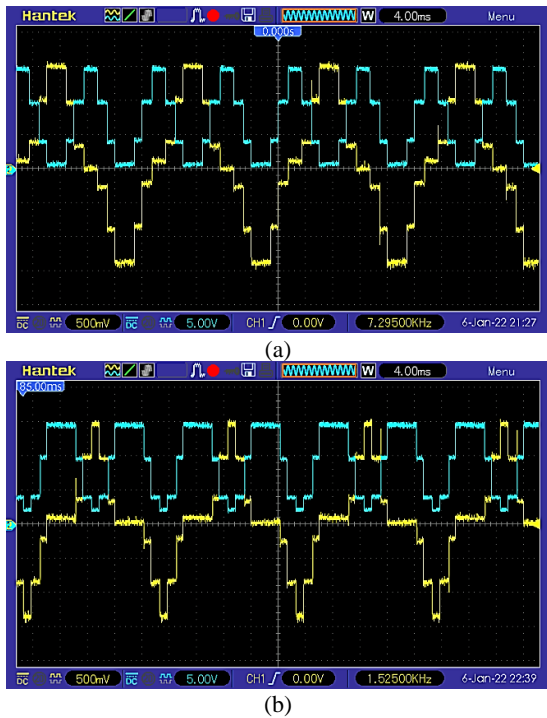
Figure 9. Experimental results with constant resistive load Z=50 Ω (for both DC and AC loads). (a) Output voltages V_{AB} (yellow wave × 50 V/div.) and V_{XY} (blue wave × 1 V/div.) under M=0.7, (b) Output voltages V_{AB} (yellow wave × 50 V/div.) and V_{XY} (blue wave × 1 V/div.) under M=0.5

level is diminished. So, it is expected that the fundamental harmonic of voltage AB is also reduced. Unlike the behavior of voltage AB, by reducing the modulation index, the width of the largest voltage XY level is increased. So, it is expected that the mean value of voltage XY is increased. It can be concluded from the above discussion, the rechargeable batteries are a suitable option for DC load when the SHE method is used as a switching strategy.

It should be noted that, in our work, two 1Ω series resistances with the AB and XY outputs have been used as current sensors. So, for achieving the real values of currents I_{AB} and I_{XY}, the amplitude of the current waveforms must be multiplied by 1. Figure 10 shows the experimental results with changing of load impedance from Z_1=58 Ω + 12 mH to Z_2=135 Ω + 66 mH under constant modulation index M=0.7. Since the impedance Z_2 is more inductive than the impedance Z_1, two events are expected to occur when the impedance Z_2 is applied to both inverter terminals.

First, according to Figure 10(a), the voltage V_{AB} becomes like a pulsating wave when the polarity changes. In this condition, due to the unipolar of the terminal XY, the voltage V_{XY} does not has the pulsating-shaped wave. Second, as shown in Figures 10(b) and 10(c), the currents I_{AB} and I_{XY} get closer to the sine wave. However, the amplitude of currents I_{AB} and I_{XY} has

(a)

(b)

(c)
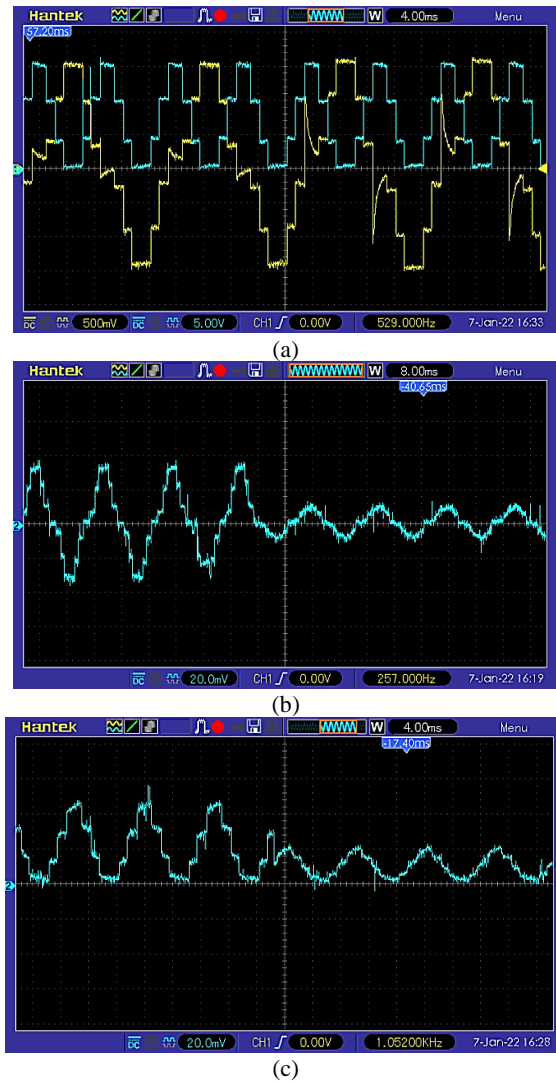
Figure 10. Experimental results with change of load impedance from Z_1=58 Ω + 12 mH to Z_2=135 Ω + 66 mH (for both DC and AC loads) under constant modulation index M=0.7. (a) Output voltages V_{AB} (yellow wave × 50 V/div.) and V_{XY} (blue wave × 1 V/div.), (b) current I_{AB}, (c) current I_{XY}. (To obtain the real values of the currents, the amplitudes of the waves (b) and (c) must be multiplied by 1 due to compensation for use of the 1-ohm series resistance as the current sensor)

been diminished from 1.8 A to 0.5 A and from 2.4 A to 1 A, respectively.

6. CONCLUSION

A new multilevel inverter based on the harvest of maximum energy was proposed in this paper. The HME-based multilevel inverter consists of two independent AC and DC outputs which can be harvested the unused energies from the XY terminal. The new structure can be

modular form. The most important merit of the proposed topology is that if the inverter input DC sources are replaced by photovoltaic systems, they can be harvested the maximum power and energy from them. So, in future work, we intend to connect the inverter to the grid with photovoltaic arrays so that it can be injected the maximum energy into it. Moreover, the number of semiconductor devices of the proposed multilevel inverter is comparable to traditional inverters. The simulation and experimental results indicate that the HME-based inverter has a good performance for the constant and variable loads under the SHE switching strategy.

7. REFERENCES

1. Fang, J., Blaabjerg, F., Liu, S. and Goetz, S.M., "A review of multilevel converters with parallel connectivity", *IEEE Transactions on Power Electronics*, Vol. 36, No. 11, (2021), 12468-12489. doi: 10.1109/TPEL.2021.3075211.

2. Tashiwa, I.E., Dung, G.D. and Adole, B.S., "Review of multilevel inverters and their control techniques", *European Journal of Engineering and Technology Research*, Vol. 5, No. 6, (2020), 659-664. doi: 10.24018/ejers.2020.5.6.1707.

3. Gupta, K.K., Ranjan, A., Bhatnagar, P., Sahu, L.K. and Jain, S., "Multilevel inverter topologies with reduced device count: A review", *IEEE Transactions on Power Electronics*, Vol. 31, No. 1, (2015), 135-151. doi: 10.1109/TPEL.2015.2405012.

4. Rahimi Mirazizi, H. and Agha Shafiyi, M., "Evaluating technical requirements to achieve maximum power point in photovoltaic powered z-source inverter", *International Journal of Engineering*, Vol. 31, No. 6, (2018), 921-931. doi: 10.5829/IJE.2018.31.06C.09.

5. Tousi, B. and Ghanbari, T., "Transformer-based single-source multilevel inverter with reduction in number of transformers", *International Journal of Engineering*, Vol. 29, No. 5, (2016), 621-629. doi: 10.5829/idosi.ije.2016.29.05b.05.

6. NANDHINI, G.M. and Ganimozhi, T., "New hybrid cascaded multilevel inverter", (2013). doi: 10.5829/idosi.ije.2013.26.11b.13.

7. Alemi-Rostami, M. and Rezazadeh, G., "Selective harmonic elimination of a multilevel voltage source inverter using whale optimization algorithm", *International Journal of Engineering*, Vol. 34, No. 8, (2021), 1898-1904. doi: 10.5829/IJE.2021.34.08B.11.

8. Arehpanahi, M. and Paknia, D., "A new single-phase symmetrical cascade multilevel inverter with low number of power switches", *International Journal of Engineering*, *Transactions B: Applications,* Vol. 31, No. 8, (2018), 1228-1233. doi: 10.5829/ije.2018.31.08b.10.

9. Liu, X., Lv, J., Gao, C., Chen, Z. and Chen, S., "A novel statcom based on diode-clamped modular multilevel converters", *IEEE Transactions on Power Electronics*, Vol. 32, No. 8, (2016), 5964-5977. doi: 10.1109/TPEL.2016.2616495.

10. Palanisamy, R., Aravindh, P. and Vijayakumar, K., "Effectual svpwm for 3-level npc-mli with grid connected pv system", *International Journal of Electrical Engineering and Technology*, Vol. 11, No. 3, (2020). doi: 10.34218/IJEET.11.3.2020.006.

11. Kopacz, R., Harasimczuk, M., Trochimiuk, P., Wrona, G. and Rąbkowski, J., "Medium voltage flying capacitor dc–dc converter with high-frequency tcm-q2l control", *IEEE Transactions on Power Electronics*, Vol. 37, No. 4, (2021), 4233-4248. doi: 10.1109/TPEL.2021.3122329.

12. Abdelhamid, E., Corradini, L., Mattavelli, P., Bonanno, G. and Agostinelli, M., "Sensorless stabilization technique for peak current mode controlled three-level flying-capacitor converters", *IEEE Transactions on Power Electronics*, Vol. 35, No. 3, (2019), 3208-3220. doi: 10.1109/TPEL.2019.2930011.

13. Mhiesan, H., Wei, Y., Siwakoti, Y.P. and Mantooth, H.A., "A fault-tolerant hybrid cascaded h-bridge multilevel inverter", *IEEE Transactions on Power Electronics*, Vol. 35, No. 12, (2020), 12702-12715. doi: 10.1109/TPEL.2020.2996097.

14. Lashab, A., Sera, D., Kerekes, T., Terriche, Y., Bouzid, A., Vasquez, J.C. and Guerrero, J.M., "A cascaded h-bridge with integrated boosting circuit", *IEEE Transactions on Power Electronics*, Vol. 36, No. 1, (2020), 18-22. doi: 10.1109/TPEL.2020.3000724.

15. Tashakor, N., Kilictas, M., Bagheri, E. and Goetz, S., "Modular multilevel converter with sensorless diode-clamped balancing through level-adjusted phase-shifted modulation", *IEEE Transactions on Power Electronics*, Vol. 36, No. 7, (2020), 7725-7735. doi: 10.1109/TPEL.2020.3041599.

16. Obara, H., Ohno, T., Katayama, M. and Kawamura, A., "Flying-capacitor linear amplifier with capacitor voltage balancing for high-efficiency and low distortion", *IEEE Transactions on Industry Applications*, Vol. 57, No. 1, (2020), 614-627. doi: 10.1109/APEC.2019.8721986

17. Sadigh, A.K., Dargahi, V. and Corzine, K.A., "New active capacitor voltage balancing method for flying capacitor multicell converter based on logic-form-equations", *IEEE Transactions on Industrial Electronics*, Vol. 64, No. 5, (2016), 3467-3478. doi: 10.1109/ECCE.2016.7855288.

18. Yang, K., Lan, X., Zhang, Q. and Tang, X., "Unified selective harmonic elimination for cascaded h-bridge asymmetric multilevel inverter", *IEEE Journal of Emerging and Selected Topics in Power Electronics*, Vol. 6, No. 4, (2018), 2138-2146. doi: 10.1109/JESTPE.2018.2808539.

19. Wang, L., Wu, Q. and Tang, W., "Novel cascaded switched-diode multilevel inverter for renewable energy integration", *IEEE Transactions on Energy Conversion*, Vol. 32, No. 4, (2017), 1574-1582. doi: 10.1109/TEC.2017.2710352.

20. Vahedi, H., Sharifzadeh, M. and Al-Haddad, K., "Modified seven-level pack u-cell inverter for photovoltaic applications", *IEEE Journal of Emerging and Selected Topics in Power Electronics*, Vol. 6, No. 3, (2018), 1508-1516. doi: 10.1109/JESTPE.2018.2821663.

21. Ye, Y., Cheng, K.W.E., Liu, J. and Ding, K., "A step-up switched-capacitor multilevel inverter with self-voltage balancing", *IEEE Transactions on Industrial Electronics*, Vol. 61, No. 12, (2014), 6672-6680. doi: 10.1109/TIE.2014.2314052.

22. Zamiri, E., Vosoughi, N., Hosseini, S.H., Barzegarkhoo, R. and Sabahi, M., "A new cascaded switched-capacitor multilevel inverter based on improved series–parallel conversion with less number of components", *IEEE Transactions on Industrial Electronics*, Vol. 63, No. 6, (2016), 3582-3594. doi: 10.1109/TIE.2016.2529563.

23. Yu, H., Chen, B., Yao, W. and Lu, Z., "Hybrid seven-level converter based on t-type converter and h-bridge cascaded under spwm and svm", *IEEE Transactions on Power Electronics*, Vol. 33, No. 1, (2017), 689-702. doi: 10.1109/TPEL.2017.2664068.

24. Babaei, E. and Hosseini, S.H., "New cascaded multilevel inverter topology with minimum number of switches", *Energy Conversion and Management*, Vol. 50, No. 11, (2009), 2761-2767. https://doi.org/10.1016/j.enconman.2009.06.032

25. Prabaharan, N., Saravanan, S., Jerin, A.R.A. and Palanisamy, K., "A reduced switch asymmetric multilevel inverter topology using

unipolar pulse width modulation strategies for photovoltaic application", *Recent Developments on Power Inverters*, (2017), 29-48. doi: 10.5772/67863.

26. Abd Halim, W., Azam, T.N.A.T., Applasamy, K. and Jidin, A., "Selective harmonic elimination based on newton-raphson method for cascaded h-bridge multilevel inverter", *International Journal of Power Electronics and Drive System (IJPEDS)*, Vol. 8, No. 3, (2017), 1193-1202. doi: 10.11591/ijpeds.v8.i3.pp1193-1202.

27. Wu, M., Wang, K., Yang, K., Konstantinou, G., Li, Y.W. and Li, Y., "Unified selective harmonic elimination control for four-level hybrid-clamped inverters", *IEEE Transactions on Power*

Electronics, Vol. 35, No. 11, (2020), 11488-11501. doi: 10.1109/TPEL.2020.2985090.

28. Dahidah, M.S., Konstantinou, G. and Agelidis, V.G., "A review of multilevel selective harmonic elimination pwm: Formulations, solving algorithms, implementation and applications", *IEEE Transactions on Power Electronics*, Vol. 30, No. 8, (2014), 4091-4106. doi: 10.1109/TPEL.2014.2355226.

29. Perez-Basante, A., Ceballos, S., Konstantinou, G., Pou, J., Andreu, J. and de Alegría, I.M., "(2n+ 1) selective harmonic elimination-pwm for modular multilevel converters: A generalized formulation and a circulating current control method", *IEEE Transactions on Power Electronics*, Vol. 33, No. 1, (2017), 802-818. doi: 10.1109/TPEL.2014.2355226.

Persian Abstract

چکیده

در اینورترهای چند سطحی، انرژی های استفاده نشده به دلیل استفاده غیر همزمان از منابع DC ورودی ایجاد می‌شوند. هنگامیکه منابع DC ورودی به وسیله سیستم‌های تجدیدپذیر مانند آرایه‌های فتوولتائیک جایگزین می‌شوند، برخی از انرژی‌های ورودی بلا استفاده می‌مانند. این مقاله یک توپولوژی اینورتر چند سطحی جدید ارائه می‌کند که می‌تواند انرژی‌های استفاده‌نشده را برداشت کند و آنها را برای یک بار دیگر برگرداند که منجر به برداشت حداکثر انرژی ورودی می‌شود. ساختار اینورتر چند سطحی مبتنی بر برداشت حداکثر انرژی (HME) از دو پایانه تشکیل شده است. یکی به بار AC و دیگری به بار DC یا باتری‌های قابل شارژ می‌تواند متصل شود. یکی دیگر از مزایای اینورتر چند سطحی پیشنهادی این است که تعداد سوئیچ‌های آن با ساختارهایی قابل مقایسه است که در آنها انرژی‌های استفاده نشده قابل برداشت نیست. روش حذف هارمونیک‌های منتخب به عنوان استراتژی سوئیچ زنی در ساختار چند سطحی پیشنهادی استفاده شده است. به منظور تأیید عملکرد توپولوژی اینورتر چند سطحی مبتنی بر HME، نتایج آزمایشگاهی برای یک اینورتر هفت سطحی توسط پردازشگر سیگنال دیجیتال TMS320F28379D DSP انجام شده است.

A Novel Fractional Analytical Technique for the Time-space Fractional Equations Appearing in Oil Pollution

B. Jalili[a], P. Jalili[*a], A. Shateri[a], D. Domiri Ganji[b]

[a] Department of Mechanical Engineering, North Tehran Branch, Islamic Azad University, Tehran, Iran
[b] Department of Mechanical Engineering, Babol Noshirvani University of Technology, Babol, Iran

P A P E R I N F O	*A B S T R A C T*
	Oil spills in the seas and oceans cause pollution and have many destructive environmental effects. The diffusion (parabolic) equations are the most reasonable option to model the propagation of this leakage and contamination. These equations allow statistics regarding the amount of oil that has outreached the ocean outlet, to be used as initial and boundary conditions for a mathematical model of oil diffusion and alteration in seas. As it involves the hyperbolic (advection/wave) component of the equation, the most reasonable choices are diffusion and Allen–Cahn (AC) equations, which are difficult to solve numerically. Equations of diffusion and Allen-Cahn were solved with different degrees of fractional derivatives (α= 0.25, α=0.5, α=0.75 and α=0.75), and the oil pollution concentration was obtained at a specific time and place. This study adopts the homotopy perturbation method (HPM) for nonlinear Allen–Cahn (AC) equation and time fractional diffusion equation to express oil pollution in the water. Fractional derivatives are portrayed in the sense of Caputo. Two presented examples illustrate the applicability and validity of the proposed method. Pollution concentrations in flow field over an interval of time and space for different degrees of fractional derivation are shown. At lower fraction derivative degrees, the pollution concentration behavior is nonlinear, and as the degree of fraction derivation increases to one, the nonlinear behavior of the pollution concentration decreases. The results produced by the suggested technique compared to the exact solutions shows that it is efficient and convenient; it is also reduces computational time.

1. INTRODUCTION

The release of liquid hydrocarbons into the ocean is called oil pollution. Humanity releases oil from without refining, tankers and carries out engineering actions, including piping, drilling and offshore rigs. These activities have catastrophic effects on the environment and the biology of marine life and lead to hazardous consequences. Therefore, the extent of the oil spill is essential for reciprocity. In this way, the natural ecosystem of the coastline is preserved. Also, a catastrophe is prevented in the early stages.

The area of spillage could be anticipated according to the governing equations of the fluid flow and the mass transfer phenomenon. The boundary and initial conditions for the a calculation for diffusion of oil and change at sea can be deduced from the statistics of the the the volume of oil that reaches the ocean outlet. The diffusion (parabolic) equations are the most reasonable option to model the propagation of this leakage and contamination. These equations allow statistics regarding the amount of oil that has outreached the ocean outlet, to be used as initial and boundary conditions for a mathematical model of oil diffusion and alteration in seas. Since it includes a hyperbolic section of the equation, the best options are the Allen Kahn (AC) and diffusion equations, which are challenging to solve mathematically. Several academics have investigated the production of oil and oil spill transfer based on the path method over the past three decades [1]. This method has been used for river and seas

[2, 3] and lake systems [4-6]. Allen Kahn's equation is a mathematical model used to analyze the phase separation procedure in binary alloys. This equation arises in fluid dynamics as a convection-diffusion equation and materials science as a reaction-diffusion equation. When a substance changes its composition or form, phase transfer occurs at the interface. It is a straightforward model of the nonlinear reaction propagation methodology. Often employed to pinnacle interface move over time, phase separation in alloys over time is used in different fields, integrating image processing, geology, biology, bio-fluid and materials science. Sutantyo et al. [7] investigated the dynamics of the modified PB DNA model by considering DNA in the Nosé-Hoover thermostat as a bio-fluid with various viscosities. In their study, viscosity variations are reviewed through temperature variations, namely thermal viscosity. They obtained the dynamical equation of DNA in the form of a nonlinear Schrödinger-like (NLS-like) equation by using the perturbation method and continuous approximation. Hariharan et al. [8] presented a Wavelet-based equivalence approach for cracking the equations for Allen-Cahn and Newell-Whitehead. The differential equation, the largest derivative was developed into the sequence of Legendre; this approximate is merged even though the boundary conditions used employing integration constants. They confirmed the conjunction of the suggested techniques. Ultimately, they have provided some numerical instances to verify the reality and relevance of the procedure. Javeed et al. [9] examine the latest exact resolutions of nonlinear fractional partial differential equations (FPDEs). The proposed technique is readily helpful and applicable, which can be executed successfully to solve various kinds of nonlinear FPDEs. Yin and Zhengyuan [10] supposed a rapid algorithm and assumed three numerical illustrations with non-smooth and smooth outcomes. They show the computational efficiency in cracking nonlinear PDEs, from which it is straightforward to see that the computing duration could be preserved. In another research, concentrating on suggesting and exploring a method for Allen-Cahn equations has been accomplished. They studied the conjunction of iterative answers. Numerical examinations were given to prove their submitted procedure.

Furthermore, it is indicated that when compared to standard finite difference iterative methods, iterative processes with extremely rare unknowns have substantially shorter computation times [11]. Khalid et al. [12] introduced a collocation technique established on redefined cubic formulation using finite differences and functions to analyze the inaccurate time-fractional Allen–Cahn equation explanation. They examined the computational efficiency of the offered approach via some numerical samples. The simulation outcomes exhibit a definitive accord with the exact solution corresponding to those seen in the publications. In another study, Olshansky et al. [13] investigated an Allen–Cahn equation expressed on a surface that changes with time as a phase separation example with order-disorder evolution in a slim layer. A standard inner-outer expansion indicates that the solution's limiting manners are a classification flow for the geodesic mean curvature in reference coordinates. They showed a fundamental stability analysis and conjunction investigation for interpolation errors and inaccurate geometry retrieval. The diffusion equation has many applications that researchers have solved in different methods. Ahmad et al. [14] used analytical methods to solve initial value issues in ocean engineering and science. They showed the accuracy of using a technique by comparing the results to an exact solution. Patel et al. [15] approached Fractional Reduced Differential Method to solve the diffusion equation in water pollution. They proved FRDTM gives fast convergence and provides highly accurate numerical results. Lin et al. [16] simulated air pollution diffusion to analyze industrial places. They investigated industrial parks in Taiwan from 2017 to 2019. The results will aid in managing the dangers of air pollution for the petrochemical sector and public health authorities. Moraga et al. [17] studied the SIMPLER algorithm's diffusion problem in fluid flow. The results exhibit that the suggested algorithm has significant advances in reducing the number of iterations and computation time. Yan et al. [18] presented the analytical model for thermal diffusion in porous media. They assess the significance of the Soret impact and temperature dependent diffusion coefficient on non-isothermal diffusion. Hayat et al. [19] considered the thermodiffusion in unsteady magnetohydrodynamic with first order chemical reaction. They showed that compared to radiation and magnetic factors, heat transfer speed is increased. The semi-analytical approach can be utilized to solve the equations governing fluid flow [8, 20, 21] and mass transfer problems. Many researchers have used semi-analytical methods to solve various engineering problems in heat transfer [22-25] and heat pumps [26-28]. One of the essential advantages of these methods is saving time, high accuracy, and proper convergence.

The diffusion equation is a parabolic one; fluid flow depicts the visible behavior of numerous micro-particles in Brownian movement, coming about from the irregular developments and collisions of the particles (Figure 1). A diffusion process is a solution to a stochastic differential equation in probability theory and statistics. The molecule's position is at that point irregular; an advection-diffusion condition represents its likelihood thickness work as a work of space and time.

The real-world phenomenon has been governed by PDEs of integer order which cannot be adequately described. Additionally, no method gives an exact
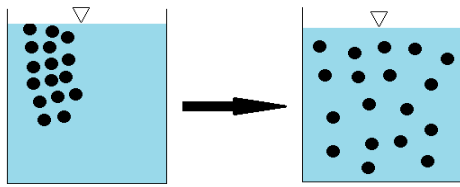
Figure 1. Scheme of diffusion trend in the water

solution for the fractional-order differential equation. Hence, nonlinear PDEs of fractional order make the research more significant. Therefore, in this paper, we have applied HPM an efficient and robust method to find the solutions to the time-fractional diffusion equation and Cahn–Allen equation arising in oil pollution. The novelty of our work is that it provides an accurate prediction of the behavior of oil and is vitally important to preserve the natural shoreline environmental system. Moreover, this method can also be applied to derive various traveling wave solutions with distinct physical structures for nonlinear fractional equations arising in ocean engineering for examining nonlinear behavior due to water waves. Equations of diffusion and Allen-Cahn were solved with different degrees of fractional derivatives (α= 0.25, α=0.5, α=0.75 and α=0.75), and the oil pollution concentration was obtained at a specific time and place.

 This study consists of five sections: In the first section, the topic and literature are discussed. In section two, time-Fractional diffusion is defined in both Riemann-Liouville and Caputo definitions. Also, we provide a review of the HPM and its application in section three and two presented examples illustrate the applicability and validity of the proposed method in section four. Finally, section five is the conclusion.

2. TIME-FRACTIONAL DIFFUSION

A fractional derivative of order α > 0 is defined in many ways [29-31]. The Riemann-Liouville and Caputo definitions are the two that are the most frequently employed. Each definition makes use of whole-order derivatives and Riemann-Liouville fractional integration. In the sense of Caputo the best definitions of fractional derivatives are compiled in this section (CFD). The general diffusion equation with nonlinearity will be taken into account to describe oil contamination in the oceans, and its form is stated as follows [14]:

$$\frac{\partial \psi}{\partial t} = D \frac{\partial^2 \psi}{\partial x^2} + \beta \psi + \gamma \psi^m \tag{1}$$

where D is the diffusion coefficient, C is the concentration, β and γ are real values and ψ is concentration. An example of a diffusion equation is the Allen-Cahn (AC) equation, which is created:
Substitution → m = 3, γ = −1 , β = 1 in Equation (1).

2. 1. Interpretation (*Fractional derivative in the sense of Caputo*)   If f be an integrable continual operation in (a, b) for t ∈ [a, b] then, the left and right Caputo fractional derivatives are ${}_{a}^{C}D_{t}^{\alpha}f(t)$ and ${}_{t}^{C}D_{b}^{\alpha}f(t)$ respectively, of order α, are characterized within the following way:

$$_{a}^{C}D_{t}^{\alpha}f(t)=\frac{1}{\Gamma(n-\alpha)}\int_{a}^{t}(t-\theta)^{n-\alpha-1}\left(\frac{d}{d\theta}\right)^{n}f(\theta)d\theta \tag{2}$$

$$_{t}^{C}D_{b}^{\alpha}f(t)=\frac{1}{\Gamma(n-\alpha)}\int_{t}^{b}(\theta-t)^{n-\alpha-1}\left(-\frac{d}{d\theta}\right)^{n}f(\theta)d\theta \tag{3}$$

2. 2. Interpretation (*Fractional derivative in the sense of Riemann-Liouville*) If f be an integrable continual operation in the interval (a,b) for $t \in [a,b]$ then, the right and left Riemann-Liouville fractional derivatives are $_{t}D_{b}^{\alpha}f(t)$ and $_{a}D_{t}^{\alpha}f(t)$ respectively of order α, are characterized by Equations (4) and (5):

$$_{a}D_{t}^{\alpha}f(t)=\frac{1}{\Gamma(n-\alpha)}\left(\frac{d}{dt}\right)^{n}\int_{a}^{t}(t-\theta)^{n-\alpha-1}f(\theta)d\theta \tag{4}$$

$$_{t}D_{b}^{\alpha}f(t)=\frac{1}{\Gamma(n-\alpha)}\left(-\frac{d}{dt}\right)^{n}\int_{t}^{b}(\theta-t)^{n-\alpha-1}f(\theta)d\theta \tag{5}$$

where $n \in N, n-1 \le \alpha < n$ and Γ is the Euler Gamma Function.

 In both definitions, if $\alpha \in N,$ give the classical derivatives, and the *A* constant's Caputo fractional derivative is always equal to zero.

3. HOMOTOPY PERTURBATION METHOD

We will provide a review of the HPM in this part. Numerous records provide information on the HPM's concepts and their applicability to numerous types of differential equations [22, 24, 32]. Consider the nonlinear differential equation.

 We look at the following equation to demonstrate the fundamental concepts behind this approach:

$$X(u) - z(r) = 0. \qquad r \in \Omega \tag{6}$$

Having a boundary condition:

$$Y(u, \frac{\partial u}{\partial n}) = 0. \qquad\qquad r \in \Gamma \tag{7}$$

$z(r)$ is a well-known analytical function, X is a generic differential operator, Y is a boundary operator and Γ is the domain boundary of Ω and L is linear and N is nonlinear, can be used to split the variable X. Therefore, Equation (10) may be expressed as follows:

$$N(u) + L(u) - z(r) = 0. \qquad r \in \Omega \tag{8}$$

The following is a diagram of the homotopy perturbation structure:

$$H(v, p) = (1-p)[L(v) - L(u_0)] + p[X(v) - z(r)] = 0. \qquad (9)$$

And:

$$v(r, p) : \Omega \times [0,1] \rightarrow R \qquad (10)$$

$p \in [0,1]$ is a parameter of embedding and u_0 is the initial approximation that meets the boundary requirement. Equation (11)'s answer can be expressed as a power series in p, as shown below:

$$v = v_0 + pv_1 + p^2 v_2 + \dots \qquad (11)$$

The following approximates the answer to the question:

$$u = \lim_{p \to 1} v = v_0 + v_1 + v_2 + \dots \qquad (12)$$

3. 1. Application of HPM   To obtain the behavior of the Allen-Cahn condition and the dissemination condition.

- Time–fractional diffusion equation

$$\frac{\partial^\alpha \psi}{\partial t^\alpha} = \frac{\partial^2 \psi}{\partial x^2} + \cos x \qquad (13)$$

- The Allen-Cahn equation with time fractions

$$\frac{\partial^\alpha \psi}{\partial t^\alpha} = \frac{\partial^2 \psi}{\partial x^2} + \psi - \psi^3 \qquad (14)$$

In this paper, the research methodology flowchart is shown in Figure 2. Problem identification is actually seeing the problem before trying to solve it. In other word, it is a first strategy in solving a problem. Numerical solution involves solving the equation by the HPM method, which, if solved, the answer will be validated by the exact solution following literature [14]. This process is repeated until an accurate answer is reached.

4. INFORMATIVE EXAMPLES

To demonstrate the effectiveness of the Homotopy Perturbation Method (HPM), we consider the following Fractional Differential Equations (FDEs) in sense of Caputo type. All the results were calculated by using the symbolic calculus Maple software. Further, the results of the hybrid approach are implemented in Maple software.

Example 4.1
Consider the time-fractional AC Equation (15) and having the initial condition as follows [14]:

$$\frac{\partial^\alpha \psi}{\partial t^\alpha} = \frac{\partial^2 \psi}{\partial x^2} + \psi - \psi^3, \quad 0 < \alpha \le 1 \qquad (15)$$

$$\psi(x,0) = \frac{1}{2} \tanh(0.3536x) - \frac{1}{2}, \qquad (16)$$
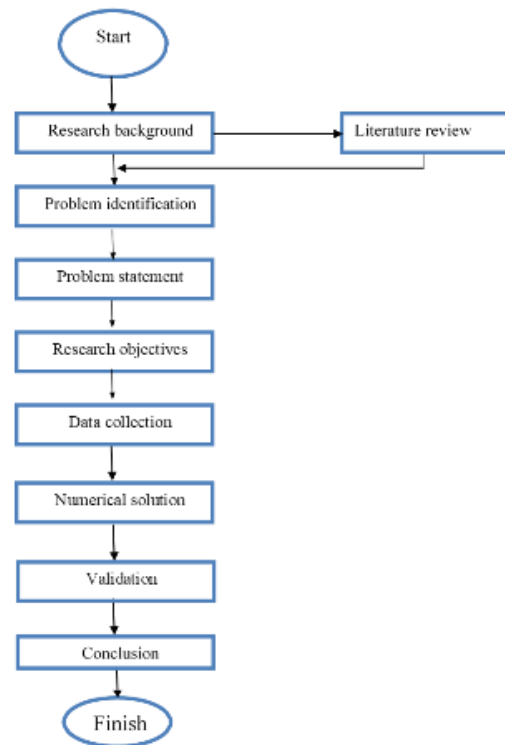
Figure 2. The research methodology flowchart

For $\alpha = 1$, the exact answer to Equation (15) is [14].

$$\psi(x,0) = \frac{1}{2} \tanh(0.3536x - 0.75t) - \frac{1}{2} \qquad (17)$$

4. 1. 1. Application of HPM   For applying the HPM on Equation (15), according to Equation (16) as an initial condition, we have

$$equ := \int_0^t \frac{0.5641895835(\frac{\partial}{\partial t}\psi(x,\tau))}{(t-\tau)^{0.5}} d\tau - \left(\frac{\partial^2}{\partial x^2}\psi(x,\tau)\right) - \psi(x,\tau) + \psi(x,\tau)^3 = 0 \qquad (18)$$

For applying the HPM on Equation (15), the homotopy form of the fractional differential equation should be written. Next, we take into account an approximate solution to the issue in terms of the different powers of P in series. Equation (26), which successfully merges to the precise answer $\psi(x,0) = \frac{1}{2} \tanh(0.3536x - 0.75t) - \frac{1}{2}$, provides the analytical approximation of the fractional order in time of Equation (15).

The effects of "t" on the solution of the AC equation are depicted in Figures 3 and 4 in accordance with the I.C $\psi(x,0) = \frac{1}{2} + \frac{1}{2} \tanh(0.3536x)$. Figure 5 also includes the three-dimensional charts. Figures 3 and 4 show the curved nonlinearity is seen for lower amounts of α, but that there are less nonlinear developments when is closer to 1 (α= 0.25, 0.5, 0.75). The outcomes have been

contrasted with the precise answer that is currently known for integer-order $\alpha= 1$. Figures 3 and 4 display the variations ψ for various values of α. Figure 3 also displays the outcomes for t=0.5, and Figure 4 displays the outcomes for t=1. Figure 5 is three-dimensional plot for the changes of $\psi(x,t)$ and Figure 6 is Abs. Error graph by HPM and MVIA–I [14] for example 1.

$$\psi(x,t) = \psi_0(x,t) + P\psi_1(x,t) + P^2\psi_2(x,t) + P^3\psi_3(x,t) + P^4\psi_4(x,t) \tag{19}$$

$$\frac{\partial}{\partial t}\psi_0(x,t) + P\left(\frac{\partial}{\partial t}\psi_1(x,t)\right) + P^2\left(\frac{\partial}{\partial t}\psi_2(x,t)\right) +$$
$$P^3\left(\frac{\partial}{\partial t}\psi_3(x,t)\right) + P^4\left(\frac{\partial}{\partial t}\psi_4(x,t)\right) =$$
$$P\left(\frac{\partial}{\partial t}\psi_0(x,t) + P\left(\frac{\partial}{\partial t}\psi_1(x,t)\right) +\right.$$
$$P^2\left(\frac{\partial}{\partial t}\psi_2(x,t)\right) + P^3\left(\frac{\partial}{\partial t}\psi_3(x,t)\right) +$$
$$P^4\left(\frac{\partial}{\partial t}\psi_4(x,t)\right)\Big) -$$
$$\left(\int_0^t \frac{0.5641895835\left(\frac{\partial}{\partial t}\psi_0(x,t)+P+P^2+P^3+P^4\right)}{(t-\tau)^{0.5}}d\tau\right) + \tag{20}$$
$$\left(\frac{\partial^2}{\partial x^2}\psi_0(x,t) + P\left(\frac{\partial^2}{\partial x^2}\psi_1(x,t)\right) +\right.$$
$$P^2\left(\frac{\partial^2}{\partial x^2}\psi_2(x,t)\right) + P^3\left(\frac{\partial^2}{\partial x^2}\psi_3(x,t)\right) +$$
$$P^4\left(\frac{\partial^2}{\partial x^2}\psi_4(x,t)\right)\Big) + P\psi_1(x,t) + P^2\psi_2(x,t) +$$
$$P^3\psi_3(x,t) + P^4\psi_4(x,t) - (\psi_0(x,t) + P\psi_1(x,t) +$$
$$P^2\psi_2(x,t) + P^3\psi_3(x,t) + P^4\psi_4(x,t)^3)$$

Then, we should define BCs

$$\psi(x,0) = \frac{1}{2}\tanh(0.3536x) - \frac{1}{2}, \tag{21}$$

After substituting initial conditions into Equation (20) and we putting $P=1$ in each equation we have

$$\psi_0(x,t) = -\frac{1}{2} + \frac{1}{2}\tan\left(\frac{221}{625}x\right) \tag{22}$$

$$\psi_1(x,t) =$$
$$-\frac{1}{3125000}\frac{t\left(103\sinh\left(\frac{221}{625}x\right)\right)+t\left(1171875\,\cosh\left(\frac{221}{625}x\right)\right)}{\cosh\left(\frac{221}{625}x\right)^3} \tag{23}$$

$$\psi_2(x,t) = -\frac{309}{6250000}\frac{1}{\cosh\left(\frac{221}{625}x\right)^5}\left(t\left(\left(\frac{781250}{103}+\right.\right.\right.$$
$$t\right)\cosh\left(\frac{221}{625}x\right)^3 + \left(\frac{2}{3}+\right.$$
$$\frac{686645513117}{120703125}t\right)\sinh\left(\frac{221}{625}x\right)\cosh\left(\frac{221}{625}x\right)^2 - \tag{24}$$
$$\frac{5}{4}\cosh\left(\frac{221}{625}x\right)t - \frac{390831}{1562500}t\sinh\left(\frac{221}{625}x\right)\Big)\Big)$$

$$\psi_3(x,t) = \frac{1}{45776367187500000000} \cdot$$
$$\frac{1}{\cosh\left(\frac{221}{625}x\right)^7}((-6437301784931250000\,t^3 - \tag{25}$$
$$4526367187500000\,t^2 -$$

$17166137695312500000\,t)\cosh\left(\frac{221}{625}x\right)^5 +$
$(-1697387699683408\,t^3 -$
$25749206741887500000\,t^2 -$
$1508789062500000\,t)\sinh\left(\frac{221}{625}x\right)\cosh\left(\frac{221}{625}x\right)^4 +$
$9657084915679687500t^2\left(t +\right.$
$\frac{241406250}{412035623069}\right)\cosh\left(\frac{221}{625}x\right)^3 +$
$3960820003063620\left(t +\right.$
$\frac{183202031250}{640909385609}\right)\sinh\left(\frac{221}{625}x\right)t^2\cosh\left(\frac{221}{625}x\right)^2 -$
$368135762890625\cosh\left(\frac{221}{625}x\right)t^3 -$
$566255996392305\sinh\left(\frac{221}{625}x\right)t^3)$

After simplifying and solving the problem, we have

$$\psi_3(x,t) = -\frac{1}{2} + \frac{1}{2}\tanh\left(\frac{221}{625}x\right) -$$
$$\frac{1}{3125000}\frac{t\left(103\sinh\left(\frac{221}{625}x\right)+1171875\cosh\left(\frac{221}{625}x\right)\right)}{\cosh\left(\frac{221}{625}x\right)^3} -$$
$$\frac{309}{6250000}\frac{1}{\cosh\left(\frac{221}{625}x\right)^5}\left(t\left(\left(\frac{781250}{103}+t\right)\cosh\left(\frac{221}{625}x\right)^3 +\right.\right. \tag{26}$$
$$(\frac{2}{3} + \frac{686645513117}{120703125}t)\sinh\left(\frac{221}{625}x\right)\cosh\left(\frac{221}{625}x\right)^2 -$$
$$\frac{5}{4}\cosh\left(\frac{221}{625}x\right)t - \frac{390831}{1562500}t\sinh\left(\frac{221}{625}x\right)\Big)\Big)$$
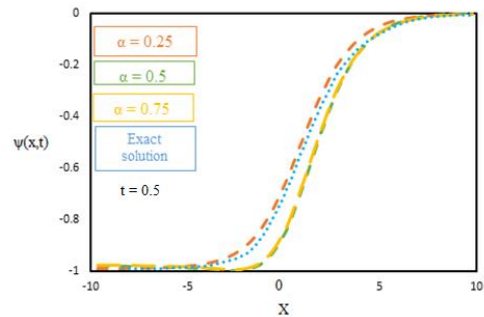

Figure 3. The changes of $\psi(x,t)$ to X in different values of α in t=0.5
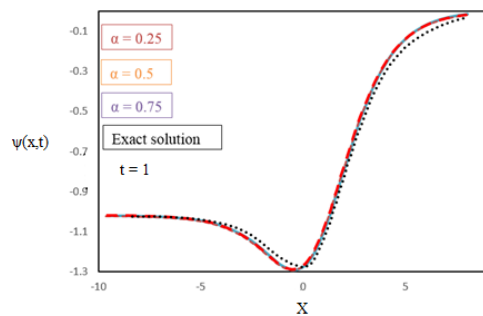

Figure 4. The changes of $\psi(x,t)$ to X in different values of α in t=1

TABLE 1. Comparison of absolute errors for different values for Example 1

x	t=1				t=0.5			
	HPM	MVIA–I [14]	LLWM [8]	ADM [24]	HPM	MVIA–I [7]	LLWM [8]	ADM [24]
-25	1.16529E-10	1.17373E-10	1.18943E-11	1.1644E-11	1.24869E-10	1.25342E-10	6.4747E-12	1.45683E-6
-15	1.37844E-07	1.38319E-07	2.36636E-9	1.37206E-8	1.47136E-07	1.47721E-07	1.35653E-10	1.23638E-9
25	1.58218E-10	1.57665E-10	9.84744E-10	4.8392E-10	1.69113E-09	1.68402E-09	7.49924E-10	1.35958E-8
30	4.60177 E-12	4.59300 E-12	3.57575E-11	1.4096E-11	4.90841E-12	4.90550E-12	2.44443E-10	3.9604E-10
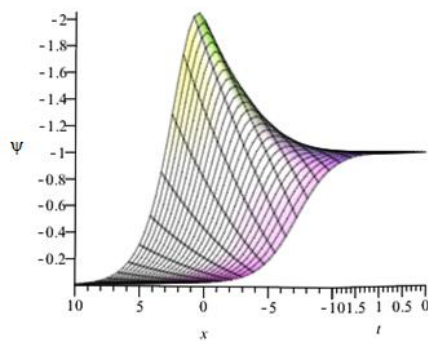
Figure 5. Three-dimensional plot for the changes of $\psi(x,t)$
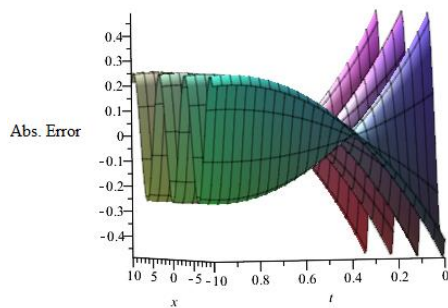
Figure 6. Abs. error graph by HPM and MVIA–I [14]

Example 4.2
Consider the diffusion Equation (27) and having the initial condition as follows [14]:

$$\frac{\partial^\alpha \psi}{\partial t^\alpha} = \frac{\partial^2 \psi}{\partial x^2} + cosx, \quad 0 < \alpha \leq 1 \tag{27}$$

$$\psi(x,0) = 0 \tag{28}$$

For $\alpha = 1$, there is an accurate solution to Equation (27) [7]:

$$\psi(x,t) = cosx\,(1 - e^{-t}) \tag{29}$$

4. 2. 1. Application of HPM   For applying the homotopy perturbation method on Equation (27),

according to the Equation (28) as an initial condition, we have:

$$equ := \int_0^t \frac{0.5641895835(\frac{\partial}{\partial t}\psi(x,\tau))}{(t-\tau)^{0.5}} d\tau - \left(\frac{\partial^2}{\partial x^2}\psi(x,\tau)\right) - \cos(x) = 0 \tag{30}$$

For applying the HPM on Equation (15), the homotopy form of the FDE should be written. The problem's approximation is then considered in terms of the various powers of P in series.

$$\psi(x,t) = \psi_0(x,t) + P\psi_1(x,t) + P^2\psi_2(x,t) + P^3\psi_3(x,t) \tag{31}$$

$$\frac{\partial}{\partial t}\psi_0(x,t) + P\left(\frac{\partial}{\partial t}\psi_1(x,t)\right) + P^2\left(\frac{\partial}{\partial t}\psi_2(x,t)\right) +$$
$$P^3\left(\frac{\partial}{\partial t}\psi_3(x,t)\right) = P\left(\frac{\partial}{\partial t}\psi_0(x,t) +\right.$$
$$P\left(\frac{\partial}{\partial t}\psi_1(x,t)\right) + P^2\left(\frac{\partial}{\partial t}\psi_2(x,t)\right) +$$
$$P^3\left(\frac{\partial}{\partial t}\psi_3(x,t)\right)\right) -$$
$$\left(\int_0^t \frac{0.5641895835\left(\frac{\partial}{\partial t}\psi_0(x,t)+P+P^2+P^3\right)}{(t-\tau)^{0.5}} d\tau\right) + \tag{32}$$
$$\left(\frac{\partial^2}{\partial x^2}\psi_0(x,t) + P\left(\frac{\partial^2}{\partial x^2}\psi_1(x,t)\right) +\right.$$
$$P^2\left(\frac{\partial^2}{\partial x^2}\psi_2(x,t)\right) + P^3\left(\frac{\partial^2}{\partial x^2}\psi_3(x,t)\right)\right) +$$
$$\cos(x))$$

Then, we should define boundary conditions

$$\psi_i(x,t) = 0, \quad i = 0, \dots, 3 \tag{33}$$

After substituting initial conditions into Equation (32) and we putting $P=1$ in each equation we have:

$$\psi_0(x,t) = 0 \tag{34}$$

$$\psi_1(x,t) = cos(x)\,t \tag{35}$$

$$\psi_2(x,t) = -\frac{1}{2}\cos(x)\,t\left(t + \frac{376126389}{250000000}\sqrt{t} - 2\right) \tag{36}$$

and simplifying and solving the problem, we have

$$\psi(x,t) = \cos(x)\, t - \frac{1}{2}\cos(x)\, t\left(t + \frac{376126389}{250000000}\sqrt{t} - 2\right) \tag{37}$$

The time-fractional diffusion problem's approximate analytical solution is shown in Equation (37) and the series solution efficiently converges for precise solution $\psi(x,t) = \cos x\,(1 - e^{-t})$ ask $\rightarrow \infty$ when $\alpha = 1$. Figures 7 and 8 illustrate the effects of 't' (t=0.5 and t=1) on the solution of the AC equation in accordance by the initial condition $\psi(x, 0) = 0$. Figure 9 also include the three-dimensional graphs. Figures 7 and 8 show that the curved nonlinearity is seen for lower values of, but that less nonlinear developments are seen as approaches 1 (α = 0.25, 0.5, and 0.75). The outcomes have been contrasted with the precise answer that is currently known for integer-order = 1. Figure 9 shows three-dimensional plot for the changes of $\psi(x,t)$, and Figure 10 is Abs. Error graph by HPM and MVIA–I [14] for example 2.

Comparison of absolute errors of HPM, MVIA-I [14], and VIA-I [15] for different values of parameters x and t is given in Tables 1 and 2, show that the error in HPM is less as compared to MVIT-I and VIA-I. Moreover, we considered only five iterations which are less than those in MVIT-I [14] and VIA-I [15]. This saves computational time and give better result. The numerical results for AC equations are reported in Tables 1 and 2. To prove the effectiveness of the planned techniques, absolute errors
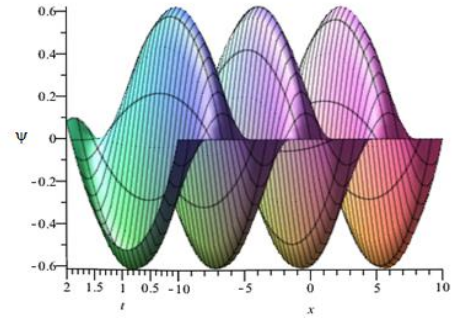

Figure 9. 3D plot for the variation of $\psi(x,t)$
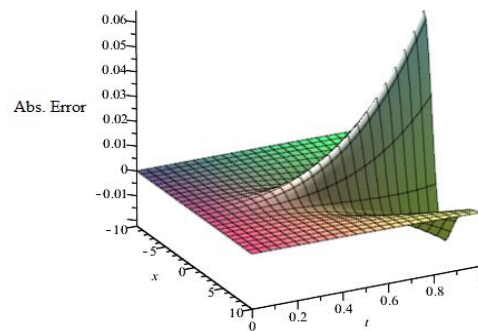
Figure 10. Abs. error graph by HPM and MVIA–I [14] for example 2
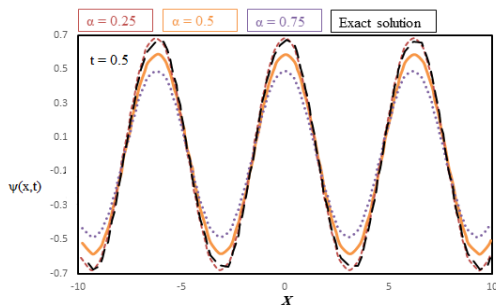
Figure 7. The changes of $\psi(x,t)$ to X in different values of α in t=0.5
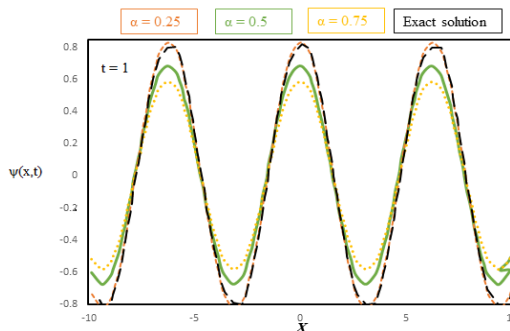
Figure 8. The changes of $\psi(x,t)$ to X in different values of α in t=1

TABLE 2. Comparison of numerical results for different values of x and t for Example 2

x	t	Abs. error in HPM	Abs. error in MVIA – I [14]	Abs. error in VIA – I [15]
1	0.5	1.242E-10	1.671E-10	6.344E-10
2	1.0	0.000E+00	3.563E-10	9.619E-09
3	1.5	2.398E-10	2.683E-09	1.905E-06
4	2.0	0.000E+00	1.871E-08	2.870E+05
5	2.5	3.667E-10	5.510E-08	1.399E-04
6	3.0	0.000E+00	5.522E-07	3.398E-03
7	3.5	2.8430E-10	2.929E-06	1.406E-02
8	4.0	0.000E+00	8.666E-07	1.141E-02
9	4.5	5.160E-09	8.689E-06	2.528E-01
10	5.0	2.600E-09	1.682E-05	7.193E-01

are reported along with the results of other methods; MVIA – I [14], ADM [47], VIA – I [15] and LLWM [1]. In comparison with other techniques results, one can ensure that the results of HPM are more precise. It is cleared from figures that the proposed method can handle the problems accurately and will be applicable in ocean engineering for studying linear and nonlinear water waves.

5. CONCLUSION

Oil pollution is defined as the emission of fluid hydrocarbon into the ocean which causes disastrous effects on marine life's eco and biological environment and leads to fatal repercussions. Thus, it is crucial to precisely predict the spread range of oil spills for an early stage countermeasure against a disaster to preserve the natural shoreline environmental system. For these reasons, in this study, the homotopy perturbation approach is used to generate approximations for the diffusion equation occurring in oil pollution in water for three different fractional orders, $\alpha = 0.25$, $\alpha = 0.5$, and $\alpha = 0.75$; and integer-order, $\alpha = 1.0$; Also, several types of AC equations are obtained using the homotopy perturbation method (HPM). Additionally, it may be used in diffusion equations for both linear and non-linear analyses of marine oil contamination. The results show that the HPM can tackle the problems perfectly, and it can be deployed in diffusion equations for analyzing oil pollution in the sea with linear and non-linear nature. The absolute error diagrams show good accuracy of the applied technique compare to MVIA–I [14] and prove that this method can be used in many scientific and engineering problems and provides highly accurate numerical results without using Adomian polynomials, discretization, transformation, shape parameters, restrictive assumptions, or linearization for nonlinear time-fractional differential equations. As with every other study, our study has had certain limitations. This study focused on the homotopy perturbation method (HPM) and was validated with the MVIA-I method. So for future work, it is highly recommended to solve diffusion equations by VIM and AGM methods.

6. REFERENCES

1. Spaulding, M.L., "A state-of-the-art review of oil spill trajectory and fate modeling", *Oil and Chemical Pollution*, Vol. 4, No. 1, (1988), 39-55. https://doi.org/10.1016/S0269-8579(88)80009-1

2. Shen, H.T. and Yapa, P.D., "Oil slick transport in rivers", *Journal of Hydraulic Engineering*, Vol. 114, No. 5, (1988), 529-543. https://doi.org/10.1061/(ASCE)0733-9429(1988)114:5(529)

3. Yapa, P.D., Shen, H.T. and Angammana, K.S., "Modeling oil spills in a river—lake system", *Journal of Marine Systems*, Vol. 4, No. 6, (1994), 453-471. https://doi.org/10.1016/0924-7963(94)90021-3

4. Lonin, S.A., "Lagrangian model for oil spill diffusion at sea", *Spill Science & Technology Bulletin*, Vol. 5, No. 5-6, (1999), 331-336. https://doi.org/10.1016/S1353-2561(99)00078-X

5. Wang, S., Shen, Y. and Zheng, Y., "Two-dimensional numerical simulation for transport and fate of oil spills in seas", *Ocean Engineering*, Vol. 32, No. 13, (2005), 1556-1571. https://doi.org/10.1016/j.oceaneng.2004.12.010

6. Wang, S.-D., Shen, Y.-M., Guo, Y.-K. and Tang, J., "Three-dimensional numerical simulation for transport of oil spills in seas", *Ocean Engineering*, Vol. 35, No. 5-6, (2008), 503-510. https://doi.org/10.1016/j.oceaneng.2007.12.001

7. Sutantyo, T., Ripai, A., Abdullah, Z., Hidayat, W. and Zen, F.P., "Soliton-like solution on the dynamics of modified peyrard-bishop DNA model in the thermostat as a bio-fluid", *Emerg. Sci. J.(ISSN: 2610-9182)*, Vol. 6, No. 4, (2022). doi: 10.28991/ESJ-2022-06-04-01.

8. Hariharan, G., "An efficient legendre wavelet-based approximation method for a few newell–whitehead and allen–cahn equations", *The Journal of Membrane Biology*, Vol. 247, No. 5, (2014), 371-380. https://doi.org/10.1007/s00232-014-9638-z

9. Javeed, S., Saif, S. and Baleanu, D., "New exact solutions of fractional cahn–allen equation and fractional dsw system", *Advances in Difference Equations*, Vol. 2018, No. 1, (2018), 1-15. https://doi.org/10.1186/s13662-018-1913-3

10. Yin, B., Liu, Y., Li, H. and He, S., "Fast algorithm based on tt-m fe system for space fractional allen–cahn equations with smooth and non-smooth solutions", *Journal of Computational Physics*, Vol. 379, (2019), 351-372. https://doi.org/10.1016/j.jcp.2018.12.004

11. Li, H. and Song, Z., "A reduced-order energy-stability-preserving finite difference iterative scheme based on pod for the allen-cahn equation", *Journal of Mathematical Analysis and Applications*, Vol. 491, No. 1, (2020), 124245. https://doi.org/10.1016/j.jmaa.2020.124245

12. Khalid, N., Abbas, M., Iqbal, M.K. and Baleanu, D., "A numerical investigation of caputo time fractional allen–cahn equation using redefined cubic b-spline functions", *Advances in Difference Equations*, Vol. 2020, No. 1, (2020), 1-22. https://doi.org/10.1186/s13662-020-02616-x

13. Olshanskii, M., Xu, X. and Yushutin, V., "A finite element method for allen–cahn equation on deforming surface", *Computers & Mathematics with Applications*, Vol. 90, (2021), 148-158. https://doi.org/10.1016/j.camwa.2021.03.018

14. Ahmad, H., Khan, T.A., Durur, H., Ismail, G. and Yokus, A., "Analytic approximate solutions of diffusion equations arising in oil pollution", *Journal of Ocean Engineering and Science*, Vol. 6, No. 1, (2021), 62-69. https://doi.org/10.1016/j.joes.2020.05.002

15. Patel, H., Patel, T. and Pandit, D., "An efficient technique for solving fractional-order diffusion equations arising in oil pollution", *Journal of Ocean Engineering and Science*, (2022). https://doi.org/10.1016/j.joes.2022.01.004

16. Lin, Y.-C., Lai, C.-Y. and Chu, C.-P., "Air pollution diffusion simulation and seasonal spatial risk analysis for industrial areas", *Environmental Research*, Vol. 194, (2021), 110693. https://doi.org/10.1016/j.envres.2020.110693

17. Moraga, N.O., Jaime, J.I. and Cabrales, R.C., "An approach to accelerate the convergence of simpler algorithm for convection-diffusion problems of fluid flow with heat transfer and phase change", *International Communications in Heat and Mass Transfer*, Vol. 129, (2021), 105715. https://doi.org/10.1016/j.icheatmasstransfer.2021.105715

18. Yan, H., Sedighi, M. and Xie, H., "Thermally induced diffusion of chemicals under steady-state heat transfer in saturated porous media", *International Journal of Heat and Mass Transfer*, Vol. 153, No., (2020), 119664. https://doi.org/10.1016/j.ijheatmasstransfer.2020.119664

19. Hayat, T., Khan, S.A. and Momani, S., "Finite difference analysis for entropy optimized flow of casson fluid with thermo diffusion and diffusion-thermo effects", *International Journal of Hydrogen Energy*, Vol. 47, No. 12, (2022), 8048-8059. https://doi.org/10.1016/j.ijhydene.2021.12.093

20. Domiri-Ganji, D., Jalili, B., Jalili, P., Shateri, A. and Mousavi, A., "Thermal analysis of fluid flow with heat generation for different logarithmic surfaces", *International Journal of Engineering,*

Transactions C: Aspects, Vol. 35, No. 12, (2022). doi: 10.5829/IJE.2022.35.12C.03.

21. Jalili, B., Sadighi, S., Jalili, P. and Ganji, D.D., "Characteristics of ferrofluid flow over a stretching sheet with suction and injection", *Case Studies in Thermal Engineering*, Vol. 14, No., (2019), 100470. https://doi.org/10.1016/j.csite.2019.100470

22. Jalili, P., Ganji, D.D., Jalili, B. and Ganji, D.R.M., "Evaluation of electro-osmotic flow in a nanochannel via semi-analytical method", *Thermal Science*, Vol. 16, No. 5, (2012), 1297-1302. doi: 10.2298/TSCI1205297J.

23. Jalili, P., Ganji, D. and Nourazar, S., "Hybrid semi analytical method for geothermal u shaped heat exchanger", *Case Studies in Thermal Engineering*, Vol. 12, No., (2018), 578-586. https://doi.org/10.1016/j.csite.2018.07.010

24. Gui, C. and Zhao, M., "Traveling wave solutions of allen–cahn equation with a fractional laplacian", in Annales de l'Institut Henri Poincaré C, Analyse non linéaire, Elsevier. Vol. 32, (2015), 785-812.

25. Pasha, P., Nabi, H., Peiravi, M.M. and Ganji, D.D., "Hybrid investigation of thermal conductivity and viscosity changeable with generation/absorption heat source", *Computational Thermal Sciences: An International Journal*, Vol. 14, No. 1, (2022). doi. 10.1615/ComputThermalScien.2021039390

26. Farid, Z., Lamdouar, N. and Ben Bouziyane, J., "A method of strip footings design for light structures on expansive clays", *International Journal of Engineering, Transactions A: Basics*

Vol. 35, No. 1, (2022), 248-257. doi: 10.5829/IJE.2022.35.01A.24.

27. Jalili, B., Aghaee, N., Jalili, P. and Ganji, D.D., "Novel usage of the curved rectangular fin on the heat transfer of a double-pipe heat exchanger with a nanofluid", *Case Studies in Thermal Engineering*, (2022), 102086. https://doi.org/10.1016/j.csite.2022.102086

28. Tarrad, A.H., "3d numerical modeling to evaluate the thermal performance of single and double u-tube ground-coupled heat pump", *HighTech and Innovation Journal*, Vol. 3, No. 2, (2022), 115-129. doi: 10.28991/HIJ-2022-03-02-01.

29. Cresson, J., "Fractional embedding of differential operators and lagrangian systems", *Journal of Mathematical Physics*, Vol. 48, No. 3, (2007), 033504. https://doi.org/10.1063/1.2483292

30. Kilbas, A.A., Srivastava, H.M. and Trujillo, J.J., "Theory and applications of fractional differential equations, elsevier, Vol. 204, (2006).

31. Miller, K.S. and Ross, B., "An introduction to the fractional calculus and fractional differential equations, Wiley, (1993).

32. Jalili, B., Jalili, P., Sadighi, S. and Ganji, D.D., "Effect of magnetic and boundary parameters on flow characteristics analysis of micropolar ferrofluid through the shrinking sheet with effective thermal conductivity", *Chinese Journal of Physics*, Vol. 71, (2021), 136-150. https://doi.org/10.1016/j.cjph.2020.02.034

Persian Abstract

چکیده

نشت نفت در دریاها و اقیانوس ها باعث آلودگی می شود و اثرات مخرب زیست محیطی زیادی دارد. معادلات انتشار (پارابولیک) معقول ترین گزینه برای مدل سازی انتشار این نشت و آلودگی است. این معادلات اجازه می دهد تا آمار مربوط به مقدار نفتی که به خروجی اقیانوس رسیده است، به عنوان شرایط اولیه و مرزی برای مدل ریاضی انتشار و تغییر نفت در دریاها مورد استفاده قرار گیرد. از آنجایی که شامل مولفه هذلولی (فرار/موج) معادله می شود، معقول ترین انتخاب معادلات انتشار و آلن کان (AC است که حل عددی آنها دشوار است. معادلات انتشار و آلن کان با درجات مختلفی از مشتقات کسری حل شد α= ۰/۲۵، α۰/۵، α۰/۷۵= و ۰/۷۵= (α و غلظت آلودگی نفتی در زمان و مکان مشخصی به دست آمد. روش اغتشاش هموتوپی (HPM) برای معادله غیرخطی آلن-کان (AC) و معادله انتشار کسری زمان برای بیان آلودگی نفتی در آب را نشان می دهد. دو مثال ارائه شده کاربرد و اعتبار روش پیشنهادی را نشان می دهد. غلظت آلودگی در میدان جریان در یک بازه زمانی و مکانی برای درجات مختلف اشتقاق کسری نشان داده شده است. در درجات مشتق کسر کمتر، رفتار غلظت آلودگی غیرخطی است و با افزایش درجه مشتق کسر به یک، رفتار غیرخطی غلظت آلودگی کاهش می‌یابد. نتایج حاصل از تکنیک پیشنهادی در مقایسه با راه‌حل‌های دقیق نشان می‌دهد که این روش کارآمد و راحت بوده و زمان محاسباتی را کاهش می‌دهد.

International Journal of Engineering

J o u r n a l   H o m e p a g e :   w w w . i j e . i r

Numerical and Experimental Investigation on Small Scale Magnetorheological Damper

S. Vivekananda Sharma*, G. Hemalatha

Department of Civil Engineering, Karunya institute of technology and Sciences, Coimbatore, India

P A P E R I N F O	*A B S T R A C T*
	This paper presents the design of an Magnetorheological (MR) damper that includes an arrangement of a piston and cylinder. This study developed a 3-D model based on the finite element method (FEM) concept on the COMSOL Multiphysics to analyze and investigate the MR damper characteristics. A prototype of the MR damper is being fabricated based on the FEM model and is put through a series of experiments using the Servo-Hydraulic material testing machine (MTS). Maximum and minimum forces, 171.5235N and 249.2749N, were measured at 0.1Hz and 1Hz, respectively, for the FEM model. The fabricated model obtained similar results at 0.1Hz and 1Hz, with maximum and minimum forces of 175.9103N and 252.7765N, respectively. Comparing these two model analyses reveals that the FEM-based model accurately depicts the experimental behaviour of the MR damper in terms of its damping force, although there is minor variation. The findings of this paper will be helpful for designers in creating MR dampers that are more efficient and reliable, as well as in predicting the characteristics of their damping force.

NOMENCLATURE

F_τ	Yield stress force(N)	Q	volumetric flow rate (mm^3/s)
F_η	Viscous Component force(N)	A_p	C/s of piston area (mm^2)
F_f	Friction Component force(N)	D	Diameter of cylinder (mm)
F_D	Total damping force(N)	d_o	Diameter of piston Rod (mm)
v	velocity of the piston (mm/s^2)	h	Height of piston (mm)
L_t	Length of Piston rod (mm)		

Greek Symbols

τ_y	Shear stress(kPa))	ω	circumference of the flow path
η	Viscosity of MR fluid	$Sgm(v)$	reciprocating motion
β	Magnetic Field density (T)		

1. INTRODUCTION

Engineers and researchers aim to learn vibration control technology since civil infrastructure, automotive systems, and industrial equipment vibrate excessively. Magnetorheological dampers,as a method of vibration control technology are used to stop excessive vibrations. It's an improved version of hydraulic damper. Magnetorheological fluid has been replaced with damper oil (MR fluid). This MR fluid contains carrier liquid and freely movable magnetic particles. MR fluid operates like damper oil without magnetic fields. Iron particles in a magnetic field generate a chain pattern. This structure dampens extrinsic vibrations in the electromagnetic field created by an electromagnet on the damper piston. Electromagnets have many copper coils and electrifying the coils creates an electromagnetic field. Shaking buildings use MR dampers as a semi-active control system. The MR damper was popular with researchers because it is controllable and used little electricity. This allowed it to reduce the vibrations in buildings. Magnetorheology is based on how a magnetic field

Corresponding Author Institutional Email:
svivekananda@karunya.edu.in (S. Vivekananda Sharma)

affects fluid rheology. Magnetic fields abruptly modify viscosity (in a few milliseconds) [1]. Magnetorheological fluid is created by combining a carrier liquid with ferromagnetic particles and additives. Ferromagnetic particles float freely in the absence of a magnetic field. Ferromagnetic particles account for 20-40% of total volume (25 to 80 percent by weight). A magnetic field is absent, whereas the presence is ON. In the ON state, ferromagnetic particles form a chain due to the magnetic field. MR damper has a strong damping force with a low magnetic field. The research needs to consider the damper's dynamic performance as a result of the various loading situations, stroke length, current input, and other factors [2].

The MR damper is most commonly used in the suspension of motor vehicles; however, its application has recently been expanded to include other critically important structures, like buildings, turbines, wind bridges, washing machines, prosthetic limbs, landing gear, and so on [3-9].

Srinivasan et al. [10] studied many different magnetorheological (MR) damper valve designs and analyzed their performance indices. These performance parameters included inductive time constant, valve ratio, dynamic range, and pressure drop. To reduce the risk of earthquakes, Daniel et al. [11] concentrated on the issue of adjusting the damping force of a shear mode magnetorheological damper. Consequently, the MR damper operating in shear mode capable of controlling vibration is studied using experimental and computational methods. Seid et al. [12] designed and analyzed an above-knee prosthesis using a magnetorheological (MR) damper. A dynamic system model for the prosthetic leg swing phase with a single-axis knee and optimal MR damper was created. The research was carried out by Hou et al. [13] to investigate the performance of an MR damper after it had been mounted on a material testing machine (MTS) and put through a series of tests with varied excitation frequencies. The reaction time parameters, energy dissipation, and responsive force were analyzed in this research. The results of the experiments served as the basis for these analyses. Wu and Cai [14] discovered in their research that MR dampers regulate the vibrations of cable-stayed bridges under various excitation frequencies, one of which is the resonant frequency. When constructing twin-tube MR dampers that are outfitted with a single coil, it is common to practice using magnetic shields and sandwiched magnetic shields. This research was conducted by Ganesha et al. [15] and concluded that the experiment was successful, as evidenced by improvements in suspension control, ride comfort, and deflection of tires.

Wani et al. [16] suggested two response-based-adaptive control techniques for reducing inter-story drift and acceleration response. Control techniques are combined with the device location algorithm to determine the optimal magnetorheological damper configuration and controls system design parameters. Fast Fourier transform response showed that the structure's reactionwas attenuated and spread throughout its modes.

Wani et al. [17] measured the in-plane motion of a five-story steel structure on a shake table using magnetorheological dampers (MR). Measurements of displacement, velocity, acceleration, displacement, story drift of the floors, and stresses in base column are collected and compared with standard data. The shake table results showed the efficiency and precision of the proposed DIC system in monitoring structural responses compared to noisy responses, highlighting the potential of this technique for monitoring, controlling, and reconnoitring a wide range of structures during and after extreme events. Daciel et al. [18] built a 10kN MR damper with an RCC frame. This frame was earthquake-excited at 0 A, 3 A, and without an MR damper for comparison. Comparisons showed displacement reductions, force increases, and crack pattern modifications. The suggested semiactive damper can reduce structural responses in moderate to high seismicity locations. Daciel et al. [19] studied which includes designing, developing, and testing a novel MR damper. Multi-coil magnetic generating was employed to boost flow gap shear force. The research examines the proposed system's element and structure-level reactions to strong ground motions. OpenSees was used to simulate a building structure to demonstrate its usefulness.

Abdeddaim et al. [20] improved SSI between a based isolated structure and soil with an MR damper. Using 100 earthquake arrays, the structure's dynamic behaviour was studied. The results showed that optimising base-isolated structures with an MR damper improved their response. Rashid et al. [21] examined a 5-story steel frame employing an ARBA method paired with a device placement optimization technique and an MR damper control system. The numerically simulated results demonstrated that MR damper locations are highly correlated to the designer's output aim. ARBA approaches outperformed uncontrolled and passive control systems in modulating the structure's acceleration response and improved dynamic serviceability. Wani et al. [22] conducted computational and experimental research to determine the efficiency and performance of a suggested MRO-based control with iterative technique using magnetorheological (MR) dampers as a control device in reducing structural reaction. Results showed the strategy's effectiveness and versatility in minimising structural responses. The control tactics were then tested on a five-story steel frame with an MR damper. The results showed MRO control is superior to passive control in minimising structural reactions.

Wani et al. [23] studied structure arrangement and damper number on response decrease. In this study, one and two MR dampers at different stories are used to evaluate the control of a five-story structure based on performance metrics. It also introduced a fail-safe current value for each floor's MR damper in case of feedback or control failure. The results suggested placing dampers on the ground floor, then the second, and lower-floor MR dampers should have a greater failsafe current value for effective passive control of the structures.

In this paper,as an extension work of Vivekananda et al. [24], a three-dimensional model employing the finite element approach is developed again by making use of the effective parameters [24] using COMSOL Multiphysics (FEM). Based on this information, the damping force obtained through computational and experimental analysis is validated for the model after the fabricated MR damper has been tested in the servo-hydraulic MTS.

2. ANALYSIS OF SMALL-SCALE MR DAMPER USING FEM

In order to simulate the behavior of a physical system or assembly, FEM breaks down a physical system or assembly's geometry into a large number of small, uniformly shaped elements, formulates equations, applies loads and constraints to the boundary conditions, and then solves the modified system equations for the relevant unknown field variables, such as strain, temperature, magnetic flux, and displacement. This work uses the widely-used FEM COMSOL Multiphysics software[1].

The study of the MR damper is an interesting and potentially gainful endeavor because it enables a controllable damping force to be generated simply by adjusting the current that flows through its coil (Figure 1). The current can be induced through a DC power supply, motor vehicle batteries, or a normal battery. With the aid of the finite element method, various researchers aim to model and design MR dampers from various design perspectives (FEM). Consequently, various MR dampers designs have emerged, each featuring a operating principle, effective range and unique geometry [25]. An MR damper's damping force depends on the magnetic field induced in the piston-cylinder clearance [26]. Figure 2 depicts the magnetic circuit of the MR damper, which was derived from a comprehensive review of the relevant literature. The MR damper is modeled with the parameters listed in Table 1.

---

2. 1. Modelling of MR damper in COMSOL   To conduct static magnetic analysis of the MR damper using the COMSOL Multiphysics. the following steps are taken.
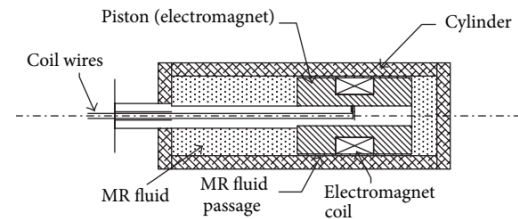

Figure 1. Schematic of MR Damper
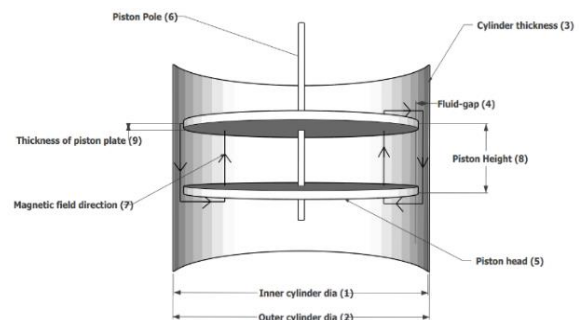
Figure 2. Flow diagram of Magnetic circuit in MR damper

TABLE 1. Dimensions of MR Damper's Prototype

Parameter	Dimension
(1) Inner Cylinder Dia	40mm
(2) Outer Cylinder Dia	44mm
(3) Cylinder Thickness	2mm
(4) Annular Fluid Gap	1mm
(5) Piston plate Dia	38mm
(6) Piston rod Dia	10mm
(8) Piston Height	50mm
(9) Piston plate Thickness	5mm

TABLE 2. MRF 132DG Properties

Properties	132DG MRF
Density	2.44 gm/cm3
Flash-Point	>170
Yield-Stress	47 kPa
Solid/Weight ratio	72
Working Temp.	-15 to 160 Celcius
Responsive time	Less than Millisecond
Viscosity	0.28(pa.s)@40oC

a) Building Physical Environment
b) Add physics properties to specific regions, and Build and mesh the model.
c) Excite boundary conditions and loading conditions.
d) Obtain solutions
e) Simulate and post-processing of results

The MR damper is an axisymmetric solid that is being stressed in an axisymmetric manner. Keeping in mind that a 2D FEM simulation is sufficient for the simulation, the 3D model has opted in this work as not much literature is available on using the 3D prototype, as presented in Figure 3. The cylinder, piston, and MR fluid annular gap are static components of the electromagnetic coil's magnetic circuit. In COMSOL modeling, 500 coil turns are utilized to measure magnetic flux density. Variable coil current produces variable magnetic flux density. As for this specific model, cylinder and piston material is adopted as steel with the relative permeability value as 2000 Coil relative permeability as 1, MR fluid as 6, and free space's magnetic permeability as 4π x10^7 H/m [26].

2. 1. 1. Physics Environment   Space requires a 3D model. The Solid Works model is loaded into COMSOL as a step file. Figure 4 shows the air-encased model. Determining the magnetic field induced by coil current flow is the issue. COMSOL Multiphysics AC/DC interface is used. Next, the issue analysis includes magnetic fields (mf) physics. Magneto-static analysis enables for stationary examination[1].

2. 1. 2. Material Attribution   Magnetic fields in the air are explored using a 3D model. The piston rod and head are made of mild steel. The electromagnetic coil uses solid copper. Inner and outer piston poles are made of mild steel. MR fluid gap incorporates Lord Corporation's MRF 132DG fluid specifications. Table 3 lists 132DG MR fluid's properties[2].
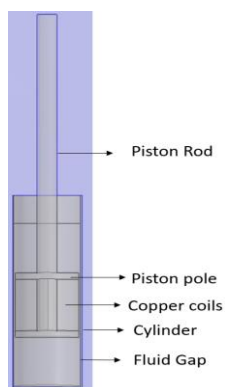

Figure 3. 3D model of MR damper in COMSOL

2. 1. 3. Meshing   Figure 4 shows the generated mesh using ultra-fine meshing in the physics-controlled domain. 8 domains, 84 edges, and 48 vertices make up the mesh model. The extreme mesh for simulation includes 10,18,846 elements, including 1,02665 border elements and 3,624 edge elements [24].

2. 1. 4. Boundary Conditions   The model's center plane is axisymmetric. Using a magnetic insulation boundary condition (air medium), the full domain's outside boundaries can be applied, provided no flux leakage beyond the work area. In COMSOL, the coil area refers to the boundary condition of the coil wire, which has a C/S area of 0.2192mm^2, or Copper wire SWG 16. Every 0.5A simulation increases the coil's current by 0.5A to 2A. The domain, excluding the coil, is subject to ampere law[3].

2. 1. 4. Solving   Time-independent stationary magnetostatics solves the problem. The problem is solved using COMSOL's Magnetic fields module. This module solves Maxwell's equations according to specified boundary conditions using a laptop with an AMD Ryzen 5 2500u processor with 4 central cores and 8 secondary cores and a base clock speed of 2.3 GHz, which is more than enough to carry out the study. Simulation solved 79,21,037 SDOF. The MUMPS solver in COMSOL Multiphysics solves the simulation using 1 as tolerance and 1000 as residual [24]. This simulation varied current and coil turns.

2. 1. 5. Post-processing of Result   COMSOL Multiphysics can show flux density flow lines in 2D as surface and in 3D as volume. Through the MR fluid gap, magnetic flux lines flow over the working domain. Between the outer and inner poles, flux lines jump. The MR fluid gap between the inner and outer poles has the most flux lines. Near the magnetic coil, the MR fluid gap exhibits few flux lines. Figure 5 shows the 3D flux density distribution. We can get the desired outcomes by adjusting the current input and coil count.

3. DAMPING FORCE CALCULATION

The magnetic flux densities computed by the COMSOL are used to determine the MR damper's damping force for
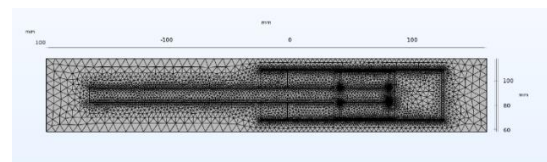

**Figure 4.** The extrafine meshing of model

---
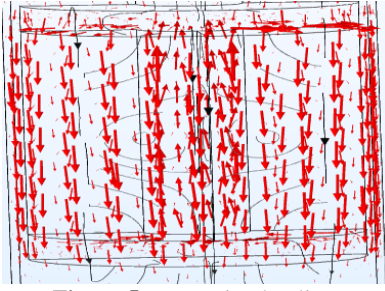
Figure 5. Magnetic Flux lines

the FEM model. For this purpose, the graphs provided by the Lord Corporation, USA, are used to develop the relationship between the shear stress (τ_y) and the magnetic flux density (B) for Lord MRF-132DG.

The final equation is displayed in Equation (1). The value of shear stress procured at specific magnetic flux levels is then used to calculate the damping force in Equation (5).

$$\tau_y = (6.9*10^2) + (4*10^4)\beta - (1*10^5)\beta^2 + (9.1*10^4)\beta^3 \tag{1}$$

Induced yield stress, denoted by F_τ And viscous components, denoted by F_η They are said to be the components that make up the damping force, F_D, in accordance with the Bingham plastic model [26-28] of plates. This is illustrated as:

$$F_D = F_\tau + F_\eta$$

$$F_D = \left[\left(2.07 + \frac{12Q\eta}{12Q\eta + 0.4\omega h^2 \tau_y}\right) \times \frac{\tau_y L A_p}{h} \, Sgm(v)\right] + \left[\left(1 + \frac{\omega h v}{2Q}\right) \times \frac{12Q\eta L_t A_p}{\omega h^3}\right] \tag{2}$$

where,

$$Q = A_p \times v \tag{3}$$

$$A_p = \frac{\pi}{4}\left(D^2 - d_o^2\right) \tag{4}$$

Q represents the rate of volumetric flow rate of the MR fluid, A_P represents the C/s of piston area, D represents the diameter of cylinder and d_0 represents the diameter of the piston rod, v represents the velocity of the piston, τ_y represents the shear yield strength of the MR fluid, η represents the viscosity without excitation, L_t represents the pole length, ω represents the mean circumference of the flow path of the damper, h represents the height of piston and $Sgm(v)$ represents the reciprocating motion of the piston.

According to the researchers [29-31] one must take into account the system's frictional forces (F_f). Considering friction is prevalent on the contact area of both the movable and the stationary components of the MR damper, it is unwise to ignore it in the study. The total damping force is represented as F_D

$$F_D = F_\tau + F_\eta + F_f \tag{5}$$

Using the Equations (1) to (5), damping force of the piston is computed numerically and presented in Table 4.

4. EXPERIMENTAL SETUP

Using the dimensions chosen in Table 1 for Finite element modeling, a prototype MR damper is constructed. Figure 6 depicts the whole assembly of the prototype MR damper's component pieces. The clearance area between the piston and cylinder in the damper allows MR fluid to flow from a higher to lower chamber and, conversely, when the piston starts moving.

Using the LORD MRF-132DG in the MR damper, the prototype magnetorheological damper is evaluated for performance using the MTS. Figure 7 represents the Servo-Hydraulic MTS setup used for the experimental analysis.

The MTS constitutes a power unit capable of exciting frequency for a range of 0.1 to 2 Hz and a rated sine force of 1000 kN. The MTS has a 127 mm peak-to-peak amplitude rating. The vibration's amplitude is adjusted at a desirable value by changing the test system's displacement input and excitation frequency. MTS can be controlled both manually or through a system-based

Figure 6. Fabricated MR damper

Figure 7. MTS setup

control mode. Only vertical vibrational analysis may be performed with the shaker. MTS Suite controls system is a system-based controller with a built-in signal recorder.

The MTS suite is programmed to collect real-time data and provides real-time data in time, acceleration, displacement, velocity, and force. The damper is positioned vertically in the loading frame of MTS, as shown in Figure 8, which is also a part of the testing system.

For safety, the MR damper's piston beginning position is managed using the control system or manually. Before the MR damper's experimental performance examination, the piston is placed in the cylinder's center.

The test is run at a fixed displacement of 10 mm for 10 cycles. Repeating the test under the same circumstances with a different frequency and supplying a steady 2A current to the MR damper's electromagnetic coil. The MTS suite control system monitors the force for every test run.

4. RESULTS

The magnetic flux density generated according to COMSOL, increases with induced MR damper current. Figure 9 and Table 3 quantify these phenomena, and the


Figure 8. MR damper on the MTS loading frame
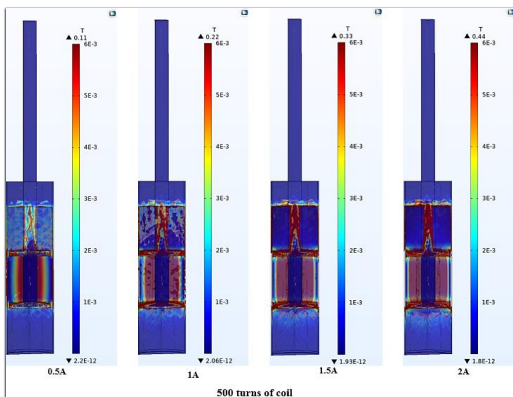
Figure 9. Effect of magnetic flux on the piston area

TABLE 3. Magnetic flux density procured using the FEM model

Input Current(A)	Magnetic Flux Density (Tesla)
0.5A	0.11T
1A	0.22T
1.5A	0.33T
2A	0.44T

effect of magnetic flux density on the piston area is also observed.It is evident from Figure 9 , how the increase in current input leading to increase in magnetic flux affects the piston area.

The experimental damping force, displacement, and velocity acquired by the piston rod are recorded by the MTS suite's built-in DAQ system. The experimental damping force that was achieved for various stimulation frequencies is given in Table 4. This damping force is contrasted with the outcomes of the numerically procured damping force via the FEM simulation data. Figure 10 qualitatively compares them.

Comparing the experimental and numerical model data, it is confirmed that the behaviour of both models is similar. Figure 10 proves that the increase in force is proportional to the excitation frequency. A significant point noted here is that the analytical model curve is smooth, whereas the experimental mode has some irregularities even though it is increasing proportionally. The irregular curve shape from 0.6hz to 0.9hz occurs due to the shear thickening of MR fluid, where MR fluid viscosity increases under shear loading.

Finally, it is highlighted through this investigation that with increased excitation frequency, with higher frequencies shear thickening phenomenon occurs in the MR damper, and the corresponding damping force also increases, which relates to higher velocity and damping coefficient.

TABLE 4. Total Damping force procured through investigation

| Frequency (Hz)	Damping Force For Numerical (N)	Damping Force for Experimental (N)
0.1	171.3267	175.9103
0.2	183.358	185.3950
0.3	191.6985	195.8292
0.4	198.4517	202.6527
0.5	200.6951	204.2349
0.6	203.6824	205.3156
0.7	207.3215	209.7016
0.8	215.1295	227.1423
0.9	230.3655	224.8602
1	249.2398	252.7765
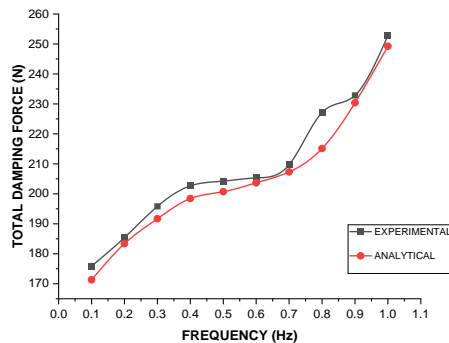
Figure 10. Relationship of force and frequency plot for various frequency

5. CONCLUSION

The most popular fluids in MR dampers for achieving variable damping coefficient are MR fluids. For the manufactured MR damper, FEM modelling has been done using the COMSOL platform. The magnetic flux density values obtained from the COMSOL study were used to calculate the overall damping force. Then, experimental damping force is achieved by running tests on the prototyped fabricated MR damper using the MTS servo-hydraulic machine with various excitation frequencies. When these two modelling results are compared, it is confirmed that the overall damping forces produced numerically and experimentally are almost equal with an error margin (1N-5N) which is negligible, throughout a broad range of excitation frequencies. It can be seen from the different graphical findings that the damper experiences a total maximum dampening force of 252.7768 N and 249.2398N at 1hz for FEM and the Experimental model respectively.

This research concludes that the Finite Element Model accurately captures the behaviour of the fabricated MR damper. The methodology used in this paper's study is sufficient for controlling and designing an MR damper. The findings of this study will aid designers in producing MR dampers that are more dependable and efficient, as well as in predicting the damping force within the engineering analysis's allowable error.

6. REFERENCES

1. Chen, E., Si, C. and Liu, J., "Experimental study of magneto-rheological materials and its damper dynamic characteristics", in 2010 Sixth International Conference on Natural Computation, IEEE. Vol. 1, (2010), 278-281.

2. Ferdaus, M.M., Rashid, M.M., Shanta, M., Tamanna, N. and Hasan, M.H., "Experimental investigation on magnetorheological damper's characterization", in Advanced Materials Research, Trans Tech Publ. Vol. 1115, (2015), 476-479.

3. Kasprzyk, J., Wyrwał, J. and Krauze, P., "Automotive mr damper modeling for semi-active vibration control", in 2014 IEEE/ASME international conference on advanced intelligent mechatronics, IEEE., (2014), 500-505.

4. Gudmundsson, K., Jonsdottir, F. and Thorsteinsson, F., "A geometrical optimization of a magneto-rheological rotary brake in a prosthetic knee", *Smart materials and Structures*, Vol. 19, No. 3, (2010), 035023. doi: 10.1088/0964-1726/19/3/035023.

5. Powell, L.A., Hu, W. and Wereley, N.M., "Magnetorheological fluid composites synthesized for helicopter landing gear applications", *Journal of Intelligent Material Systems and Structures*, Vol. 24, No. 9, (2013), 1043-1048. doi: 10.1177/1045389X13476153.

6. Nguyen, Q., Choi, S.-B. and Woo, J., "Optimal design of magnetorheological fluid-based dampers for front-loaded washing machines", *Proceedings of the Institution of Mechanical Engineers, Part C: Journal of Mechanical Engineering Science*, Vol. 228, No. 2, (2014), 294-306. doi: 10.1177/0954406213485908.

7. Motra, G.B., Mallik, W. and Chandiramani, N.K., "Semi-active vibration control of connected buildings using magnetorheological dampers", *Journal of Intelligent Material Systems and Structures*, Vol. 22, No. 16, (2011), 1811-1827. doi: 10.1177/1045389X11412640.

8. Oh, J.-S., Shin, Y.-J., Koo, H.-W., Kim, H.-C., Park, J. and Choi, S.-B., "Vibration control of a semi-active railway vehicle suspension with magneto-rheological dampers", *Advances in Mechanical Engineering*, Vol. 8, No. 4, (2016), 1687814016643638. doi: 10.1177/1687814016643638.

9. Martynowicz, P. and Szydło, Z., "Wind turbine's tower-nacelle model with magnetorheological tuned vibration absorber", in Proceedings of the 14th international Carpathian control conference (ICCC), IEEE., (2013), 238-242.

10. Srinivasan, S., Kebede, S. and Chandramohan, S., "Performance evaluation of magnetorheological damper valve configurations using finite element method", *International Journal of Engineering, Transactions B: Applications* Vol. 30, No. 2, (2017), 303-310. doi: 10.5829/idosi.ije.2017.30.02b.18.

11. Daniel, C., Hemalatha, G., Sarala, L., Tensing, D. and Sundar Manoharan, S., "Seismic mitigation of building frames using magnetorheological damper", *International Journal of Engineering, Transactions B: Applications,* Vol. 32, No. 11, (2019), 1543-1547. doi: 10.5829/ije.2019.32.11b.05.

12. Seid, S., Chandramohan, S. and Sujatha, S., "Design and evaluation of a magnetorheological damper based prosthetic knee", *International Journal of Engineering*, *Transactions A*: *Basics*, Vol. 32, No. 1, (2019), 146-152. doi: 10.5829/ije.2019.32.01a.19.

13. Hou, Z.N., Feng, Z.M., Hu, H.G. and Wu, G.B., "Experimental study on performance characteristics of magnetorheological damper", in Applied Mechanics and Materials, Trans Tech Publ. Vol. 37, (2010), 439-443.

14. Wu, W. and Cai, C., "Experimental study of magnetorheological dampers and application to cable vibration control", *Journal of Vibration and Control*, Vol. 12, No. 1, (2006), 67-82. doi: 10.1177/1077546306061128.

15. Ganesha, A., Patil, S., Kumar, N. and Murthy, A., "Magnetic field enhancement technique in the fluid flow gap of a single coil twin tube magnetorheological damper using magnetic shields", *Journal of Mechanical Engineering and Sciences*, Vol. 14, No. 2, (2020), 6679-6689.

16. Wani, Z.R., Tantray, M. and Farsangi, E.N., "Investigation of proposed integrated control strategies based on performance and positioning of mr dampers on shaking table", *Smart Materials and Structures*, Vol. 30, No. 11, (2021), 115009.

17. Wani, Z.R., Tantray, M. and Farsangi, E.N., "In-plane measurements using a novel streamed digital image correlation for shake table test of steel structures controlled with mr dampers", *Engineering Structures*, Vol. 256, (2022), 113998.

18. Cruze, D., Gladston, H., Farsangi, E.N., Banerjee, A., Loganathan, S. and Solomon, S.M., "Seismic performance evaluation of a recently developed magnetorheological damper: Experimental investigation", *Practice Periodical on Structural Design and Construction*, Vol. 26, No. 1, (2021), 04020061.

19. Cruze, D., Gladston, H., Farsangi, E.N., Loganathan, S., Dharmaraj, T. and Solomon, S.M., "Development of a multiple coil magneto-rheological smart damper to improve the seismic resilience of building structures", *The Open Civil Engineering Journal*, Vol. 14, No. 1, (2020). doi.

20. Abdeddaim, M., Djerouni, S., Ounis, A., Athamnia, B. and Farsangi, E.N., "Optimal design of magnetorheological damper for seismic response reduction of base-isolated structures considering soil-structure interaction", in Structures, Elsevier. Vol. 38, (2022), 733-752.

21. Rashid, Z., Tantray, M. and Noroozinejad Farsangi, E., "Acceleration response-based adaptive strategy for vibration control and location optimization of magnetorheological dampers in multistoried structures", *Practice Periodical on Structural Design and Construction*, Vol. 27, No. 1, (2022), 04021065.

22. Wani, Z.R., Tantray, M. and Farsangi, E.N., "Shaking table tests and numerical investigations of a novel response-based adaptive control strategy for multi-story structures with magnetorheological dampers", *Journal of Building Engineering*, Vol. 44, (2021), 102685.

23. Wani, Z.R., Tantray, M.A., Iqbal, J. and Farsangi, E.N., "Configuration assessment of mr dampers for structural control

using performance-based passive control strategies", *Structural Monitoring and Maintenance*, Vol. 8, No. 4, (2021), 329-344.

24. Sharma, S.V., Hemalatha, G. and Ramadevi, K., "Analysis of magnetic field-strength of multiple coiled mr-damper using comsol multiphysics", *Materials Today: Proceedings*, (2022). doi: 10.1016/j.matpr.2022.05.279.

25. Jolly, M. and Sun, J., "Lord corporation, thomas lord research center", *Smart Structures and Materials: Passive Damping*, (1994), 194.

26. Guo, N., Du, H. and Li, W., "Finite element analysis and simulation evaluation of a magnetorheological valve", *The International Journal of Advanced Manufacturing Technology*, Vol. 21, No. 6, (2003), 438-445.

27. Dixon, J.C., "The shock absorber handbook, John Wiley & Sons, (2008).

28. Carlson, J.D., Catanzarite, D. and St. Clair, K., "Commercial magneto-rheological fluid devices", *International Journal of Modern Physics B*, Vol. 10, No. 23n24, (1996), 2857-2865.

29. Xu, Z.-D., Jia, D.-H. and Zhang, X.-C., "Performance tests and mathematical model considering magnetic saturation for magnetorheological damper", *Journal of Intelligent Material Systems and Structures*, Vol. 23, No. 12, (2012), 1331-1349.

30. Wang, X. and Gordaninejad, F., "Dynamic modeling of semi-active er/mr fluid dampers", in Smart structures and materials 2001: Damping and isolation, SPIE. Vol. 4331, (2001), 82-91.

31. Jiang, X., Wang, J. and Hu, H., "Designing and modeling of a novel magneto-rheological fluid damper under impact load", in 3rd International Conference on Mechanical Engineering and Mechanics, Beijing, China., (2009), 203-207.

Persian Abstract

چکیده

این مقاله طراحی یک دمپر مغناطیسی (MR) را ارائه می‌کند که شامل آرایش پیستون و سیلندر است. این مطالعه یک مدل سه بعدی را بر اساس مفهوم روش المان محدود (FEM) در COMSOL Multiphysics برای تجزیه و تحلیل و بررسی ویژگی‌های دمپر MR ایجاد کرد. یک نمونه اولیه از دمپر MR بر اساس مدل FEM ساخته می‌شود و با استفاده از Servo-Hydraulic MTS تحت یک سری آزمایش قرار گرفته است. حداکثر و حداقل نیرو، N۱۷۱.۵۲۳۵ و N۲۴۹.۲۷۴۹، به ترتیب در Hz۰.۱ و Hz۱، برای مدل FEM اندازه گیری شد. مدل ساخته شده نتایج مشابهی را در ۰.۱ هرتز و ۱ هرتز، با حداکثر و حداقل نیروهای N۱۷۵.۹۱۰۳ و N۲۵۲.۷۷۶۵ به دست آورد. مقایسه این دو تحلیل مدل نشان می‌دهد که مدل مبتنی بر FEM به دقت رفتار تجربی دمپر MR را از نظر نیروی میرایی آن به تصویر می‌کشد، اگرچه تغییرات جزئی وجود دارد. یافته‌های این مقاله برای طراحان در ایجاد دمپرهای MR که کارآمدتر و قابل اعتمادتر هستند و همچنین در پیش‌بینی ویژگی‌های نیروی میرایی آنها مفید خواهد بود.

AIMS AND SCOPE

The objective of the International Journal of Engineering is to provide a forum for communication of information among the world's scientific and technological community and Iranian scientists and engineers. This journal intends to be of interest and utility to researchers and practitioners in the academic, industrial and governmental sectors. All original research contributions of significant value focused on basics, applications and aspects areas of engineering discipline are welcome.

This journal is published in three quarterly transactions: Transactions A (Basics) deal with the engineering fundamentals, Transactions B (Applications) are concerned with the application of the engineering knowledge in the daily life of the human being and Transactions C (Aspects) - starting from January 2012 - emphasize on the main engineering aspects whose elaboration can yield knowledge and expertise that can equally serve all branches of engineering discipline.

This journal will publish authoritative papers on theoretical and experimental researches and advanced applications embodying the results of extensive field, plant, laboratory or theoretical investigation or new interpretations of existing problems. It may also feature - when appropriate - research notes, technical notes, state-of-the-art survey type papers, short communications, letters to the editor, meeting schedules and conference announcements. The language of publication is English. Each paper should contain an abstract both in English and in Persian. However, for the authors who are not familiar with Persian, the publisher will prepare the latter. The abstracts should not exceed 250 words.

All manuscripts will be peer-reviewed by qualified reviewers. The material should be presented clearly and concisely:

- *Full papers* must be based on completed original works of significant novelty. The papers are not strictly limited in length. However, lengthy contributions may be delayed due to limited space. It is advised to keep papers limited to 7500 words.
- *Research* notes are considered as short items that include theoretical or experimental results of immediate current interest.
- *Technical notes* are also considered as short items of enough technical acceptability with more rapid publication appeal. The length of a research or technical note is recommended not to exceed 2500 words or 4 journal pages (including figures and tables).

Review papers are only considered from highly qualified well-known authors generally assigned by the editorial board or editor in chief. Short communications and letters to the editor should contain a text of about 1000 words and whatever figures and tables that may be required to support the text. They include discussion of full papers and short items and should contribute to the original article by providing confirmation or additional interpretation. Discussion of papers will be referred to author(s) for reply and will concurrently be published with reply of author(s).

INSTRUCTIONS FOR AUTHORS

Submission of a manuscript represents that it has neither been published nor submitted for publication elsewhere and is result of research carried out by author(s). Presentation in a conference and appearance in a symposium proceeding is not considered prior publication.

Authors are required to include a list describing all the symbols and abbreviations in the paper. Use of the international system of measurement units is mandatory.

- On-line submission of manuscripts results in faster publication process and is recommended. Instructions are given in the IJE web sites: www.ije.ir-www.ijeir.info
- Hardcopy submissions must include MS Word and jpg files.
- Manuscripts should be typewritten on one side of A4 paper, double-spaced, with adequate margins.
- References should be numbered in brackets and appear in sequence through the text. List of references should be given at the end of the paper.
- Figure captions are to be indicated under the illustrations. They should sufficiently explain the figures.
- Illustrations should appear in their appropriate places in the text.
- Tables and diagrams should be submitted in a form suitable for reproduction.
- Photographs should be of high quality saved as jpg files.
- Tables, Illustrations, Figures and Diagrams will be normally printed in single column width (8cm). Exceptionally large ones may be printed across two columns (17cm).

PAGE CHARGES AND REPRINTS

The papers are strictly limited in length, maximum 8 journal pages (including figures and tables). For the additional to 8 journal pages, there will be page charges. It is advised to keep papers limited to 3500 words.

Page Charges for Papers More Than 8 Pages (Including Abstract)	
For International Author ***	**$55 / per page**
For Local Author	**100,000 Toman / per page**

AUTHOR CHECKLIST

- Author(s), bio-data including affiliation(s) and mail and e-mail addresses).
- Manuscript including abstracts, key words, illustrations, tables, figures with figure captions and list of references.
- MS Word files of the paper.